TAILORING FUNCTIONAL II-CONJUGATED POLYMERS AND MOLECULES FOR ORGANIC PHOTOVOLTAIC APPLICATIONS

A Dissertation
Presented to
The Academic Faculty

by

Chi Kin Lo

In Partial Fulfillment
of the Requirements for the Degree
Doctor of Philosophy in the
School of Chemistry & Biochemistry

Georgia Institute of Technology
May 2017

TAILORING FUNCTIONAL II-CONJUGATED POLYMERS AND

MOLECULES FOR ORGANIC PHOTOVOLTAIC APPLICATIONS

Approved by:

Dr. John R. Reynolds, Advisor
School of Chemistry & Biochemistry
Georgia Institute of Technology

Dr. Jean-Luc Brédas
School of Chemistry & Biochemistry
Georgia Institute of Technology

Dr. Elsa Reichmanis
School of Chemical and Biomolecular Engineering
Georgia Institute of Technology

Dr. Seth R. Marder
School of Chemistry & Biochemistry
Georgia Institute of Technology

Dr. Joseph P. Sadighi
School of Chemistry & Biochemistry
Georgia Institute of Technology

Date Approved: January 17th, 2017

"Remember to look up at the stars and not down at your feet. Try to make sense of what you see and wonder about what makes the universe exist. Be curious. And however difficult life may seem, there is always something you can do and succeed at."

- Stephen Hawking

"It was a heroic time. It was not the doing of any one man; it involved the collaboration of scores of scientists from many different lands."

- J. Robert Oppenheimer

"Whenever you find
Yourself doubting how
Far you can go,
Just remember how
Far you have come.
Remember everything
You have faced,
All the battles
You have won,
And all the fears
You have overcome."

- Unknown

To

Lou and my parents

for their unconditional love and unwavering support

ACKNOWLEDGEMENTS

Completing a Ph.D. is one of the most humbling and transformative experiences in a person's life. From someone who finished his MBA with no job prospect and little scientific training to a person who is a confident scientist and an effective leader, I can sincerely say that my transformation is gratifying. *"It takes a whole village to raise a child"* is a fitting way to describe the training of a Ph.D. scientist, and my "upbringing" has definitely required "a village". Here, I would like to express my most heartfelt gratitude towards the "villagers" who had helped me every step of this journey.

First, I must thank Dr. Lou Kavar, who has shown me what unconditional love means. He has supported all of my life and career decisions since we met 14 years ago. He has always provided me the space I need to do what feel right. The same goes for my parents, Lo Wai Ping and Chan Lai Mui, who have taught me determination and have provided me all the necessary resources to (often waywardly and stubbornly) chase after my dreams.

My gratitude also goes to my Ph.D. research advisor, Dr. John R. Reynolds. I am glad to be the first Ph.D. graduate in his Georgia Tech era. I have said many times during my Ph.D. study, I could not have gotten the number of opportunities in any other group but the Reynolds Group. Dr. Reynolds has pushed me to become a strong leader since our "official handshake". His encouragement and support have allowed me to succeed as the scientist in my TI:GER team, as the synthesis laboratory coordinator, as the group lead in the MURI-CAOP program, as a collaborator in my research projects, and as a student

leader in GTPN. As always, he has shown that an academic research advisor can be just like a father, who treats his students and colleagues with care, kindness, and respect. I would also like to thank my undergraduate research advisor, Dr. Jennifer Aitken. While my stay in her laboratory was short, her confidence in my experimental techniques and her support of my pursuit of a doctorate degree in Chemistry were critical in my scientific journey. I want to also thank my thesis committee members, Dr. Seth Marder, Dr. Jean-Luc Brédas, Dr. Elsa Reichmanis, and Dr. Joseph Sadighi for their scientific input, direction, and encouragement.

My Ph.D. work would not have been possible without the collaborative work from a group of enthusiastic and world-class scientists: Dr. Iordania Constantinou, Xueping Yi, and Dr. Franky So at the University of Florida and the North Carolina State University; Dr. Bhoj Gautam and Dr. Kenan Gundogdu at the North Carolina State University; Dr. Zilong Zheng, Dr. Raghunath Dasari, Dr. Veaceslav Coropceanu, Dr. Cheng-Yin Wang, Dr. Canek Fuentes-Hernendez, and Dr. Bernard Kippelen at Georgia Tech; Dr. Stefan Oosterhout and Dr. Michael Toney at SLAC National Accelerator Laboratory; and Philipp Selter and Dr. Michael Ryan Hansen at Westfälische Wilhelms-Universität Münster. I also want to acknowledge the financial support from the Office of Navy Research, the Georgia Tech TI:GER fellowship program, and the Georgia Tech COPE fellowship program which made my research possible.

Entering the fields of organic electronics, organic chemistry, and polymer chemistry was a daunting task, and I am thankful for the guidance of a group of generous and patient research scientists, curious and supportive group mates, and endearing and energetic friends who have walked by my side during the past five years. Considered to

be “the next Caroline” in the Reynolds Group since the day I joined and till today, I first want to thank Dr. Caroline Grand for introducing me to our organic chemistry laboratory through the synthesis and purification of isoindigo, for showing me optoelectronic and physical characterization techniques, and for teaching me how to fabricate and evaluate organic photovoltaic devices. Many thanks to Dr. Natasha Teran for her scientific advice especially during the year I began working on glyme chemistry and for her emotional support throughout the years. Thank you to Rylan Michael Webster Wolfe for keeping me in check with my chemistry and for sharing with me his fondness towards a specific variety of adult malt beverage. I want to acknowledge a group of individuals for their encouragement and knowledge, particularly during my early time in the Ph.D. program: Dr. Justin Kerszulis, Dr. Toan Pho, Dr. Coralie Richard, Dr. Anna Österholm, Dr. Eric Shen, Dr. Hayden Black, Dr. Aubrey Dyer, Dr. Leandro Estrada, Dr. Gaëlle Deshayes, Dr. Ray Bulloch, James Ponder, Dr. Purva Kodlekere, Erica Chen, Melissa Martinez, Rebecca Hill, Dr. Sai Shum, and Jimmy Deininger. I also want to encourage the “young” Reynolds Group members to continue living up to our group’s standard: Linda Nhon, Sandy Pittelli, Ian Pelse, Xiaochu Ba, Melony Ochieng, Brian Schmatz, Dylan Christiansen, Gus Lang, Abi Advincula, and Lisa Savagian.

I was fortunate to receive help from a group of passionate administrative professionals who made navigating graduate school a much easier process: Thanks to Dr. Cam Tyson and Dr. Kenyetta Johnson for their academic advice; Aeryal Herrod, Jackie Ferrell, and Venese Blake-Leggett who worked tirelessly on coordinating my many business trips and setting up documents.

A very special thank you to Dr. Stephen Hawking, to whom I truly owe my scientific career. On a late evening during the early Spring of 2010, while I was contemplating my next move during unemployment, his book, The Universe in a Nutshell, lit the fire of scientific curiosity in me and motivated me to make the brave decision to pursue a doctorate degree in chemistry.

I still recall how insecure I felt when I was going through the Ph.D. candidacy examination. Dr. Anna Österholm's encouragement had helped me a great deal during that process. She said that the day she defended her thesis was the day during her Ph.D. study when she felt she knew the least, because she had just finished the highest academic degree in the field of chemistry but yet still knew very little about science. The knowledge we discover and the contribution we make in science are so focused on just one or a few particular areas. We must humbly recognize, just like training a young scientist, that it truly takes a whole village (a collection of scientists in different disciplines) to raise a child (unveil the secrets of the universal).

TABLE OF CONTENTS

LIST OF TABLES

LIST OF FIGURES

LIST OF SCHEMES

LIST OF SYMBOLS AND ABBREVIATIONS

ACN	Acetonitrile
AFM	Atomic force microscopy
BDT	Benzodithiophene
BHJ	Bulk heterojunction
BOE	Buffer oxide etch
CB	Chlorobenzene
CIGS	Copper indium gallium selenide
CT	Charge transfer
CV	Cyclic voltammetry
DCM	Dichloromethane
DFT	Density functional theory
DIO	1,8-Diiodooctane
$Đ_M$	Dispersity
DMF	*N*,*N*-dimethylformamide
DPP	Diketopyrrolopyrrole
DPV	Differential pulse voltammetry
DSC	Differential scanning calorimetry
EA	Electron affinity
EC	Electrochromic
E_g	Energy gap
E_g^{opt}	Optical energy gap
ETL	Electron transport layer

Fc/Fc^+	Ferrocene/ferrcenium
FET	Field-effect transistor
FF	Fill factor
GIWAXS	Grazing Incident Wide Angle X-ray Scattering
GPC	Gel permeation chromatography
HOMO	Highest occupied molecular orbital
HPLC	High-performance liquid chromatography
HTL	Hole transport layer
ICP-MS	Inductively Coupled Plasma Mass Spectrometry
IDT	Indacenodithiophene
iI	Isoindigo
IP	Ionization potential
IPCE	Incident photon to current efficiency
IRF	Instrument response function
ITO	Indium tin oxide
J_{sc}	Short-circuit current
k_B	Boltzmann's constant
LB	Langmuir-Blodgett
LbL	Layer-by-layer
LUMO	Lowest unoccupied molecular orbital
M_n	Number average molecular weight
NBS	*N*-Bromosuccinimide
NDI	Naphthalene diimide
*o*DCB	*ortho*-Dichlorobenzene
OFET	Organic field-effect transistor

OLED	Organic light-emitting diode
OPA	Optical parametric amplifier
OPV	Organic photovoltaic
$PC_{61}BM$	[6,6]-Phenyl-C71-butyric acid methyl ester fullerene
$PC_{71}BM$	[6,6]-Phenyl-C71-butyric acid methyl ester fullerene
PCE	Power conversion efficiency
$Pd(PPh_3)_4$	Tetrakis(triphenylphosphine)palladium(0)
$Pd_2(dba)_3$	Tris(dibenzylideneacetone)dipalladium(0)
PDI	Perylene diimide
PEDOT:PSS	Poly(3,4-ethylenedioxythiophene):poly(styrenesulfonate)
P_{max}	Maximum power
q	Elementary electron charge
RFID	Radio-frequency identification
R_s	Series resistance
R_{sh}	Shunt resistance
SCLC	Space-charge limited-current
TAS	Transient absorption spectroscopy
$TBAPF_6$	Tetrabutylammonium hexafluorophosphate
T_c	Crystallization temperature
TCB	1,2,4-Trichlorobenzene
T_g	Glass transition temperature
TGA	Thermogravimetric analysis
THF	Tetrahydrofuran
TiI	Thienoisoindigo
T_m	Melting temperature

TPD	Thienopyrrolodione
TR	Transfer ratio
V_{oc}	Open-circuit voltage
ε	Extinction coefficient
ε_r	Dielectric constant

SUMMARY

Understanding the structure-property relationship in organic photovoltaic (OPV) materials is crucial to continue the recent improvement in device performance. However, many high performing donor polymers with power conversion efficiencies (PCEs) of 8-10% have different molecular structures, frontier energy levels, and physical properties. Even polymers with structural similarities may not be easily compared because of their batch-to-batch variances which is an intrinsic drawback of polymeric materials. The first part of Chapter 3 of this dissertation presents a family of photoactive conjugated polymers with only a "one-atom" minimal change. This showcases the use of thorough cross-coupling polymer synthesis and purification as well as structural and physical characterization techniques to elucidate structure-property understanding in designing OPV materials. The second part of the chapter continues with the theme of structure-property investigation, focusing on a series of donor-acceptor polymers containing various election-deficient conjugated moieties such as isoindigo, diketopyrrolopyrrole, and thienoisoindigo. This family of polymers is used to explain how the structures and frontier energy levels of the acceptor units affect the open-circuit voltages, the active layer morphologies, and device performances.

Supramolecular assembly of π-conjugated materials is crucial in high performance organic electronic device fabrication. Materials that self-assemble into ordered domains with length scale of 5 and 100 nm can bridge the gap between single molecule electronics, in which molecular orientation and conformation dictate charge carrier direction and mobility, and polymer electronics, in which dispersities and

backbone defects can hinder device performance. Many of these materials are amphiphilic in nature, leading to high degrees of intermolecular organization as a result of the nanoscale phase separation between the hydrophilic and hydrophobic moieties which assemble into highly ordered domains. Non-covalent interactions such as π-π interactions, hydrogen bond, dipole-dipole interactions, and steric effect determine the spontaneous self-organization process. However, this self-assembly process, both in solution and during film formation, is thermodynamically driven and is controlled by the choice of deposition technique. To obtain full control in bottom-up assembly, layer-by-layer (LbL) deposition emerges as an excellent candidate for depositing organic materials. Langmuir-Blodgett (LB) is an LbL technique that can achieve a true molecular monolayer buildup. In Chapter 4, characterizations of these LbL thin-films are the main focus, especially with morphological and structural studies on the Langmuir-Blodgett films of two amphiphilic conjugated molecules. Both OPV and OFET performances are discussed, showing the use of Langmuir-Blodgett deposition to create well-ordered material layers in organic electronic applications.

Despite its popularity as a universal acceptor in an OPV device, fullerene derivatives have high production cost, weak absorption, and limited chemical stability. To improve device performance, the OPV field has focused on designing non-fullerene acceptors. Chapter 5 first introduces the design regarding a family of polymeric acceptors. The syntheses of the polymers based on acceptor moieties including isoindigo, thienoisoindigo, diketopyrrolopyrrole, and thienopyrrolodione highlight the use of direct arylation reaction to achieve pure and high molecular weight conjugated polymers. The different acceptor moieties are selected to allow systematic adjustment of the energy

levels in order to enhance the absorption of low energy photons. Structural designs and morphological investigations are presented to correlate with the charge carrier transport property, which is proven to be critical for the development of high performance non-fullerene acceptors.

Finally, an outlook of the organic photovoltaics is discussed in Chapter 6. Niche applications are presented and serve as examples for future market opportunities of the OPV technology. This chapter also highlights the potentials of each material class in this dissertation for real world organic photovoltaics market applications.

CHAPTER 1

INTRODUCTION

1.1. General Background on Organic Electronics

The utilization of organic semiconducting π-conjugated materials in electronic applications introduces the possibility of fabricating light-weight and flexible devices such as field effect transistors (OFETs),[1,2,3,4,5] electrochromic (EC) devices,[6] photovoltaics (OPVs)[7,8,9,10] and photosensors,[11,12] memory devices,[13,14,15] as well as commercially available light emitting diodes (OLEDs).[16,17] The potential of non-energy intensive, low-cost, and solution processed manufacturing makes organic electronics an attractive field of study. Unlike their inorganic counterparts such as silicon and metal oxide semiconductors, organic semiconductors possess many intrinsic advantages. For example, the physical and electronic properties are controlled by structural design and modification, leading to an endless variety of possible materials; their solution processability allows for high throughput deposition onto large-area devices *via* industrial-compatible roll-to-roll coating methods; and their thin-film and colorful design improves application versatility.

Organic electronics emerged as a field of study when Alan MacDiarmid, Hideki Shirakawa, and Alan Heeger discovered the metallic conductivity of iodine-doped polyacetylene in the 1970s. This discovery led to the award of the Nobel Prize in Chemistry to the three scientists in 2000. In 1974, Shirakawa and coworkers polymerized acetylene *via* the Ziegler-Natta reaction.[18] The resulting polyacetylene formed a silvery

film with metallic appearance, which had low conductivity in its neutral form. Upon doping by iodine vapor, the conductivity of the polyacetylene film increased seven orders of magnitude to ~ 10^2 S cm^{-1} (in comparison, the conductivities of silver and copper are at $10^5 – 10^6$ S cm^{-1}) at room temperature.[19,20]

1.2. Electronic Structures of Conjugated Systems

An important aspect of conjugated polymers is the presence of alternating single and double bonds between adjacent carbon atoms, resulting in a connection of sp^2 orbitals along the backbones and the $2p_z$ orbital situating above and below the internuclear plane. The overlapping of the $2p_z$ orbitals between adjacent carbon atoms results in a connected network of π-bonds, which gives rise to the electronic properties in the conjugated materials. To understand the electronic structure of conjugated systems, we can examine polyacetylene, as it is arguably the conjugated polymer with the simplest structure. As illustrated in Figure 1-1, as the conjugation extends from ethylene, butadiene, to polyacetylene, the energy gaps between the highest occupied molecular orbital (HOMO) and the lowest unoccupied molecular orbital (LUMO) decrease as a result of the increasing number of overlapping p orbitals. In a hypothetical case, if all the carbon-carbon bonds in the conjugated system were equivalent in length, as the conjugation increased, the energy gap would disappear and the material should have conductivity like a metal. However, a quasi one-dimensional system with an equally spaced chain is unstable and a distortion in the periodicity leads to a net stabilization,[21,22,23] a phenomenon known as the Peierls distortion. The physical effect is known as bond length alternation, which gives alternating short and long bonds between adjacent carbons in a

π-system. This stabilization effect lowers the energy of the HOMO and leads to a higher energy LUMO, resulting in an energy gap, and thus the semiconducting properties in conjugated polymers.

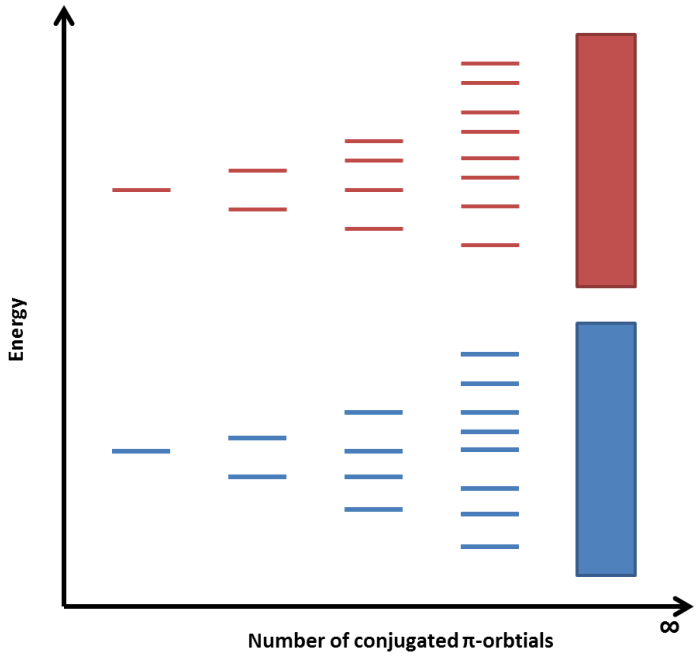

Figure 1-1. Schematic diagram of the progression in energy gaps between the highest occupied molecular orbital (HOMO) and the lowest unoccupied molecular orbital (LUMO) as conjugation increases. (Adapted from reference[22].)

1.2.1. Comparison of Inorganic and Organic Semiconductors

Currently, most electronic devices make use of inorganic semiconductors. For instance, roof-top solar panels consist of multicrystalline silicon. If organic materials are to replace inorganic semiconductors for electronic applications, it is necessary to understand the differences between organic and inorganic semiconductors.

Silicon is a popular material for light absorption applications due to its low bandgap of 1.1 eV. Silicon solar panels usually consist of thick silicon active layers of ~100 μm due to the indirect energy gap intrinsic to silicon, resulting in a low absorption

coefficient (10^3 cm^{-1} at 700 nm).[24,25] For a material with an indirect energy gap, as shown in Figure 1-2, the crystal momentum at the bottom of the conduction band is different from that at the top of the valence band (i.e. different k-vector in the Brillouin zone).[26,27] In this case, the transition of an electron from the valence band to the conduction band requires the energy of a photon *and* the assistance of a phonon to offset the change in momentum. This additional requirement, involving the interaction between a photon, an electron, *and* a phonon, results in the weak absorptions of indirect band gap materials. In contrast, gallium arsenide (GaAs) is also an inorganic material used for photovoltaics, but with a band structure that leads to a direct energy gap.[28] For direct energy gap materials, only an electron-photon interaction is required for light absorption since their valence and conduction bands are vertically aligned. Organic semiconductors are usually direct band gap semiconductors and often have absorption coefficients on the order of 10^4 to 10^5 cm^{-1} in the visible region. This allows thin-films to be used in organic photovoltaic applications. The thin-film design also enhances charge extraction within the devices, which is especially important since charge mobility is generally lower for organic semiconductors than their inorganic counterparts. The higher mobility of inorganic materials is a result of their ordered crystalline structures providing well-defined pathways for the charges to travel across the materials. In order to achieve the highly ordered crystal structure, silicon semiconductors used in electronic devices must have extremely high purities with low defect concentrations because defects are detrimental to their electronic properties.[29] In contrast, organic semiconductors are usually semicrystalline or amorphous. They can be processed *via* less energy intensive methods

such as solution deposition as opposed to vapor-phase epitaxial growth used in fabricating devices using crystalline silicon materials.

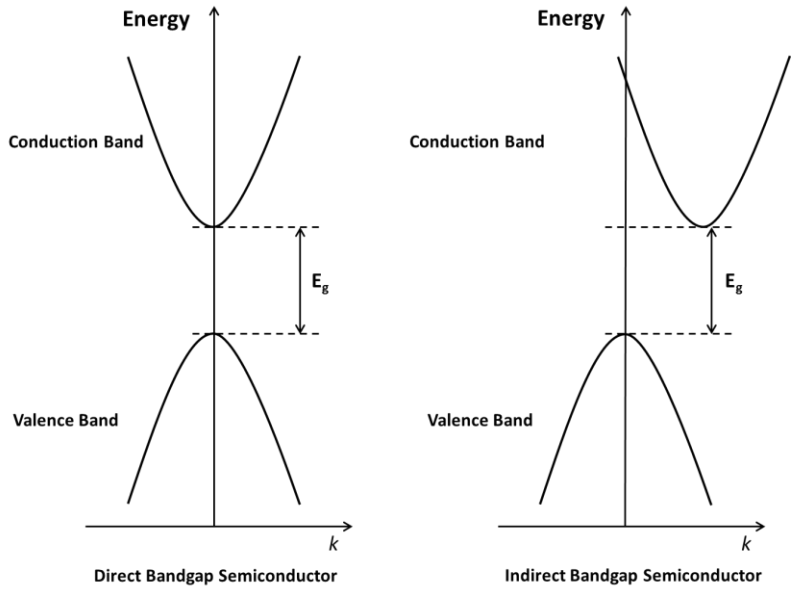

Figure 1-2. Direct and indirect band gaps along crystal momentum k-vector.

1.3. Design of Conjugated Materials for Frontier Orbital Energy and Morphology Control

1.3.1. Structural Control of Optoelectronic Properties

The emission spectrum and the intensity of the incident sunlight determine the amount of light energy available to a photovoltaic device. In a laboratory setting, the illumination is generated by a solar simulator which produces an Air Mass 1.5 (AM 1.5) solar irradiance spectrum (Figure 1-3). Close to 80% of the total cumulative photon flux is generated by photons in the region between 300 and 1500 nm. In order to fully exploit the sun's irradiation, the light absorbing materials within the active layer of OPV devices

should have sufficiently low energy absorption bands, which lie within the wavelength where the photon flux is the highest. The structural versatility and availability of organic semiconductors with different energy gaps allow efficient light absorption across the visible region of the solar irradiation spectrum.

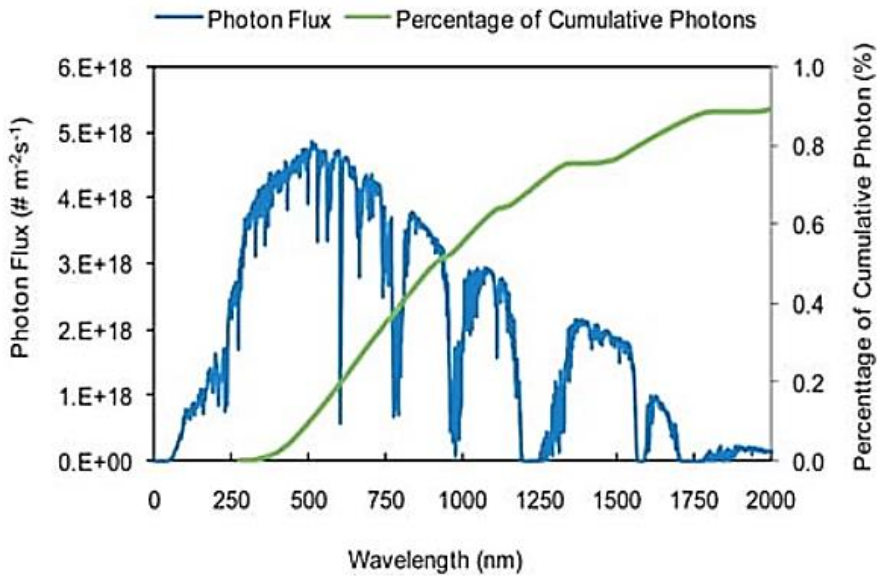

Figure 1-3. The AM1.5 global photon flux spectrum and the percentage of the cumulative photon flux showing that the majority of the solar photons are located in the spectral region of 300–1500 nm. (Reproduced with permission from reference[30].)

To maximize the amount of sunlight absorbed, the ground and excited states of the donor should also have high vibrational wave function overlaps (Franck–Condon principle) to achieve high oscillator strength, which leads a large extinction coefficient of the material. The acceptor, usually a fullerene derivative such as $PC_{61}BM$ and $PC_{71}BM$, complementarily absorb photons between 350 nm and 700 nm. The main advantage of using fullerene derivatives as the electron acceptor in OPV devices is that their ionization potential (IP) and electron affinity (EA) allow for favorable offsets against the energy levels of many donor materials, leading to efficient charge transfer and separation. Non-

fullerene acceptors, which have gained popularity over the past five years, will also be discussed later in Chapters 5 and 6.

1.3.2. Energy Gap Control with the Donor-Acceptor Approach

A popular way to adjust the energy gap in semiconducting organic materials is covalently coupling conjugated electron-rich and electron-poor units, an approach pioneered by Havinga *et al.*[31] As illustrated in Figure 1-4, the resulting material has a reduced energy gap arising from the orbital mixing between the electron-rich and electron-poor moieties, which enhances the absorption of low energy photons and can improve photocurrent generation. However, a conflict exists between achieving high J_{sc} and high V_{oc}. Lowering the energy gap of a donor material often also reduces the difference between its ionization potential and the electron affinity of the acceptor, thus limiting the photovoltage of an OPV device.

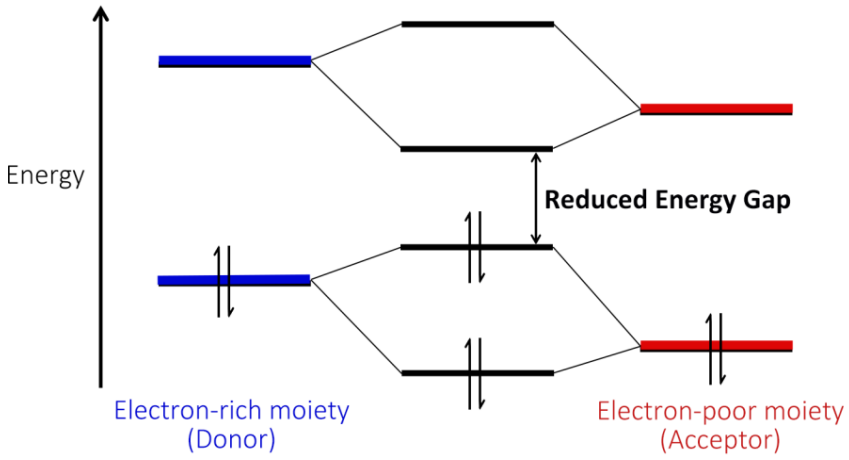

Figure 1-4. Illustration for the frontier energy levels of the donor and acceptor units. The orbital mixing in an electron-rich and electron-poor (donor-acceptor or D-A) system leads to a lowering of the overall energy gap in the resulting materials. (Adapted from reference [31].)

When designing donor materials, aromaticity and bond length alternation, backbone rigidity and planarity, functionalization, and interchain interactions should be taken into consideration. For example, the backbone rigidity of the donor polymer can be controlled by introducing multi-fused ladder-type arenes such as dithienosilole, dithienogermole, and indacenodithiophene.[32] By substituting the electron-poor units with electron-withdrawing functional groups such as fluorine[33] and nitrile,[34] molecules and polymers can be engineered to have appropriate ionization potentials, resulting in broad absorptions across the visible region of the solar spectrum leading to high Jsc, as well as large difference between the donor's IP and the acceptor's EA resulting in high V_{oc} in OPV devices.

D-A systems usually have dual-band absorption profiles, which is generally believed to arise from the higher energy π-π^* transition and the lower energy donor-acceptor intramolecular charge transfer transition.[35,36,37,38] The donor materials shown in Figure 1-5 contains both electron-rich and electron-poor moieties and can be used to conveniently synthesize conjugated molecules and polymers by cross coupling reactions such as Stille, Suzuki, and direct arylation reactions.[39] Some of the most widely used electron-poor building blocks[9] in materials for OPVs include isoindigo (iI), thienopyrrolodione (TPD), diketopyrrolopyrrole (DPP), and thienoisoindigo (TiI). This dissertation will present molecular and polymeric materials synthesized using the aforementioned building blocks, with an aim to study the structural, morphological, and electronic effects on organic photovoltaic device performance.

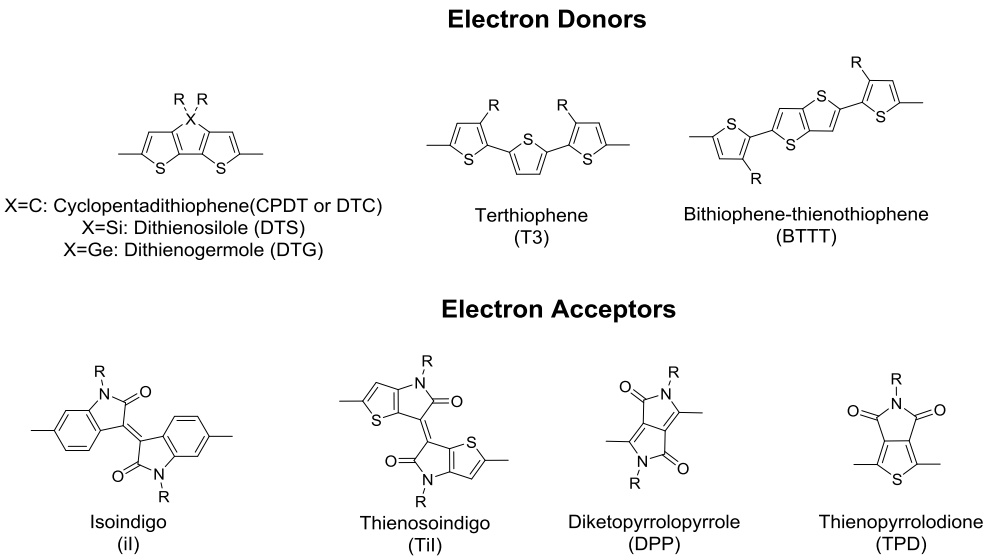

Figure 1-5. Structures of electron donors and the electron acceptors as building blocks for efficient oligomeric and polymeric systems for OPV applications.

1.3.3. Polymers vs. Discrete Conjugated Molecules

In this dissertation, both molecular and polymeric semiconducting materials will be presented. Molecular materials refer to those materials with well-defined molecular structures; polymeric materials refer to those materials with higher, but dispersed molecular weights. Both molecular and polymeric materials have been studied extensively in the organic electronics community; each has its own advantages and disadvantages. Molecular semiconductors have well-defined chemical structures, thus having minimal batch-to-batch variations. They can be easily purified by column chromatography to achieve high purity for device applications. However, molecular systems tend to be more crystalline and can be problematic during solution processing and film formation. Polymeric materials, in contrast, have excellent film forming ability and are also more mechanically robust. However, their optoelectronic properties are molecular weight dependent, so obtaining optimal and reproducible molecular weight polymers is crucial for material processing and device performance. The purification of

polymeric materials is also more complicated, with residual metal catalyst potentially trapped in the polymer matrix affecting device performance.

1.4. Organic Photovoltaics (OPVs): Operating Principles

1.4.1. OPV Device Operating Principles

The photovoltaic process in OPVs is fundamentally different from its silicon counterpart as a result of the low intrinsic dielectric constants of organic materials. As opposed to the one-component design in silicon cells, the active layers in OPV devices are usually made up of a bulk heterojunction (BHJ) design with an interpenetrating network consisting of π-conjugated organic oligomeric or polymeric materials as donors and fullerenes as acceptors.[40,41] This light absorbing blend harvests photons from the incident radiation and generates an electrical current. The general structure of the light absorbing polymer includes: the π-conjugated backbone which controls the semiconducting properties and can be fine-tuned by altering the chemical nature and structure of the moieties; and the flexible side chains which allow for solution processability and promote interchain interactions. Organic materials used in OPVs are usually based on the thiophene moieties. They have broad absorptions across the visible region of the solar spectrum as well as high ionization potentials (IPs) $\geq$ 4.7 eV (for example, IP of poly(3-hexylthiophene) is 4.65 eV measured by ultraviolet photoemission spectroscopy),[42] and thus can be air-stable.

The field of OPVs has developed into an active research topic in applied polymer, materials, and chemical sciences over the past two decades due to the continuous improvement in device performance. The solution-processability of the organic active

layer materials allows for the development of low-cost, flexible, and lightweight solar devices which can be manufactured through a variety of high-throughput roll-to-roll printing methods[43,44,45,46] such as blade coating, slot-die coating, spray coating, and ink-jet printing.

1.4.2. Active Layer Architectures: Bilayer vs. Bulk Heterojunction

For both organic and inorganic materials, photoexcitation leads to the generation of excitons, which are defined as coulombically bound electron-hole pairs. The exciton then needs to split into separate charges to produce photocurrent in a solar device. Since inorganic materials have high bulk dielectric constants, the generated excitons are weakly bound with a binding energy on the order of 10 meV. In comparison, organic materials have low dielectric constants and higher exciton binding energies at ~ 0.2 - 0.5 eV, as a result of the material's low dielectric constant.[47,48,49] This value is too high for a spontaneous thermal separation (kT = 0.025 eV at room temperature).

To overcome the higher exciton binding energy, in the early days of OPVs, the active layer in the device had a bilayer heterojunction design that consisted of a donor layer (hole transporting) and an acceptor layer (electron transporting) as shown in Figure 1-6a. Such design put two semiconducting materials with different ionization potential and electron affinity in contact and was first reported by Tang[50], achieving 1% power conversion efficiency (PCE). At the heterojunction, the energetic offset between the two components allow for the overcoming of the binding energy, leading to electron transfer and charge separation (Figure 1-6b).

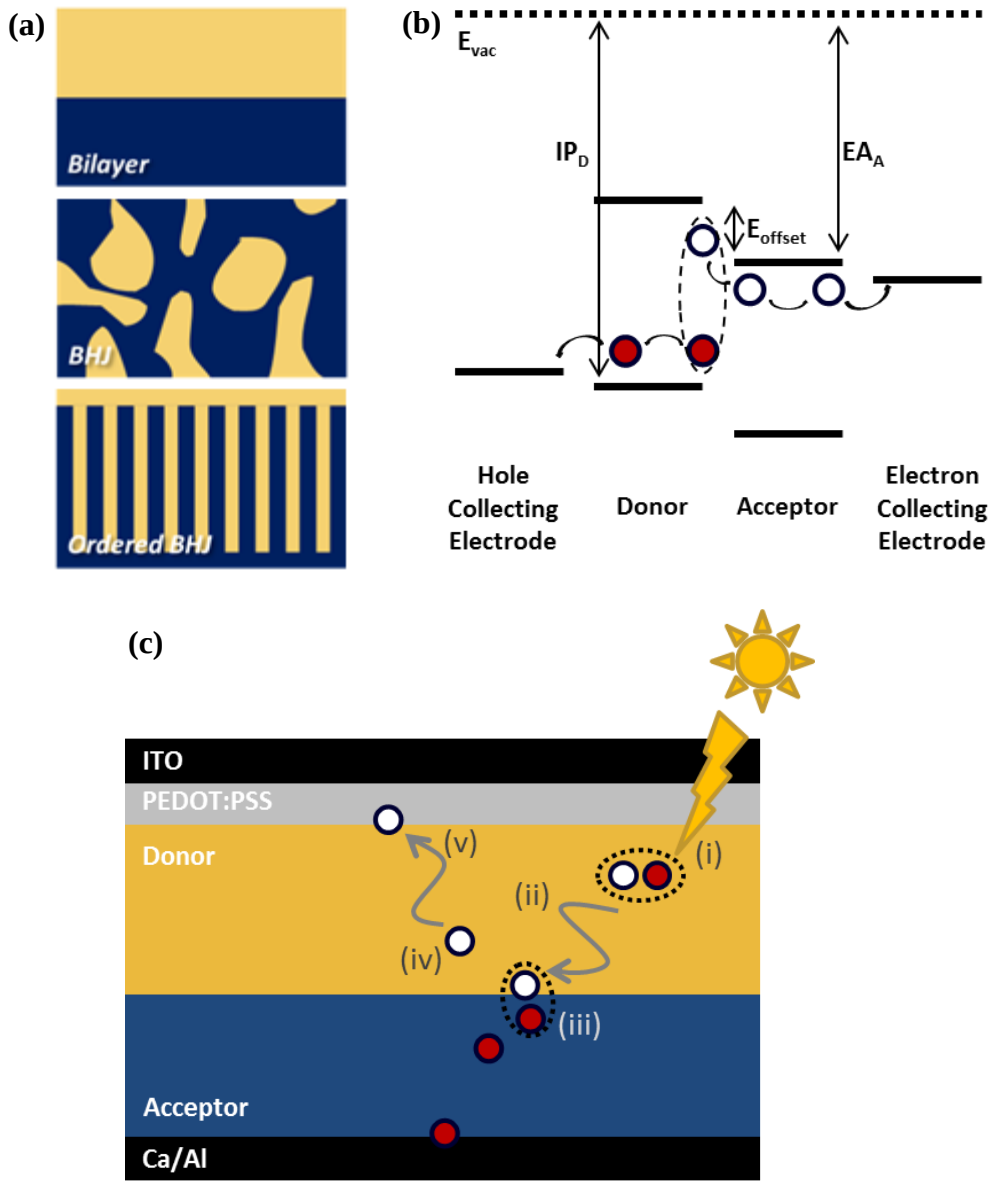

Figure 1-6. (a) Bilayer, random bulk heterojunction, and ordered bulk heterojunction donor and acceptor designs in the active layer of OPVs. (b) Energy level diagram of an organic heterojunction. IP_D and EA_A are ionization potential of the donor and the electron affinity of the acceptor, respectively. An exciton formation in the donor and charge transfer to the acceptor are shown. E_{offset} represents the energy offset between the electron affinities of the donor and acceptor. (c) Schematic layout of the functions and processes in OPVs. (i) Photoexcitation and exciton generation, (ii) exciton diffusion, (iii) charge transfer at donor:acceptor interface, (iv) charge separation (CS), and (v) charge collection. (Adapted from reference [51].)

Pioneered by Wudl and Heeger,[40] the BHJ design later replaced the bilayer design, where the donor and acceptor materials were intermixed together within the active layer. The main reason for the donor-acceptor BHJ design is that the active layer thickness needs to be on the order of hundreds of nanometers to balance between maximizing light absorption and reducing charge recombination due to low charge carrier mobility. However, the exciton diffusion length is typically on the order of 10 nm,[52] therefore a bilayer active layer (i.e. 50 nm of each of the donor and acceptor) is too thick for the electron-hole pair to efficiently migrate to the donor-acceptor interface before charge recombination. The BHJ active layer is designed to solve this shortcoming by increasing the donor-acceptor interfacial area for charge dissociation. Currently, obtaining the desirable morphology of the bulk heterojunction relies on the spontaneous phase separation between the donor and the acceptor, which can be difficult to control and predict. It is important to note that the two-phase system is an idealized representation of the active layer morphology. In reality, the bulk heterojunction layer may also be considered as a three-phase system with a donor-rich phase, a mixed amorphous phase of the donor and acceptor, and an acceptor-rich phase.[53] Ultimately, an ordered BHJ morphology can ensure optimal domain sizes of the donor and acceptor components and continuous pathways for electron and hole extractions in the OPV devices.

Figure 1-6c provides a schematic illustration of the electronic processes in OPVs: (i) The photoexcitation of the active layer materials creates an exciton; (ii) this bound electron-hole pair must migrate to the donor-acceptor interface; (iii) where there is a

thermodynamic driving force sufficient for charge transfer (CT) from the donor material to the acceptor material; (iv) after charge transfer, the bounded electron-hole pair must undergo charge separation in order to generate free carriers; (v) these free carriers then drift towards their respective electrodes as a result of the built-in voltage.

1.4.3. Device Architecture

In the conventional device architecture (Figure 1-7a), the BHJ active layer is deposited on top of poly(3,4-ethylenedioxythiophene):poly(styrenesulfonate) (PEDOT:PSS) and indium tin oxide (ITO), which are the hole transport layer (HTL) and the transparent hole collecting electrode, respectively. Calcium/aluminum or lithium fluoride/aluminum, which acts as the electron collecting electrode, are then deposited onto the active layer to complete the device. Both the PEDOT:PSS and the low work function cathode materials are known to degrade over time. PEDOT:PSS is hygroscopic,[54,55] while the calcium and aluminum degrade when in contact with moisture and oxygen. To overcome these stability issues in the conventional architecture, an inverted device structure (Figure 1-7b) has been designed to introduce high work function metals such as silver as the top hole collecting electrode. It also replaces the HTL with n-type metal oxides such as ZnO, which has high electron mobility, high transparency, low cost, non-toxicity, and air stability.[56,57]

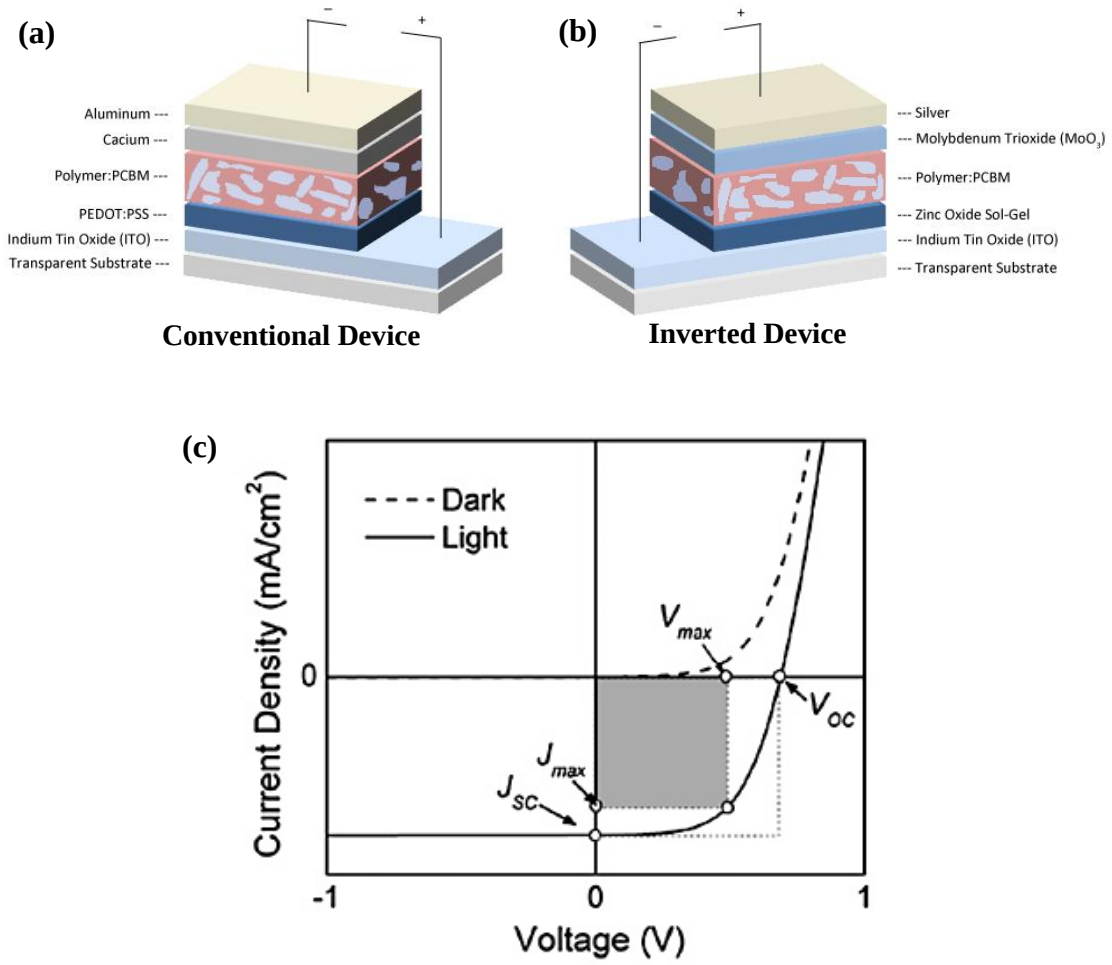

Figure 1-7. (a) Conventional and (b) inverted OPV device architectures. (c) An example of current density-voltage (J-V) curves for an OPV device under illumination and in the dark. The area shaded in grey represents the maximum power generated by the device. (Reproduced with permission from reference[48].)

1.4.4. Device Characterization

All photovoltaic cells are photodiodes capable of generating current and voltage from incident light. Under illumination, the power attainable at any point along the J-V curve is equal to the product of the current density and voltage. As shown in Figure 1-7c, the maximum power (P_{max}) is at the point on the J-V curve at which the product of the current and voltage is at maximum. The short-circuit current (J_{sc}) represents the maximum current flow without an applied bias. The J_{sc} parameter depends on the

efficiencies of every stage in the photovoltaic process, such as light absorption, exciton diffusion, charge transport, charge separation, and charge collection. The open-circuit voltage (V_{oc}) represents the maximum electrochemical potential of the device without a current flow. As shown in Figure 1-8, OPV devices usually have high energy losses limiting the V_{oc}, which includes many factors such as exciton splitting (up to 0.3 eV), CT state binding energy (up to 0.35 eV), interfacial disorder (up to 0.2 eV), and charge recombination (up to 0.7 eV).[58]

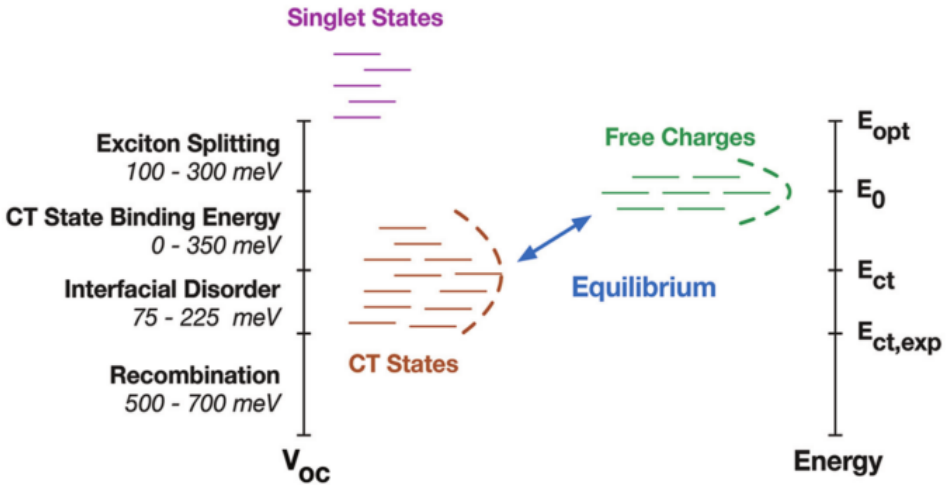

Figure 1-8. Energy losses in an organic solar cell from the optical energy gap (E_{opt}). E_0, E_{ct}, $E_{ct,exp}$ represent effective energy gap (the difference between electron affinity of the acceptor and the ionization potential of the donor), average energy of the charge transfer states, and the charge transfer energy estimated by experimental measurement. (Reproduced with permission from reference[58].)

The power conversion efficiency of a photovoltaic device can be calculated using Equation 1.1, as the percentage of the maximum output power (P_{out}) in relation to the power of the incident light (P_{in}). The ratio of P_{max} to the theoretical power obtained at J_{sc} and V_{oc} ($P_{max,theo}$) is known as the fill factor (FF), as calculated by Equation 1.2. FF is

illustrated in Figure 1-7c as the ratio of the shaded grey area to the area defined by the dotted grey line.

$$PCE = \frac{P_{out}}{P_{in}} = \frac{J_{max} \cdot V_{max}}{P_{in}} = \frac{J_{sc} \cdot V_{OC} \cdot FF}{P_{in}} \quad (1.1)$$

$$FF = \frac{J_{max} V_{max}}{J_{sc} V_{OC}} \quad (1.2)$$

Where J_{max} and V_{max} are the J and V values at P_{max}.

FF represents the collection efficiency of the photogenerated charges at their respective electrodes. The J-V curve can be used to determine how well the active layer materials work in the device, for example, energy level matching between donors, acceptors, and interlayers, and balance between hole mobility and electron mobility. However, the control of FF is not as well understood as that of J_{sc} and V_{oc}.

While the fundamental processes and device architecture are different between OPVs and inorganic p-n junction solar cells, it is generally accepted that the equivalent circuit model developed for inorganic PVs can be applied to OPVs. In this model, as presented by Equation 1.3 and Figure 1-9, the total current generated is equal to the current generated by a photovoltaic device minus the current losses from current leakage and current losses to external load (as opposed to flowing to the diode).[59,60,61] The current leakage and the current losses to external load are represented by shunt resistance (R_{sh}) and series resistance (R_s), respectively.

$$J = J_{SC} - J_D - J_{SH} = J_{SC} - J_0 \left(e^{\frac{q(V+JR_S)}{k_B T}} - 1 \right) - \frac{V+JR_S}{R_{SH}} \quad (1.3)$$

where J_D is the photodiode dark current density, J_{SH} is the shunt current, R_S is the series resistance, R_{SH} is the shunt resistance, J_0 is the reverse saturation current density, q is the elementary electron charge, V is the applied bias voltage, k_B is Boltzmann's constant, and T is the absolute temperature.

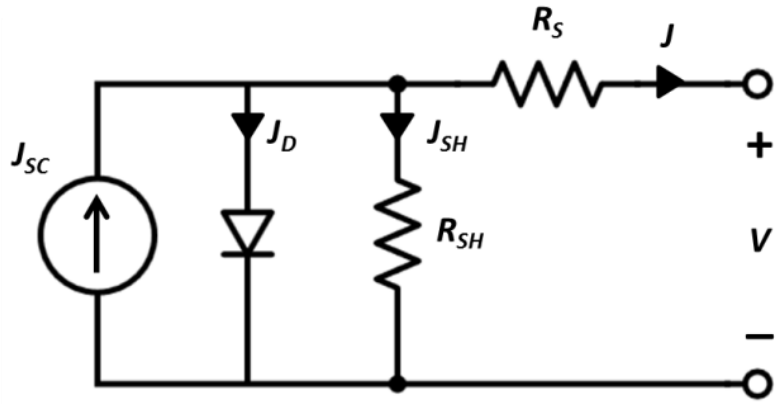

Figure 1-9. The single diode equivalent circuit model diagram. (Reproduced in part with permission from reference[62].)

R_S is determined by measuring the slope of the J-V curve at J_{sc}, and should be 0 under ideal circumstances, which means all photocurrent flows through the diode. R_{SH} results from current leakage, usually from pinholes, trap states, and edge effects. Ideally, R_{SH} should be infinite and no current flows through the resistor in the equivalent circuit model.

In a practical sense, the fill factor in OPVs is influenced by a number of factors including interfacial layer choice,[63] geminate recombination (recombination before exciton dissociation), [64,65] and the competition between non-geminate recombination and charge extraction/collection.[66] It is generally believed that non-geminate recombination can be greatly reduced with high and balanced hole and electron mobilites,[67,68,69] since low charge carrier mobility increases the chance of the opposite charges finding each

other and combining, and unbalanced charge carrier mobility leads to the buildup of space charge and limits photocurrent.

1.5. Influence of Side Chains on Device Properties

One of the advantages of organic materials is their solution processability, which can be induced by attaching side chains on the conjugated backbones, as mentioned earlier in this chapter. The improved solubility during polymerization also can lead to higher molecular weights.[70,71] The balance between solubility and intermolecular order is crucial in choosing the suitable side chain. Unlike the conductive conjugated backbones, side chains used in organic electronic materials are usually insulators, which hamper charge transport in the thin-film.[72] A list of common flexible side chains used in conjugated materials including linear and branched alkyl, oligoether, and hybrid side chains is shown in Figure 1-10.

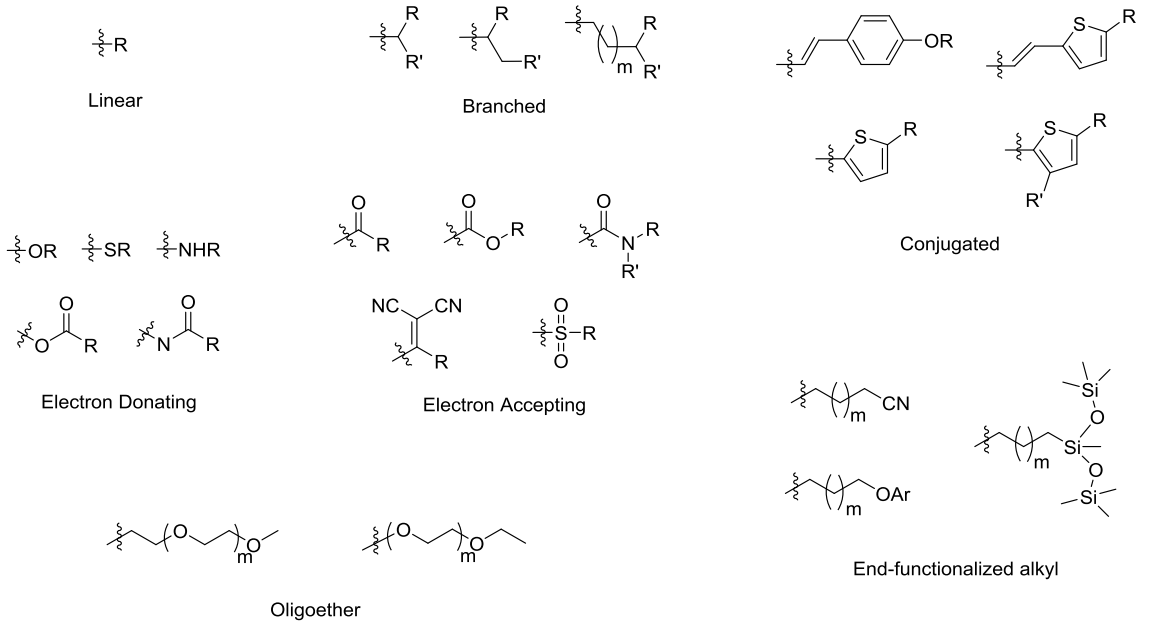

Figure 1-10. Commonly used side chains in conjugated materials

1.5.1. Alkyl side chains: linear vs. branched

The most common side chains used for solubilizing conjugated materials are saturated alkyl substituents, which have a molecular formula of $-C_nH_{2n+1}$ (n is the number of carbon atoms). Both linear and branched chains are used on conjugated backbones and can be applied to strategically control intermolecular packing. Linear chains including relatively short hexyl (C_6H_{13}) to longer octadecyl ($C_{18}H_{37}$) have been attached to conjugated materials.[73] Historically, side chains with an even numbers of carbon atoms are usually found in the literature rather than their odd number counterparts, since the even-numbered carbon chains are more commonly available commercially. The odd-even alkyl chain effect on conjugated molecules has been reported[74] in a family of 5,5′-bis(4-alkylphenyl)-2,2′-bithiophene (P2TP) molecules. By analyzing the spin-coated films using x-ray scatteting, the authors showed that the molecules with alkyl chains having an odd numbers of carbon atoms had smaller tilt angles against the substrate compared to those with an even numbers of carbon atoms. Interestingly, the overall crystal packing motif was unaltered as a result of the change in tilt angle, leading to similar field-effect charge carrier mobility among the molecules studied.

The major difference between straight and branched alkyl chains is their steric bulkiness. A well-studied, thiophene-based polymer poly-bithiophene-alt-thienothiophene, PBTTT, has been shown to exhibit interchain interdigitation (Figure 1-11) because of its linear hexadecyl (C16) alkyl chains, leading to its highly ordered semi-crystalline properties.[75,76] On the other hand, the steric bulk resulting from branched alkyl chains hinders intermolecular order and prevents interchain interdigitation.[77] For the same amount of carbon, branched chains have higher solubility due to the increase in torsional disorder as a result of the steric interactions.[78] It is important to note that

branched alkyl chains can introduce chirality to the polymer backbone. While commercially available branched chain precursors are usually racemic mixtures of the R and S species, Zerdan *et al.* has presented an investigation of chiral purity on diketopyrrolopyrrole molecules and find that they impart different molecular packing upon thermal annealing, which in turn alter optical absorptions, and thus the photocurrent generation and short-circuit currents in the OPV devices.[79] Specifically, the molecule with (R)-2-ethylhexyl side chain and (S)-2-ethylhexyl side chain attached to each of the opposite nitrogen atoms on the DPP core has higher crystallization tendency and shows higher crystallinity than the other stereoisomers, leading to the highest J_{sc} and PCE in the OPV device. In another chiral side chain study on DPP molecules, Liu et al. showed that, compared to the optically pure isomers, the meso isomer has a coplanar backbone which favors π-π stacking, leads to a closer plane-to-plane distance, and results in an order of magnitude greater hole mobility.[80]

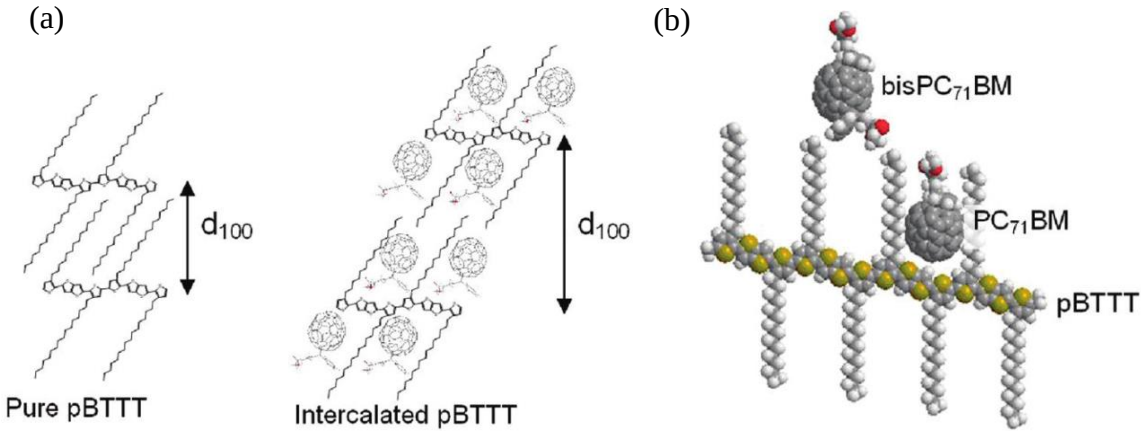

Figure 1-11. (a) Schematic representation of the effect on the lamellar d_{100} spacings from the interchain interdigitation of pure PBTTT and the intercalation of fullerene between the straight hexyldecyl (C16) alkyl chains. (b) Illustration on the impact of fullerene size and steric on intercalation. (Reproduced with permission from reference[76].)

Graham *et al.* have suggested that the strategic placement of straight and branched alkyl chains on the donor and acceptor moieties along the polymer backbone can effectively direct interaction between polymer and fullerene.[81] By alternating the straight and branched chains on the donor and acceptor moieties of benzo[1,2-b:4,5-b′]dithiophene−thieno[3,4-c]pyrrole-4,6-dione polymers (PBDTTPD) (Figure 1-12), the authors find that, within this family of polymers, the best performance arises from the polymer in which the bulky branched chains are attached on the donor (benzodithiophene) BDT unit; while the linear alkyl chain is substituted on the acceptor TPD, allowing fullerene to dock with the acceptor moiety of the polymer. Graham proposes two explanations for the observation: the intermolecular interactions between the polymer acceptor moiety and the fullerene create a favorable energy landscape due to a partial charge transfer, dipole-induced dipole, or quadrupolar interactions. Up to a few hundred meV differences have been shown to result from the interface energetics, the stabilization effects of the induced dipoles, and the quadrupolar interactions because of certain interfacial molecular arrangements. Furthermore, it is generally believed that the energetic disorder for both polymer and fullerene are reduced when the fullerene is directed to dock with either the electron-poor or electron-rich moieties on the polymer backbone. For the PBDTTPD system, theoretical calculations were used to further confirm the effects of side chain bulkiness on controlling fullerene interactions with the polymer backbone. While exciton dissociation is similar regardless of the fullerene docking location, charge recombination is expected to be more efficient when the fullerene is situated closer to the electron rich moiety of the polymer backbone.[82,83]

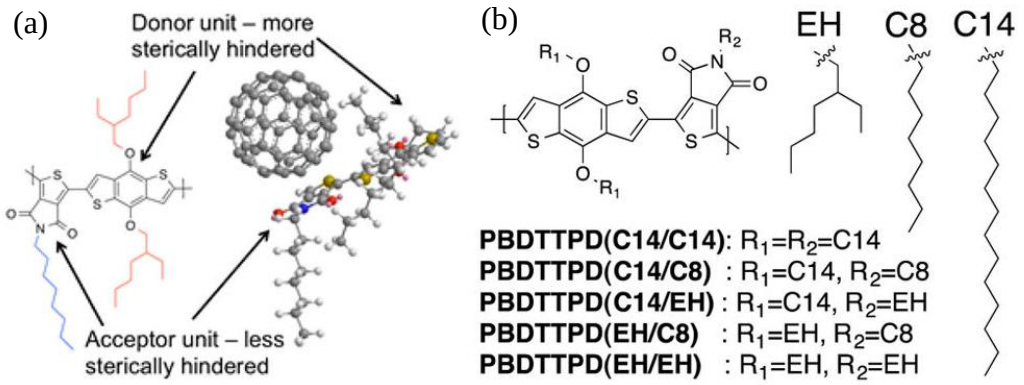

(c)

material	architecture	J_{SC} (mA/cm^2)	V_{OC} (V)	FF	PCE (%)
C14/C14	BHJ	6.3 ± 0.1	0.94 ± 0.01	0.65 ± 0.07	3.8 ± 0.1
C14/C8	BHJ	6.9 ± 0.3	0.90 ± 0.02	0.53 ± 0.02	3.3 ± 0.2
C14/EH	BHJ	3.6 ± 0.2	0.97 ± 0.01	0.48 ± 0.03	1.7 ± 0.2
EH/C8	BHJ	9.6 ± 0.2	0.94 ± 0.01	0.66 ± 0.01	6.0 ± 0.3
EH/EH	BHJ	6.6 ± 0.4	0.96 ± 0.03	0.50 ± 0.03	3.2 ± 0.3
C14/C14	BL	1.3 ± 0.1	0.84 ± 0.02	0.63 ± 0.02	0.70 ± 0.03
C14/C8	BL	1.2 ± 0.1	0.80 ± 0.01	0.66 ± 0.01	0.63 ± 0.02
C14/EH	BL	1.5 ± 0.3	0.85 ± 0.01	0.58 ± 0.05	0.70 ± 0.08
EH/C8	BL	2.7 ± 0.3	0.87 ± 0.01	0.66 ± 0.01	1.5 ± 0.1
EH/EH	BL	2.1 ± 0.1	0.89 ± 0.03	0.58 ± 0.02	1.1 ± 0.1

Figure 1-12. (a) Schematic illustration of directing polymer:fullerene interaction *via* the steric effect of linear and branched alkyl chains. (b) Structural design of the PBDTTPD polymer family. (c) Summary of device performance highlighting the favorable effects on J_{sc} and FF as a result of strong interaction between the acceptor TPD moiety on PBDTTPD and fullerene. (Reproduced with permission from reference[81].)

1.5.2. Oligoether side chains

Oligoether side chains are a well-known hydrophilic moiety and have been used to promote material solubility in water and other polar organic solvents. Thus, it is attractive to the organic electronics community to append polar oligoether side chains to conjugated materials, allowing solution processing in non-halogenated or even aqueous solvents. By replacing a $–CH_2–$ unit with a –O– unit, the oligoether chain is more flexible due to the elimination of steric hindrance.[84]

Oligoethers have also been shown to effectively increase the dielectric constant(ε_r) of the resulting molecules and polymers (Figure 1-13) compared to the alkylated versions, resulting from the high chain flexibility and the rapid rotation around

the polar components.[85] ε_r values have been measured to be between 5 to 40 for ethylene glycol and triethylene glycol at frequencies of 1-20 GHz.[86] It has been suggested that this increase in ε_r can yield improvement in charge dissociation efficiency in OPV devices.[87]

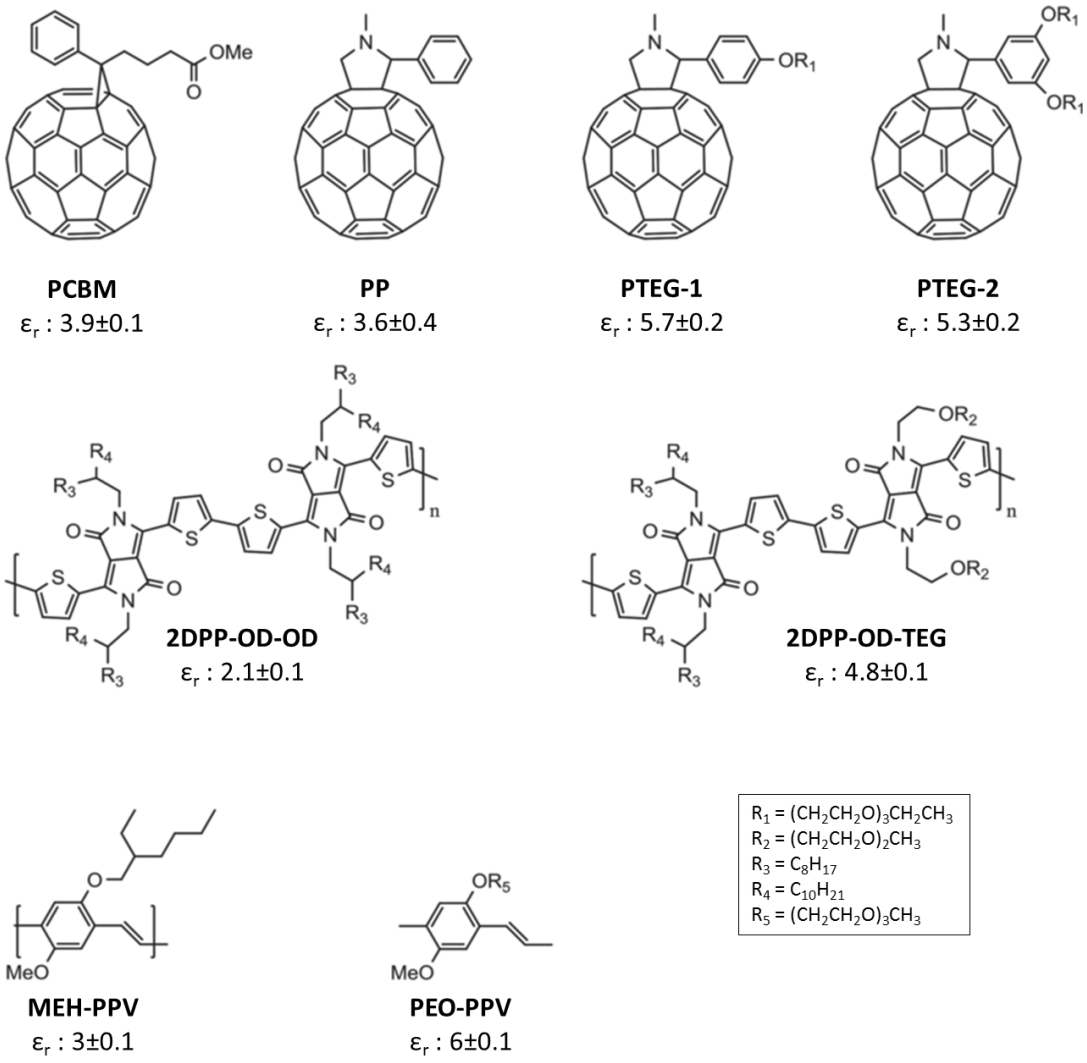

Figure 1-13. Chemical structures of molecular and polymeric derivatives functionalized by oligoethers with enhanced ε_r. (Reproduced in part with permission from reference[87].)

Regarding dielectric constant, it is important to note that the relevant value should come from measuring the polymer:fullerene blend. Constantinou *et al.* shows that the dielectric constants of the blends are higher than that of the pristine polymer and fullerene.[88] This correlates to the degree of intermixing between polymer and fullerene, where small domains lead to larger interface dipoles and result in higher permittivity. The electroabsorption spectra further indicates that, the optimum morphology in the active layer enhances the excited state polarizability, resulting in more efficient charge transfer and higher performing devices.

Despite its ability to enhance ε_r, the use of oligoether side chains is uncommon in organic electronics. Firstly, device fabricated with polymers with oligoether side chains suffered from extensive phase separation, leading to large PCBM clusters and hindering charge extraction and device performance.[89] Secondly, materials containing oligoether side chains are believed to have high affinities toward moisture and ionic impurities as a result of their compatibilities with polar solvents. OFET devices with an oligoether containing semiconducting polymer poly(3-(2-(2-(2-methoxyethoxy)ethoxy)ethoxy)methyl-thiophene) processed from water achieved low mobility on the order of 10^{-5} cm^2 V^{-1} s^{-1}, even when fibrillar morphology similar to regular alkyl polythiophene was observed under AFM.[90]

Another strategy to employ oligoether side chains in structural design was reported by McCullough and co-workers in synthesizing amphiphilic polythiophene alternating copolymers with both triglyme and dodecyl substituents.[91] Due to the combination of polar and non-polar side chains, this material was found to self-assemble on the water/air interface when processed on a Langmuir-Blodgett (LB) trough. In a

similar side chain alternating design, Kanimozhi *et al.* demonstrated that a DPP-based polymer with triglyme and branched 2-octyldodecyl chains achieved field effect transistors (FET) electron mobility close to 3 $cm^2 V^{-1} s^{-1}$ and device on/off ratio of 10^4 in their spin-coated films, owing to the close π-π stacking distance and a dominant n-channel behavior.[92]

1.5.3. Functionalized side chains

As shown in Figure 1-10, functionalized side chains have been used in material designs to fine tune the electron density along the polymer backbones. More specifically, electron donating side chains containing alkoxyl (−OR),[93,94,95,96] alkylthiol (−SR),[97,98] acetate (−OCOR), alkylamino (−NHR),[99] and amide (NHCOR) groups have been shown to raise the HOMO energy levels; while electron withdrawing side chains containing acetyl (−COR),[100] amide (−CONHR),[101] ester (−COOR),[102,103] and sulfonyl ($-SO_3R$)[104] can be used to lower the LUMO energy levels of the conjugated materials. Conjugated side chains with phenylene and thiophene units have gained popularity recently to both impact the energy levels, as well as broaden the absorption *via* enhanced conjugation. He *et al.* synthesized PTB7-Th as shown in Figure 1-14, a derivative of PTB7, by replacing the oxygens along the two 2-ethylhexyloxy alkyl chains on the benzodithiophene moiety with thiophenes. Single-junction OPV devices with PTB7-Th achieved PCE above 10%, improving from 7.4% in PTB7 as a result of a slightly larger open circuit voltage (a difference of 30 mV) and higher short circuit current (a difference of 4 mA/cm^2) resulting from closer π−π stacking, and higher charge mobility. [105,106,107]

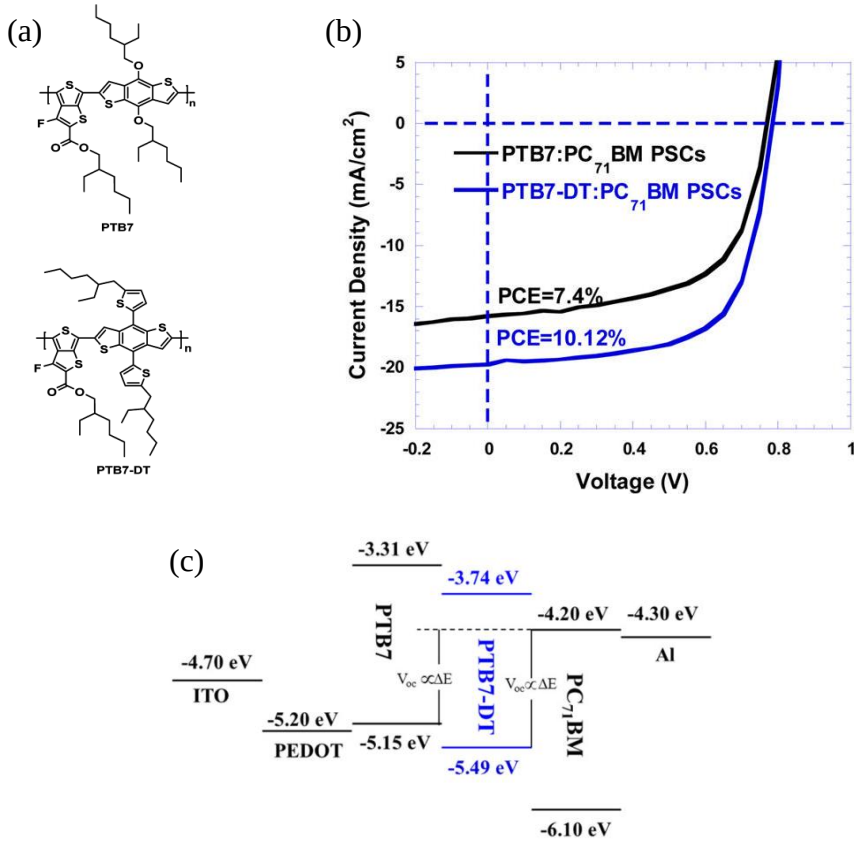

Figure 1-14. (a) Polymer repeating unit structures of PTB7 and PTB7-Th (also known as PTB7-DT). (b) J-V curve of OPV devices from the two polymers. (c) Estimated energy level diagrams indicating that the thiophene-containing side chains on PTB7-Th increase both ionization potential and electron affinity, as well as lead to an overall reduction of the energy gap. (Reproduced with permission from reference[107].)

1.6. Processing Techniques

1.6.1. Controlled Self-Assembly *via* Layer-by-Layer Deposition

As mentioned above, the use of a polymer donor and fullerene acceptor in the BHJ active layer design can create a bicontinuous and interpenetrating network, overcoming the short exciton diffusion length of organic materials. However, achieving optimal crystallinity, domain size, structural orientation, and morphology within the active layers relies on the spontaneous nanoscale phase separation of the donor and acceptor components.[7] This phase separation behavior is highly dependent on the

processing conditions, including solvents, additives, and annealing conditions, and is still challenging to control and predict.

One way to circumvent the random BHJ device is to build the active layer *via* layer-by-layer (LbL) deposition. Using LbL methods, the deposition and the formation of donor and acceptor layers can be optimized and controlled independently. Since the donor-acceptor interface is confined to each phase, charge generation and extraction should improve due to the reduction of bimolecular recombination.

There are multiple LbL methods for depositing organic materials. Dip-coating is a popular technique used in industrial roll-to-roll process. It is also used in academic research due to its easy setup. The quality and quantity of the adsorbed layer can be controlled by the solvent choice, concentration of material, adsorption time, temperature, drying conditions, and dipping speed. To ensure the stability of each deposited layer, especially when multiple materials are used, the dipping sequence of layers requires optimization and strict control. [108,109] For laboratory scale LbL depositions, such as spin and spray coatings, orthogonal solvents can be used to dissolve and deposit multiple materials sequentially.[110] The thickness of the deposited layer can be controlled by solution concentrations as well as deposition conditions, i.e. spinning and spraying speeds and durations.[111,112,113] Industrially compatible roll-to-roll coating techniques[114] such as blade coating,[115] slot-die coating,[45,116,117] and ink-jet printing[118,119,120] are also gaining popularity in the field of organic electronics.

1.6.2. Langmuir-Blodgett and Langmuir-Schaefer Depositions

Langmuir-Blodget deposition is an LbL technique that can achieve a true molecular monolayer buildup. In this technique, as shown in Figure 1-15a, a monolayer

of molecules or polymer chains is organized on a liquid surface, and subsequently transferred onto a solid substrate forming a thin film.

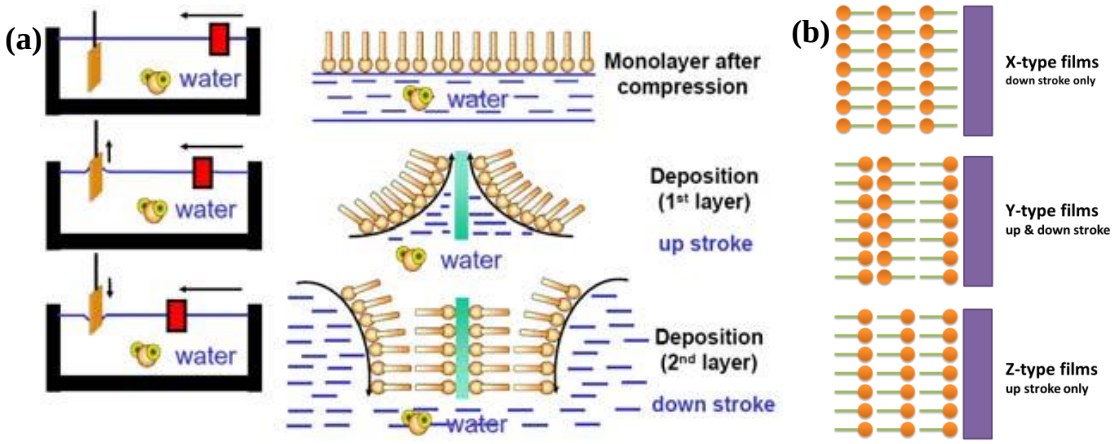

Figure 1-15. (a) Schematic of Langmuir-Blodgett deposition during up stroke and down stroke. (Reproduced with permission from reference[121].) (b) X-, Y-, and Z-type films as a result of the deposition conditions. Orange circles and brown lines represent the hydrophilic heads and the hydrophobic tails on a classic amphiphilic organic molecule such as stearic acid.

This technique was developed at the General Electric Company by Irving Langmuir and Katharine Blodgett. In 1917, Langmuir successfully transferred monolayers of fatty acid, ester, and alcohol from a water surface onto a solid substrate.[122] In 1932, Langmuir was awarded the Nobel Prize in Chemistry for his studies of surface chemistry, employing monolayers on liquid surfaces to learn about intermolecular forces. In 1935, Blodgett successfully constructed a multiple layer film of calcium stearate *via* an LbL Langmuir-Blodgett vertical dipping method.[123] A similar technique, the Langmuir-Schaefer method, named after Langmuir and colleague Vincent Schaefer at General Electric, was also developed to construct multiple layer films *via* horizontal dipping.[124]

A Langmuir film is a monolayer on a liquid surface, which is usually a water/air interface. The self-organized monolayer formation is a result of intermolecular self-assembly interactions. The organic materials used usually consist of hydrophobic

("water-hating") and hydrophilic ("water-loving") moieties, which interact favorably with the air and the water subphase, respectively. Many classes of materials have been used in Langmuir monolayer formation, including lipids, proteins, nanoparticles, and polymers.[125]

To process amphiphilic organic materials *via* LB, the molecule or polymer is first dissolved in a volatile organic solvent, such as chloroform, and subsequently added dropwise onto the aqueous subphase in the LB trough. The monolayer spreads across the surface and once the organic solvent evaporates completely, the movable barriers are adjusted to reduce the surface area of the monolayer, and thus increase the surface pressure due to the compression of the molecules. This allows the molecule to organize and self-assemble at the water/air interface due to its amphiphilic nature. The surface pressure is monitored by a Wilhelmy plate, a thin platinum plate partially submerged into the water subphase, measuring the change in surface tension, which is converted into surface pressure during the compression of the monolayer.[126] Once the desired surface pressure is reached, a substrate is immersed into the trough vertically to allow the transfer of the LB monolayer onto the surface. The surface compression pressure can be adjusted to control the quality of the deposited layer, the monolayer coverage, and the orientation of the molecules.

An example of a Langmuir isotherm is presented in Figure 1-16, which shows the progression of the monolayer formation from deposition to collapse. Upon deposition of the amphiphilic material into the trough, the intermolecular interaction between molecules is minimal due to the large distance between them. At this stage, the uncompressed monolayers are considered to be in a gas/vapor phase. As the compression

begins and the overall surface area per molecule reduces, the repulsive force between neighboring molecules creates a measurable surface pressure. The onset of the surface pressure growth marks the beginning of the liquid-condensed phase for the monolayer. As the monolayer continues to be compressed, a phase change occurs (marked by a plateau in the isotherm) when the liquid phase turns into a tilted solid mesophase. A sharp increase in the slope of the isotherm follows, indicative of the onset of the solid-condensed phase with molecules packing closely within the monolayer. Further compression of the monolayer leads to its collapse with a sharp drop in surface pressure.

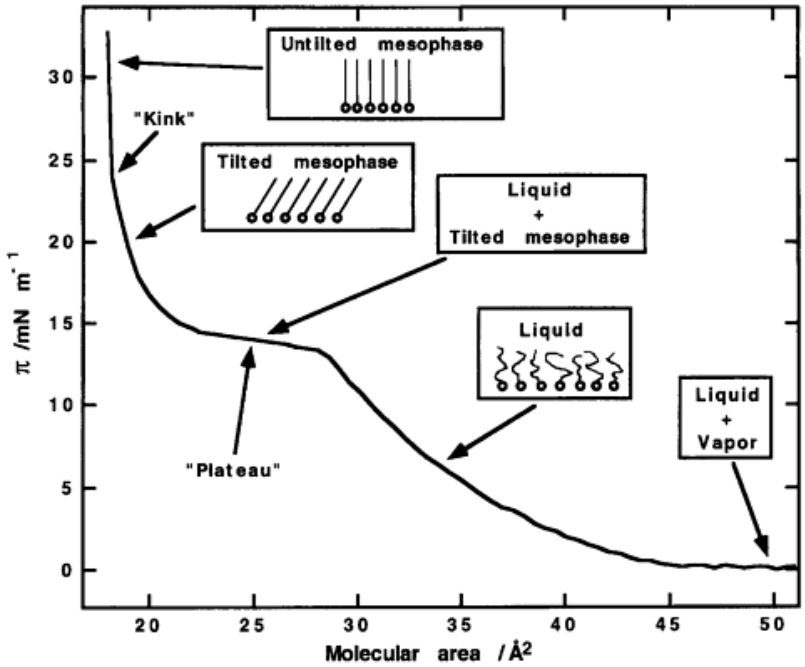

Figure 1-16. An example of Langmuir isotherm of a pentadecanoic acid monolayer at 30 °C with water as the subphase. This is known as a π-A isotherm, measuring the surface pressure (π) as a function of the mean molecular area (A). (Reproduced with permission from reference[126].)

LB multilayers can be constructed by passing the substrate through a Langmuir monolayer upwards and downwards in an alternate fashion (Figure 1-15a). Different types of LB multilayers can be produced based on the deposition conditions. [126,127] The

most common type is called a Y-type multilayer, which is obtained when the layers are deposited onto the solid substrates during both up stroke and down stroke directions. As illustrated in Fig 1-15b, the hydrophobic tails on one monolayer are oriented towards the hydrophobic tails on the next layer, while the hydrophilic heads in two adjacent layers interact with each other. X-type and Z-type multilayers refer to monolayer deposited only in the down stroke or up stroke directions, respectively. These two types of films consist of amphiphilic molecules facing only one (but opposite) direction.

During monolayer deposition, the transfer ratio (TR) is used to determine the quality of the monolayer transfer. TR is defined as the ratio between the trough area decrease and total surface area of the substrate. A TR ratio of unity indicates stable deposition of the monolayer, with molecules orienting similarly on the substrate as they do on the subphase. When the TR deviates from unity, it means either the molecules change their orientation during transfer or transfer of the monolayer is poor, which may be a result of an unstable monolayer and weak interactions between the molecules and the substrate.

1.6.3. Melt Processing

While conjugated materials are solution processable, enabling the use of roll-to-roll printing to manufacture electronic devices, many of them are only soluble in toxic chlorinated solvents. Melt processing is an attractive alternative to solution processing that eliminates the use of processing solvents; however, given the typically high melting temperatures of conjugated alternating copolymers, heating them to melt is energy intensive.[128] In an attempt to vary the melt temperatures of conjugated polymers, Zhao *et al.* synthesized a family of diketopyrrolopyrrole polymers with varying lengths of flexible

conjugation-breaking alkyl segments along the polymer backbones (Figure 1-17).[129] While these conjugation-breakers halt intrachain charge transport, the polymers with the spacers exhibit higher crystallinity. Interestingly, even at only 1 wt% addition of the fully conjugated version of the polymer into the polymer with a propylene spacer, the resulting blend achieved FET mobility up to 1 cm^2 V^{-1} s^{-1}, showing that the fully conjugated polymer chain, even at low loading ratio, is sufficient to establish connectivity between crystalline aggregates in the polymer with conjugation-breakers. More importantly, the length of alkyl spacers can be used to adjust the melting temperatures. From an ethylene spacer to a dodecylene, the melting temperatures of the polymers range from 221 ˚C to 94 ˚C, with minimal changes in optoelectronic properties.[130]

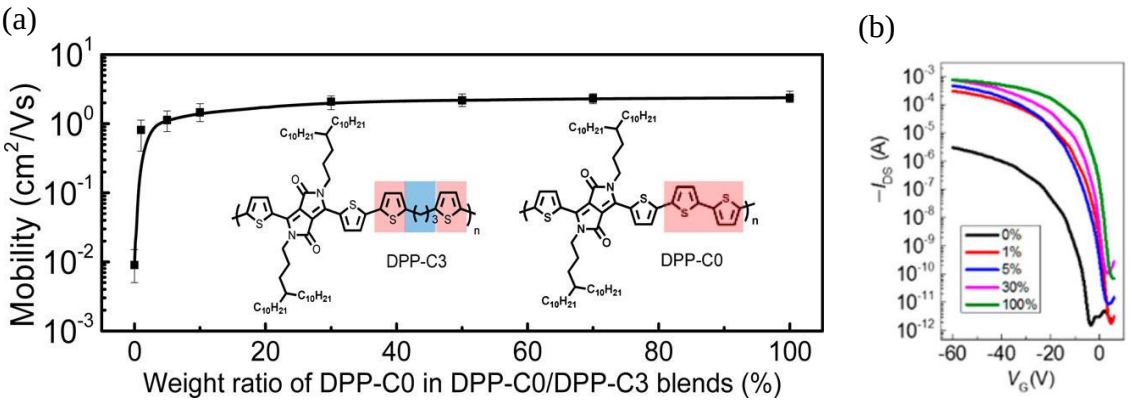

Figure 1-17. (a) Field-effect transistor charge mobility as a function of fully conjugated diketopyrrolopyrrole polymer loading ratio into the polymer with a propylene spacer. (b) Transfer characteristic of the FET devices. (Reproduced with permission from reference[129].)

1.7. Thesis of Dissertation

Organic semiconducting π-conjugated materials allow for the development of low-cost, flexible, and lightweight electronic devices for applications in photovoltaics, light-emitting diodes, field-effect transistors, electrochromics, and sensors. Using

previously established structure-property relationships, synthetic chemists can tune the physical and electronic properties of conjugated materials catering to specific applications. In organic photovoltaics, novel materials containing thienyl- and phenyl-based building blocks including diketopyrrolopyrrole, isoindigo, and thienopyrrolodione have led to improved device performance. This dissertation will present molecular and polymeric systems synthesized based on these building blocks to study the impact of the structural, morphological, electronic, and photophysical properties on organic photovoltaic performance.

In Chapter 2, experimental methods and characterization techniques used throughout this dissertation will be introduced, highlighting the details of synthetic handle, material design, optoelectronic property, physical property, and device fabrication.

Chapter 3 will introduce two families of donor-acceptor polymers acting as the p-type materials in the active layers of OPV devices. The first family contains three Group 14 atom-bridged dithieno-co-thienopyrrolodione polymers, which will reveal the impact of minimal structural change along the polymer backbone on fundamental photovoltaic device parameters including morphology, photophysical processes, and device performance. The second family includes six polymers containing isoindigo, thienoisoindigo, and diketopyrrolopyrrole as acceptors; and thiophene derivatives as donors. The goal of this study is to control the energy gaps and morphological changes in these materials and document how these factors affect device performances.

Chapter 4 will focus on the supramolecular self-assembly of two families of DPP-based donor-acceptor molecules. The first part will discuss the design and synthesis of

two amphiphilic molecules in an attempt to achieve desirable structural and electronic properties arising from guided self-assembly. The Langmuir-Blodgett technique allows for controlled layer-by-layer deposition of monolayers, with morphological and structural studies revealing the qualities and degrees of order in the thin films. Their structural, physical, optoelectronic properties, and device performance in OFETs and OPVs will be presented.

In Chapter 5, four low bandgap polymers with strong light absorption properties are synthesized *via* direct arylation polymerizations. The morphological and transport properties of these materials will be correlated to device performances to highlight the importance of structure-property relationship in designing materials for specific applications.

Chapter 6 will discuss the current status of the photovoltaic market and the commercialization prospect of organic photovoltaics. Analyses of fundamental scientific research, advanced engineering approach, and market opportunity will be explored. More specifically, this chapter will provide an overview of each material class presented in this dissertation (high power conversion efficiency in D/A polymer; choice of high-throughput deposition methods for device fabrication; and extended fused ring and three-dimensional systems for designing acceptor materials) and highlight their potentials in transferring the current organic electronic technology into real world market applications.

CHAPTER 2

EXPERIMENTAL METHODS AND CHARACTERIZATION TECHNIQUES

2.1. Materials and Reagents

Starting materials and reagents were purchased from various commercial sources. All reactions were performed under argon unless otherwise stated. Solvents used in polymerizations and device fabrications, and solvents transferred into the glovebox were degassed *via* at least four "freeze, pump, thaw" cycles and dried with 4Å molecular sieves. While molecular sieves can be activated by heating in a microwave oven, the most effective drying method involves heating them under vacuum. The sieves are put into a round bottom flask under high vacuum (i.e. belt-driven vacuum pump at the hood) and heated to 300 ˚C in a sand bath for 2 hours. Pay close attention to the sand bath temperature to prevent overheating and implosion of the round bottom flask. The activated sieves can be stored in a sealed container inside a desiccator for later use. Silica (60 Å porosity, 40-64 μm particle size) was purchased from Sorbent Technologies, Inc for use in column chromatography.

2.2. Synthetic Methods

Specific synthetic approaches to the conjugated precursors presented in this dissertation are discussed in their respective chapters. Here, an overview of common cross-coupling reactions in conjugated material synthesis is presented to provide an

introduction to new researchers. The reader is also encouraged to consult current literature.[131,132,133,134]

Usually, conjugated molecules and polymers are synthesized through the Suzuki, Stille, or Negishi cross-coupling reactions, which involve the preparation of organoboron, organotin or organozinc compounds, respectively.[33,135,136] The advantages of these cross-coupling reactions include the retention of configurations at the sp^2 carbons where the couplings occur, and the reactive sites are confined to the organometallic and the halogenated carbons. Equation 2.1 is the representation of the above cross-coupling reactions,

$$R_1\text{-}m + R_2\text{-}X \xrightarrow[\text{(additive)}]{M} R_1\text{-}R_2 + m\text{-}X \qquad (2.1)$$

where R_1 and R_2 are the conjugated monomer units, m represents the functionality of monomer 1 (B for Suzuki reaction, Sn for Stille reaction and Al, Zr or Zn for Negishi reaction), X is halogen, M is the transition metal (such as nickel and palladium) catalyst. Common additives in cross-coupling reactions include acids, bases, and ligands for catalyst stability.

2.2.1. Stille Cross-Coupling Reaction

The Stille reaction involves the coupling between an organotin and a variety of organic electrophiles which are usually halides. Special care should be used when handling organotin compounds such as trimethyl tin chloride (NFDA Health = 4, LD50 = 12.6 mg kg^{-1}) and tributyltin chloride (NFDA Health = 2, LD50 = 129 mg kg^{-1}) due to their toxicity.[137] Solvent and byproduct wastes generated during the reaction should be

collected and labeled in a separate container for chemical waste pickup. Even with the toxic nature of the precursors and byproducts, the Stille reaction is still one of the most common C-C coupling synthetic methods owing to its already-optimized reaction conditions, high yields, and high molecular weights in the polymerization products. As shown in the catalytic cycle in Scheme 2-1, the palladium-catalyzed Stille reaction begins with the oxidative addition of the organohalide to the Pd(0) catalyst, forming the Pd(II) complex. The transmetallation step exchanges the halide of the Pd(II) complex with the R group on the organotin compounds. Reductive elimination finishes the C-C coupling reaction and regenerates palladium catalyst to Pd(0), which can enter the catalytic cycle to continue the coupling process.

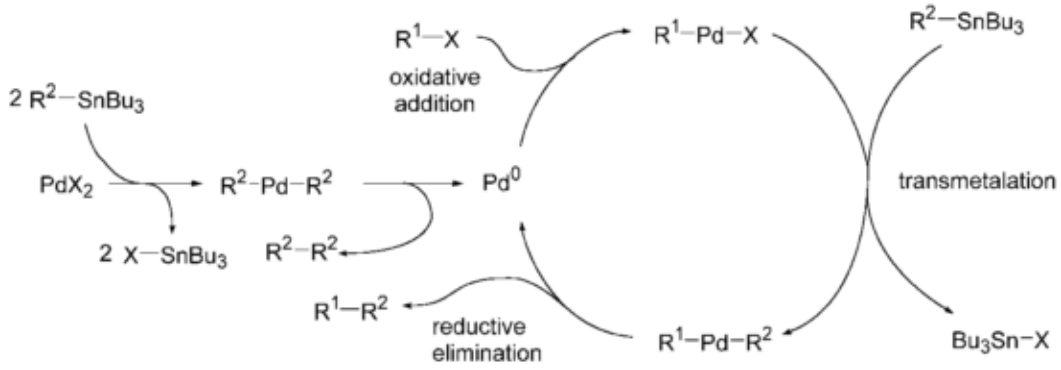

Scheme 2-1. Catalytic cycle of palladium-catalyzed Stille reaction. (Reproduced with permission from reference[138,139.])

2.2.1.1. Proper Storage and Handling of Palladium Catalysts

Commonly used catalysts and ligands in cross-coupling reactions are listed in Table 2-1. Commercially available palladium catalysts such as tris(dibenzylideneacetone)dipalladium(0) ($Pd_2(dba)_3$) are known to contain Pd nanoparticles as a result of decomposition, leading to homo-coupled fragments along the backbones. ^{1}H NMR is a quick and an effective way to confirm the purity of the

palladium catalyst.[140] To prevent the decomposition, and thus incorrect catalyst loading from affecting the molecular weights of the polymers[141], it is crucial to properly store and handle catalysts. They should be stored at -20 ˚C under an inert atmosphere. If possible, the catalysts should only be handled in glovebox under an inert atmosphere. In any case, the catalyst should not be exposed to ambient conditions for an extended period.

Table 2-1. List of common palladium catalysts

Catalyst	Remarks
Tris(dibenzylideneacetone)dipalladium(0)-chloroform adduct $Pd_2(dba)_3 \cdot CHCl_3$	Excellent for Stille and Suzuki polymerizations
Palladium(II) acetate $Pd(OAc)_2$	Universal catalyst
Tetrakis(triphenylphosphine)palladium(0) $Pd(PPh_3)_4$	Excellent for molecule cross-coupling reactions
trans-Bis(acetato)bis[o-(di-o-tolylphosphino)benzyl]dipalladium(II) Herrmann-Beller catalyst	Excellent for Direct Arylation reactions
1,1'-bis(diphenylphosphino)ferrocenepalladium(II)dichloride dichloromethane complex $Pd(dppf)Cl_2$	Excellent for in-situ Suzuki polymerizations

2.2.1.2. Purification of Organotin Monomers

The organotin monomers can be purified under ambient conditions using common purification techniques such as distillation, column chromatography, and recrystallization. Extra care should be given when purifying organotin monomers due to its toxicity and its likelihood of deprotonating silica gel, and thus losing the tin functionality. While a basically treated silica gel column, usually prepared by flushing the packed column with 1% trimethylamine solution, can be used to deactivate the acidic nature of silica, our experience in the Reynolds Group has shown that this basic treatment

may not be as effective as expected to prevent destannylation of the Stille monomers. We find that reverse-phase high-performance liquid chromatography (HPLC) is a superior way to purify the tin precursor to achieve high yield and purity (> 99%). Usually, the crude tin monomer is analyzed on an analytical HPLC column to identify the amount of impurity, the resolution of the separation, and the ideal solvent mixture ratio. For typical conjugated materials with alkyl side chains, a mixture of acetone and acetonitrile (or THF) is used. Preparative HPLC column is used once the ideal solution mixture and the flow rate (pressure) are identified. The different compounds are detected as they elute by their refractive index and absorption property (*via* a diode array detector) and collected into different fractions. Their purities are confirmed by analytical HPLC and NMR spectroscopy. The tin monomers are usually shelf stable and can be placed within a desiccator in a freezer at -20 ˚C for long-term storage.

2.2.1.3. Reaction Setup

As in traditional polymer science for step-growth polymerization, the stoichiometric imbalance in conjugated polymer synthesis is detrimental to achieving high molecular weight polymers, and thus affecting the physical and electronic properties of materials. (Note that stoichiometric imbalance is sometimes used to control the molecular weight of a polymer, as in the case of the Stille polymerization of naphthalene diimide polymers,[142,143] since a balanced stoichiometric monomer loading leads to high weight polymer that can be difficult to process.) Measuring solid monomer should not pose too big of a difficulty, and an antistatic gun has proven to be a worthy investment to help weighting out “flaky” monomers. On the other hand, measuring oil/liquid monomer is not as trivial. An oil monomer should be weighed in a tared vial. Benign solvents, such

as hexanes, dichloromethane, and chloroform, which can be easily removed under reduced pressure by a rotary evaporator, are used to dissolve and transfer the monomer into the reaction chamber (i.e. Schlenk tube). For solid monomers, all reaction substrates should be measured into the Schlenk tube within an argon-filled glovebox. When one or more oil monomers are involved in the reaction, the catalyst and ligand should be added into the reaction chamber last to prevent homocoupling, which can occur if the catalyst and ligand have greater solubility in one of the oil monomers. The catalyst and ligand are measured and placed in a vial and sealed with a septum in a glovebox. The catalyst and ligand can be added into the flask containing the monomers and reaction solvent immediately before the start of the reaction by a needle and syringe using a minimal amount of solvent. Quick sonication (5 seconds) may be used to enhance the solubility of the catalyst and ligand during the transfer process.

2.2.2. Direct Arylation Reaction

Recently direct arylation, or C-H activation, cross-coupling reaction involving a reaction between a halogenated and a hydrogenated compound is gaining popularity in the field of conjugated material synthesis.[134,144,145,146,147,148,149] This method leads to the formation of C–C bonds by coupling a halogenated aromatic compound with a hydrogenated (or unfunctionalized) aromatic compound. Equation 2-2 shows a general scheme of C-H activation,

$$R_1\text{-}H \quad + \quad R_2\text{-}X \quad \xrightarrow[\text{(additive)}]{M} \quad R_1\text{-}R_2 \quad + \quad H^+ \quad + X^- \qquad (2.2)$$

where R_1 and R_2 are conjugated monomer units, X is halogen, M is the transition metal catalyst.

Since the direct arylation polymerization of conjugated materials is only popularized recently, it is important to understand the reaction mechanism during the catalyst-aided polymerization. Scheme 2-2 shows two plausible C-H activation pathways suggested by Lafrance and Fagnou.[150] Similar to Stille and Suzuki reactions, both pathways begin with a palladium catalyst. Through oxidative addition, the aryl bromide is inserted onto the palladium catalyst, which is stabilized by the conjugated base of the pivalic acid. After the removal of the bromide ion, a transition state is formed when the arene is inserted onto the catalyst and coordinated with the pivalic acid. A proton from the arene is then transferred to the pivalic acid, and the C-H activation reaction is completed when the C-C bond is formed between the two aryl groups and leaves the catalytic cycle through reductive elimination. The reduced palladium catalyst is regenerated and recycled into the catalytic cycle for the next coupling reaction. The only difference between Pathways A and B is whether or not the pivalic acid remains bounded to the palladium catalyst throughout the catalytic cycle; either pathway results in the same coupling product.

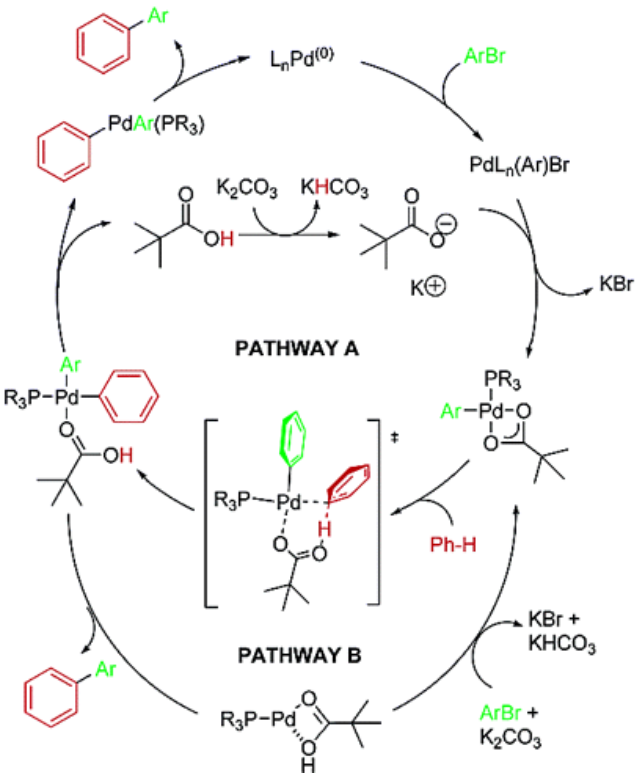

Scheme 2-2. Plausible pathways for benzene arylation suggested by Lafrance and Fagnou. (Reproduced with permission from reference[150])

This C-H activation polymerization has some advantages over the traditional cross-coupling reactions. (1) Avoidance of using organometallic reagents, which could lead to toxic byproducts (organotin compounds) and wastes, (2) fewer synthetic steps, (3) higher yields, (4) higher atom economy.[145,151] While C-H activation possesses many advantages over traditional cross-coupling reactions for conjugated polymer syntheses, its success rate depends on the optimization of reaction parameters including the intrinsic chemical properties of the monomers (i.e. stability of the functional groups), the palladium catalysts, the phosphine ligands, the reaction solvents, and the bases. Finding the ideal conditions could take time and effort through trial and error. In fact, research has shown that the physical properties (molecular weights, dispersities, and yields) of the polymers vary greatly when the reaction parameters are altered. If C-H activation can be

used to synthesize the targeted polymers, further optimizations through the choice of catalyst, ligand, base, solvent, reaction duration, and temperature can be done to improve their physical properties. For example, the Hermann Catalyst, a dimeric palladium catalyst, is stable under high temperature during polymerization. Ligands such as tris(o-anisyl)phosphine and tris-(o-dimethylaminophenyl)phosphine, are bulky and contains methoxy groups and amino groups, respectively, to stabilize the palladium catalyst through coordination.[152]

Readers are encouraged to explore C-H activation for synthesizing conjugated materials further in the open literature.[144,145,153,154,155] Figure 2-1 summarizes the three cross-coupling reactions commonly employed to synthesize conjugated materials.

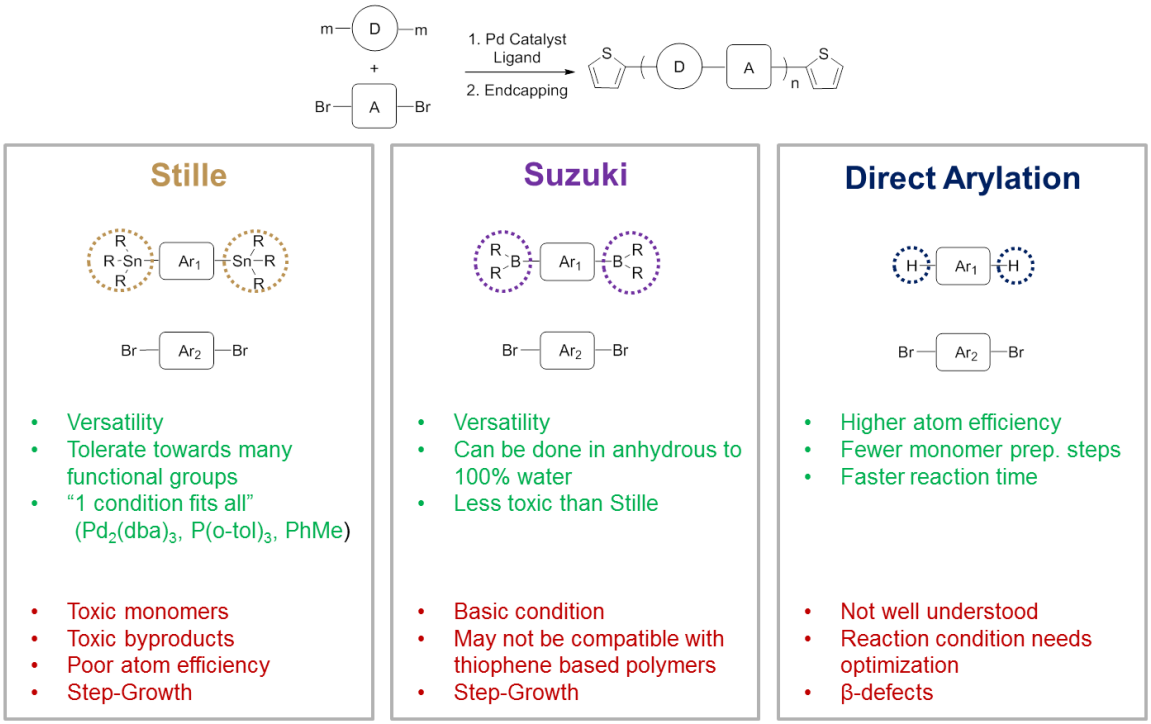

Figure 2-1. Summary of common cross-coupling reactions used for synthesizing conjugated polymers.

2.2.3. End-capping of Polymer

After the initial polymerization reaction is completed, "end-cappers" can be added to the reaction to remove the functional groups on the polymer chain ends. Tin, boron, and bromide groups can act as charge trapping sites, hindering the efficiency of charge transport and charge extraction in electronic devices. For Stille polymerization, 0.1 mol. eq. of 2-tributyltin thiophene is added and allowed to react for 8 hours and 0.2 mol. eq. of 2-bromothiophene is added subsequently and allowed to stirred for another 8 hours. While Koldemir *et al.* has shown that only partial end-capping is achieved in conjugated polymer synthesis, OFETs devices fabricated with the non-end-capped polymers have lower carrier mobility than those with the end-capped polymers.[156]

2.2.4. Post-Polymerization Workup and Handling

Once the cross-coupling polymerization is finished, the crude solution is usually precipitated into methanol, in which the salts and ligands are soluble and can be removed by filtration. The crude polymer precipitate is collected on a PTEF or a nylon filter using a fritted glass base filtration funnel assembly[157] (also known commonly as a "break-apart" funnel).

Further purification is necessary to remove residual metal contaminants in the polymer matrix, which can affect device performances. Palladium can act as charge trapping sites, hindering charge transport efficiency. Diethyldithiocarbamic acid diethylammonium salt (CAS# 2391-78-8), a palladium scavenger, is efficient in removing residual palladium. After the polymerization and end-capping reaction, the reaction flask is usually cooled to 60 ˚C and a spatula tip amount of the palladium scavenger is added and the mixture is stirred for 12 hours. The crude polymer solution is

then once again precipitated in MeOH, filtered, and collected. To further remove metal contents such as potassium salts, the polymer is redissolved in solvents, stirred with 18-crown-6 for at least four hours, precipitated and filtered. Soxhlet extraction is used to fractionate the polymers based on the molecular weight. The common sequence of solvents used for fractionating conjugated polymers is: MeOH (removal of catalyst, salt, palladium scavenger), acetone, hexanes (removal of low molecular weight oligomers), dichloromethane, chloroform. High molecular weight (>10 kg/mol) polymers are usually collected in the dichloromethane and/or chloroform fractions. Solvents with higher boiling points such as toluene, chlorobenzene, and o-dichlorobenzene are sometimes used to extract polymers of high molecular weights. Note that these polymer fractions from higher boiling point solvents are likely difficult to process during device fabrication due to their limited solubilities.

2.3. Structural Characterizations and Polymer Characterizations

^{1}H and ^{13}C NMR spectra were collected using a Varian Mercury Vx 300 MHz spectrometer or a Bruker Corporation DRX 500 MHz spectrometer. The chemical shifts for chloroform-d as the internal standard were referenced to the residual solvent peak, ^{1}H: δ = 7.26 ppm, ^{13}C: δ = 77.23 ppm. The chemical shifts for 1,1,2,2-tetrachloroethane-d_2 as the internal standard were referenced to the residual solvent peak, ^{1}H: d= 6.00 ppm. High-resolution mass spectroscopy was performed at The Georgia Institute of Technology Bioanalytical Mass Spectrometry Facility by Mr. David Bostwick and Dr. Cameron Sullards using LTQ Orbitrap XL™ ETD Hybrid Ion Trap-Orbitrap Mass Spectrometer and Applied Biosystems Voyager-DE™ STR Workstation. Elemental

compositions were analyzed for the carbon, hydrogen, nitrogen, and sulfur contents at Atlantic Microlab, Inc. Number average molecular weight (M_n) and dispersity ($Đ_M$) estimations of polymeric materials were obtained using gel permeation chromatography (GPC) performed at 30 °C with chloroform as the eluent using a Waters Associates GPCV2000 liquid chromatography system at UCSB's Material Research Laboratory by Dr. Rachel Behrens or 140 °C with 1,2,4-trichlorobenzene as the eluent using a Tosoh EcoSEC GPC System at The Georgia Institute of Technology. Trace element analysis on the palladium, tin, and phosphorus (or others) residual contents was performed by Dr. George Kamenov in the Department of Geological Sciences at the University of Florida using ThermoFinnigan Element2 HR-ICP-MS.

2.4. Electrochemical Experiments

Electrochemistry was performed to estimate the ionization potentials and the electron affinities of the electroactive materials using an EG&G Princeton Applied Research model 273A potentiostat-galvanostat. Cyclic voltammograms (CV) and differential pulse voltammograms (DPV), step size 2 mV, step time 50 ms, pulse amplitude 100 mV, of the materials were collected. The electrochemical cell setup included a Pt flag counter electrode, with a Ag/Ag^+ reference electrode, and a platinum disc working electrode with a surface area of 0.01 cm^2. For polymeric materials, a thin film of the polymer was deposited onto the disc electrode *via* drop-casting from a 1 mg/mL chloroform solution. A micropipette (20 μL) can be used to precisely measure the amount of solution used for deposition. Once the solution is deposited onto the button electrode, a beaker can be placed around the electrode to allow for longer drying time,

which usually produces a better film with higher coverage on the button surface. Note that making a thin-film button electrode requires trial and effort. The experimenter should create 3 to 4 electrodes of different thicknesses with the same polymeric materials to investigate how film thickness affects the electrochemical response. The electrochemical experiment was performed with a 0.5 M tetrabutylammonium hexafluorophosphate ($TBAPF_6$, 98% pure purchased from Acros and recrystallized in ethanol) in acetonitrile (obtained inside the glovebox from the solvent purification system) electrolyte solution. This electrolyte solution was also used to make the Ag/Ag^+ reference electrode by preparing a 0.01 M $AgNO_3$ solution. For molecules, solution electrochemistry was done instead since the thin-film of molecular species tended to be less robust and could delaminate during the experiment. A 1 mg/mL solution was prepared in the glovebox with 0.1 M $TBAPF_6$ in dichloromethane (dried under molecular sieves and degassed by "freeze-pump-thaw") electrolyte solution.

The background current from -2.0 V to +2.0 V with the electrolyte solution was first measured to ensure the electrochemical cell was absent of or contained little impurities. The electrochemical cell was then calibrated against ferrocene/ferrocenium (Fc/Fc^+) versus the Ag/Ag^+ reference. The potential of Fc/Fc^+ is assumed to be -5.1 eV versus vacuum. The potential of Fc/Fc^+ versus vacuum is a debatable topic among different research groups. For a detailed discussion on the potential of Fc/Fc^+ versus vacuum, the reader is directed to Barry Thompson's dissertation[158] and a journal article by Cardona et al.[159] Because different research groups use different Fc/Fc^+ energy levels versus vacuum, the reader should pay attention when exploring open literature to adjust

the ionization potential and electron affinity figures so they can be compared between different studies.

After scanning a blank button electrode to ensure the purity of the electrolyte solution and the components of the electrochemical cell, measurement can be performed on the conjugated materials. If the material is stable for both oxidation and reduction, oxidative and reductive electrochemistry can be done on the same film or solution. Otherwise, oxidative and reductive experiments should be performed separately and on a new film or solution. First, ten CV scans at 50 mV/s (usually between -2.0 V and +1.5 V but should be adjusted according to the reduction and oxidation properties of the material and the stability of the electrolyte and solvent) are performed to "break-in" the film, allowing the diffusion of electrolyte into the polymer film. DPV forward and backward scans should follow before scan rate dependence CV experiments (i.e. 20, 50, 100, 150, 200, 250, 300 mV/s for 3-5 cycles each). After the scan rate dependence experiments, DPV should be repeated to ensure film stability by comparing the onsets and magnitudes of peaks before and after scan rate dependence CV sweeps.

2.5. Optical and Spectroscopic Methods

2.5.1. Steady-state UV-Vis-NIR Absorption Spectroscopy

Since one of the main purposes of the active layer materials in an OPV device is light absorption, it is important to characterize their absorbing ability. Absorption spectroscopy is used to study the how a material interacts with the electromagnetic spectrum in the ultraviolet-visible-near infrared region, typically between 200 and 2000

nm. The absorption in the visible region, 400 – 700 nm, affects the perceived color of the materials.

The absorption of a photon excites a molecule or a polymer from its ground state to its excited state. This can also be seen as an electronic transition, in which the energy of the incident photon promotes an electron from an occupied orbital to an unoccupied orbital. For conjugated materials, the absorption of light results in a π to π^* transition and possibly intramolecular charge transfer transition between the donor and the acceptor moieties. Absorption spectroscopy can be carried out in the solid-state (thin-film) or the solution (in organic solvent) of the materials. By interpreting the absorption spectra, one can determine the optical energy gap and degree of conjugation (onset of absorption), the degree of aggregation and the intermolecular packing (appearance of low energy shoulder).

A stock solution of 1 mg/mL in chloroform was prepared. Parallel dilutions were performed to obtain at least five solutions of different concentrations, usually within the range of 10^{-4} to 10^{-6} M. The absorption intensity of each solution was recorded in order to evaluate the molar absorptivity of the material and ensure the concentration and absorbance follow a linear relationship according to Beer's Law. For thin-film samples, a solution of 5 mg/mL in chloroform (or other organic solvents) was prepared and deposited onto a 1" by 1" microscope slide glass substrate by spin or blade coatings. Absorption spectra were measured using a Varian Cary 5000 Scan UV-Vis-NIR spectrophotometer.

2.5.2. Ultrafast Transient Absorption Spectroscopy

Transient absorption spectroscopy (TAS) is a technique used to measure non-emissive charge carriers generated from photoexcitation. It is a "pump-probe" experiment, where a pump laser excites the molecule or the polymer from their ground to the excited states. A probing light source, usually generated from a xenon arc lamp, is then used to measure the absorption spectrum of the compound at various time delays after excitation. The unabsorbed probe light is measured by a photodiode array, and the data is analyzed to produce the absorption spectrum of the excited state.[160,161] TAS is a powerful technique since it can measure the absorption of dilute solutions and thin films, making it an ideal analytical tool to study the thin-film active layer of OPV. TAS has been used to study the photophysical phenomena in OPV materials and devices including photoabsorption, exciton generation, charge transfer at the donor-acceptor interface, and charge recombination, separation and collection. The resulting data is correlated to the device performance, especially short-circuit current and fill factor to understand the charge carriers dynamics in solar devices.[162]

Transient absorption spectroscopy was carried out by Dr. Bhoj Gautam in the Gundogdu Group at The North Carolina State University. The transient absorption spectroscopy setup consists of the spectrometer (Ultrafast Helios system) and amplified Ti:Sapphire Laser. The output of amplified Ti:Sapphire Laser provides 800 nm fundamental pulses at 1 kHz repetition rate which were split into two optical beams to generate the pump and probe pulses. One fundamental beam was used to generate pump beam using an optical parametric amplifier (OPA) system (Coherent Opera Solo). A white light/NIR probe was generated by focusing another fundamental beam into a flint glass. The pump and probe beams were directed onto the sample and the probe light was

collected by a charge-coupled device (CCD) device. The spectral detection region is 0.8 eV to 1.6 eV. The thin film samples were encapsulated using UV curable clue before measurement to prevent ambient exposure. The instrument response function (IRF) was ~100 fs FWHM. The samples measured in this dissertation were excited with the excitation energy 1.91 eV (650 nm) and the fractional change in transmission was detected in the probe range 0.8-1.6 eV at several time delays. These values should be adjusted accordingly to each sample's absorption property.

2.6. Thermal Characterizations

The thermal stability of materials is crucial since heat is often applied during material processing, device fabrication, and device usage. In material processing, molecular systems are sometimes deposited *via* thermal evaporation at temperature above 150 ˚C. In electronic devices, photoactive materials in photovoltaic devices are usually exposed to heat from solar irradiation reaching 80 °C; transistor materials must endure high temperatures required for device operation.

Usually, thermal properties are studied under two categories: 1. decomposition temperature (T_d) at which chemical decomposition of the material occurs; 2. temperature at which morphological or phase changes occur. For amorphous polymeric materials, a morphological change occurs first at the glass transition temperature (T_g), when the polymer changes from a brittle glass state to an elastic solid state as a result of greater segmental chain motions at an elevated temperature. At T_g, the heat capacity of the polymer increases due to the increase in chain motions, but there is no transfer of heat. Therefore, glass transition is considered a second-order phase transition. Materials can

also possess a melting temperature (T_m), which occurs at a higher temperature than T_g. T_m is the temperature at which the crystallites in the polymer melt due to heating. The difference between T_m and T_g is that T_m is a first order transition involving both changes in heat capacity and latent heat. It is noteworthy to state that the melting point (temperature at T_m) is described as a physical transition of the material from a crystalline or semi-crystalline phase to a solid amorphous phase. This is in contrast to a solid-to-liquid transition, at which point the material is considered to exist as both a solid and a liquid in equilibrium at the same time. Donor-acceptor type conjugated alternating copolymers are usually shown to be semi-crystalline with T_m between 250 and 350 ˚C. They also have high thermostabilities in an inert atmosphere and decompose above 400 ˚C.

Thermogravimetric analysis was carried out on a PerkinElmer Pyrus 1 TGA. Into a platinum pan 5 mg of material was placed and heated from 50 ˚C to 500 ˚C with a heating rate of 10 ˚C min^{-1} under a continuous flow of nitrogen (20 mL/min). Differential scanning calorimetry (DSC) was performed using a TA Instruments Q200 DSC with a heating and cooling rate of 10 ˚C min^{-1}. Usually, the temperature range is from -50 ˚C to 300 ˚C, but can be adjusted according to T_d measured by TGA and for the temperatures of the expected phase transitions. Typically three heating and cooling cycles are performed - the first one for erasing the thermal history of the sample, the second and third cycles are collected to ensure reproducibility and stability. T_m and crystallization temperature (T_c) are estimated by reporting the peak of the transitions.

Flash differential scanning calorimetry (Flash DSC) is a recently developed technique to study the metastability, reorganization, and kinetic of materials during fast

heating and cooling.[163] The METTLER TOLEDO Flash DSC 1 is capable of a heating rate of up to 40,000 K s^{-1} and cooling rate of as fast as 4,000 K s^{-1}. Flash DSC with scan rate at 1,000 K s^{-1} of conjugated polymers has shown enhanced melting and crystallization transitions.[164] Flash DSC is accessible at the Shofner Group in the School of Materials Science and Engineering at The Georgia Institute of Technology.

2.7. Langmuir-Blodgett Deposition

Langmuir-Blodgett experiments were performed with a KSV NIMA KN 2002 LB Trough at The Surface Engineering and Molecular Assemblies Laboratory in the Tsukruk Group at The Georgia Institute of Technology. The trough was first cleaned by chloroform and washed with ultrapure water (Millipore system, resistivity 18.2 MΩ.cm at 25 ˚C). Millipore water was employed as the subphase. The spreading solution was prepared by dissolving the amphiphilic materials in chloroform at 0.5 mg/mL. The solution (100 μl) was added dropwise onto the subphase using a micropipette. The floating film was left for at least 10 minutes to allow solvent evaporation and molecular spreading across the surface. The film was compressed by two Teflon barriers at a moving rate of 10 mm/min. Surface pressure was recorded by a Wilhelmy plate creating an isotherm of the monolayer compression. The surface compression pressure is used to control the quality of monolayer. A silicon or glass substrate is immersed into the trough vertically to allow the transfer of the LB monolayer onto the surface at the desirable compression pressure in the up stroke operation at a rate of 5 mm/min. Multilayer films were deposited *via* both up stroke and down stroke (y-type) at a rate of 5 mm/min.

2.8. Film Characterizations

2.8.1. Polarized Optical Microscopy (with Hot Stage)

An optical microscope is designed to produce magnified visual images of small samples. For uses in the field of organic electronics, an optical microscope can be used to observe the topography of a solid thin-film, the phase changes of the films during heating and cooling, and the aggregation of the material in solution. When a polarizer is added, the optical microscopy can be used to detect structural order within the materials. When a cross-polarized light passes through a birefringent material with structural order, it is split into different paths as a result of the phenomenon known as double refraction. Polarized optical microscopy (POM) was performed with an Olympus BX51 Polarizing Microscope. M-Plan Fluorite objectives at 10X, 20X, and 50X for magnification and U-PO3 polarizer were equipped with the microscope. A QImaging MicroPublisher 5.0 RTV camera was used to capture digital images, which were processed with Linksys 32 DV software. Linkam Scientific LTS420 hotstage was used on the POM for in-situ observation of phase transition. The maximum temperature on the hot stage is 420 ˚C. When operating above 200 ˚C, a water cooling pump must be used in combination with the LNP95 liquid nitrogen cooling pump.

2.8.2. Profilometry

Thin film thickness and roughness were measured by a Bruker Dektak XT profilometer in contact mode. A diamond stylus moved laterally to measure the variation in thickness across the sample. For thin films (thickness between 30 nm and 1 μm) deposited onto ITO substrates, two perpendicular line scratches were made with a wooden rod dipped in toluene (or another high boiling point solvent in which the film

dissolves) to allow two flat surfaces for leveling. The stylus traced across the first scratch, onto the sample, and the second scratch, measuring the height difference between the sample and the substrate. Multiple measurements were collected to obtain an average and a standard deviation on the film thickness.

2.8.3. Atomic Force Microscopy

Atomic force microscopy (AFM) is a type of high-resolution (sub-nanometer) scanning probe microscopy utilizing a fine tip at the end of a cantilever to scan across a surface to study its topography. As a result of the attractive or repulsive forces experienced between the tip and the surface, the cantilever bends towards or away from the surface. The surface phase and height properties can be probed by monitoring the bending of the cantilever. The AFM images displayed in this dissertation were obtained in tapping mode, in which the probe vibrates at or close to the resonant frequency of the cantilever as a result of an applied piezoelectric crystal at the tip holder. The oscillation of the tip generated by this resonant vibration taps onto the sample and studies the surface. The tapping method is commonly used on soft materials, which otherwise would have been damaged by contact method. This makes tapping mode AFM a desirable surface topography technique to study conjugated thin films.

Surface topology images were generated from the changes in oscillation amplitude as a result of the interaction between the tip and the sample surface. This oscillation amplitude is controlled to dampen when the tip encounters a protrusion along the surface. The photodiode detector registers the change and adjusts the scanner head to maintain the set oscillation amplitude. The changes in the scanner height, Z, across the surface is recorded and used to generate the surface topology image.

Mastering the AFM imaging technique takes practice and trials. Several parameters can be adjusted during setup and image acquisition to ensure the forward and backward line traces overlap with each other. The reader is encouraged to adjust the PID (proportional, integral, and derivative) of the feedback loop, the oscillation amplitude set point, and the data collection frequency during scan.[165] An optimal image can be achieved by increasing the P and I parameters to just below the point of noise appearance.

The tapping mode AFM images in this dissertation were obtained with a Bruker Icon AFM microscope, using 300 kHz tips with 40 N/m spring constant from Bruker (model: RTESP, part: MPP-11100-10).

2.8.4. Grazing Incident Wide Angle X-ray Scattering (GIWAXS)

Grazing Incident Wide Angle X-ray Scattering (GIWAXS) is a technique used to determine the structural order and orientation of conjugated molecules and polymers. As the name indicates, the synchrotron X-ray beam is at a grazing incidence angle at 0.12˚ or 0.20˚, both of which are slightly above the critical angle of the polymer film but below that of the silicon substrate, allowing for the penetration of the whole film and suppressing the scattering from the substrate.[166,167,168] This allows for sampling full thickness of the film and maximizing the diffraction signal. For the materials analyzed in this dissertation, GIWAXS measurements were performed on beamline 11-3 at the Stanford Synchrotron Radiation Lightsource. Pristine polymer and the blend of polymer:$PC_{71}BM$ thin films are spin-coated or blade-coated onto silicon wafers with the same conditions as in device fabrication. The photon energy of the x-ray beam is 12.7 keV. The scattering pattern is recorded using a MAR345 imaging plate or a Rayonix MX225 X-ray detector located at a distance of 300 mm from the sample center. The

images are calibrated using a lanthanum hexaboride (LaB6) standard. Each substrate is loaded into a helium-purged chamber to reduce air scattering and beam damage to the samples. X-ray irradiation durations vary between one and five minutes to achieve desirable signal intensity. Images are processed using the Nika software package for Wavemetrics Igor Pro,[169] in combination with custom-written Igor scripts to map the detector data to reciprocal space using equations published by Stribeck and Noechel.[170]. The signals are analyzed according to the modified Bragg's law, $q = 2\pi/\lambda$. For more details on the background of x-ray diffraction and data interpretation in polymer research, the reader is encouraged to consult Caroline Grand's dissertation[171] and a review article by Portale *et al.*[172]

2.9. Device Fabrication

2.9.1. Organic Photovoltaic Devices

To ensure reproducibility when fabricating OPV devices, the handling of all materials and processing conditions should be kept consistent. These include substrate cleaning, deposition conditions of common materials (i.e. metal contacts, HTL/ETL, vacuum level of evaporation chamber, etc.) Patterned ITO substrates supplied by Tinwell Technology (tinwell@incnets.com, project TI1678D) were cleaned by sonication for 15 minutes each in 0.1% sodium dodecyl sulfate solution, ultrapure water (Millipore system, resistivity 18.2 MΩ.cm), acetone, and isopropyl alcohol. The substrates were exposed to UV-ozone for two 10-minute treatments. PEDOT:PSS (Clevios™ P VP AI 4083) was purchased from Heraeus Deutschland GmbH & Co. KG. and was spin-coated in air onto the ITO substrate at 5,000 RPM for one minute (45 nm). Commercially available

$PC_{61}BM$ (ADS61BFA, 99.5% purity grade as indicated) and $PC_{71}BM$ (ADS71BFA, 99.0% purity grade as indicated) were purchased from American Dye Source, Inc. Donor and acceptor solutions were prepared in separate vials. They were first dissolved in the processing solvents and stirred for at least four hours before they were combined and allowed to mix overnight. Processing additives, such as 1,8-diiodooctane (DIO), were added usually when the donor and acceptor solutions were combined, allowing for overnight stirring. Note that in the solution preparation process according to Dr. Danae Constantinou in the Franky So Group at the North Caroline State University, DIO was usually added immediately before spin coating deposition of the active layer. The reader is encouraged to optimize the addition and stirring duration of the solvent additives. The active layer solutions were filtered through a 0.45 μm PTFE membrane filters attached to a glass syringe unless the aggregates in solution clogged the filters and prevented the solutions from passing through. The usage of plastic syringes should be prevented since Graham[173] and Carr[174] have shown respectively that the PDMS and silicone contents in plastic syringe can act as additives and alter device performance. The active layer was deposited onto the substrate by spin coating in an argon-filled glovebox or blade coating in ambient conditions. Top metal contacts were evaporated onto the active layer at 10^{-6} torr through a metal mask to produce 0.07 or 0.25 cm^2 active pixels.

In the Reynolds Group's solid state device laboratory (SSDL), the AM 1.5 illumination at 100 mW/cm^2 intensity was generated using a Newport Oriel 69907 power supply connected to a 150 W xenon arc lamp (Newport 6255) with collimating lenses in a Newport Oriel 94021A simulator lamp housing. J-V characteristics were recorded in an argon-filled glovebox with 2410 Keithley SourceMeter® SMU Instruments.

The V_{oc}, J_{sc}, FF, and the PCE measured under AM1.5 irradiation are the important parameters in evaluating the performance of an OPV device. The incident photon to current efficiency (IPCE) is an additional technique to measure quantum efficiency of a solar cell as a function of the wavelength. IPCE can be calculated using Equation 2-3:

$$IPCE\ (\%)\ =\ \frac{\#electron_{out}}{\#electron_{in}}\ \times\ 100 = \frac{h \cdot c \cdot I}{e \cdot \lambda \cdot P}\ \times\ 100 \qquad (2\text{-}3)$$

where h is Planck constant = 6.626×10^{-34} J s^{-1}, c is the speed of light = 3.00 x 10^8 m s^{-1}, I is the device current with no applied bias (mA cm^{-2}), e is the elementary charge = 1.602×10^{-19} C, λ is the wavelength of the incident light (nm), and P is the incident light radiant power (mW cm^{-2}).

IPCE measurements were conducted in air using a setup consisting of a Newport 66485 xenon lamp, an Oriel® CS260™ VIS-NIR 1/4 m monochromator, and a Merlin™ 70104 Digital Lock-in Radiometry Detector System.

2.9.2. Organic Field Effect Transistor Devices

To investigate the parallel charge transport characteristics, top-contact bottom-gate OFET devices were fabricated on Si/SiO_2 substrates[175] (Silicon Quest Inc. resistivity < 0.005 Ω·cm) by Dr. Chang-Yin Wang in the Kippelen Group. The purpose of SiO_2 was serving as gate dielectric, and it was thermally grown to a thickness of 200 nm. Fabrication started by removing the backside SiO_2 from Si/SiO_2 substrates. Positive photoresist (PR) (SPR 220-7.0) was spin-coated onto the wafers at 1500 rpm for 60 s and annealed at 110 °C for 5 minutes on a hotplate. The wafers were submerged in a buffer oxide etch (BOE) made up of 6:1 v/v of 40% NH_4F solution to 49% HF solution for 3

minutes to remove the backside oxide. BOE was washed off the wafers by dipping into two containers of distilled water sequentially for 1 minute each. Si/SiO_2 substrates were sonicated in acetone, distilled water, and isopropanol sequentially for 5 minutes each. After the cleaning steps, the active layer films were coated by Langmuir-Blodgett technique or by spin-coating. 10 nm of MoO_3 and 50 nm of Ag source/drain electrodes were deposited onto the active layer through shadow masks in a thermal evaporator. The channel width and length were 1200 μm and 100 μm, respectively. All measurements were obtained using an Agilent E5272A source/monitor unit in a glovebox with O_2 and $H_2O < 0.1$ ppm.

CHAPTER 3

DONOR-ACCEPTOR POLYMERS FOR ORGANIC PHOTOVOLTAICS DEVICES

The field of organic photovoltaics (OPVs) has shown significant improvements over the past five years with devices breaking the 10% barrier in power conversion efficiencies (PCEs). While much effort has shifted into the development non-fullerene acceptors, researchers continue to develop donor materials to further improve performance. An effective strategy in donor design involves conjugated frameworks with multiple fused rings. This ladder-type design forces the conjugated backbone into planarity, which extends conjugation lengths, reduces rotational disorder along the backbone, and enhances physical, chemical, and mechanical stabilities of the polymers.[32] Popular multiple ring electron-rich moieties include benzodithiophene (BDT), cyclopentadithiophene (CPDT or DTC), dithienosilole (DTS), and dithienogermole (DTG). On the electron deficient side, thienopyrrolodione (TPD), isoindigo (iI), diketopyrrolopyrrole (DPP), and benzothiadiazole (BTD) all consist of fused structures.

The first part of this chapter will begin with the hypothesis and objective behind the "one-atom" change high performing donor-acceptor polymer project. A family of photoactive conjugated polymers with only a "one-atom" minimal change was designed and synthesized. Each alternating copolymer has a repeat unit containing a bithiophene unit with a center Group 14 atom (C, Si, Ge) and a TPD moiety. Synthetic strategies including monomer purification, handling of catalyst, reaction setups, parallel

polymerizations, and polymer purifications will be explained. An extensive polymer structural characterization including molecular weights and elemental compositions will be shown to confirm the purities of the polymers. Detailed characterizations of material properties will be presented, focusing on collaborative efforts in intermolecular packing, exciton generation and decay mechanisms, charge mobility, dielectric constant, and theoretical correlation to device performance.

The second part of the chapter will present work on isoindigo, diketopyrrolopyrrole, and thienoisoindigo co-thiophene donor-acceptor polymers to understand the structure-property effects of different acceptors and thiophene derivatives on OPV device performances when blended with fullerene. It will specifically focus on how the structures and the frontier energy levels of the acceptor units affect the open-circuit voltages, the active layer morphologies, and device performances. This chapter will end with synthetic approaches to materials.

3.1. Group 14 Atom-bridged Dithieno-TPD based Donor-Acceptor Polymers

In this study, we employ a family of photoactive conjugated polymers with only a "one-atom" minimal change. Each alternating copolymer has a repeating unit containing a bithiophene donor with a center Group 14 atom (C, Si, Ge – resulting in DTC, DTS, DTG) and a TPD acceptor. Previous studies[176,177,178,179,180,181,182,183,184,185] (summarized in Table 3-1) have shown polymers based on repeating units DTC-TPD, DTS-TPD and DTG-TPD leading to PCE as high as 3.7%, 8.1%, and 8.5%, respectively, showing the substantial impact of a minimal change in polymer chemical structure on OPV device performance. However, it is important to recognize that a direct comparison of these

materials from different studies is not sufficient to isolate and elucidate their structural impact and device properties since they have different synthesis approaches, molecular weights, and purities, and the solar devices have different processing methods and architectures. Similar "one-atom" change investigations have been conducted but the polymers prepared in these previous studies had variations in molecular weights, dispersities, and polymerization methods. [178,186]

Here, we used parallel polymer syntheses and purifications to obtain polymers with similar molecular weights, dispersities, chemical, and structural purities allowing us to isolate the effect of changing the center "one-atom" on photovoltaic properties. We investigated the solution-state properties with proton NMR, solid-state properties with stable-state and transient absorption spectroscopies, electrochemistry, and GIWAXS, and repeat unit structures with theoretical study to reveal the effect of intermolecular packing between polymer chains on OPV device performance. We found that the longer C-Si and C-Ge bonds led to different aggregation behaviors in both solution and solid states, which impacted the backbone orientations against the substrates. Transient absorption spectroscopy results indicate a more efficient bimolecular recombination between separated charges in the DTC polymer due to a more stable triple, which was confirmed by theoretical calculation.

Table 3-1. Published properties of the polymers with the same backbones as in the one-atom change project.

	M_n (kDa)	$Đ_M$	Catalyst	IP	EA	Film λ^{onset}	Fullerene	Polymer to PCBM Ratio	Additive	Solvent	Device	V_{oc}	J_{sc}	FF	PCE	Ref
DTC	16.0	1.26	$Pd(PPh_3)_4$	-5.73	-3.55	741	$PC_{71}BM$	1:2	None	*o*-DCB	Conventional	0.80	10.0	47%	3.7%	[178]
	16.0	1.26	$Pd(PPh_3)_4$	-5.73	-3.55	741		1:2	2% CN	*o*-DCB	Conventional	0.80	9.4	45%	3.5%	[178]
	17.0	1.25	$Pd_2(dba)_3$	-5.67	-3.95	740		1:1	None	*o*-DCB	Conventional	0.86	8.5	43%	3.1%	[179]
	17.0	1.25	$Pd_2(dba)_3$	-5.67	-3.95	740		1:2	None	*o*-DCB	Conventional	0.86	6.9	48%	2.9%	[179]
DTS	13.6	1.43	$Pd(PPh_3)_4$	-5.74	-3.47	734	$PC_{71}BM$	1:2	None	*o*-DCB	Conventional	0.91	2.3	56%	1.2%	[178]
	13.6	1.43	$Pd(PPh_3)_4$	-5.74	-3.47	734		1:2	2% CN	*o*-DCB	Conventional	0.85	6.6	37%	2.1%	[178]
	24.2	2.40	$Pd(PPh_3)_4$			740		1:1.5	2.5% DIO	*o*-DCB	Conventional	0.91	11.1	50%	5.0%	[180]
	17.0	2.11	$Pd(PPh_3)_4$	-	-	740		1:2	30 mg/ml 1,5-DMN	TMB	Inverted	0.90	13.5	67%	8.1%	[181]
	17.0	2.11	$Pd(PPh_3)_4$	-	-	740		1:2	3% DIO	CB	Inverted	0.91	12.3	65%	7.3%	[181]
	-	-	-	-	-	-		1:2	3% DIO	*o*-DCB	Conventional	0.90	11.0	63%	6.2%	[182]
	-	-	-	-	-	-		1:1.5	2% MeN + 3% DIO	Xylene	Conventional	0.89	11.7	59%	6.2%	[182]
	29.0	1.80	$Pd_2(dba)_3$	-5.82	-4.09	717		1:2	3% DIO	CB	Inverted	0.89	11.9	65%	6.8%	[183]
	31.0	1.58	-	-	-	717		1:2	3% DIO	CB	Conventional	0.91	12.1	70%	7.5%	[183]
	42.5	1.54	$Pd_2(dba)_3$	-5.65	-3.50	717		1:1.5	5% DIO	CB	Inverted	0.89	11.5	65%	6.6%	[176]
DTG	16.3	1.90	$Pd(PPh_3)_4$	-5.76	-4.03	742	$PC_{71}BM$	1:2	3% DIO	CB	Conventional	0.80	9.7	53%	4.1%	[184]
	-	-	$Pd_2(dba)_3$	-	-	-		1:1.5	5% DIO	CB	Conventional	0.86	15.9	63%	8.5%	[185]
	47.5	1.73	$Pd_2(dba)_3$	-5.60	-3.50	734		1:1.5	5% DIO	CB	Inverted	0.86	14.0	67%	8.5%	[177]
	47.5	1.73	$Pd_2(dba)_3$	-5.60	-3.50	734		1:1.5	5% DIO	CB	Inverted	0.85	12.6	68%	7.3%	[176]

3.1.1. Polymer Synthesis of P(DTC-TPD), P(DTS-TPD), and P(DTG-TPD)

To synthesize this family of one-atom change polymers containing a bridged bithiophene and thienopyrrolodione (TPD) units, Stille cross-coupling polymerization was chosen because of reproducibility and high yield. The synthesis of TPD monomer was described in Scheme 3-1. The precursor 3,4-thiophenedicarboxylic acid underwent basic hydrolysis and subsequent ring closure to from the cyclic anhydride species (Compound 3-1). *N*-alkylated imides (Compound 3-3) were obtained *via* a 4-carbamoyl-thiophene-3-carboxylic acid (Compound 3-2) by refluxing with thionyl chloride. Bromination with *N*-Bromosuccinimide (NBS) afforded the TPD monomer (Compound 3-4).[187] Note that Rylan Wolfe has shown a modified TPD synthesis, in which a non-hydrogen-functionalized TPD was obtained, eliminating the *N*-alkylation step and improving the versatility of TPD synthesis and functionalization.

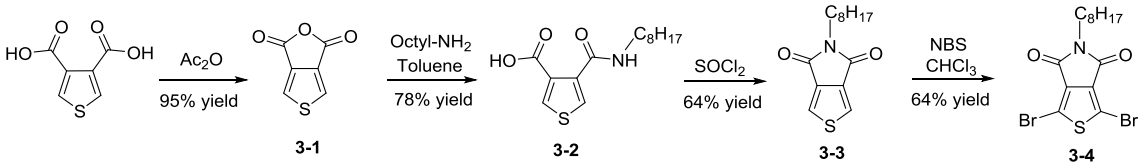

Scheme 3-1. Synthesis of thienopyrrolodione

The synthesis of the donors is described as follow. The dibromo-functionalized version of cyclopentadithiophene (CPDT) or "dithienocarbon" (DTC), was purchased from Bepharm Ltd. DTC can also be synthesized from scratch following published procedures.[188] Stannylation of dibromodithienocarbon afforded the distannylated monomers (Compound 3-5). Dithienosilole and dithienogermole were synthesized by Dr. Junxiang Zhang and Rylan Wolfe, respectively. These compounds were synthesized

following published literature procedures.[176,189] All the stannylated compounds were purified using preparative HPLC in a solvent mixture of acetone and acetonitrile according to the method described in Chapter 2.

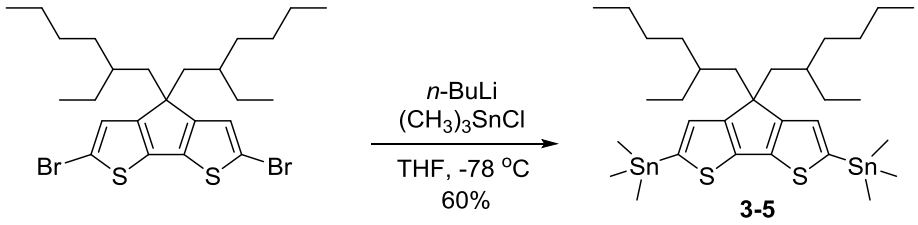

Scheme 3-2. Synthesis of DTC.

3.1.1.1. Stille Cross-Coupling Polymerization

Scheme 3-3 outlines the Stille polymerizations process used to produce the one-atom change polymers at 90 ˚C for 120 hours using $Pd_2(dba)_3$ and P(*o*-tol)$_3$ as the catalyst and ligand, respectively (Scheme 1). Diethyldithiocarbamic acid diethylammonium salt, a palladium scavenger, was used to remove palladium from the crude polymers. The concentrated crude polymer solutions were precipitated into methanol, filtered, and subsequently fractionated *via* soxhlet extraction. The chloroform fractions were concentrated and the mixtures passed through 4" plugs containing 1:1:1 volume mixtures of silica, basic alumina, and celite using chloroform as the eluent. The polymer solutions were concentrated to solids and redissolved in a minimal amount of chloroform. The solutions were filtered through 0.45 μm nylon membrane filters directly into an excess of acetone. After stirring for 30 minutes, the precipitated polymers were filtered onto 0.45 μm nylon filters. The collected polymers were dried under high vacuum for 24 hours.

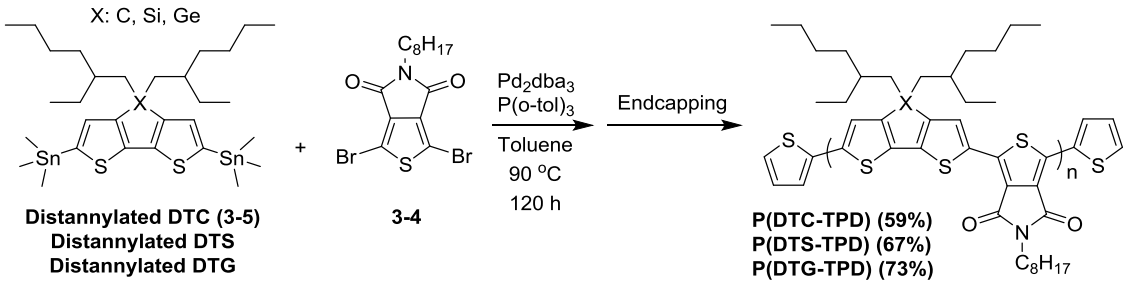

Scheme 3-3. Stille polymerization of **P(DTC-TPD)**, **P(DTS-TPD**), and **P(DTG-TPD)**.

3.1.2. Control of molecular weight, dispersity, and purity

The physical and chemical characteristics of the polymers are summarized in Table 3-2. All three polymers have similar number average molecular weights (M_n) and dispersities ($Đ_M$) at 20-27 kDa and 1.4-1.7, respectively. To further understand the chemical and structural purities of our polymers, elemental analysis was performed to validate the elemental accuracies, which found that for all polymers, the contents of C, H, N, and S were within 0.4% of calculated values. Inductively Coupled Plasma Mass Spectrometry (ICP-MS) was used to confirm low residual phosphorus, palladium, and tin contents within the polymer matrices.

To fully digest the polymer matrix (a transparent solution without residual precipitates), microwave-assisted acid digestion in sulfuric acid and nitric acid was performed. To a 10 mL microwave vial, 10 mg of polymer matrix and 1 mL of conc. H_2SO_4 were added. The vial was heated to 200 ˚C for 10 minutes to dehydrate the polymer. Subsequently, 1 mL of conc. HNO_3 was added to the microwave vial and heated to 110 ˚C for 10 minutes to fully digest the polymer matrix. A control containing a mixture of the mineral acids was used to calibrate the signals. Note that conversion heating with H_2SO_4 and HNO_3 in an oil bath was unsuccessful in fully digesting the polymer matrix. Aqua regia was also used but the outcome was similarly dissatisfying.

Previous elemental investigations by ICP-MS on conjugated materials synthesized by cross-coupling reactions such as Stille and direct arylation polymerizations have shown residual Sn, Pd, and P contents as high as two orders of magnitude greater than our analyses. [156,190] The low residual elemental contents in our polymers confirm that the purification process through end-capping, reprecipitation, palladium scavenging, and column chromatography allow us to afford three highly pure polymers, and thus reduce the number of potential charge trapping sites within the polymer matrix.[191,192]

Table 3-2. Physical properties, elemental accuracies, and residual metal contents of the polymers

	Yield[a]	GPC[b]	Elemental Analysis Actual (Theoretical)				ICP-MS		
	(mg)	M_n(kDa)/ $Đ_M$	C (%)	H (%)	N (%)	S (%)	P (ppm)[c]	Pd (ppm)	Sn (ppm)
P(DTC-TPD)	374.6 (59%)	26.4/1.4	70.54 (70.33)	8.14 (8.32)	2.16 (2.10)	14.57 (14.44)	bdl	24.61	26.35
P(DTS-TPD)	423.4 (67%)	24.5/1.8	67.25 (66.91)	7.85 (8.13)	2.10 (2.05)	14.47 (14.10)	bdl	31.39	25.67
P(DTG-TPD)	482.8 (73%)	20.8/1.9	63.06 (62.81)	7.20 (7.63)	2.03 (1.93)	13.42 (13.24)	bdl	38.13	56.74

[a] Yields in chloroform soxhlet fractions. [b] Molecular weights and dispersities were determined by gel permeation chromatography with polystyrene as the calibration standard and 1,3,4-trichlorobenzene at 140 ˚C as the eluent. [c] Phosphorus levels for all polymer samples were below detection limit (bdl).

3.1.3. Optical, Electrochemical, and Thermal Properties of P(DTC-TPD), P(DTS-TPD), and P(DTG-TPD)

3.1.3.1. Optoelectronic Properties – Difference in Solid State Aggregation

Ionization potentials and electron affinities of the polymers were estimated by electrochemistry using differential pulse voltammetry (Figure 3-1). The polymers have similar IPs and increasing EAs going from C to Si to Ge, which can be attributed to the enhancement of orbital interactions between the π* orbitals of the butadiene on the thiophenes and the σ* bonds of the center Group 14 atom, as the atomic sizes increase down the group.[193] The thin-film onsets of absorption for all the polymers are ~730 nm

(Figure 3-2a). The absorption profiles of poly(dithienosilole-alt-thienopyrrolodione), **P(DTS-TPD)**, and poly(dithienogermole-alt-thienopyrrolodione), **P(DTG-TPD)**, are similar with λ_{max} at ~671 nm. Poly(dithienocarbon-alt-thienopyrrolodione), **P(DTC-TPD)**, shows a stronger absorption profile between 430 and 680 nm. The ratio of the absorption intensity between the vibronic features is used to identify the polymer aggregation patterns. After normalizing the 0-0 transition peaks (~675 nm) of the polymers, we observed that the 0-1 vibronic feature at ~600 nm was clearly stronger for **P(DTC-TPD)**. In both solution (Figure 3-2b) and thin-film absorptions, **P(DTC-TPD)** has a lower I_A^{0-0}/I_A^{0-1} ratio than the **P(DTS-TPD)** and **P(DTG-TPD)**, indicating **P(DTC-TPD)** has a higher H-aggregate population.[194] The optoelectronic properties are summarized in Table 3-3. The difference in solution and solid state aggregating interactions in this family of polymers was further studied by nuclear magnetic resonance and grazing incidence wide-angle X-ray scattering.

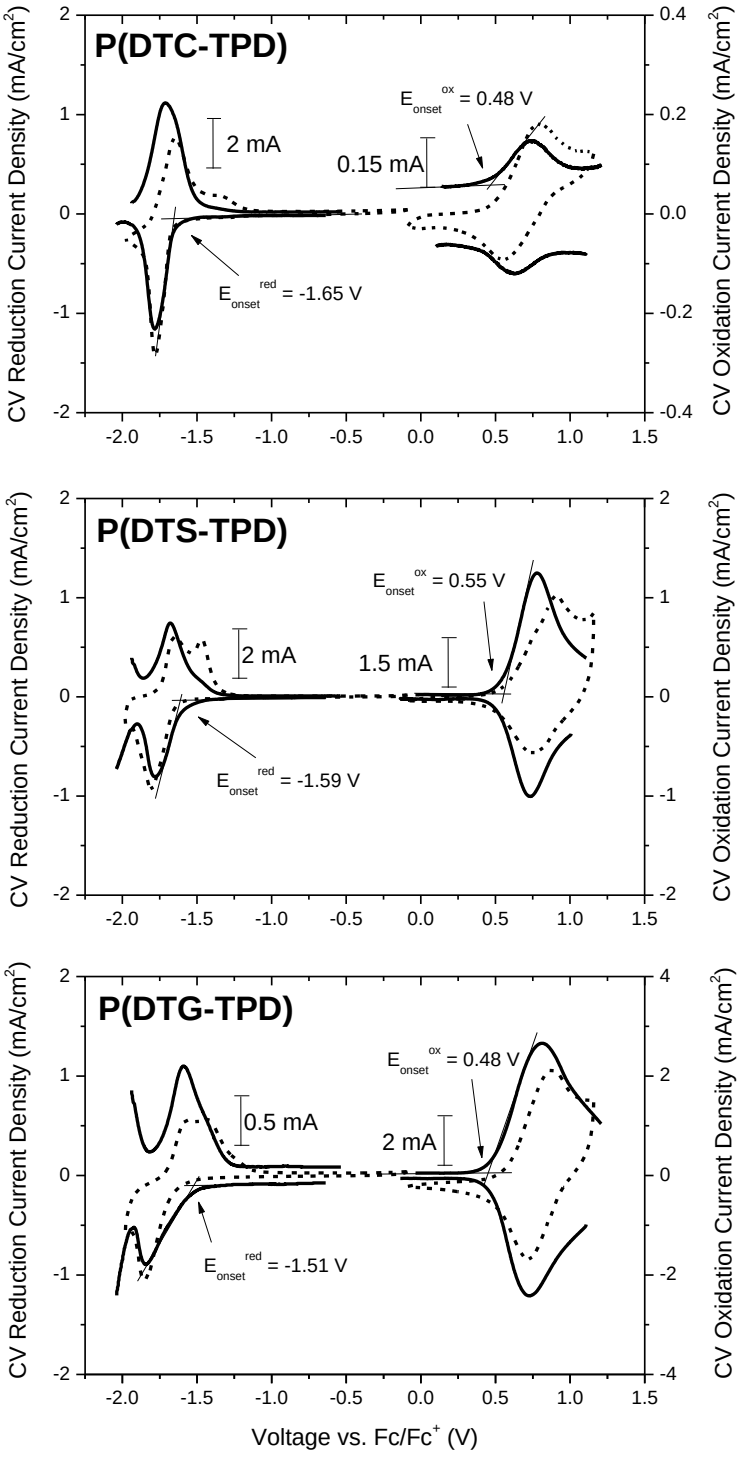

Figure 3-1. Cyclic voltammograms and differential pulse voltammograms of the polymers. Electrochemistry was recorded with thin films drop-casted from chloroform solutions onto platinum button electrodes. CV (scan rate 50 mV/s) and DPV (step size 2 mV, step time 50 ms, pulse amplitude 100 mV) of the polymers were measured using 0.01 cm^2 Pt disc electrodes in 0.5 M $TBAPF_6$/ACN, a Ag/Ag^+ reference electrode (0.01 M $AgNO^3$), and Pt flag counter electrode.

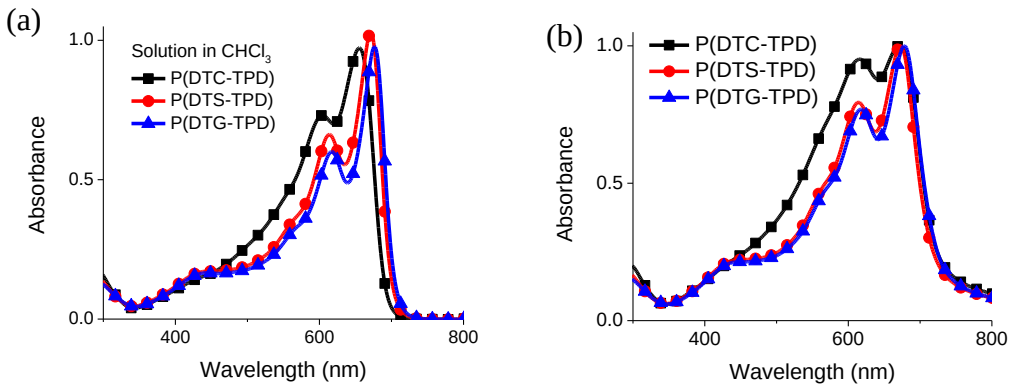

(c)

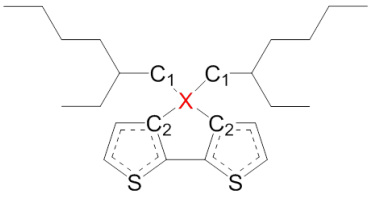

	Bond length (Å)	
	X – C1	X – C2
X = C	1.527	1.564
X = Si	1.893	1.898
X = Ge	1.978	1.984

Figure 3-2. (a) Solution and (b) normalized thin-films absorption spectra of the polymers. (c) Carbon-to-center atom bond lengths calculated at the DFT//B3LYP/6-31G** level.

Table 3-3. Optical and electrochemical properties of polymer films

	Absorption				Electrochemistry[c]		
	λ_{max} (nm)	λ_{onset}[a] (nm)	E_{gap}^{opt}[b] (eV)	I_A^{0-0}/I_A^{0-1}	IP (eV)	EA (eV)	E_{gap}^{echem} (eV)
P(DTC-TPD)	615, 671	724	1.71	1.05	-5.60	-3.47	2.13
P(DTS-TPD)	613, 672	725	1.71	1.26	-5.67	-3.53	2.14
P(DTG-TPD)	617, 678	730	1.69	1.30	-5.60	-3.61	1.99

[a] thin films spin-coated on glass slides from 5 mg/mL solution in Chloroform. [b] $E_g^{opt} = 1240 / \lambda^{onset,film}$. [c] Oxidation and reduction potentials were measured by thin-film electrochemistry using different pulse voltammetry scan. IP and EA values were calculated by assuming SCE to be 4.74 eV vs. vacuum and Fc/Fc^+ to be +0.38 eV with respect to SCE.

3.1.4. Temperature-dependent NMR - Difference in Solution Aggregation

^{1}H NMR spectra were collected to confirm the polymer structures, but they had shown unexpected results related to differences in polymer aggregation. Due to the symmetry of the polymer repeating structure, the two aromatic protons on the fused bithiophene moiety were expected to display one aromatic proton signal. However, as shown in Figure 3-3, the spectra revealed different characteristic aromatic peaks between the three polymers. At room temperature, **P(DTC-TPD)** showed one multiplet at ~8.1 ppm, while **P(DTS-TPD)** and **P(DTG-TPD)** displayed two peaks at ~7.5 and ~8.5 ppm. It has been suggested that polymer aggregates can result in the two distinct aromatic proton NMR signals on the DTG moiety when they experience different magnetic environments.[195] In an attempt to break up the aggregates and allow the polymer backbones to overcome rotational barriers, variable-temperature NMR was performed at 110 ˚C. The two peaks seen at room temperature resolved, and a new peak arose at ~8.1 ppm for **P(DTS-TPD)** and **P(DTG-TPD)** when the solutions were heated. These new aromatic signals were at chemical shifts comparable to that of **P(DTC-TPD)**, confirming the extra peaks at room temperature were the result of polymer aggregations. Since the solution concentrations (~ 10 mg/mL) for these NMR investigations are comparable to the processing solutions for OPV device fabrication, we expect this solution "pre-aggregation" behavior to affect the intermolecular interaction in their corresponding thin-films.

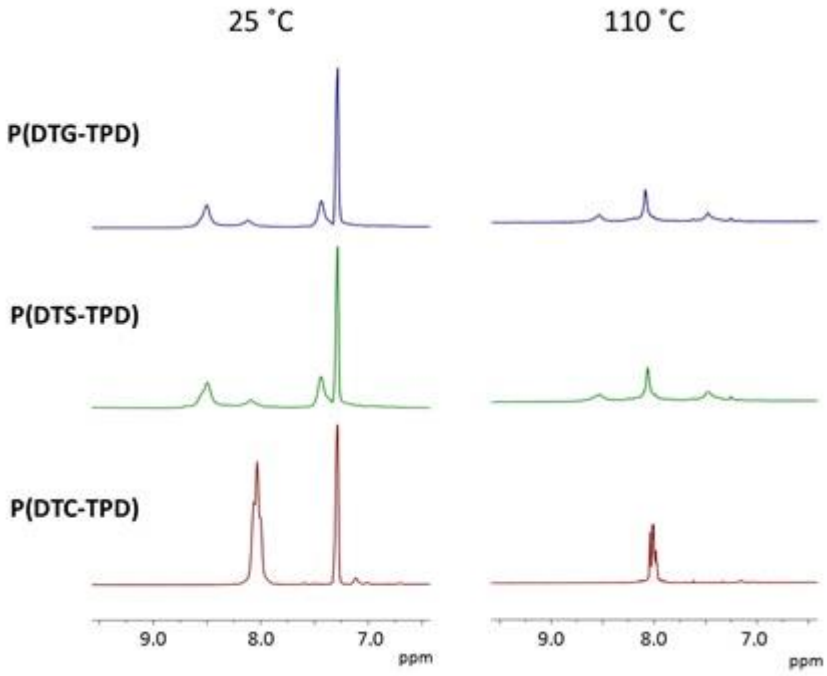

Figure 3-3. Room temperature ^{1}H NMR spectra of the polymers showing multiple aromatic peaks for **P(DTS-TPD)** and **P(DTG-TPD)** compared to **P(DTC-TPD)**. Peaks at 7.26 arise from $CHCl_3$-d. Variable-temperature spectra in 1,1,2,2-tetrachloroethane-d_2 show the peaks of **P(DTS-TPD)** and **P(DTG-TPD)** resolve at elevated temperature, indicating different aggregation behaviors in the three polymers.

3.1.5. Grazing Incidence Wide-angle X-ray Scattering: Edge-on for P(DTC-TPD) and Face-on for P(DTS-TPD) and P(DTG-TPD)

To investigate the intermolecular interactions and polymer packing, grazing incidence wide-angle X-ray scattering (GIWAXS) measurements were performed on thin-films of the pristine polymers and the polymer:fullerene blends. The scattering signals were indexed and correlated to the polymer intermolecular packings and orientations against silicon substrates, with (010) planes corresponding to π-π stacking and (100) planes to lamellar order. Interplane distances were calculated using the modified Bragg's law, $q = 2\pi/\lambda$.

The scattering images revealed differences in polymer orientations for **P(DTC-TPD)** compared to the Si and Ge polymers. The pristine thin-films of **P(DTS-TPD)** and

P(DTG-TPD) showed strong out-of-plane π-π (010) and in-plane lamellar (100) diffractions (Figure 3-4) indicating face-on orientations of the polymer backbones against the silicon substrates. Their face-on orientations were retained in the polymer:$PC_{71}BM$ blends. **P(DTC-TPD)**, on the contrary, displayed in-plane π-π (010) and out-of-plane lamellar (100) signals that were evidences of edge-on orientation. Interestingly, temperature annealing the pristine polymer thin-film also led to changes in thin-film for **P(DTC-TPD)** (Figure 3-5). The diffraction pattern became more anisotropic indicating a more distinct orientation of polymer crystallites. We attributed this to the greater crystallinity of **P(DTC-TPD)** shown in the differential scanning calorimetry study (Figure 3-6), where only **P(DTC-TPD)** displayed melting and crystallization phase transition signals.

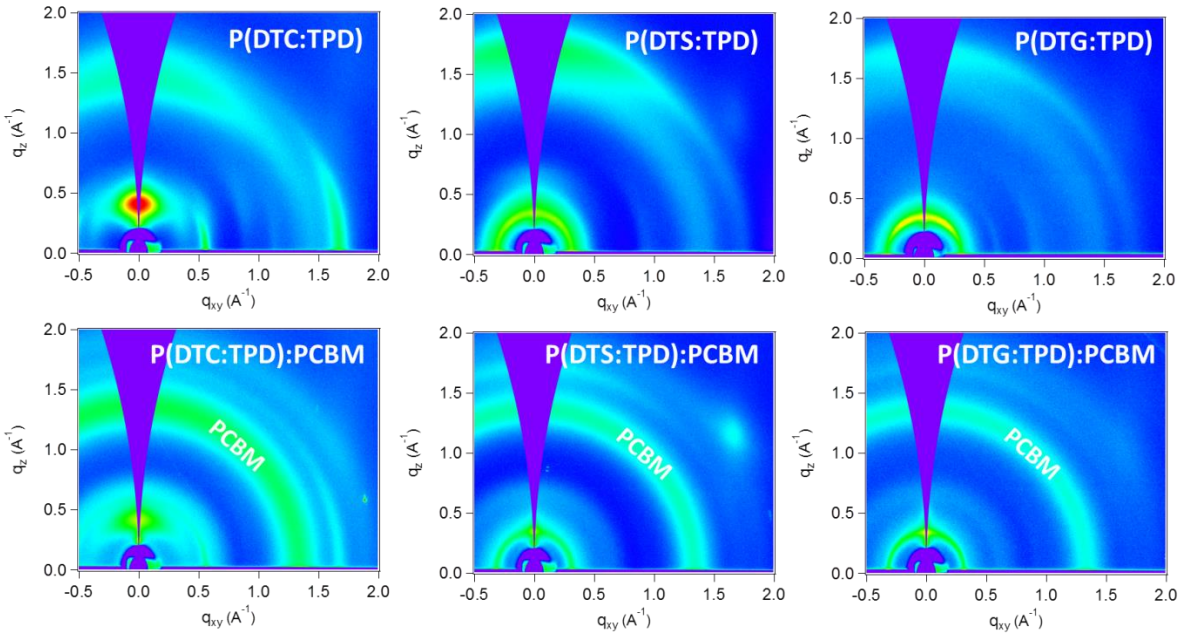

Figure 3-4. GIWAXS patterns for pristine polymer thin-films (top) and polymer:$PC_{71}BM$ blends (bottom).

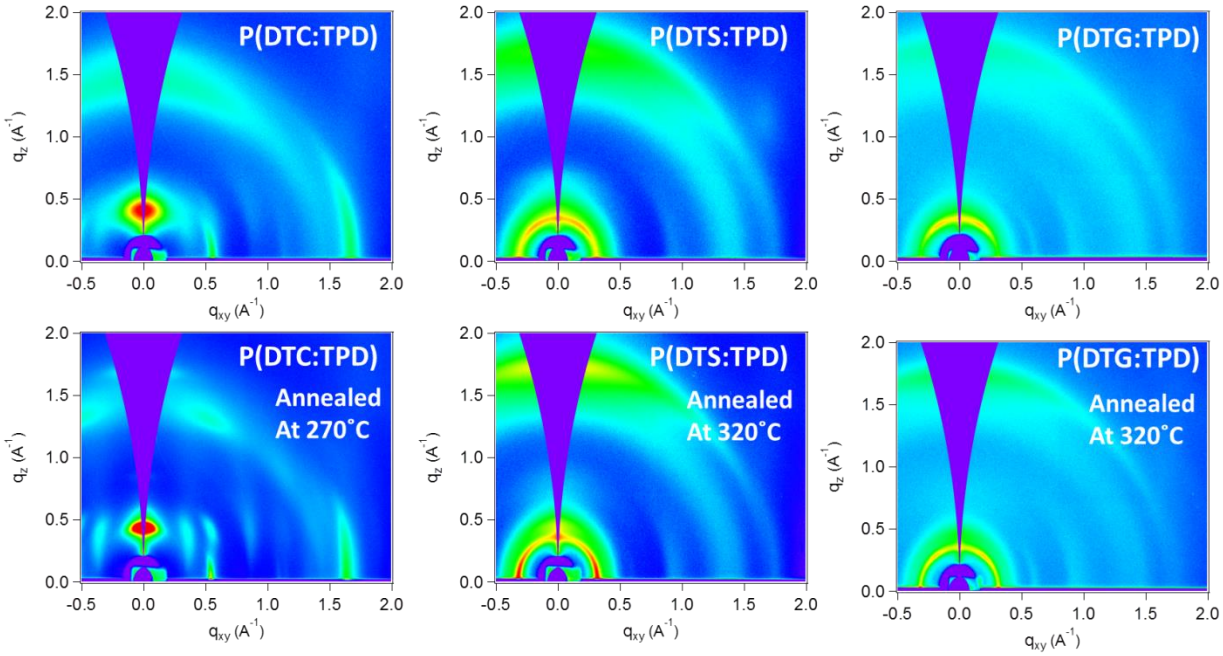

Figure 3-5. GIWAXS patterns for pristine polymer thin-films as-cast (top) and post temperature annealing (bottom).

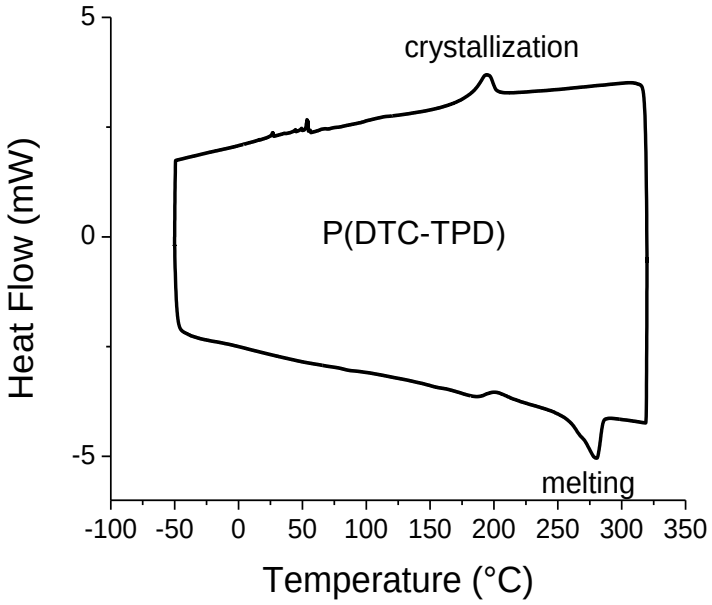

Figure 3-6. Differential scanning calorimetry scan of **P(DTC-TPD)** at a rate of 10 ˚C/min.

While all three polymers had similar π-π interplane distances of ~3.7 Å, their lamellar distances were significantly different, with **P(DTC-TPD)** having a significantly closer packing at 14.8 Å vs. **P(DTS-TPD)** and **P(DTG-TPD)** (19.6 and 18.6, respectively). As mentioned earlier, we found via DFT calculation that the C-C bond length is substantially shorter than the C-Si and C-Ge bonds. This bond length difference is believed to impact the extension and orientation of the 2-ethylhexyl alkyl moieties attached to the polymer backbones, thus changing the lamellar stacking distances. Charge mobility is generally believed to be constrained by interchain charge hopping.[196] The similarity in the π-π stacking distances of the three polymers translates into minimal differences in the charge carrier mobility (Table 3-4). The amorphous characteristics of the polymers thin-films observed in the DSC result can be used to explain the similarities in charge mobility for the pristine polymers and the blended thin-films with fullerene molecules added. All devices have balanced space charge limited current (SCLC) hole and electron mobility on the order of 10^{-3} to 10^{-4} cm^2 V^{-1} s^{-1}, which is ideal for preventing charge build-up that limits photocurrent in the OPV devices.

Table 3-4. Space charge limited current transport properties of polymer:fullerene blends.

Device	**Hole Mobility cm^2 V^{-1} s^{-1}**	**Electron Mobility cm^2 V^{-1} s^{-1}**
P(DTC-TPD) :$PC_{71}BM$	$5.2*10^{-4} \pm 1.7*10^{-5}$	$2.9*10^{-3} \pm 2.8*10^{-4}$
P(DTS-TPD) :$PC_{71}BM$	$1.4*10^{-3} \pm 3.3*10^{-5}$	$2.8*10^{-3} \pm 5.2*10^{-4}$
P(DTG-TPD) :$PC_{71}BM$	$4.3*10^{-4} \pm 3.5*10^{-5}$	$2.4*10^{-3} \pm 1.8*10^{-4}$

3.1.6. Organic Photovoltaic Devices – Difference in Fill Factor and Power Conversion Efficiency

Bulk heterojunction (BHJ) OPV devices were fabricated using the three polymers in the conventional device architecture (indium tin oxide (ITO)/poly(3,4-ethylenedioxythio-phene):polystyrene sulfonate (PEDOT:PSS)/polymer:$PC_{71}BM$/lithium fluoride (LiF)/Al). Interestingly, the optimized processing conditions for all polymer:fullerene blends were identical, requiring 1:1.5 weight ratio of polymer to fullerene, 5 vol% of diiodooctane (DIO), and no thermal or solvent annealing. The current density-voltage curves and the summary of device performances are presented in Figure 3-7a and Table 3-5, respectively. **P(DTS-TPD)** and **P(DTG-TPD)** had open-circuit voltages (V_{oc}) approaching 0.88 V, while V_{oc} for **P(DTC-TPD)** was slightly higher at 0.92 eV. It is reasonable that **P(DTC-TPD)** has a slightly higher V_{oc} values due to its low EA and large energy gap observed from the electrochemical result. All three devices have similar short-circuit currents (J_{sc}) at 11-13 mA/cm^2, which indicates that they have similar light absorption, charge generation, and transport properties. To confirm the J_{sc} results from PCE measurements, incident photon-to-current efficiency (IPCE) spectra were collected to determine the spectral responses. As shown in Figure 3-7b, in the wavelength range corresponding to photocurrents from the polymers between 550 nm and 700 nm, **P(DTG-TPD)** has the highest IPCE approaching 67%, followed by **P(DTS-TPD)** at 62% and **P(DTC-TPD)** at 58%. The photocurrent values calculated from the IPCE spectral integrations for the solar devices with **P(DTC-TPD)**, **P(DTS-TPD)**, and **P(DTG-TPD)** are 11.74, 12.40, and 12.74 mA/cm^2, respectively, which are consistent with the short-circuit current measurements from the current density-voltage curves.

The power conversion efficiency (PCE) of the device with **P(DTC-TPD)** is 5.7%, significantly lower than those of **P(DTS-TPD)** and **P(DTG-TPD)** at 7.0% and 7.7%, respectively. The main difference lies in the lower fill factor (FF) of the **P(DTC-TPD)** device at 54% vs. 67% and 70% for **P(DTS-TPD)** and **P(DTG-TPD)**. As mentioned in Chapter 2, FF in OPVs is influenced by factors such as electrode choice,[63] geminate and non-geminate recombinations, and charge extraction/collection. To understand the differences in FF between the three polymer solar cells, morphological studies, charge mobility measurements, and photophysical investigations were performed to elucidate the differences in charge carrier generation, separation, and collection in these OPV devices.

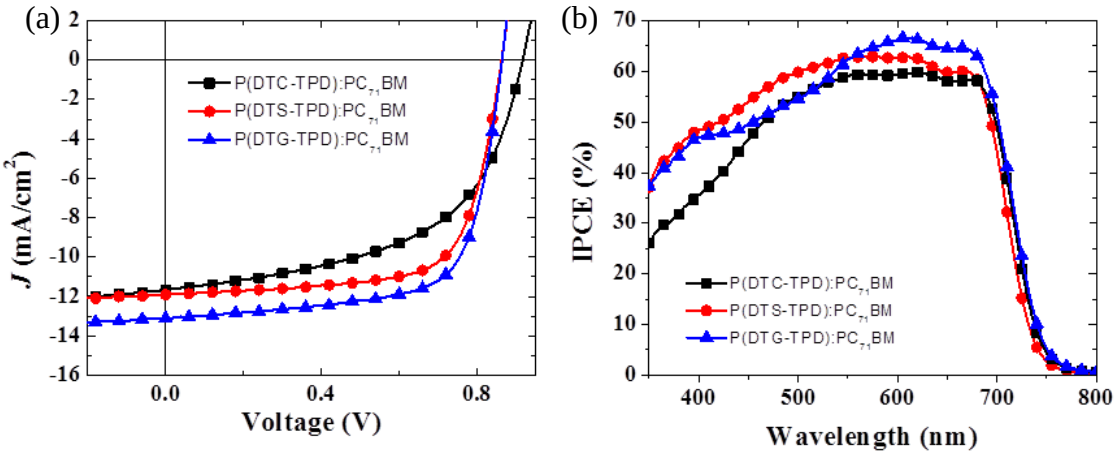

Figure 3-7. (a) Current density-voltage characteristics of OPV devices (ITO/PEDOT:PSS/Polymer:$PC_{71}BM$/LiF/Al device architecture). (b) IPCE spectra of OPV devices.

Table 3-5. Average and best (in parentheses) device characteristics

	J_{sc} (mA/cm^2)	V_{oc} (V)	FF (%)	PCE (%)
P(DTC-TPD):PC$_{71}$BM	11.3±0.4 (11.5)	0.92±0.01 (0.93)	54±1 (56)	5.7±0.2 (5.9)
P(DTS-TPD):PC$_{71}$BM	11.7±0.4 (11.9)	0.88±0.03 (0.91)	67±1 (70)	7.0±0.3 (7.4)
P(DTG-TPD):PC$_{71}$BM	12.8±0.4 (13.3)	0.87±0.00 (0.87)	70±0 (71)	7.7±0.3 (7.9)

3.1.7. Similarity in Blend Morphologies and Photoluminescence Quenching Efficiencies

Active layer blend morphologies, shown in Figure 3-8, were obtained by tapping mode atomic force microscopy and showed that all polymer:PCBM blends exhibited high degrees of mixing. Steady-state photoluminescence (PL) spectra of neat and blended films were measured to probe the exciton harvesting efficiency. Comparison of the PL spectra between the blend films and the neat films indicates strong quenching of polymer photoluminescence upon the addition of fullerene. The PL quenching efficiencies of 96.7%, 99.9%, and 98.0% were observed for **P(DTC-TPD):PC$_{71}$BM**, **P(DTS-TPD):PC$_{71}$BM**, and **P(DTG-TPD):PC$_{71}$BM** blends respectively, confirming the efficient charge transfer from polymer to fullerene following photoexcited charge generation.

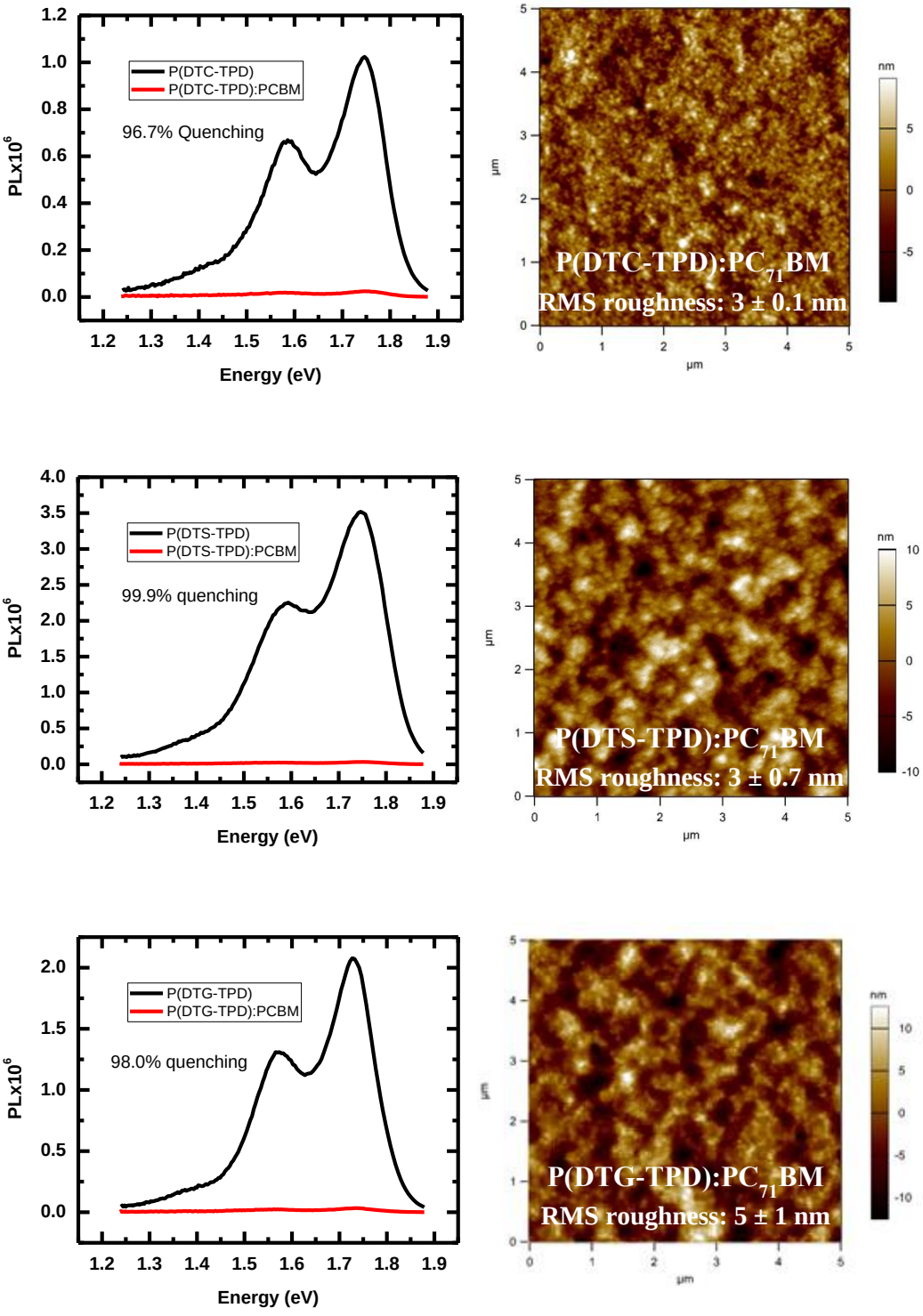

Figure 3-8: PL spectra (left) of neat polymer and polymer:PCBM films. AFM height images (right) of blends.

3.1.8. Photophysics Investigation

3.1.8.1. Photoluminescence Lifetime

Time-resolved photoluminescence measurements were performed using time-correlated single photon counting (TRSPC). The PL lifetime of **P(DTC-TPD)** homopolymer (Figure 3-9) is faster than other two polymers. The characteristics PL lifetimes, extracted by double exponential function are, 97 ps (87%) and 452 ps (13%) for **P(DTC-TPD)**, 197 ps (81%) and 458 ps (19%) for **P(DTS-TPD)**, and 139 ps (87%) and 469 ps (13%) for **P(DTG-TPD)**. Short exciton lifetime of the polymers limits the performance of the solar cell devices. Recently, reduction in intrinsic exciton lifetime with increased polymer crystallinity has been reported in low band gap polymers.[197] This hints at a higher crystallinity of **P(DTC-TPD)** relative to other two polymers. This is supported by both differential scanning calorimetry measurement where melting and crystallinity trannsitions are observed for P(DTC-TPD) in Figure 3-6 and GIWAXS where the diffraction intensities of the pristine polymer and the polymer:PCBM blend were stronger for P(DTC-TPD) in Figure 3-4 and 3-5. Blended films also show the same trend on the PL dynamics. Interestingly, the blended films have time components longer than that of the neat polymers. The slower time components for the blends suggests that there is mixing between the singlet excitons and the charge transfer states in these blends.

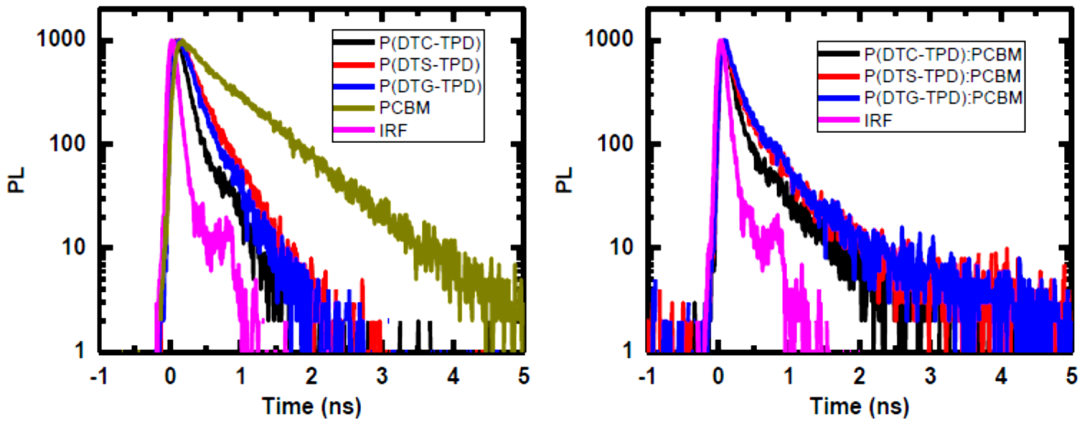

Figure 3-9: PL dynamics for (a) neat polymer films and (b) blended films.. Blend films are **P(DTC-TPD):PC$_{71}$BM**, **P(DTS-TPD):PC$_{71}$BM,** and **P(DTG-TPD):PC$_{71}$BM**.

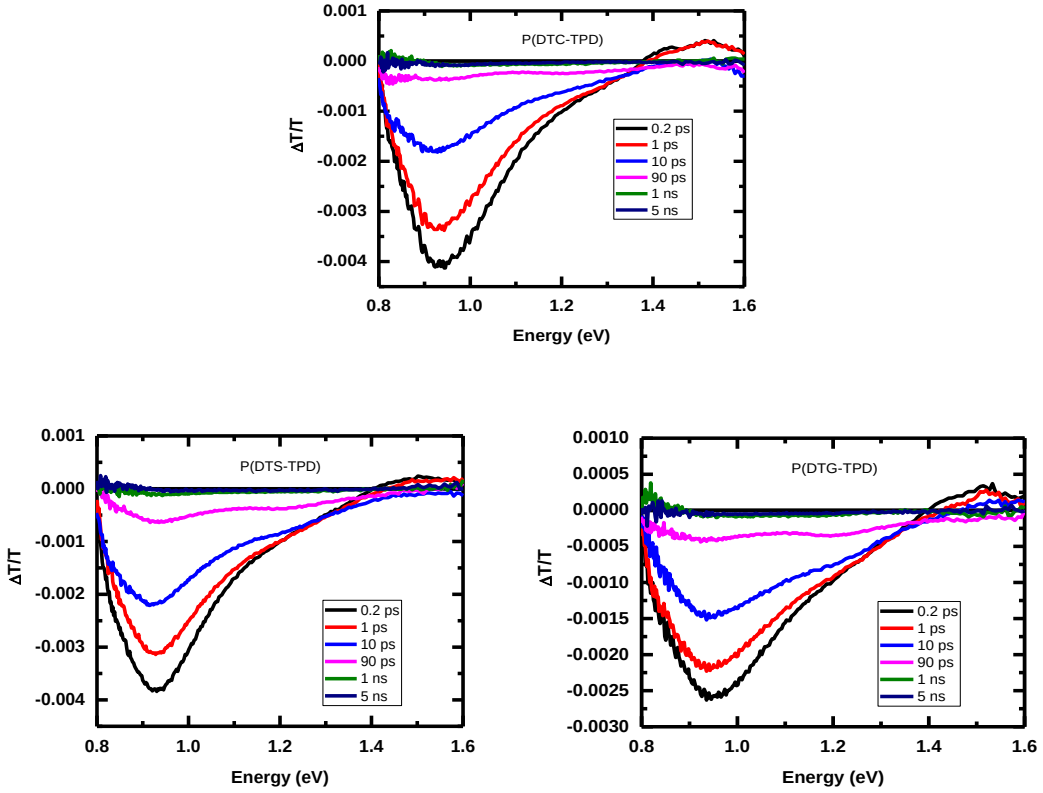

Figure 3-10: Transient absorption spectra of **P(DTC-TPD)**, **P(DTS-TPD)** and **P(DTG-TPD)** films.

3.1.8.2. Transient Absorption Spectroscopy

In order to track the exciton and charge generation dynamics, we performed femtosecond Transient Absorption Spectroscopy (TAS) in the three polymer:fullerene blends. Figure 3-11 (a,c,e) show the transient absorption in the IR region of the spectra at several delays after the samples are excited using pump pulses tuned to 1.91 eV (650 nm), which predominantly create excitons in the donor polymer. The spectra exhibit two absorption features at ~0.95 eV and ~1.2 eV for all blends. These two peaks correspond to the excited state absorption of polymer singlet exciton and polaron features, respectively. Their spectral assignments are consistent with published results of TAS in polymer blends.[198,199,200] Transient absorption spectra of neat polymer films are presented in Figure 3-12, which supports these assignments.

Figure 3-12 shows the time evolution of the features at ~0.95 eV and ~1.2 eV for the three blends. In order to compare the time evolution of excitons and polarons in different blends, we isolated individual contributions of these species by deconvolution of spectra using Gaussian fitting.[199] Interestingly, the photoinduced electron transfer time from donor to acceptor is 0.7 ps in all blends as given by the exciton dynamics at 0.95 eV (Figure 3-12). This time is an order of magnitude faster than neat polymers (Figure 3-13) indicating high efficiency of photoinduced transfer in all blends. This conclusion is further supported by the photoluminescence quenching data shown in Figure 3-8. In addition, we observed an increase in the transient signal of 0.95 eV peak on later delays. The rise time constants for **P(DTC-TPD)**:$PC_{71}BM$, **P(DTS-TPD):$PC_{71}BM$**, and **P(DTG-TPD):$PC_{71}BM$** blends are 300 ps, 225 ps, and 186 ps respectively. We also monitored the dynamics of the polaron peak ~1.2 eV. The decay of polaron peak is correlated with the rise of 0.95 eV peak (Figure 3-11). The decay time constants for polaron peak are 240

ps and 2.4 ns for **P(DTC-TPD):PC_{71}BM**, 212 ps and 1.96 ns for **P(DTS-TPD):PC_{71}BM**, and 146 ps and 1.25 ns for **P(DTG-TPD):PC_{71}BM**.

In order to understand the origin of the new exciton appearance after charge separation, we performed fluence intensity dependent TAS. A strong intensity dependent dynamic of the exciton signals at ~0.95 eV was observed (Figure 3-14). We attribute this to the triplet exciton generation through bimolecular recombination of the electrons and holes (polarons).[201,202,203] Triplet populations increased with higher excitation fluence intensity and the rate of triplet formation was correlated with the recombination rate of charges on all blends. Figure 3-11b, 3-11d, and 3-11f show the fluence intensity dependent TAS at 5 ns time delay for the polymer:fullerene blends of **P(DTC-TPD)**, **P(DTS-TPD)**, and **P(DTG-TPD)**, respectively. For the **P(DTC-TPD)**:PC_{71}BM blend, we observed a higher triplet population (peak intensity) than the population of the separation charges at all excitation fluences, which was in contrast to other two blends.

The formation of polymer triplet excitons from the free charges involves the formation of the singlet and triplet charge transfer excitons (CTEs). The decay of the recombined triplet CTEs to the ground state is spin-forbidden whereas the relaxation to the polymer triplet is favorable.[203] Our observation indicated that this relaxation process was more efficient for **P(DTC-TPD):PC_{71}BM**. This difference is likely due to the energy alignments at the interface, namely, the offset between the CTE/charge separated state (CS) and triplet exciton level of the blends.

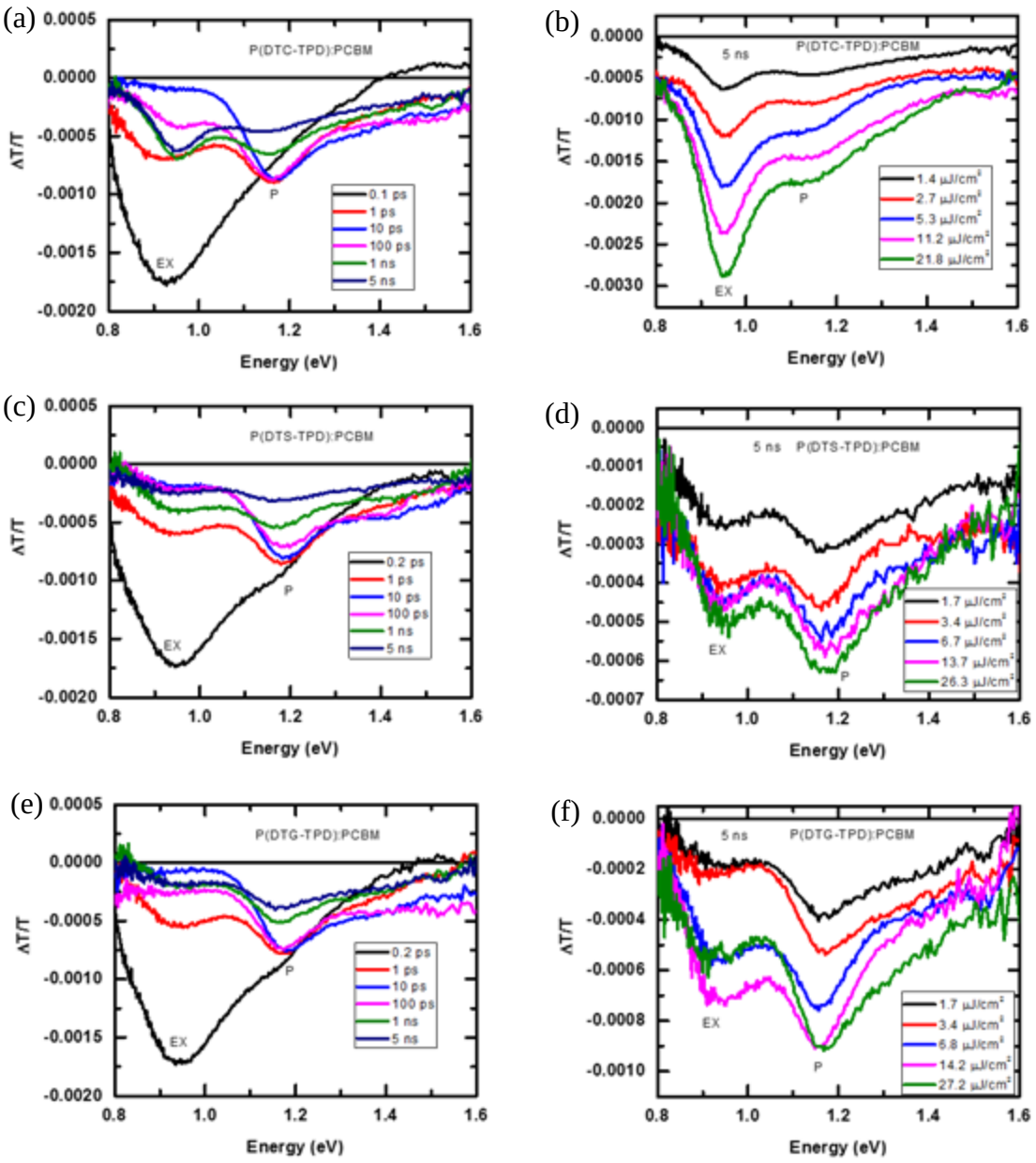

Figure 3-11: Transient absorption spectra for (a) **P(DTC-TPD):PC$_{71}$BM**, (c) **P(DTS-TPD):PC$_{71}$BM** and (e) **P(DTC-TPD):PC$_{71}$BM**. EX and P refer to polymer exciton and polymer polaron, respectively. The intensity dependent spectra at 5 ns delay are shown in (b), (d), and (f). **P(DTC-TPD):PC$_{71}$BM** showed a higher triplet exciton population than polaron population, indicative of a more efficient bimolecular recombination pathway from the charge separated state to the triplet state.

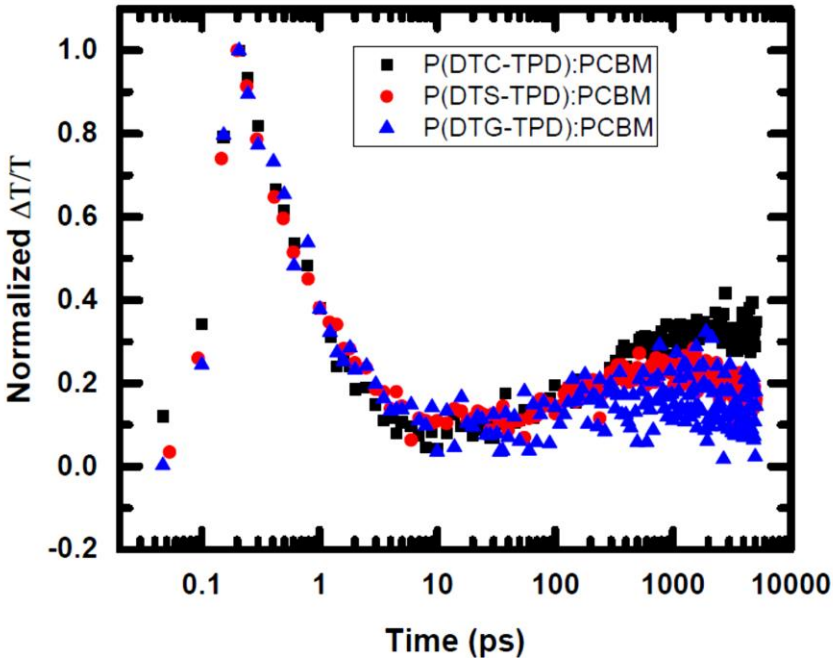

Figure 3-12: Singlet exciton PIA dynamics of the 0.95 eV peaks for **P(DTC-TPD):$PC_{71}BM$**, **P(DTS-TPD):$PC_{71}BM$** and **P(DTG-TPD):$PC_{71}BM$** films.

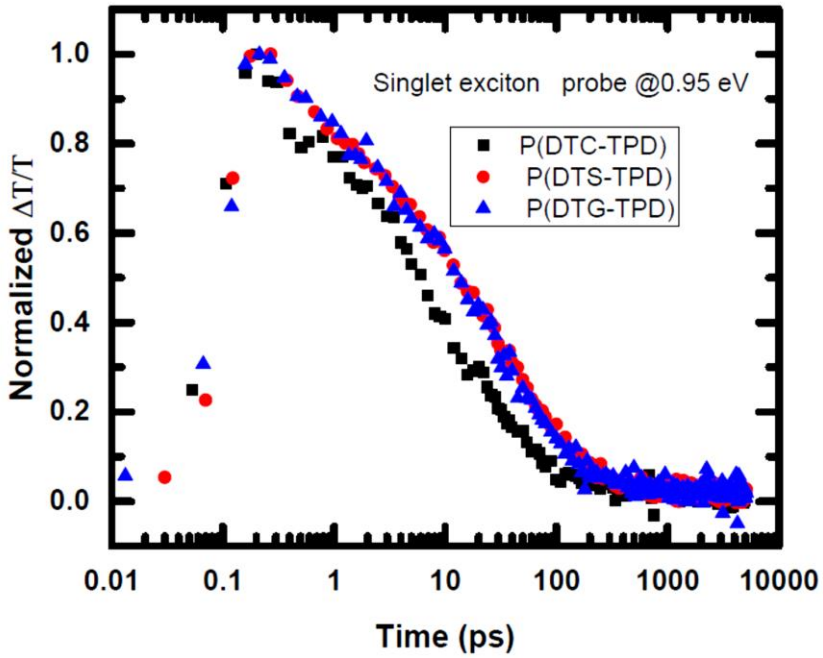

Figure 3-13: Singlet exciton PIA dynamics of the 0.95 eV peaks for **P(DTC-TPD)**, **P(DTS-TPD)** and **P(DTG-TPD)**.

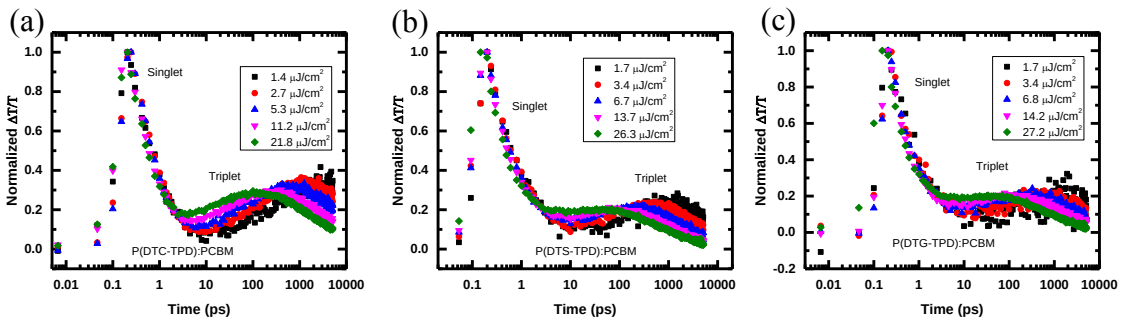

Figure 3-14: Intensity dependent triplet exciton PIA dynamics of the 0.95 eV peaks for (a) **P(DTC-TPD):PC$_{71}$BM**, (b) **P(DTS-TPD):PC$_{71}$BM**, and (c) **P(DTG-TPD):PC$_{71}$BM** films.

3.1.9. Energetic Offsets on Charge Recombination Efficiency: CT Energies vs. Triplet Energy

To validate our CS/CT and triplet energy alignment hypothesis, we directed investigation to the CT energy and triplet energy. We measured the sub-energy gap EQE signal to measure the CT state energetics of the polymer:fullerene blends. The spectra for the blends **P(DTC-TPD):PC$_{71}$BM**, **P(DTS-TPD):PC$_{71}$BM**, and **P(DTG-TPD):PC$_{71}$BM** are shown in Figure 3-15. The plots clearly show that the sub-energy gap responses for all blends are nearly identical, with CT energy estimated at ~1.4 eV after fitting the spectra to the nonadiabatic electron transfer theory.[204]

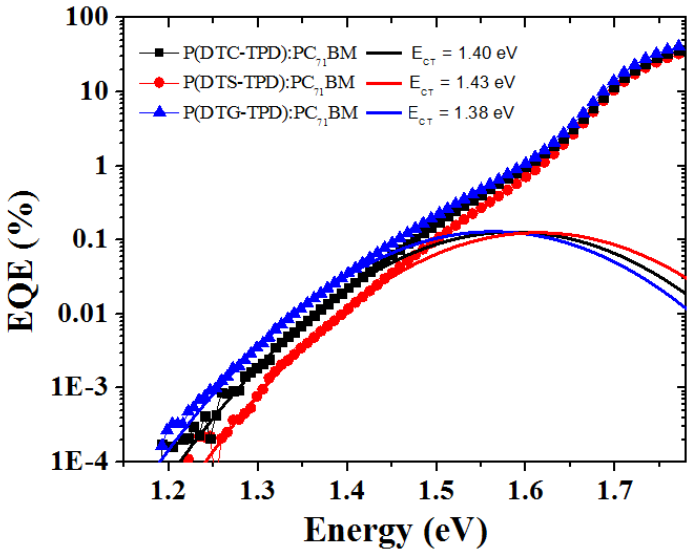

Figure 3-15. Sub-energy gap external quantum efficiency plots of polymer:fullerene blends. The fittings of the shoulder-like features were used to determine the charge transfer energies.

Next, we focused our efforts on investigating the triplet energy. Using DFT calculation performed at b3lyp/6-31G(d) level, we find that the lowest energy triplet exciton (T_1) of P(DTC:TPD) is at 1.08 eV, lying lower than those of P(DTS:TPD) and P(DTG:TPD) (1.21 eV). As illustrated in Figure 3-16, a more stable T_1 explains the higher recombination efficiency and rate of triplet formation in P(DTC:TPD) observed in the transient absorption spectra, confirming our hypothesis of the energy level alignment between the CS/CT and T_1 as the reason for a higher triplet exciton population.

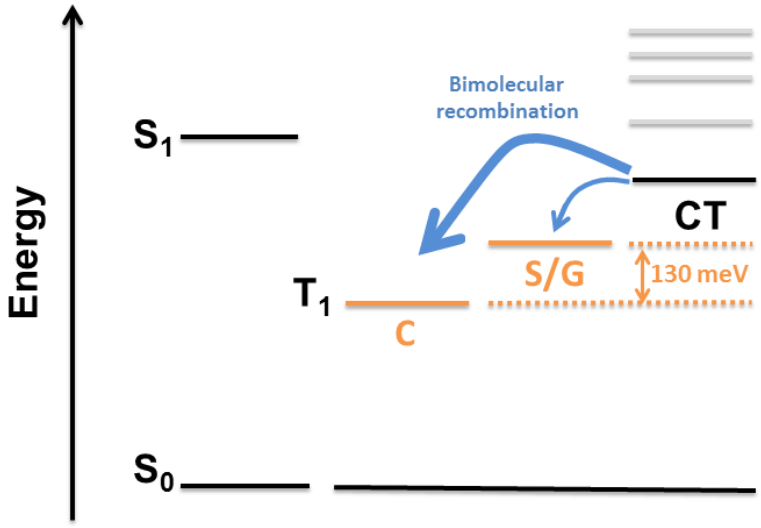

Figure 3-16. Electronic state diagram illustrating the bimolecular recombination and the formation of triplet. **P(DTC-TPD)** has a more stable T_1 (lowest energy triplet exciton), leading to a higher recombination efficiency.

3.1.10. Summary of One-atom Change Donor-Acceptor Polymers

Three "one-atom" change polymers were successfully synthesized by switching the bridging atom between carbon, silicon, and germanium on a bithiophene conjugated moiety to study the effect of the center atom on OPV performance. A careful parallel polymer synthesis *via* Stille polymerization and thorough polymer purification and characterization allowed the confirmation of physical similarity and chemical purity in this family of polymers. The shorter C-C bonds at the bridging atom allowed for a shorter interchain lamellar distance in **P(DTC-TPD)** (~15 Å vs. ~19 and ~20 Å for **P(DTS-TPD)** and **P(DTG-TPD)**, respectively). We observed different aggregation behaviors in the polymer solutions in the ^{1}H NMR study, which in turn led to variations in **P(DTC-TPD)**'s aggregation and polymer backbone orientation. UV-vis absorption spectra indicated **P(DTC-TPD)** having a more pronounced H-aggregate characteristic and GIWAXS showed edge-on backbone orientation against the silicon substrate. OPV

devices with the P(DTC-TPD):PCBM blend shows a lower PCE as a result of a lower FF. Transient absorption spectra of the polymer:PCBM blends at 5 ns time delay indicated higher triplet population resulting from bimolecular recombination in the **P(DTC-TPD):PCBM**, which contributed to the lower FF in the OPV device. DFT calculation found that **P(DTC-TPD)** has its triplet energy 130 meV more stable than the other two polymers, resulting in its higher charge recombination efficiency, and thus triplet formation.

3.2. Thiophene-based Donor-Acceptor Polymers

In this next investigation, we studied a family of donor-acceptor copolymers with different acceptor moieties and thiophene-based donors shown in Figure 3-17. The accepting monomers used in this work are isoindigo (iI), thienoisoindigo (TiI), and diketopyrrolopyrrole (DPP). The donor moieties in this study are 2,5-bis(3-alkylthiophen-2-yl)thieno[3,2-b]thiophene (BTTT) and 3,3"-dialkyl- 2,2':5',2"-terthiophene or terthiophene (T3).

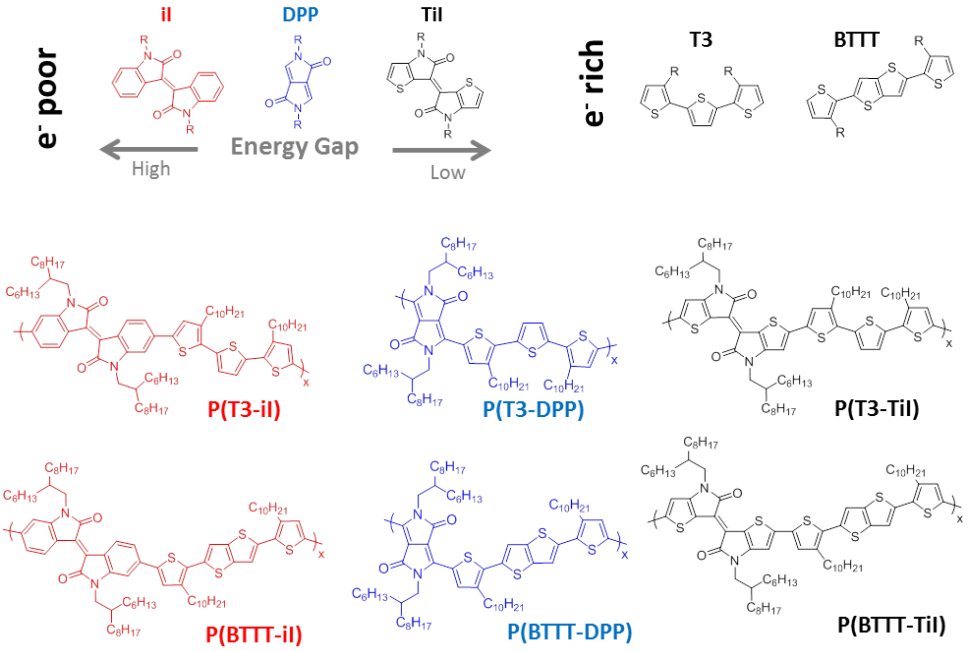

Figure 3-17. Structures of electron donors and the electron acceptors as building blocks for thiophene-based donor-acceptor polymers: **P(T3-iI)**, **P(BTTT-iI)**, **P(T3-DPP)**, **P(BTTT-DPP)**, **P(T3-TiI)**, and **P(BTTT-TiI)**.

On the acceptor side, isoindigo was first suggested for organic electronics applications in a patent by CIBA.[205] It was first used in organic electronics applications by Mei *et al.*[206] Isoindigo is a natural pigment and a structural isomer of the famous indigo pigment. The advantage of using pigments in the active layer of a solar cell is their

high extinction coefficients (i.e. a molecule containing isoindigo, iI-bithiophene-iI, has a molar absorptivity of 47,300 M^{-1} cm^{-1} at 579 nm in THF),[207] which enhance light absorption. An isoindigo molecule contains two electron-deficient lactam functional groups, and the π-conjugated backbone makes it an attractive accepting moiety for organic electronics. The Andersson Group has synthesized an isoindigo D-A polymer containing a terthiophene spacer and achieves 6.3% power conversion efficiency (PCE).[208] With the ease of a two-step synthetic route and processability from *N*-alkylation, iI is a promising material in organic electronics.[206]

In 2012, thienoisoindigo, a derivative of isoindigo, was first reported in the open literature for organic electronics by Ashraf *et al.*[209] and Van Pruissen *et al.*[210] in two separate publications. The chemical structure of thienoisoindigo replaces the phenyl rings in isoindigo with thiophene rings, which can lead to the planarization of the polymer backbone due to the favorable intramolecular sulfur-oxygen interactions.[211] The more electron-rich thiophene rings should also destabilize the frontier energy levels. Compared to the other two acceptors in this project, thienoisoindigo is relatively new to the organic electronic community, providing opportunities for novel studies.

Another widely studied pigment molecule is diketopyrrolopyrrole. Like iI and TiI, DPP also has lactam functional groups and a π-conjugated backbone, which fits the requirements of an acceptor in the D-A design. It can also be *N*-alkylated, allowing solution processability. The highly planar conjugated lactam structure provides strong π-π interactions in the resulting polymers, which leads to improved charge transport.[212] Yang has fabricated 6.5% single junction OPV cells with DPP as the acceptor.[213]

3.2.1. Polymer Synthesis of P(T3-iI), P(BTTT-iI), P(T3-DPP), P(BTTT-DPP), P(T3-TiI), and P(BTTT-TiI)

Syntheses of the isoindigo[206], thienoisodigo[209], terthiophene and bithiophene-thienothiophene[214] follow existing literature. The modified synthesis of diketopyrrolopyrrole is shown in Scheme 3-4. First, 4-decylthiophene-2-carbonitrile (Compound 3-8) was synthesized from 3-decylthiophene *via* 4-decylthiophene-2-carbaldehyde (Compound 3-6) and the subsequent condensation reaction with hydroxylamine to form 4-decylthiophene-2-carboxaldoxime (Compound 3-7). The rest of the DPP synthesis follows the traditional route.

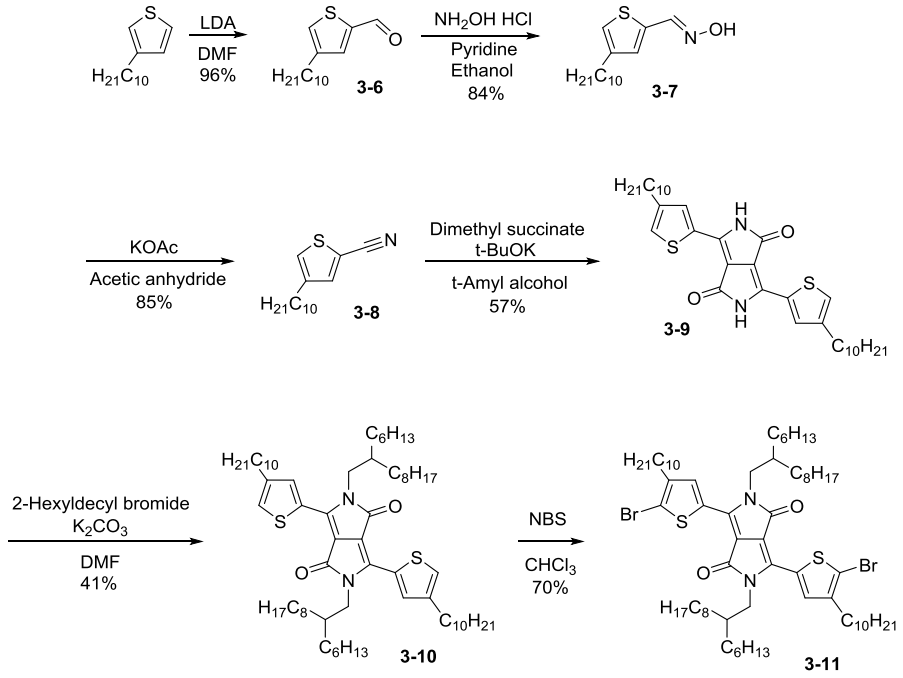

Scheme 3-4. Synthesis of 2,5-dihydro-1,4-dioxo-3,6-di(2-bromo-3-alkyl)thienylpyrrolo [3,4-c]-pyrrole

Scheme 3-5 outlines the Stille polymerizations process used to synthesize all polymers at 95 ˚C for 72 hours using $Pd_2(dba)_3$ and P(*o*-tol)$_3$ as the catalyst and ligand, respectively. Diethyldithiocarbamic acid diethylammonium salt, a palladium scavenger,

was used to remove palladium from the crude polymers. The concentrated crude polymer solutions were precipitated into methanol, filtered, and subsequently fractionated *via* soxhlet extraction. Either the dichloromethane or chloroform fractions were concentrated and precipitated into methanol. The polymer precipitates were collected on PTFE membrane filters and dried under vacuum overnight to remove residual solvents.

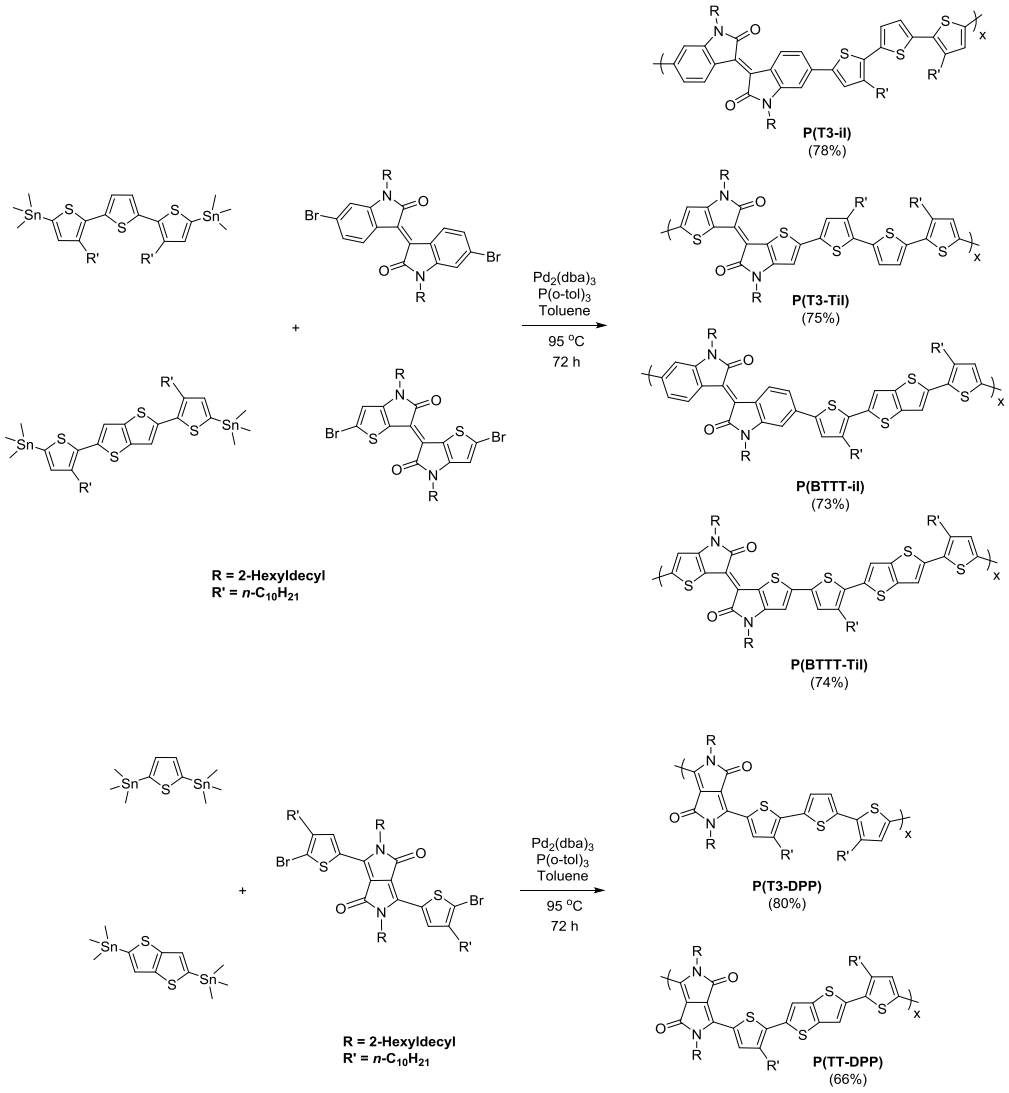

Scheme 3-5. Synthetic routes for **P(T3-iI)**, **P(BTTT-iI)**, **P(T3-TiI)**, **P(BTTT-TiI)**, **P(T3-DPP)**, **P(BTTT-DPP)**.

3.2.2. Optoelectronic Properties of P(T3-iI), P(BTTT-iI), P(T3-DPP), P(BTTT-DPP), P(T3-TiI), and P(BTTT-TiI)

Due to the difference in electron-withdrawing strengths, these different acceptors along the polymer backbones should result in different ionization potentials in the copolymers, allowing for systematic adjustment in the effective energy gap in the OPV devices. The UV-Vis absorption spectra confirmed this hypothesis, with iI-based polymers possessing the highest energy gaps. As shown in Figure 3-18, the optical bandgaps of the DPP polymers are red-shifted compared to isoindigo ones. TiI-based polymers are further red-shifted with onsets of absorption as low as 1 eV. These bathochromic shifts in absorption onsets are results of the more electronic-rich thiophene moieties in DPP and TiI.

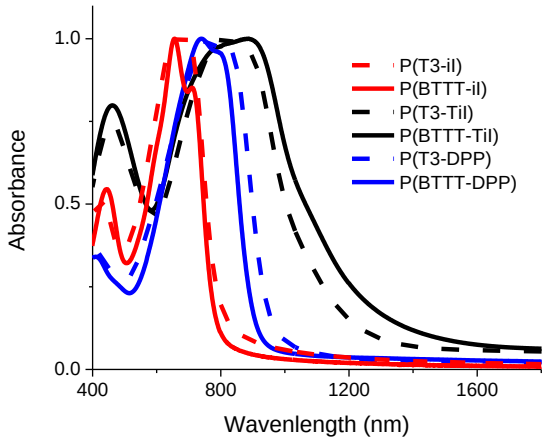

Figure 3-18. Normalized absorption spectra of the polymer thin-films of **P(T3-iI)**, **P(BTTT-iI)**, **P(T3-DPP)**, **P(BTTT-DPP)**, **P(T3-TiI)**, and **P(BTTT-TiI)**.

3.2.3. Donor-Acceptor Polymer/PCBM blend OPV Device

3.2.3.1. Power Conversion Efficiency under AM 1.5

BHJ OPV devices were fabricated with the polymers as donors and $PC_{71}BM$ as the acceptor in the active layers in 1:1.5 ratios and the current density-voltage

characteristics are presented in Figure 3-19. Conventional architectures with PEDOT:PSS on top of patterned ITO substrates and reflective calcium/aluminum back electrodes were used. DIO is chosen as additives (2.5% v/v) since it allows the active layer to achieve optimal phase separated morphology for charge transfer, transport, and extraction, resulting in higher short-circuit currents.[215] This is primarily a result of DIO selectively solubilizing fullerene, preventing it from forming large crystals and aggregates, and thus allowing it to intermix and interpenetrate into the polymer matrix.[216,217] A summary of device performance is presented in Table 3-6. As expected, open-circuit voltage follows the trend in the electron-withdrawing strength of the acceptor moieties with iI devices having the highest V_{oc}, followed by DPP and TiI. The low V_{oc} in the TiI devices are a result of low ionization potentials which significantly reduce the effective energy gaps in the devices, hindering device performances in the TiI polymers. High V_{oc} in the two iI polymers led to their best performances **P(T3-iI)** and **P(BTTT-iI)** had PCE of 4.9% and 3.1%, respectively. The main difference in device characteristic is in their J_{sc}, with **P(T3-iI)** having a J_{sc} of 12.75 mA/cm^2 and **P(BTTT-iI)** at 8.55 mA/cm^2. Similarly, in the DPP polymers, **P(BTTT-DPP)** has a higher J_{sc} value (10.38 vs. 5.62 mA/cm^2) which led to a higher PCE than **P(T3-DPP)**.

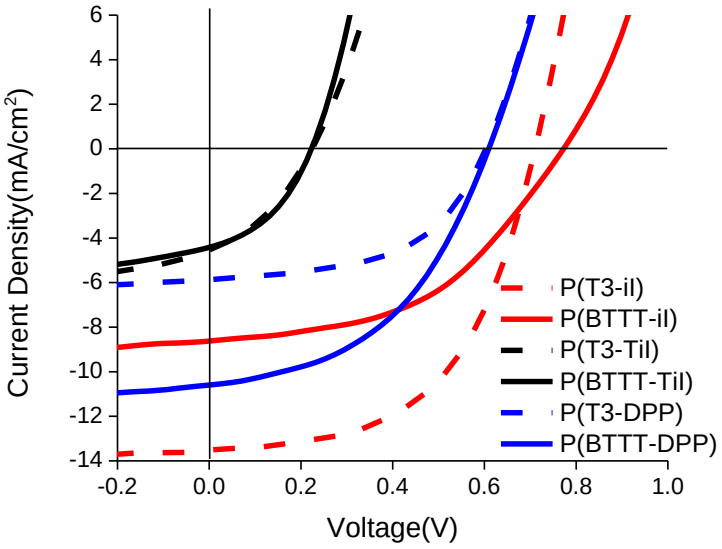

Figure 3-19. Current density-voltage characteristics of OPV devices for polymer:$PC_{71}BM$ blends under AM1.5 solar simulated illumination.

Table 3-6. Summary of physical, optical, electrochemical, and OPV device properties of thiophene-based polymers

	$M_n/Đ_M$[a] (kDa)	T_d[b] (˚C)	IP[c] (eV)	Optical E_g (eV)	J_{sc} (mA/cm^2)	V_{oc} (V)	FF (%)	Efficiency (%)
P(T3-iI)	66.3 (2.2)	403	-5.66	1.53	12.75	0.71	54.8	4.9
P(BTTT-iI)	16.2 (2.5)	393	-5.61	1.57	8.55	0.77	47.1	3.1
P(T3-DPP)	11.4 (3.2)	404	-5.36	1.30	5.62	0.62	53.1	1.9
P(BTTT-DPP)	12.0 (3.4)	411	-5.33	1.37	10.38	0.61	46.4	3.0
P(T3-TiI)	11.2 (1.9)	395	-5.18	1.07	4.32	0.23	35.4	0.4
P(BTTT-TiI)	15.7 (1.9)	388	-5.21	1.00	4.36	0.24	40.2	0.4

[a] Molecular weights and dispersities were determined by gel permeation chromatography with polystyrene as the calibration standard and hot 1,3,4-trichlorobenzene as the eluent. [b] Decomposition temperature (T_d) was determined by thermogravimetric analysis at 5% weight loss with a heating rate of 10 ˚C/min under nitrogen. [c] IP values were calculated from DPV measurements by assuming SCE to be 4.74 eV vs. vacuum and Fc/Fc^+ to be +0.38 eV with respect to SCE.

3.2.3.2. Morphological Characterizations

The differences in J_{sc} indicate that there are different morphologies and intermolecular interactions within the active layers, affecting the charge separation, transport, and extraction. To gain insight into the topography of the active layers, AFM was used to examine the morphology of the polymer:$PC_{71}BM$ thin films. Comparing the AFM height images of the iI polymers in Fig. 3-20c and 3-20d show that, **P(T3-iI):$PC_{71}BM$** has a higher degree of mixed interpenetrating network in the active layer blend. We also observed similar features in the DPP polymers with **P(BTTT-DPP)** (Figure 3-20b) having more intermixed domains. These interpenetrated networks allow the diffusion of excitons to the donor-acceptor interface for efficient charge transfer and separation, thus leading to higher J_{sc} and device performance in these devices.[218]

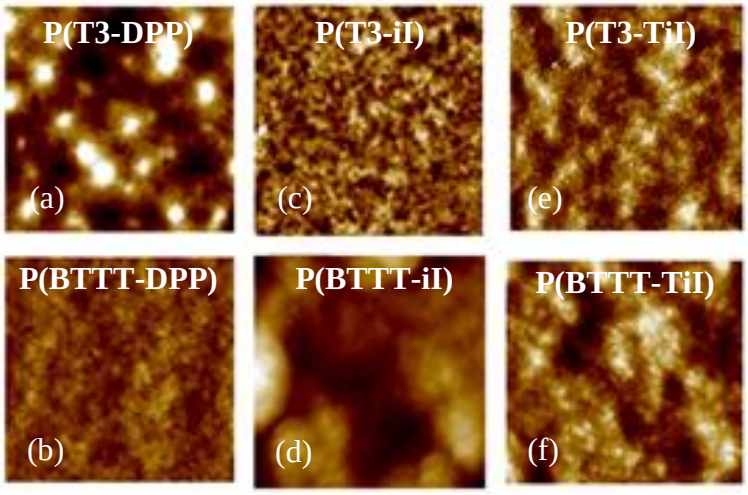

Figure 3-20. AFM height images of the polymer:$PC_{71}BM$ films. All blend ratios are 1:1.5 with 2.5% v/v DIO as addtive. Image size: 2 μm × 2 μm. Height scale ranges from 0 nm (light) to 20 nm (dark).

3.2.4. OPV Devices with Diketopyrrolopyrrole Polymers

3.2.4.1. Device Optimization

We also selected the DPP polymers to carry out a more in-depth study due to the additional side chain on the flanking thiophene units. We successfully synthesized DPP units with *n*-decyl side chains attached to the 4-position of the adjacent thiophenes in order to investigate the side chain effects on intermolecular interaction.[219]

Device optimization for the DPP polymers focused on three parameters: ratio of polymer:PCBM, choice of processing solvent, and DIO loading. Table 3-7 summarizes the device processing condition and performance. For both DPP polymers, the best performing devices were achieved by processing the polymer:PCBM blends at 1:1.5 ratio with 2.5 w% DIO in o-dichlorobenzene. High PCBM ratio (1:4 polymer:PCBM) led to a reduction in J_{SC}. To be discussed further in Chapter 5, PCBM has low extinction coefficient, its poor light absorption ability reduces the amount of generated photocurrent. Higher quantity of PCBM may also lead to aggregation and reduce the interfacial area for charge separation.

Table 3-7. OPV device performances from processing optimization

Polymer	Polymer: $PC_{71}BM$ ratio	Processing Solvent	Concentration (mg/mL)	DIO (V/V)	J_{sc} (mA/cm^2)	V_{oc} (V)	FF (%)	PCE (%)
P(DPP-T)	1:1.5	*o*-DCB	20	2.5%	5.50 ± 0.24	0.62 ± 0.01	54.4 ± 2.3	1.84 ± 0.07
P(DPP-T)	1:4	*o*-DCB	20	2.5%	3.76 ± 0.16	0.62 ± 0.00	63.6 ± 1.0	1.47 ± 0.07
P(DPP-TT)	1:1.5	*o*-DCB	20	2.5%	10.45 ± 0.39	0.61 ± 0.01	46.5 ± 1.9	3.00 ± 0.21
P(DPP-TT)	1:4	*o*-DCB	20	2.5%	6.68 ± 0.22	0.64 ± 0.01	61.6 ± 1.1	2.63 ± 0.07
P(DPP-T)	1:1.5	*o*-DCB	20	0%	2.80 ± 0.13	0.60 ± 0.01	61.7 ± 1.6	1.04 ± 0.07
P(DPP-T)	1:1.5	CHCl3	8	2.5%	2.42 ± 0.12	0.59 ± 0.02	39.2 ± 0.9	0.56 ± 0.05
P(DPP-T)	1:1.5	CHCl3	8	5%	2.19 ± 0.33	0.59 ± 0.01	37.0 ± 6.0	0.49 ± 0.14
P(DPP-TT)	1:1.5	*o*-DCB	20	0%	4.77 ± 0.17	0.62 ± 0.01	54.1 ± 0.7	1.60 ± 0.06
P(DPP-TT)	1:1.5	CHCl3	8	2.5%	3.71 ± NA	0.60 ± NA	35.5 ± NA	0.79 ± NA
P(DPP-TT)	1:1.5	CHCl3	8	5%	1.61 ± 0.19	0.61 ± 0.01	26.8 ± 1.3	0.26 ± 0.04

3.2.4.2. GIWAXS

GIWAXS experiments were performed on both pristine polymer and polymer:PCBM blend films using optimized device processing conditions to gain insight into the active layer nanostructures. As shown in Fig. 3-21a and 3-21b, pristine films of both polymers showed reflection peaks at Q_{xy} = ~ 0.29 $Å^{-1}$ along the in-plane (horizontal xy) directions (Figure 3-22), corresponding to interchain d-spacings of 2.2 nm. Another reflection peaks at Q_z = ~ 1.57 $Å^{-1}$ along the out-of-plane (vertical z) directions corresponded to π-π stacking distances of 4.0 Å. Since both polymers have their interchain lamellar stackings in the xy-directions and their π-π stackings in z-directions, they are oriented face-on against the substrates. The specular diffraction patterns and their analyses are presented in Figure 3-20. Comparing **P(T3-DPP)** to its corresponding non-alkylated version with π-π stacking distance of 3.7 Å and lamellar stacking distances of 1.74 nm,[220] the polymer in this study with the additions of n-decyl side chains on the adjacent thiophene units experienced increased intermolecular distances, leading to higher π-π and lamellar stacking distances. As illustrated in Figure 3-23, the added side chains extend from the polymer backbones, increasing the intermolecular packing distances. In the polymer:PCBM blends, the diffractions from the π-π stacking and interchain lamellar stacking disappear and are replaced by amorphous halos from the PCBM aggregates as seen in Fig. 3-21c and 3-21d, indicating that the active layer blends are more amorphous than the pristine polymers.

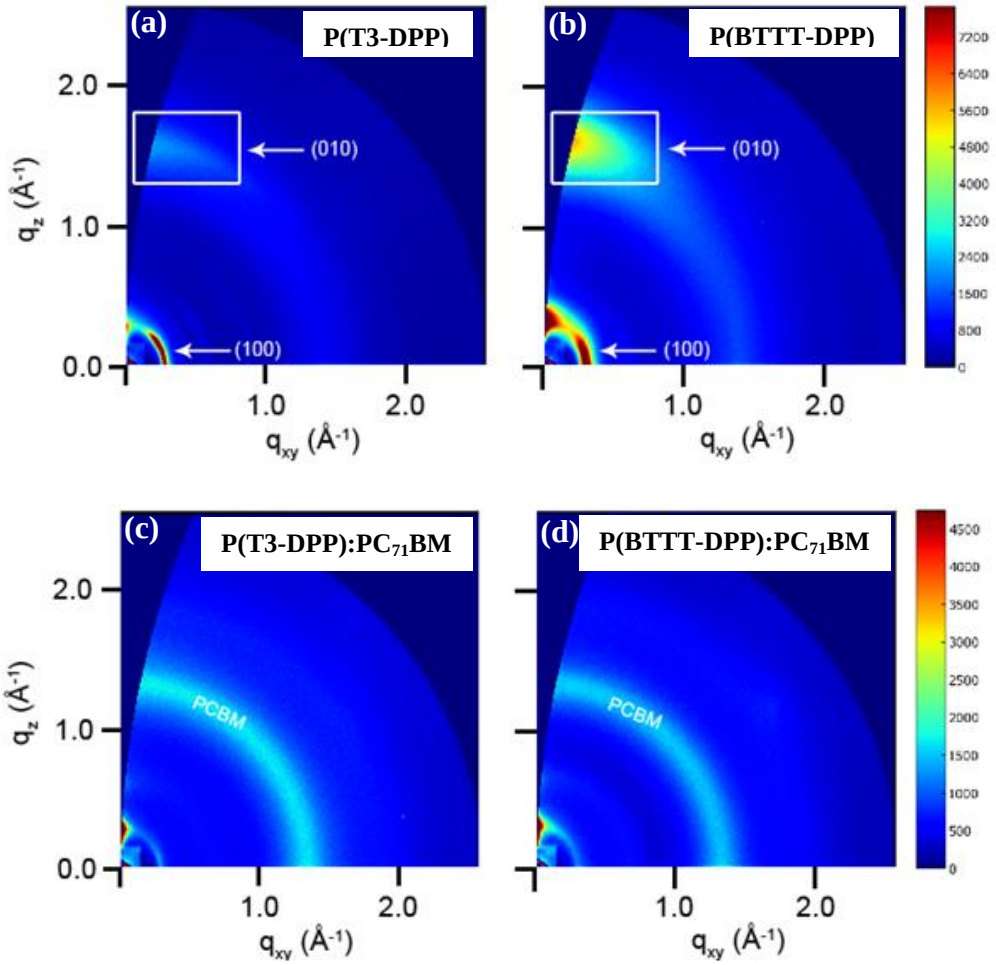

Figure 3-21. Two-dimensional (2D) grazing incidence wide-angle X-ray scattering (GIWAXS) images of (a) pristine **P(T3-DPP)**, (b) pristine **P(BTTT-DPP)**, (c) **P(T3-DPP):$PC_{71}BM$** blend, and (d) **P(BTTT-DPP):$PC_{71}BM$** blend (1:1.5 polymer:$PC_{71}BM$ with 2.5% v/v DIO). Samples were spin-coated onto silicon substrates with the same conditions as device fabrication.

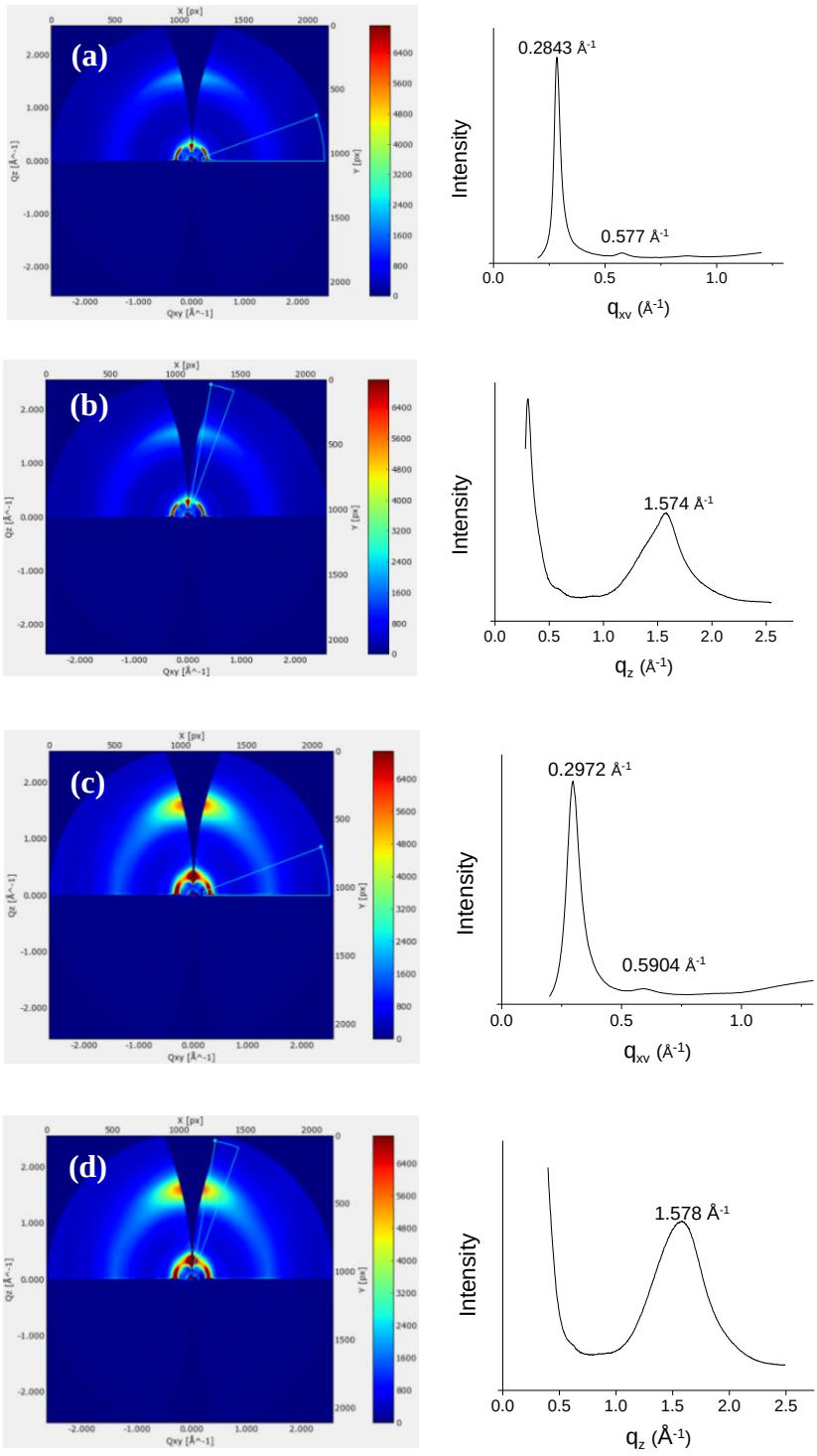

Figure 3-22. Two-dimensional (2D) grazing incidence wide-angle X-ray scattering (GIWAXS) images of (a) and (b) **P(T3-DPP):PC$_{71}$BM** and (c) and (d) **P(BTTT-DPP):PC$_{71}$BM** and their corresponding specular X-ray diffraction patterns showing the q_{xy} and q_z scans. The blue boxes in the scattering images indicate where the specular diffraction patterns are measured.

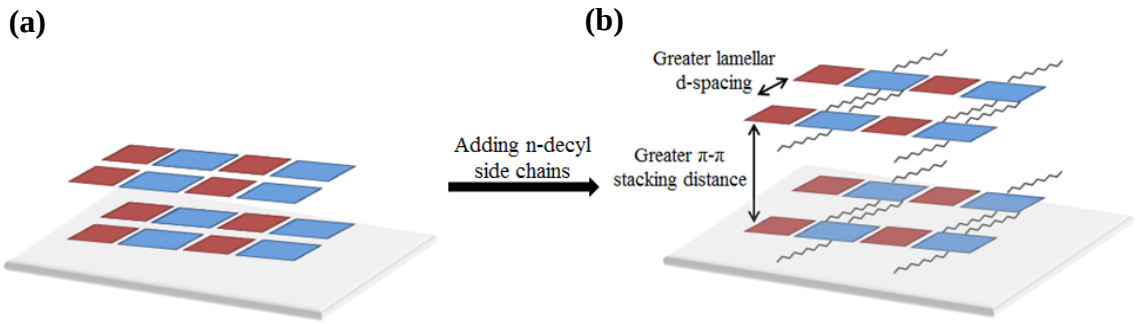

Figure 3-23. A schematic illustrating the proposed polymer packing models comparing (a) the non-alkylated polymers and (b) the polymers with the addition of n-decyl side chains on the flanking thiophenes.

3.2.5 Summary of Thiophene-based Donor-Acceptor Polymers

A family of donor-acceptor polymers based on acceptor moieties including isoindigo, diketopyrrolopyrrole, and thienoisoindigo, was synthesized to study how the differences in their electron deficiency affect OPV device performance. We discovered that the acceptor strength was effective in systematically controlling the ionization potentials of the polymers, which led to differences in open-circuit voltage, and thus device performance. Overall, the isoindigo polymers had the highest ionization potentials, highest open-circuit voltages, and power conversion efficiencies. On the other hand, the low ionization potentials of thienoisoindigo polymers limited the open-circuit voltage, leading to low power conversion efficiency. We also confirmed that the short-circuit current was affected by the degree of intermixing between the donor polymer and the acceptor fullerene. Blends with higher degrees of intermixing led to higher short-circuit currents.

We have also successfully synthesized DPP units with *n*-decyl side chains attached to the 4-position of the adjacent thiophenes. The two resulting DPP polymers in this study have enhanced solubilities in common organic solvents (up to 40 mg/mL). The

two polymers show similar physical, structural, and optoelectronic, allowing us to carry out a morphological and structural study and their impacts on OPV device performance as a result of the added side chains. **P(T3-DPP)** showed a higher device performance as a result of the higher short-circuit current density. This improved performance corresponded to higher charge transport and extraction efficiencies resulting from optimal domain sizes and a higher degree of interpenetrated networks of the donor and acceptor moieties within the active layer. The additional *n*-decyl side chains increase the intermolecular packing distances in both polymers and can be used strategically to control intermolecular stacking distances to further optimize the degree of mixing in the BHJ polymer and fullerene blend and enhance the charge transport and extraction in the OPV devices.

3.3. Synthetic Details

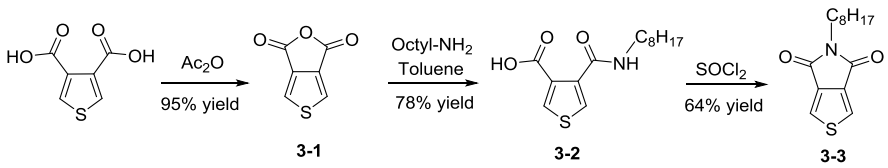

5-Octylthieno[3,4-c]pyrrole-4,6-dione (3-3).[187,221] To a 300 mL round bottom flask thiophene-3,4-dicarboxylic acid (6.0 g, 35 mmol) and acetic anhydride (150 mL) were added and stirred at 140 ˚C overnight. Solvent was removed under reduced pressure to afford Compound 3-1 as brown crystals (5.2 g, 34 mmol, 97%) which were used in the next step without purification. To a 500 mL round bottom flask, 5.2 g of Compound 3-1 and *n*-octylamine (7.0 g, 54 mmol, 1.5 equiv) and 300 ml of toluene were added. A condenser was attached to the flask, and the mixture was refluxed for 24 hours. After

cooling to room temperature, the solvent was removed under reduced pressure. The air-sensitive brown oil (Compound 3-2) was dissolved in thionyl chloride (200 mL) and the mixture was refluxed for 4 hours. The reaction was quenched with MeOH (200 mL). Water (200 mL) was added to the crude mixture, which was extracted with DCM, washed with water (2 × 150 mL), brine (100 mL), and dried over $MgSO_4$. After solvent was removed under reduced pressure, the crude solid was purified by column chromatography using 1:1 hexanes:DCM. The brown solid was further purified by recrystallization in hexanes to afford Compound 3-3 as white needles (3.4 g, 13 mmol, 37%). ^{1}H NMR (300 Hz, $CDCl_3$, ppm): δ: 7.80 (s, 2H), 3.60 (t, *J* = 7.2 Hz, 2H), 1.64 (m, 2H), 1.25 (m, 10H), 0.87 (t, *J* = 6.8 Hz, 3H).

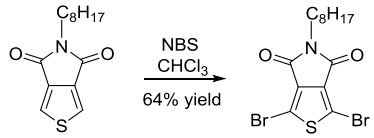

3-3 3-4

1,3-Dibromo-5-octylthieno[3,4-c]pyrrole-4,6-dione (3-4).[187,221] To a 100 mL round bottom flask, Compound 3-3 (2.7 g, 10 mmol) was dissolved in a mixture of sulfuric acid (15 mL) and trifluoroacetic acid (50 ml) at room temperature. *N*-bromosuccinimide (5.4 g, 30 mmol) was added in three portions over 15 minutes and the reaction mixture was stirred at room temperature for 12 hours. The reaction was monitored by TLC. After the reaction finished, the mixture was poured into water (100 mL), extracted with DCM (2 × 30 mL). The organic portions were combined, washed with water (2 × 100 mL), brine (100 mL), and dried over $MgSO_4$. After solvent was removed under reduced pressure, the crude product was purified by column chromatography using 1:1 hexanes:DCM to afford

the white crystals (3.3 g, 79%). ^{1}H NMR (300 Hz, $CDCl_3$, ppm): δ: 3.59 (t, *J* = 7.2 Hz, 2H), 1.63 (m, 2H), 1.26 (m, 10H), 0.87 (t, *J* = 6.7 Hz, 3H).

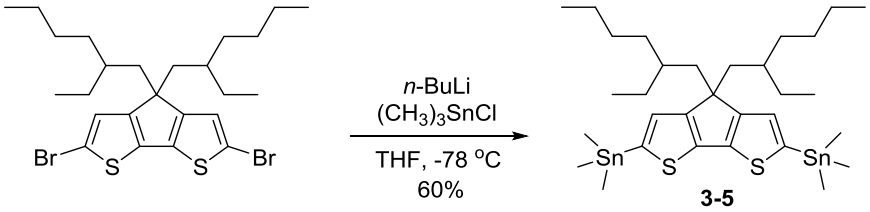

3-5

1,1'-[4,4-Dis(2-ethylhexyl)-4*H*-cyclopenta[2,1-*b*:3,4-*b*']dithiophene-2,6-diyl]bis[1,1,1-trimethylstannane (3-5).[222] To a 100 mL round bottom flask, 2,6-dibromo-4,4-bis(2-ethylhexyl)-4*H*-Cyclopenta[2,1-*b*:3,4-*b*']dithiophene and THF (30 mL) were added. The mixture was cooled to -78 ˚C. A portion of *n*-BuLi (7.2 mL of 2.5 M in hexanes, 18 mmol) was added dropwise over 30 minutes. The mixture was allowed to warm to room temperature and stirred for 1 hour, then cooled back to -78 °C. A portion of trimethyltin chloride (21 mL of 1.0 M in anhydrous THF, 21 mmol) was added to the reaction mixture dropwise over 30 minutes and was stirred overnight at room temperature. After the reaction was finished, the mixture was quenched with water (30 mL), extracted with hexanes (3 × 100 mL), and washed with sodium bicarbonate solution (100 mL). The combined organic layer was washed with water (2 × 100 mL), brine (50 mL) and dried over $MgSO_4$. After solvent was removed under reduced pressure, the crude yellow oil was purification by reversed phase HPLC (60:40 ACN:acetone) to afford a clear oil. (1.3 g, 1.8 mmol, 60%). ^{1}H NMR (300 Hz, $CDCl_3$, ppm): δ 6.99 (s, 2H), 1.83 (m, 4H), 1.32 (m, 2H), 0.91 (m, 16H), 0.78 (t, *J* = 6.9 Hz, 6H), 0.64 (t, *J* = 7.2 Hz, 6H), 0.37 (m, 18H).

DTS and DTG ditin monomers were synthesized by Dr. Junxiang Zhang and Mr. Rylan Michael Webster Wolfe respectively according to published procedures. [176,189] The crude yellow oils were purification by reversed phase HPLC (60:40 ACN:acetone).

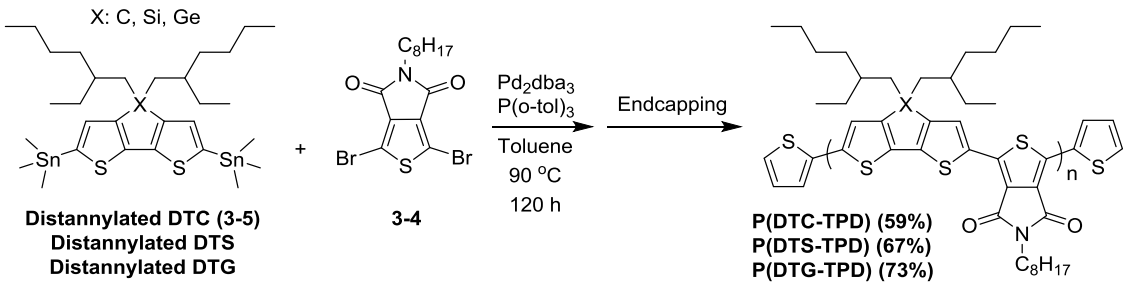

General Procedures of Stille Cross-Coupling Polymerizations[176] for P(DTC-TPD), P(DTS-TPD), and P(DTG-TPD):

To a 25 mL Schlenk tube, 1,3-dibromo-5-octylthieno[3,4-c pyrrole-4,6-dione (408 mg, 1 mmol) and ditin-dithiophene monomers (1 mmol) were added and charged with argon for 3 pump-fill cycles. $Pd_2(dba)_3$ (697 mg, 1.5 mol% catalyst loading or 3 mol% Pd), and P(*o*-tol)$_3$ (405 mg, 4.5 mol%) were added to a vial in an argon-filled glovebox and sealed with a septum to prevent ambient exposure after removal from the glovebox. Toluene (5 mL) was added to the vial to dissolve the catalyst and ligand; a quick sonication was helpful to ensure full dissolution. To the Schlenk tube, toluene (5 mL) was added, followed by the catalyst and ligand *via* a syringe and needle. The reaction mixture was heated to 90 ˚C and stirred for 72 hours. After the polymerization, of 2-(tributylstannyl)thiophene (0.1 mL, 0.3 mmol) was added and stirred for 14 hours at 90 ˚C, followed by the addition of 2-bromothiophene (0.1 mL, 1 mmol). The mixture was stirred for an additional 10 hours. After cooling to 60 ˚C, a spatula-tip amount of diethyldithiocarbamic acid diethylammonium salt (CAS# 2391-78-8) was added and

stirred for 10 hours to scavenge the palladium catalyst. A portion of toluene (10 mL) was added and the mixture was precipitated into methanol and filtered onto a PTFE membrane. The crude polymer underwent soxhlet extractions with methanol, acetone, hexanes, dichloromethane, and chloroform. The chloroform fraction was concentrated to a volume in which the entire sample was still soluble in room temperature chloroform (approximately 150 mL). The mixture was passed through a 4" plug of 1:1:1 (by volume) mixture of silica, basic alumina, and celite. Additional chloroform was used as the eluent, until all polymer had passed through the plug. The polymer was concentrated to a dry solid. The polymer was dissolved in a minimal amount of chloroform, and filtered through a 0.45 μm nylon filter directly into a large excess of acetone. The precipitated polymer was allowed to stir for 30 min before being collected on a 0.45 μm nylon filter. The polymer was dried under vacuum for 24 hours and obtained as a dark blue solid.

P(DTC-TPD). 375 mg (59%). GPC (1,3,4-trichlorobenzene at 140 ˚C vs polystyrene standards, RI): M_n = 26.4 kg/mol, $Đ_M$ = 1.4. Anal. Calcd for $C_{39}H_{53}NO_2S_3$ (%): C, 70.54; H, 8.04; N, 2.11; S, 14.49. Found (%): C, 70.54; H, 8.14; N, 2.16; S, 14.57.

P(DTS-TPD). 423 mg (67%). GPC (1,3,4-trichlorobenzene at 140 ˚C vs polystyrene standards, RI): M_n = 24.5 kg/mol, $Đ_M$ = 1.7. Anal. Calcd for $C_{38}H_{53}NO_2S_3Si$ (%): C, 67.11; H, 7.85; N, 2.06; S, 14.1. Found (%): C, 67.25; H, 7.85; N, 2.10; S, 14.47.

P(DTG-TPD). 483 mg (73%). GPC (1,3,4-trichlorobenzene at 140 ˚C vs polystyrene standards, RI): M_n = 20.8 kg/mol, $Đ_M$ = 1.7. Anal. Calcd for $C_{38}H_{53}NO_2S_3Ge$ (%): C, 62.98; H, 7.37; N, 1.93; S, 13.27. Found (%): C, 63.06; H, 7.20; N, 2.03; S, 13.42.

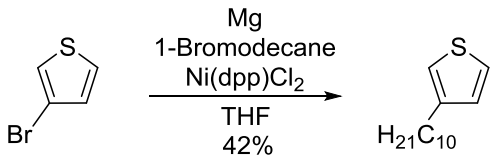

3-Decylthiophene.[223] To a 500 mL 3-neck round bottom flask fitted with a 200 mL additional funnel and a condenser, a solution of ground magnesium turnings (4.9 g, 200 mmol) in dry ethyl ether (10 mL) was added. A portion of 1-bromodecane (40.9 g, 185 mmol) in anhydrous THF (50 mL) was added dropwise *via* an additional funnel. Once the addition was over, the reaction mixture was refluxed for two hours. To a separate 1000 mL 3-neck round bottom flask, 3-bromo-thiophene (25.3 g, 155 mmol), $Ni(dpp)Cl_2$ (0.8 g, 1.535 mmol) and anhydrous THF (100 mL) were added. The Grignard reagent containing Mg and 1-bromodecane was transferred into an additional funnel attached to the second round bottom flask, and was added dropwise over 1 hour. (A heat gun was required to dissolve the Grignard reagent and aided the transfer). After addition, the golden brown solution was refluxed at 90 ºC overnight. After cooling to room temperature, water (200 mL) was added to quench the reaction. The crude mixture was extracted with DCM (200 mL), washed with water (2 × 200 mL), brine (200 mL), and dried over $MgSO_4$. After filtration, solvent was removed under reduced pressure to afford a brown oil. Purification *via* Kugelrohr distillation (0.5-1.0 mmHg) resulted in two main fractions at 100 ˚C. The fraction remained in the original loading bulb was collected as a colorless oil (14.5 g, 62 mmol, 42%). ^{1}H NMR (300 Hz, $CDCl_3$, ppm): δ 7.23 (dd, J = 4.8, 3.0 Hz, 1H), 6.96 – 6.90 (m, 2H), 2.66 (t, J = 7.5 Hz, 2H), 1.66 (m, 2H), 1.32 (m, 14H), 0.93 (t, J = 7.4 Hz, 3H).

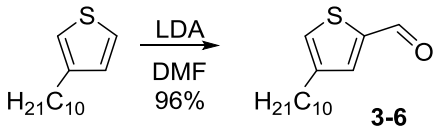

3-6

4-Decylthiophene-2-carbaldehyde (3-6). To a solution of 50 mL tetrahydrofuran (THF) 3-decylthiophene (2.76 g, 12.5 mmol) was added. The mixture was cooled to -78 ˚C and stirred for 10 minutes. Lithium diisopropylamide (LDA) in THF (2.0 M, 6.25 mL, 12.5 mmol) was added dropwise over 20 minutes. Dimethylformamide (DMF) (1.4 mL, 18.7 mmol) was added in one portion and the mixture was stirred for 1 hour. The reaction was warmed to room temperature. Water (50 mL) was added and the mixture was extracted with ether (3 × 30 mL). The combined organic extracts were dried over anhydrous $MgSO_4$, filtered, and concentrated. The colorless oil was used without further purification (2.85 g, 96%).

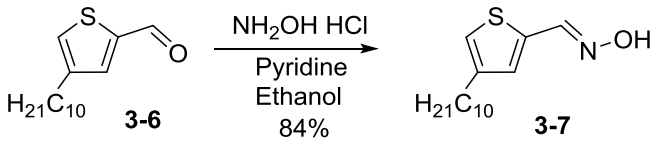

3-6 **3-7**

4-Decylthiophene-2-carboxaldoxime (3-7). To a 100 mL glass pressure vessel with (1.21 g, 17.4 mmol) hydroxylammonium chloride, pyridine (10 mL), and ethanol (10 mL), 4-decylthiophene-2-carbaldehyde (2.70 g, 10.7 mmol) was added in one portion. The vessel was sealed and purged with argon. The mixture was heated to 100 ˚C and stirred for 16 hours. The mixture was cooled to room temperature and concentrated. Water (50 mL) was added and the mixture was extracted with chloroform (3 × 20 mL). The combined organic extracts were dried over anhydrous $MgSO_4$ and concentrated. The colorless oil was used without further purification (2.4 g, 83.9%).

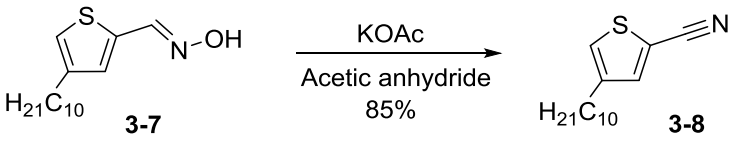

4-Decylthiophene-2-carbonitrile (3-8). To a 50 mL round bottom flask with potassium acetate (0.1 g, 1 mmol) and acetic anhydride (15 mL), 4-decylthiophene-2-carboxaldoxime (2.4 g, 9.0 mmol) was added in one portion. The vessel was sealed and purged with argon. The mixture was heated to 140 ˚C and stirred for 4 hours and subsequently cooled to room temperature. Sodium hydroxide solution (5%) was added until the reaction mixture was neutralized. Water (100 mL) was added and the mixture was extracted with ether (3 × 50 mL). The combined organic extracts were dried over anhydrous $MgSO_4$ and concentrated. The crude was purified by silica gel column chromatography with an eluent of 4:1 hexanes:DCM. The product was obtained as a yellow oil (1.9 g, 7.7 mmol, 85%). ^{1}H NMR (300 MHz, $CDCl_3$, ppm): δ 7.43 (d, J = 1.5 Hz, 1H), 7.18 (d, J = 1.5 Hz, 1H), 2.60 (t, J = 7.4 Hz, 2H), 1.68 – 1.49 (m, 2H), 1.39 – 1.12 (m, 15H), 0.87 (t, J = 6.7 Hz, 3H). ^{13}C NMR (75 MHz, $CDCl_3$, ppm): δ 144.09, 138.23, 127.48, 114.48, 109.32, 31.89, 30.29, 29.91, 29.58, 29.54, 29.35, 29.32, 29.10, 22.68, 14.12. Note: ^{1}H NMR indicated that 3-decylthiophene-2-carbonitrile was formed at a byproduct (~8%). This mixture of products was used in the next step, in which the desirable product was obtained. Some peaks in the ^{13}C NMR spectrum are overlapping and cannot be resolved. Anal. Calcd for $C_{15}H_{23}NS$ (%): C, 72.23; H, 9.30; N, 5.62; S, 12.85. Found (%): C, 71.94; H, 9.54; N, 5.66; S, 12.65. HRMS (EI) calc'd for $C_{15}H_{23}NS$ (M^+), 249.1551; found, 249.1545.

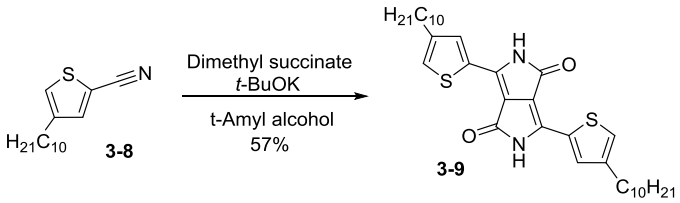

3,6-Bis(4-decylthiophen-2-yl)-pyrrolo[3,4-c]pyrrole-1,4-dione (3-9). To a 25 mL round bottom flask with (0.38 g, 4.0 mmol) of sodium *tert*-butoxide and 2-methylbutan-2-ol (7 ml), 4-decylthiophene-2-carbonitrile (1.0 g, 4.0 mmol) was added in one portion. The mixture was stirred and heated to 120 ˚C. Diisopropyl succinate (0.29 g, 1.4 mmol) was dissolved in 2-methylbutan-2-ol (3 mL), and the mixture was added to the reaction dropwise over 2 hours. The mixture was kept at 120 ˚C and stirred for an additional 16 hours. The mixture was cooled to room temperature and added to water (50 mL). The red solid was filtered and first washed with water then cold methanol and dried under vacuum. The dark red solid was used without further purification (1.34 g, 57%). Note: The compound was not sufficiently soluble in common solvents to obtain NMR spectra. Anal. Calcd for $C_{34}H_{48}N_2O_2S_2$ (%): C, 70.30; H, 8.33; N, 4.82; S, 11.04. Found (%): C, 68.34; H, 8.14; N, 4.53; S, 10.16. Note: The inaccuracies in the EA data may be a result of the simple washing purification method. Due to the compound's insolubility in organic solvents, silica column chromatography purification was not possible. HRMS (MALDI-TOF) calc'd for $C_{34}H_{48}N_2O_2S_2$ (M^+), 580.3157; found, 580.3143.

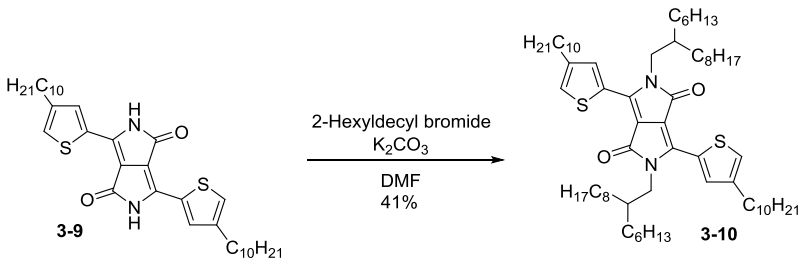

3,6-Bis(4-decyl-thiophen-2-yl)-*N,N'*-bis(2-hexyldecyl)-pyrrolo[3,4-c]pyrrole-1,4-dione (3-10). To a 25 mL round bottom flask with potassium carbonate (0.72 g, 5.2 mmol) and DMF (10 mL), Compound 3-9 (1 g, 1.7 mmol) was added in one portion. The mixture was heated to 120 ˚C. To the mixture, 2-hexyldecyl bromide (1.31 g, 4.3 mmol) was added dropwise over 30 minutes. The reaction mixture was stirred for 16 hours and subsequently cooled to room temperature. Ether (25 mL) was added and the organic phase was washed with water (5 × 30 mL) and brine (1 × 30 mL) and dried over anhydrous $MgSO_4$. The mixture was filtered, concentrated, and purified by silica gel column chromatography with an eluent of 9:1 hexanes:DCM. The product was obtained as a red waxy solid (0.72 g, 41%). ^{1}H NMR (300 MHz, $CDCl_3$, ppm): δ 8.69 (s, 2H), 7.21 (s, 2H), 3.99 (d, J = 7.7 Hz, 4H), 2.69 (t, J = 7.9 Hz, 4H), 1.91 (s, 2H), 1.68 (m, 4H), 1.45-1.10 (m, 80H), 0.92 – 0.78 (m, 18H). ^{13}C NMR (75 MHz, $CDCl_3$, ppm): δ 161.74, 144.75, 140.27, 136.21, 129.52, 125.72, 107.69, 46.09, 37.63, 31.91, 31.88, 31.76, 31.12, 30.47, 30.31, 30.03, 29.68, 29.63, 29.51, 29.44, 29.38, 29.34, 29.31, 26.14, 22.69, 22.67, 22.63, 14.12, 14.09. Note: some peaks in the ^{13}C NMR spectrum are overlapping and cannot be resolved. Anal. Calcd for $C_{66}H_{113}N_2O_2S_2$ (%): C, 76.98; H, 10.96; N, 2.72; S, 6.23. Found (%): C, 77.02; H, 11.14; N, 2.54; S, 6.31. HRMS (MALDI-TOF) calc'd for $C_{66}H_{113}N_2O_2S_2$ (MH^+), 1029.8216; found, 1029.8244.

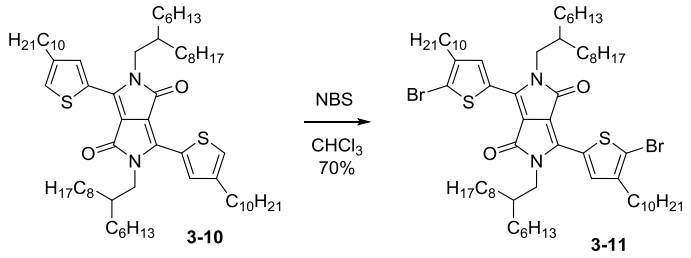

3,6-Bis(5-bromo-4-decyl-thiophen-2-yl)-*N,N'*-bis(2-hexyldecyl)-pyrrolo[3,4-c]pyrrole-1,4-dione (3-11). To a 50 mL round bottom flask with Compound 3-10 (0.86 g, 0.84 mmol), chloroform (20 mL) was added in one portion. The mixture was cooled to 0 ˚C and kept in the dark. *N*-Bromosuccinimide (0.33 g, 1.9 mmol) was added in three portions over 15 minutes. The mixture was allowed to slowly return to room temperature and stirred for 16 hours in the dark. Water (50 mL) was added and the mixture was extracted with dichloromethane (3 × 20 mL). The combined organic extracts were dried over anhydrous $MgSO_4$, filtered, and concentrated. The crude was purified by silica gel column chromatography with an eluent of hexanes. The product was obtained as a red waxy solid (0.69 g, 70%). ^{1}H NMR (300 MHz, $CDCl_3$, ppm): δ 8.54 (s, 2H), 3.90 (d, J = 7.7 Hz, 4H), 2.63 (t, J = 7.7 Hz, 4H), 1.89 (m, 2H), 1.71 – 1.59 (m, 4H), 1.42 – 1.13 (m, 80H), 0.85 (m, 18H). ^{13}C NMR (75 MHz, $CDCl_3$, ppm): δ 161.42, 143.90, 139.31, 135.49, 129.25, 116.17, 107.82, 46.18, 37.66, 31.91, 31.75, 31.10, 30.00, 29.70, 29.62, 29.51, 29.39, 29.34, 29.31, 26.11, 22.69, 22.68, 22.63, 14.12, 14.09. Note: some peaks in the ^{13}C NMR spectrum are overlapping and cannot be resolved. Anal. Calcd for $C_{66}H_{111}N_2O_2S_2Br_2$ (%): C, 66.75; H, 9.34; N, 2.36; S, 5.40. Found (%): C, 66.85; H, 9.08; N, 2.56; S, 5.60. HRMS (MALDI-TOF) calc'd for $C_{66}H_{111}N_2O_2S_2Br_2$ (MH^+), 1185.6503; found, 1185.6454.

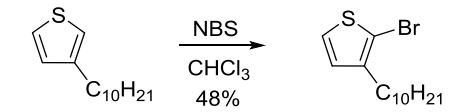

2-Bromo-3-decylthiophene.[224] *N*-bromosuccinimide (NBS) (6.4 g, 35.6 mmol) was added in three portions over 20 minutes to a solution of 3-decylthiophene (8 g, 35.6 mmol) in acetic acid (15 mL) and $CHCl_3$ (15 mL) at 0 °C in the dark. The mixture was stirred for 15 minutes, allowed to warm to room temperature, and stirred overnight. The mixture was added to water (100 mL). The crude mixture was extracted with hexanes (100 mL) and washed with water (2 × 100 mL), brine (100 mL), and dried over $MgSO_4$. After filtration, solvent was removed under reduced pressure. The crude material passed through a silica plug using hexanes as the eluent to give a yellow oil (5.2 g, 17.1 mmol, 48%). ^{1}H NMR (300 Hz, $CDCl_3$, ppm): 7.19 (d, J = 5.9 Hz, 1H), 6.81 (d, J = 5.7 Hz, 1H), 2.59 (t, J = 7.5 Hz, 2H), 1.61 (m, 2H), 1.31 (m, 14H), 0.93 (t, J = 6.6 Hz, 3H).

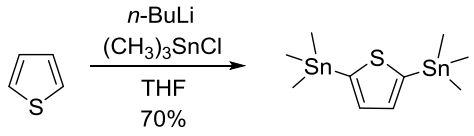

2,5-Bis(trimethylstannyl)-thiophene.[224] To a 1000 mL round bottom flask, *n*-BuLi (22 mL of 2.5 M in hexanes, 55 mmol) was added dropwise over 1 hour to 2,5-dibromothiophene (2.5 mL, 22 mmol) in anhydrous THF (440 mL) at -78 °C. The mixture was stirred for 1 hour. A portion of trimethyltin chloride (10.95 g, 55 mmol) dissolved in anhydrous THF (10 mL) was added to the reaction mixture dropwise over 30 minutes and was stirred overnight at room temperature. After the reaction was finished, the mixture was poured into water (600 mL), extracted with diethyl ether (3 × 150 mL), and washed with water (2 × 150 mL), brine (100 mL) and dried over $MgSO_4$. After

solvent was removed under reduced pressure, the crude white powder was recrystallized in hot diethyl ether twice to afford the white crystals (6.4 g, 15.6 mmol, 70%). ^{1}H NMR (300 Hz, $CDCl_3$, ppm): 7.38 (s, 2H), 0.37 (s, 18H).

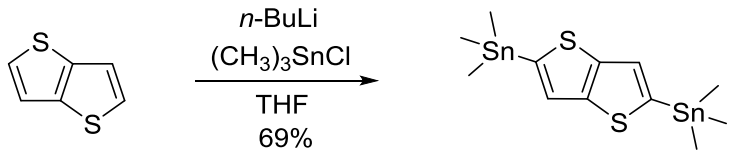

2,5-Bis(trimethylstannyl)-thieno[3,2-b]thiophene.[37] To a 500 mL round bottom flask, *n*-BuLi (3.6 mL of 2.5 M in hexanes, 2.5 mmol) was added dropwise over 1 hour to thieno[3,2-b]thiophene (500 mg, 1 mmol) in anhydrous THF (80 mL) at -78 °C. The mixture was allowed to return to room temperature and stirred for 2 hours, then cooled back to -78 °C. Trimethyltin chloride (8.9 mL of 1.0 M in anhydrous THF, 8.9 mmol) was added to the reaction mixture dropwise over 30 minutes and was stirred overnight at room temperature. After the reaction was finished, the mixture was quenched with MeOH (20 mL), poured into water (400 mL), extracted with diethyl ether (3 × 100 mL), and washed with water (2 × 100 mL), brine (50 mL) and dried over $MgSO_4$. After solvent was removed under reduced pressure, the crude white powder was recrystallized in hot diethyl ether twice to afford the white crystals (1.2 g, 2.5 mmol, 69%). ^{1}H NMR (300 Hz, $CDCl_3$, ppm): 7.26 (s, 2H), 0.39 (s, 18H).

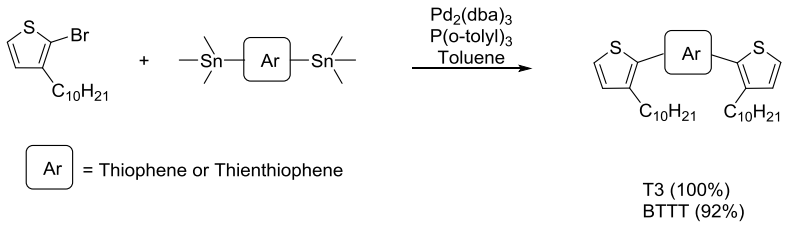

General procedures of decyl-terthiophene derivatives:

To a 35 mL microwave vial, a mixture of 2,5-bis(trimethylstannyl)-thiophene or -thieno[3,2-b]thiophene (2.5 mmol), 2-bromo-3-decylthiophene (1.82 g, 6 mmol), $Pd_2(dba)_3$ (45 mg, 0.05 mmol, 2 mol% of catalyst or 4 mol% of Pd), P(*o*-tolyl)$_3$ (60 mg, 0.2 mmol, 8 mol%), and 20 mL of toluene were added inside a glovebox under argon. The reaction tube was sealed and removed from the glovebox. Microwave reaction was performed in a CEM Corporation Discover SP microwave synthesizer. The reaction mixture was heated to 160 ˚C and stirred for 1 hour. After cooling to room temperature, toluene was removed under reduced pressure. The crude oil was purified by silica column chromatography with hexanes as the eluent. The products were afforded as pale yellow oils.

3,3''-Didecyl- 2,2':5',2''-terthiophene.[224] (1.33 g, 2.5 mmol, 100%). ^{1}H NMR (300 Hz, $CDCl_3$, ppm): δ 7.18 (d, *J* = 5.3 Hz, 2H), 7.07 (s, 2H), 6.95 (d, *J* = 5.1 Hz, 2H), 2.80 (t, *J* = 7.8 Hz, 4H), 1.67 (m, 4H), 1.28 (m, 28H), 0.90 (t, *J* = 6.9 Hz, 6H).

2,5-Bis(3-decyl-2-thienyl)-thieno[3,2-b]thiophene.[225] (1.33 g, 2.27 mmol, 92%). ^{1}H NMR (300 Hz, $CDCl_3$, ppm): δ 7.24 (s, 2H), 7.22 (d, *J* = 5.3 Hz, 2H), 6.97 (d, *J* = 5.2 Hz, 2H), 2.80 (t, *J* = 7.5 Hz, 4H), 1.66 (m, 4H), 1.27 (m, 28H), 0.88 (t, *J* = 6.5 Hz, 6H).

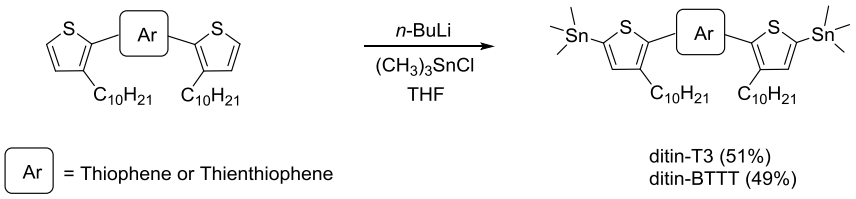

General procedures of ditin-decyl-terthiophene derivatives:

To a 500 mL round bottom flask, *n*-BuLi (2.5 mL of 2.5 M in hexanes, 6.3 mmol) was added dropwise over 30 minutes to the decyl-terthiophene derivatives (2.5 mmol) in anhydrous THF (100 mL) at -78 °C. The mixture was allowed to return to room temperature and stirred for 2 hours, then cooled back to -78 °C. A portion of trimethyltin chloride in THF (6.3 mL of 1.0 M in THF, 6.3 mmol) was added to the reaction mixture dropwise over 30 minutes and was stirred overnight at room temperature. After the reaction was finished, the mixture was poured into water (100 mL), extracted with diethyl ether (150 mL), and washed with water (2 × 100 mL), brine (100 mL) and dried over $MgSO_4$. Solvent was removed under reduced pressure, and the crude mixture was purification by reversed phase HPLC (60:40 ACN:acetone) to afford a clear oil.

5,5''-Bis(trimethylstannyl)-3,3''-didecyl-2,2':5',2''-terthiophene.[226] (1.10 g, 1.29 mmol, 51%). ^{1}H NMR (300 Hz, $CDCl_3$, ppm): δ 7.03 (s, 2H), 7.01 (s, 2H), 2.81 (t, *J* = 7.5 Hz, 4H), 1.68 (m, 4H), 1.27 (m, 24H), 0.88 (t, *J* = 6.3 Hz, 6H), 0.38 (s, 18H).

1,1'-[Thieno[3,2-b]thiophene-2,5-diylbis(4-hexyl-5,2-thiophenediyl)]bis[1,1,1-trimethyl-stannane.[225] (1.10 g, 1.22 mmol, 49%). ^{1}H NMR (300 Hz, $CDCl_3$, ppm): δ 7.21 (s, 2H), 7.02 (s, 2H), 2.80 (t, *J* = 8.0 Hz, 4H), 1.67 (m, 4H), 1.26 (m, 24H), 0.87 (t, *J* = 6.5 Hz, 6H), 0.39 (s, 18H).

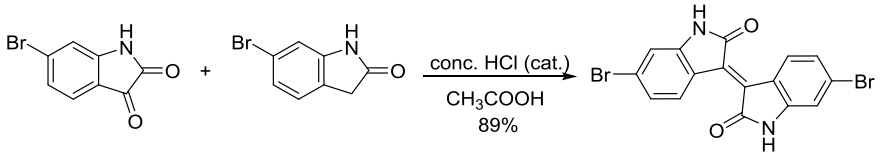

6,6'-Dibromoisoindigo.[206,227] In a 500 mL pressure reaction vessel with 6-bromoisatin (9.0 mg, 40 mmol) and 6-bromooxindole (8.5 g, 40 mmol) in acetic acid (250 mL), concentrated HCl solution (1.7 mL) was added. The reaction mixture was heated to 120 °C and stirred for 24 hours. The mixture was allowed to cool to room temperature and filtered. The solid material was washed with DI water (2 × 300 mL), ethanol (250 ml) and ethyl acetate (100 mL). After drying under vacuum overnight, the product was collected as a maroon powder (30.0 g, 71 mmol, 89% yield). ^{1}H NMR (300 Hz, Dimethyl sulfoxide-d_6, ppm): δ 11.10 (s, 2H), 9.00 (d, J = 8.7 Hz, 2H), 7.20 (m, 4H).

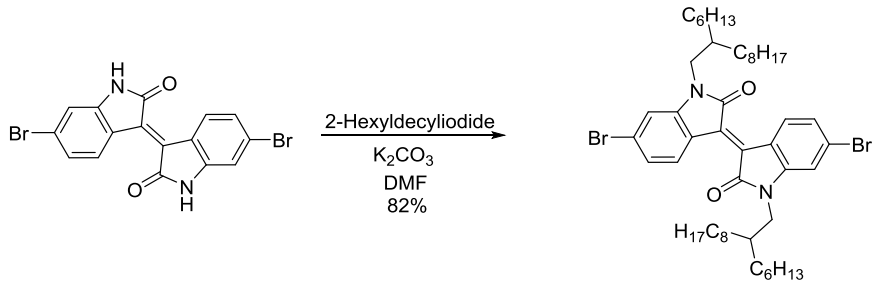

6,6'-Dibromo-*N*,*N*'-bis(2-hexyldecyl)-isoindigo.[206,227] In a 500 mL round bottom flask, 6,6'-dibromoisoindigo (8.16 g, 14 mmol) and K_2CO_3 (11.32 g, 82 mmol) were dried by heating to 60 °C under vacuum for 30 min. Dry DMF (175 mL) was added *via* cannula into the flask. 2-hexyldecyliodide (14.5 g, 41 mmol) was injected into the reaction mixture. The reaction was heated to 100 °C and stirred for 20 hours, then cooled to RT. water (500 mL) was added to quench the reaction. The mixture was extracted with DCM, washed with water (3 × 300 mL), brine (200 mL), and dried over $MgSO_4$. After a silica

gel column (4:1 hexanes:DCM as the eluent), the product was obtained as a maroon waxy solid (9.69 g, 82% yield). ^{1}H NMR (300 MHz, $CDCl_3$, ppm): δ 9.07 (d, *J* = 8.3 Hz, 2H), 7.14 (dd, *J* = 8.7, 1.8 Hz, 2H), 6.93 (d, *J* = 1.7 Hz, 2H), 3.61 (d, *J* = 8.1 Hz, 4H), 1.88 (m, 2H), 1.24 (m, 48H), 0.87 (m, 12H).

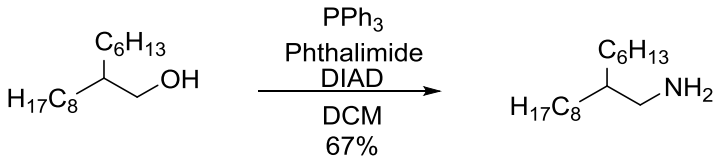

2-Hexyldecan-1-amine.[210] To a 300 mL round bottom flask with DCM (125 mL), 2-hexyl-1-decanol (21.8 g, 90 mmol) and triphenylphosphine (26.2 g, 100 mmol) were added and cooled to 0 ˚C. Phthalimide (14.7 g, 100 mmol) were added in one batch and the reaction mixture was stirred for 15 minutes. Diisopropyl azodicarboxylate (20.2 g, 100 mmol) was added dropwise over 30 minutes before the mixture was returned to room temperature and stirred for 1 hour. Solvent was removed under reduced pressure. Hexanes (50 mL) were added to dissolve the desired product and the filtrate was allowed to pass through a short silica plug and concentrated. To 500 mL round bottom flask fitted with a condenser, MeOH (300 mL), the oil, and hydrazine (8.3 g) were added and refluxed at 90 ˚C overnight. After removal of solvent under reduced pressure, the crude oil was extracted with DCM (200 mL), 10% KOH solution (100 mL), water (2 × 150 mL), brine (100 mL), and dried over $MgSO_4$. Purification *via* Kugelrohr distillation (0.5-1.0 mmHg) at 150 ˚C afford a clear oil as product (14.5 g, 60 mmol, 67%). ^{1}H NMR (300 Hz, $CDCl_3$, ppm): δ 2.52 (d, *J* = 4.5 Hz, 2H), 1.20 (m, 25H), 1.03 (br, 2H), 0.82 (m, 6H).

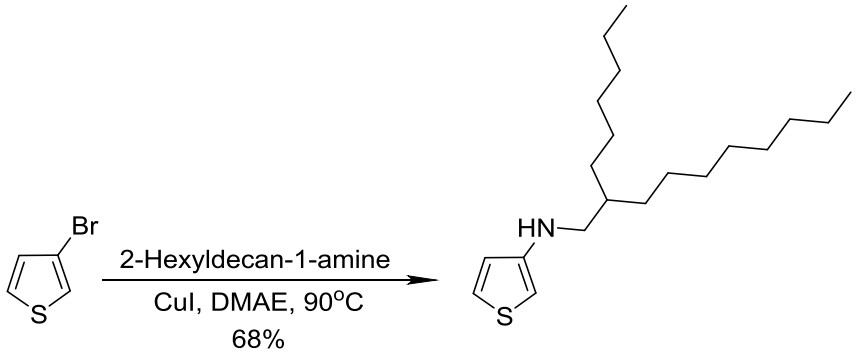

***N*-(2-hexyldecyl)thiophen-3-amine.**[210] A mixture of 3-bromothiophene (6.7 g, 40 mmol), 2-hexyldecan-1-amine (14.5 g, 60 mmol), copper (0.13 g, 2 mmol), copper(I) iodide (0.38 g, 2 mmol), and potassium phosphate tribasic (17 g, 80 mmol) in dimethylaminoethanol (100 mL) was heated to 80 ˚C for 48 hours under an argon atmosphere. The reaction mixture was cooled to room temperature and filtered. The residue was washed with ethyl acetate. The filtrate was concentrated under reduced pressure. The crude oil was subjected to silica column chromatography (1:1 Hexanes:DCM) to give 6.9 g (27 mmol 68%) of air sensitive compound. ^{1}H NMR (300 Hz, $CDCl_3$, ppm): δ 7.15 (dd, *J* = 5.1, 3.0 Hz, 1H), 6.62 (dd, *J* = 5.1, 1.5 Hz, 1H), 5.92 (dd, *J* = 3.0, 1.8 Hz, 1H), 3.58 (br, 1H), 2.98 (d, *J* = 6.0 Hz, 2H), 1.53 (m, 1H), 1.31 (m, 24H), 0.91 (m, 6H).

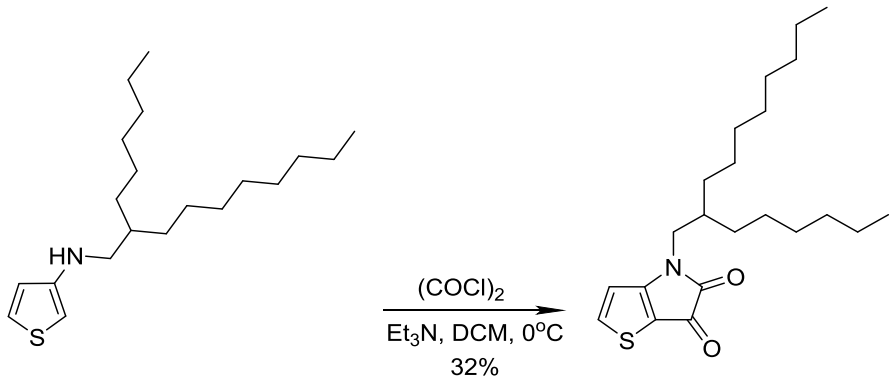

4-(2-Hexyldecyl)-4H-thieno[3,2-b]pyrrole-5,6-dione.[210] To a solution of DCM (100 mL) and *N*-(2-hexyldecyl)thiophen-3-amine (44.0 g, 136 mmol) at 0 ˚C, oxalyl chloride (22.5 g in 80 mL DCM) was added dropwise *via* an additional funnel to the reaction mixture. After stirring for 15 minutes, triethylamine (62 g in 250 mL DCM) was added dropwise *via* an additional funnel to the reaction mixture. (White smoke appeared in the reaction flask. Additional of triethylamine solution should be slow to allow the reaction mixture and smoke to settle). After the addition, the reaction mixture was warmed to room temperature and stirred for 16 hours. The crude mixture was filtered and the filtrate was concentrated under reduce pressure. The brown oil was purified by silica column chromatography with a 1:1 hexanes:DCM as the eluent. The orange-brown oil was collected (16.6 g, 44 mmol, 32%). ^{1}H NMR (300 Hz, $CDCl_3$, ppm): δ 8.00 (d, J = 5.0 Hz, 1H), 6.74 (d, J = 4.6 Hz, 1H), 3.54 (d, J = 7.4 Hz, 2H), 1.78 (m, 1H), 1.28 (m, 24H), 0.88 (m, 6H).

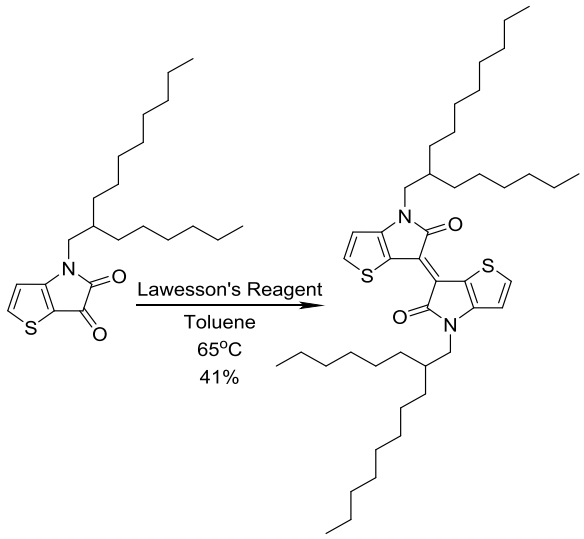

(E)-4,4”-bis(2-hexyldecyl)-[6,6”-bithieno[3,2-b]pyrrolylidene]-5,5”(4H,4”H)-dione.[210] To a 100 mL round bottom flask with anhydrous toluene (45 mL), Lawesson’s reagent (4.0 g, 10 mmol) and a solution of 4-(2-Hexyldecyl)-4H-thieno[3,2-b]pyrrole-5,6-dione (7.5 g, 20 mmol) were added. The mixture was heated to 65 ˚C and stirred for 1 hour. After cooling to room temperature, the solvent was removed under reduced pressure. The crude solid was subjected to silica column chromatography with 2:1 hexanes:DCM as the eluent to afford a purple solid (2.9 g, 41%). ^{1}H NMR (300 Hz, $CDCl_3$, ppm): δ 7.52 (d, *J* = 5.1 Hz, 2H), 6.78 (d, *J* = 5.1 Hz, 2H), 3.68 (d, *J* =7.2 Hz, 4H), 1.89 (m, 2H), 1.23 (m, 48H), 0.85 (m, 12H).

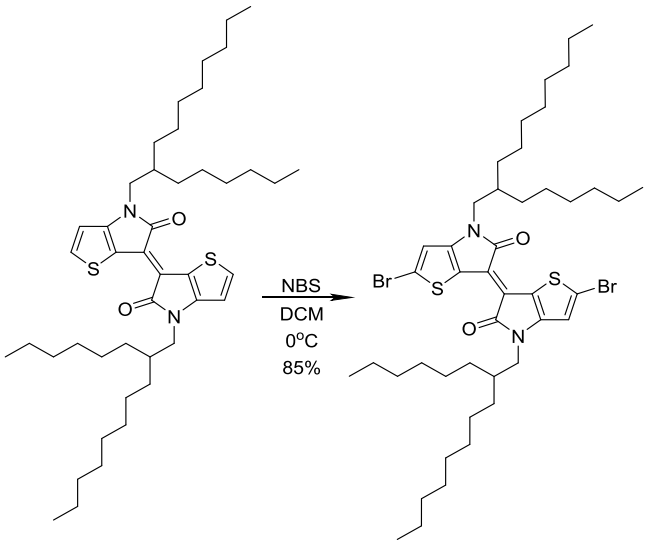

(E)-2,2”-dibromo-4,4”-bis(2-hexyldecyl)-[6,6”-bithieno[3,2-b]pyrrolylidene]-5,5”(4H,4”H)-dione.[210] To 100 mL round bottom flask, (E)-4,4”-bis(2-hexyldecyl)-[6,6”-bithieno[3,2-b]pyrrolylidene]-5,5”(4H,4”H)-dione (723 mg, 1 mmol) and DCM (30 mL) were added and cooled to 0 ˚C. *N*-bromosuccinimide (355 mg) was added to the reaction mixture in the dark. The reaction mixture was allowed to warm to room temperature and stirred for 16 hours. The crude mixture was extracted with DCM (50 mL), washed with water (2 × 100 mL), brine (50 mL), dried over $MgSO_4$. After removal of solvent under reduced pressure, the crude solid was purified by a silica column with 3:1 hexanes:DCM as the eluent to give a royal purple solid (748 mg, 0.85 mmol, 85%).^{1}H NMR (300 Hz, $CDCl_3$, ppm): δ 6.80 (s, 2H), 3.61 (d, J = 7.2 Hz, 4H), 1.82 (m, 2H), 1.23 (m, 48H), 0.86 (m, 12H).

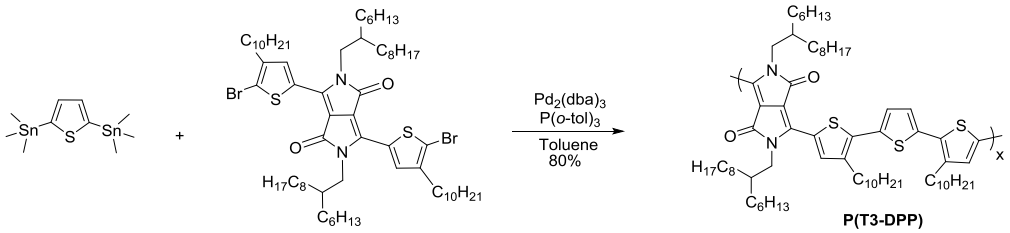

Poly(thiophene-alt-diketopyrrolopyrrole) P(T-DPP). To a 25 mL Schlenk tube with 2,5-bis(trimethylstannyl) thiophene (33.4 mg, 0.082 mmol), $Pd_2(dba)_3$ (3.0 mg, 4 mol% catalyst or 8 mol% of Pd), and P(*o*-tol)$_3$ (1.5 mg, 6 mol%), 3,6-bis(5-bromo-4-decyl-thiophen-2-yl)-*N,N'*-bis(2-hexyldecyl)-pyrrolo[3,4-c]pyrrole-1,4-dione (M1) (96.8 mg, 0.082 mmol) was added under argon. The flask was subjected to three pump/purge cycles with argon. Toluene (3 mL) was added and the reaction mixture was heated to 95 ˚C and stirred for 72 hours. The reaction mixture was cooled to 60 ˚C and stirred for 12 hours with a spatula-tip amount of diethyldithiocarbamic acid diethylammonium salt (CAS# 2391-78-8) to scavenge the palladium catalyst. The mixture was precipitated into methanol and filtered onto a PTFE membrane. The crude polymer underwent soxhlet extractions with methanol, acetone, hexanes, and dichloromethane. The dichloromethane portion was concentrated under reduced pressure and precipitated into methanol and filtered onto a PTFE membrane. After drying under vacuum, the product was obtained as a blue-green solid (72 mg, 80%). ^{1}H NMR (300 MHz, $CDCl_3$, ppm): δ 8.84 (s), 7.05 (s), 4.03 (br), 2.91 (br), 1.99 (br), 1.77 (br), 1.23 (m), 0.83 (m). GPC (1,3,4-trichlorobenzene at 140 ˚C vs polystyrene standards, RI): M_n=11.4 kg/mol, $Đ_M$=3.2. Anal. Calcd for $C_{70}H_{112}N_2O_2S_3$ (%): C, 75.62; H, 10.33; N, 2.52; S, 8.65. Found (%): C, 74.63; H, 10.11; N, 2.40; S, 8.66.

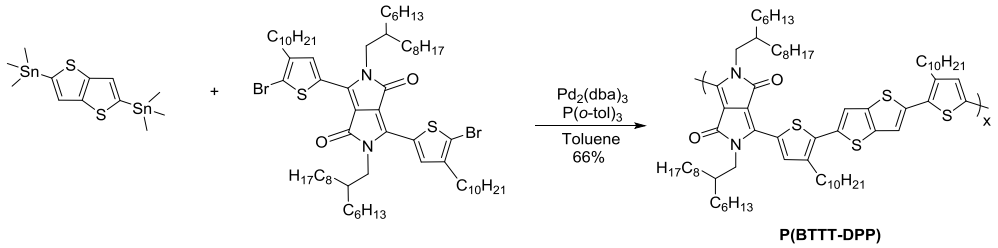

Poly(thienothiophene-alt-diketopyrrolopyrrole) P(TT-DPP). The synthesis of **P(TT-DPP)** followed the same procedure as the synthesis of **P(T-DPP)** with the following starting materials: 3,6-bis(5-bromo-4-decyl-thiophen-2-yl)-*N,N'*-bis(2-hexyldecyl)-pyrrolo[3,4-c]pyrrole-1,4-dione (96.0 mg, 0.081 mmol), 2,5-bis(trimethylstannyl)thieno[3,2-b]thiophene (37.6 mg, 0.081 mmol), $Pd_2(dba)_3$ (3.0 mg, 4 mol% of catalyst or 8 mol% of Pd), and P(*o*-tol)$_3$ (1.5 mg, 6 mol%). The product was obtained as a blue-green solid (62 mg, 66%). ^{1}H NMR (300 MHz, $CDCl_3$, ppm): δ 8.85 (s), 7.11 (s), 4.04 (br), 2.91 (br), 1.96 (br), 1.77 (br), 1.26 (m), 0.88 (m). GPC (1,3,4-trichlorobenzene at 140 ˚C vs polystyrene standards, RI): M_n=12.0 kg/mol, $Đ_M$=3.4. Anal. Calcd for $C_{72}H_{112}N_2O_2S_4$ (%): C, 74.04; H, 9.84; N, 2.40; S, 10.98. Found (%): C, 73.05; H, 9.63; N, 2.41; S, 11.40.

General Procedures of Stille Cross-Coupling Polymerizations[176] for P(T3-iI), P(BTTT-iI), P(T3-TiI), and P(BTTT-TiI):

To a 25 mL Schlenk tube, thiophene donors (1 eq.) and isoindigo/thienoisoindigo acceptors (1 eq.) were added and charged with argon for 3 pump-fill cycles. $Pd_2(dba)_3$ (1.5 mol% of catalyst or 3 mol% of Pd), and P(*o*-tol)$_3$ (4.5 mol%) were added to a vial in an argon-filled glovebox and sealed with a septum. Toluene was added to the vial to dissolve the catalyst and ligand. To the Schlenk tube, toluene was added, followed by the catalyst and ligand mixture *via* a syringe and needle. The reaction mixture was heated to

90 ˚C and stirred for 72 h. After the polymerization, 2-(tributylstannyl)thiophene (0.3 eq.) was added and stirred for 14 hours at 90 ˚C, followed by the addition of 2-bromothiophene (1 eq.). The mixture was stirred for an additional 10 hours. After cooling to 60 ˚C, a spatula-tip amount of diethyldithiocarbamic acid diethylammonium salt (CAS# 2391-78-8) was added and stirred for 10 hours to scavenge the palladium catalyst. Toluene (10 mL) of was added and the mixture was precipitated into methanol and filtered onto a PTFE membrane. The crude polymer underwent soxhlet extractions with methanol, acetone, hexanes, dichloromethane, and chloroform. The dichloromethane and chloroform fractions were concentrated, precipitated into methanol, and collected on a 0.45 μm nylon filter. The polymer was dried under vacuum for 24 hours.

P(T3-iI). 650 mg (78%). GPC (Chloroform at 30 ˚C vs polystyrene standards, RI): M_n=124.7 kg/mol, $Đ_M$=1.89. Anal. Calcd for $C_{80}H_{118}N_2O_2S_3$ (%): C, 77.72; H, 9.64; N, 2.27; S, 7.78. Found (%): C, 77.66; H, 9.79; N, 2.19; S, 7.61.

P(BTTT-iI). 253 mg (73%). GPC (Chloroform at 30 ˚C vs polystyrene standards, RI): M_n=16.2 kg/mol, $Đ_M$=2.53. Anal. Calcd for $C_{82}H_{118}N_2O_2S_4$ (%): C, 76.21; H, 9.22; N, 2.17; S, 9.92. Found (%): C, 76.04; H, 9.21; N, 2.23; S, 9.64.

P(T3-TiI). 190 mg (75%). GPC (1,3,4-trichlorobenzene at 140 ˚C vs polystyrene standards, RI): M_n=14.0 kg/mol, $Đ_M$=1.64. Anal. Calcd for $C_{76}H_{114}N_2O_2S_5$ (%): C, 73.12; H, 9.22; N, 2.24; S, 12.84. Found (%): C, 73.03; H, 9.04; N, 2.29; S, 12.42.

P(BTTT-TiI). 216 mg (74%). GPC (1,3,4-trichlorobenzene at 140 ˚C vs polystyrene standards, RI): M_n=15.2kg/mol, $Đ_M$=1.70. Anal. Calcd for $C_{78}H_{114}N_2O_2S_6$ (%): C, 71.82; H, 8.83; N, 2.15; S, 14.74. Found (%): C, 71.57; H, 8.63; N, 2.36; S, 13.92.

CHAPTER 4

DONOR-ACCEPTOR DIKETOPYRROLOPYRROLE AMPHIPHILIC DISCRETE MOLECULES

4.1. DPP-based Donor-Acceptor Discrete Molecules with Polar Triglyme Side Chains

As mentioned in the introductory chapter, the performance of an OPV device depends on the nanostructure of polymer donor and fullerene acceptor within the active layer. Achieving optimal physical properties such as domain size, morphology, and crystallinity, along with intermolecular orientation and structure relies on the spontaneous phase separation between the donor and the acceptor in the blend. One way to gain full control of the active layer formation is *via* layer-by-layer deposition. This chapter will focus on the supramolecular self-assembly of two families of DPP-based donor-acceptor molecules. Herein, we report the LbL deposition of two donor-acceptor-donor (D-A-D) amphiphilic molecules *via* Langmuir-Blodgett technique to construct highly ordered molecular monolayers for organic electronic devices. Two molecules containing oligoether side chains were synthesized to study the effect of their molecular sizes on LB deposition stability. In molecular design of conjugated molecules, the D-A-D approach has been employed to tune the energy gap in the system by mixing molecular orbitals and controlling the intramolecular charge transfer energy between the donor and acceptor moieties.[228,229] More specifically, D-A-D molecules with the popular diketopyrrolopyrrole (DPP) as the acceptor unit reported by Nguyen and co-workers have promising device performances in OPVs and OFETs applications.[230,231,80] Mei *et al.* have

shown the self-assembly of amphiphilic D-A-D DPP molecules can be controlled by the evaporation time of the casting solvent.[232] To the best of our knowledge, the LB-deposition of D-A-D based conjugated molecules has not been previously reported. We successfully transferred the monolayer of both molecules, **DPP-A** and **DPP-S** displayed in Scheme 4-1, onto solid substrates and found that the quality of the monolayer and the coverage can be precisely controlled by adjusting the compression pressure atop the surface of the LB trough. We found that the intermolecular interaction and order in the thin films depend on the deposition methods, with LB-coated and blade-coated films resulting in higher order, anisotropic and specific edge-on orientation on silicon substrates. Both OFET devices with monolayers of the semiconducting molecules and OPV devices in bulk heterojunction and bilayer active layer architectures were fabricated, allowing us to correlate the fundamental impact of structural order resulting from the glyme side chains on organic electronic applications.

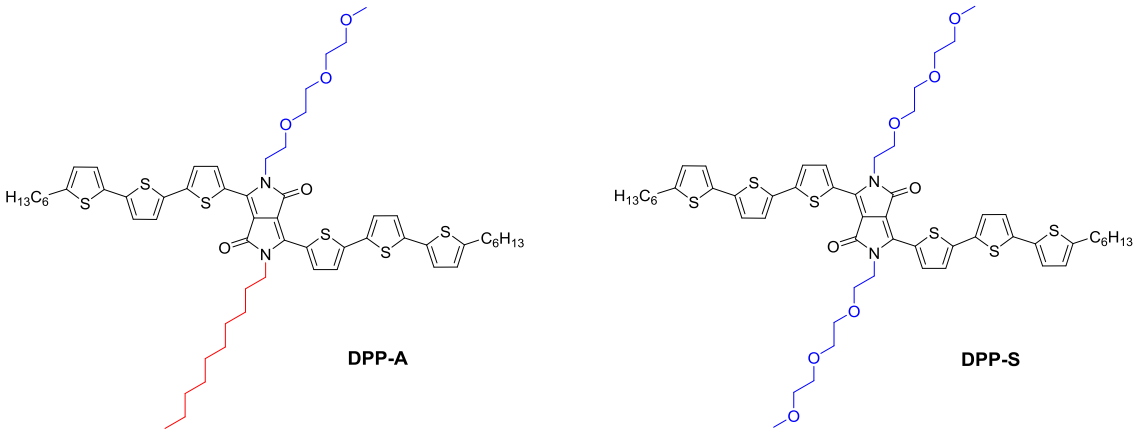

Scheme 4-1. Chemical structures of **DPP-A** and **DPP-S**

4.1.1. Molecule Synthesis of DPP-A and DPP-S

4.1.1.1 Asymmetric substitution on the DPP core

Scheme 4-2 outlines the synthetic approach of the asymmetrically substituted and ditriglyme substituted DPP. The reaction for side chain substitution on the DPP core was a "one-pot synthesis", where both asymmetrical (Compound 4-1) and diglyme- (Compound 4-2) substituted DPPs were afforded in one reaction. Several reaction conditions were evaluated for the side chain addition as shown in Table 4-1. In this optimized one-pot synthesis, due to the reactivity difference between the triglyme tosylate and 1-bromodecane with the DPP core, the former was allowed to first react for 16 hours before the addition of the latter. After the initial workup, purification proceeded through column chromatography with a gradient mixture of dichloromethane, ethyl acetate and acetone and the two desirable precursors were obtained in high yields.

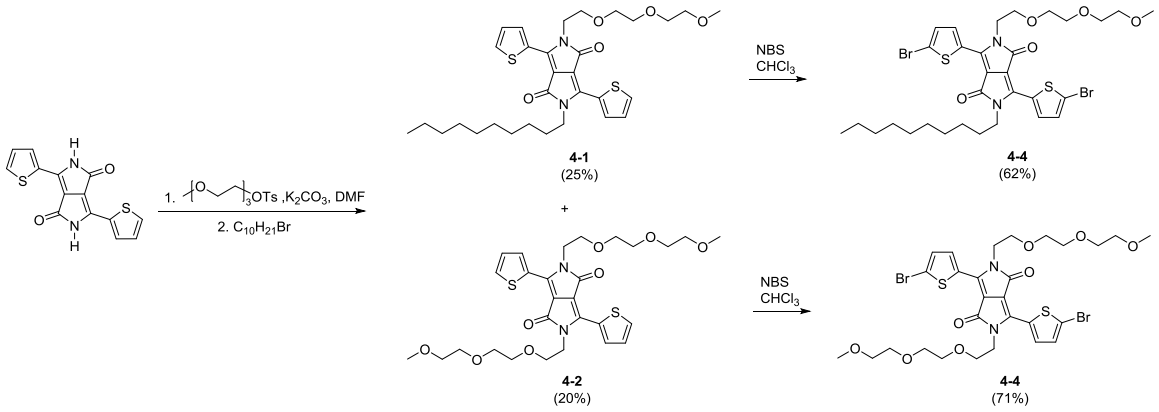

Scheme 4-2. "One-pot" synthesis and bromination of glyme-containing diketopyrrolopyrrole

Table 4-1. Optimization of the one pot side chain attachment on the DPP precursors

	1-Bromodecane	Triglyme tosylate	Equivalent (DPP : Br : Tos)	Yield (4.1/4.2/4.3)[a]
1	Added at the same time		1 : 1 : 1	10% / 28% / 12%
2	First added; stirred for 12h	Then added; stirred for 7h	1 : 1 : 1	18% / 23% / 14%
3	First added; stirred for 12h	Then added; stirred for 7h	1 : 1.5 : 1.5	25% / 20% / 15%

[a] Compound 4-3 represents dialkyl-DPP as a side product of the one pot reaction.

4.1.1.2. Stille Cross-Coupling Reaction and Choice of Catalyst

Several palladium catalytic systems were examined for the Stille reactions of the amphiphilic DPP molecules as shown in Table 4-2. Scheme 4-3 highlights the Stille cross-coupling reactions for the final molecules. Using $Pd(PPh_3)_4$ as the catalyst we synthesized **DPP-A** and **DPP-S**, which were purified by recycling column chromatography. Each molecule was obtained in above 80% yield with high accuracies in elemental compositions. As usual, the palladium catalyst was handled only inside an argon-filled glovebox and otherwise stored at -20 ˚C under an inert atmosphere to prevent decomposition. It is noteworthy to mention that a different synthetic approach was performed using tris(dibenzylideneacetone)dipalladium(0) ($Pd_2(dba)_3$) as the catalyst and tri(*o*-tolyl)phosphine as the ligand, which led to lower overall yield. When a catalytic system of $Pd_2(dba)_3$/P(*o*-tol)$_3$ were used, only 37% and 53% yields were obtained for **DPP-A** and **DPP-S** respectively. As mentioned previously, commercially available $Pd_2(dba)_3$ has been shown to contain up to 40% of Pd(0) nanoparticles, which initiates a heterogeneous catalytic reaction and lead to homo-coupled products.[140,233] $Pd(PPh_3)_4$ is an ideal catalyst for a cross-coupling reaction on molecular systems. While the phenyl groups on $Pd(PPh_3)_4$ could “endcap” and terminate the grow of polymer chains,[234] it is

less of a concern for molecular Stille syntheses. Furthermore, as the catalyst decomposes the color of $Pd(PPh_3)_4$ changes from bright yellow to orange-brown as a result of the formation of Pd(0) nanoparticles,[235] which is easily distinguishable by careful observations during reaction setup.

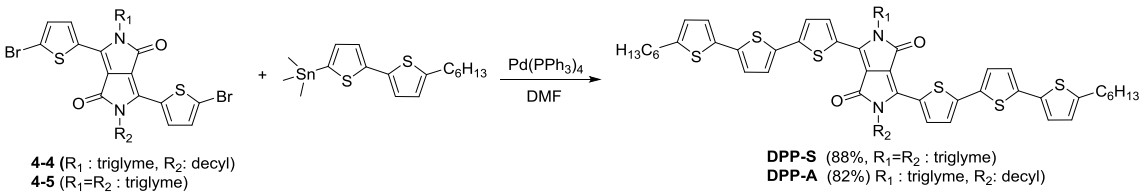

Scheme 4-3. Stille cross-coupling reaction of **DPP-A** and **DPP-S**

Table 4-2. Optimization of the microwave-assisted Stille cross-coupling step in the syntheses of **DPP-A** and **DPP-S**

	Reaction condition	Product	Yield	Purification
1	$Pd_2(dba)_3$, P(*o*-tol)$_3$, Toluene, 160 ˚C, 1h	**DPP-A**	37%	2 columns (4:1 DCM:EtOAc)
2		**DPP-S**	53%	2 columns (1:1 DCM:Acetone)
3	$Pd(PPh_3)_4$, DMF, 80 ˚C, 1h	**DPP-A**	82%	1. Recycling column (EtOAc) 2. Eluting product (1:1 DCM:EtOAc)
4		**DPP-S**	88%	1. Recycling column (EtOAc) 2. Eluting product (1:1 DCM:Acetone)

4.1.2. Theoretical Electronic and Structural Analysis

Density functional theory (DFT) calculations were performed to correlate theoretical evaluation of the molecules' electronic properties with experimental results. The geometries of the two molecules were optimized *via* DFT at the B3LYP/6-31G(d) level, and the energy of the highest occupied molecular orbital (HOMO) and lowest unoccupied molecular orbital (LUMO) were calculated with a much larger basis set, 6-311++G(d, p). The difference in side chains between **DPP-A** and **DPP-S** does not significantly impact their energy levels; $\in_{HOMO}$ of both monomers are around -4.9 eV,

while $\in_{LUMO}$ are around -3.0 eV, which are comparable to previously calculated results.[236]

To identify the most energetically favorable conformation, we plotted the torsional potentials at B3LYP/6-31G(d) level. The torsion angles are between the thiophene arms and the DPP core, at the donor-acceptor connections. As shown in Figure 4-1, the syn (0˚) conformations were more energetically favorable for both molecules, with the relative energies stabilized by ~5 kcal/mol comparing to the anti (180˚) conformations. Since both values are substantially larger than thermal energy at room temperature (0.6 kcal/mol), we conclude that there are significant influences of the oxygen-hydrogen and sulfur-hydrogen interactions on conformation stability in these molecules. Jackson *et al.* have shown that, despite the general belief of a stabilizing sulfur-oxygen interaction, oxygen-hydrogen interactions in DPP-thiophene and thienopyrrolodione-thiophene allow for stronger energetic preferences to backbone planarity.[237]

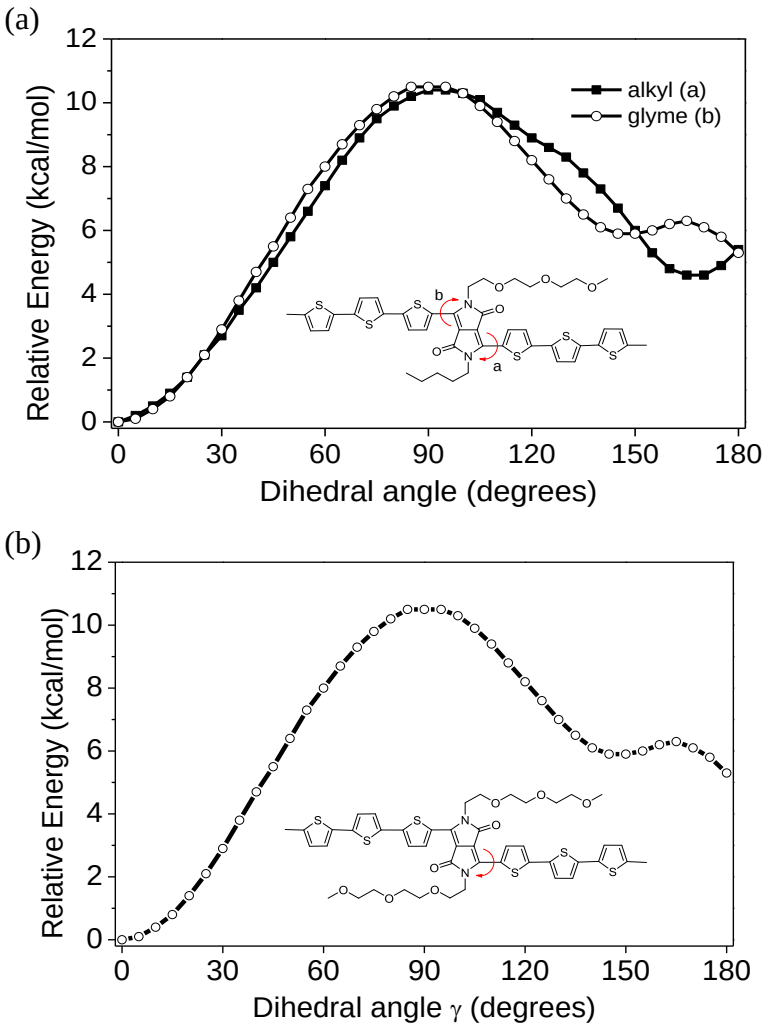

Figure 4-1. Torsional potentials for (a) **DPP-A** and (b) **DPP-S**. The molecular conformation in each plot is the syn (0°) conformation. Rotation occurs around the inter-ring C−C bond between the DPP core and the thiophene arms. For **DPP-A**, torsional angles against both arms were calculated due to its asymmetrical substitution.

4.1.3. Optoelectronic and Thermal Characterizations of DPP-A and DPP-S

4.1.3.1. UV-Vis-NIR Absorption in Solutions and Thin Films

Similar to typical donor-acceptor type conjugated materials, both **DPP-A** and **DPP-S** display two main absorption features originated from the high energy π-π*

transitions and the low energy intramolecular charge transfer transitions. These results correlate well with our theoretical calculation with a strong absorption maximum at ~627 nm and another weak absorption maximum at ~ 476 nm. Comparing the solution to the thin-film UV-Vis spectra in Figure 4-2a and 4-2b, both molecules have bathochromic shifts of over 100 nm in their solid state absorption onsets, showing their strong intermolecular interactions. To investigate the nature of the interaction, temperature dependent UV-Vis in toluene was used to study whether the red-shift in absorption was the result of strong intermolecular aggregations. When the temperature increased from 20 to 105 ˚C, the spectra of both molecules exhibited the disappearance of the lowest energy peaks at 680 nm along with moderate hypsochromic shifts. These are evidence of aggregations in these molecules even at low concentrations in toluene (5×10^{-5} M), potentially a result of separate interactions of the alkyl and the glyme side chains promoting self-assembly. By drop casting the two solutions and allowing them to dry slowly in an environment with high solvent vapor content, we observed the formation of large fibrils in micron length scale (Figure 4-3), further proving these molecules can self-assemble into ordered domains. A previous study by Mei *et al.* using similar DPP molecules containing oligoether side chains[232] shows that the fibril size can be controlled by solvent evaporation time during the drop-casting process. Large fibrils (~0.5 μm wide) are formed during a long drying time, which allows the molecules to self-assemble into large aggregates. These extended fibrillar networks could be advantageous for charge transport and mobility in solution-processed field-effect transistor (FET) devices.

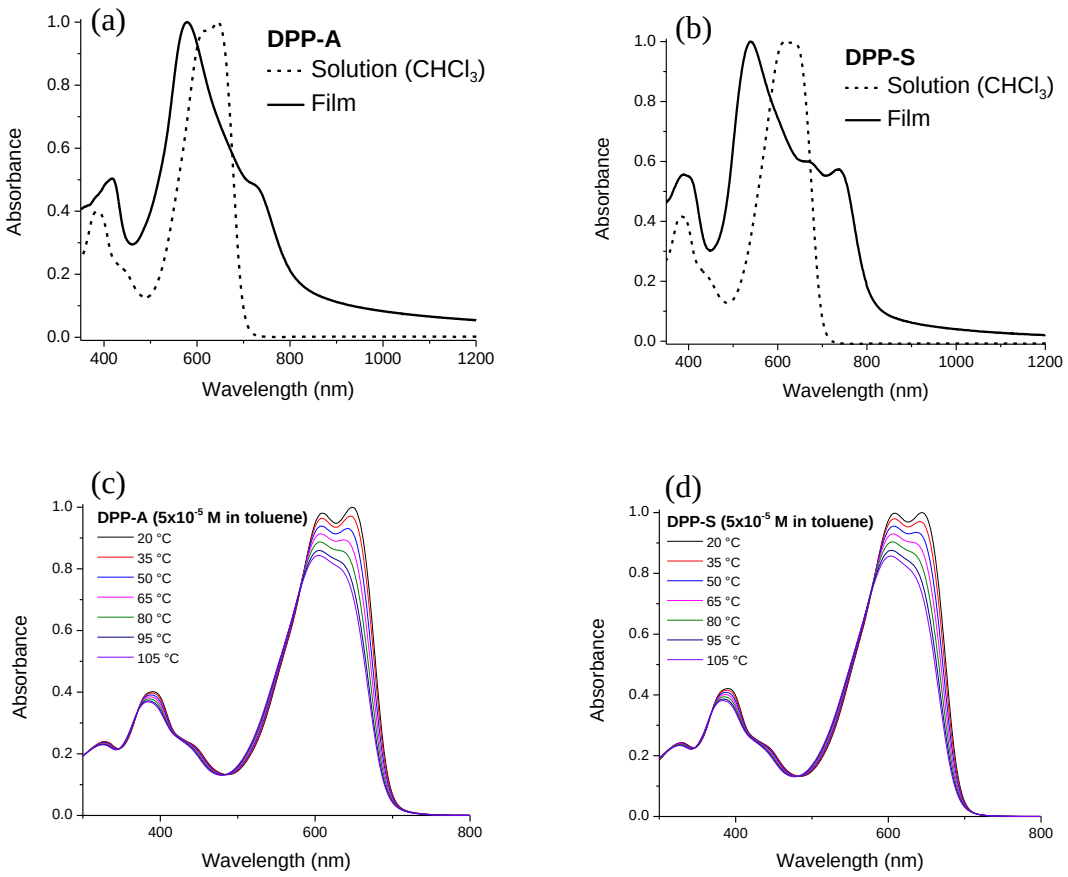

Figure 4-2. Comparisons of solution and thin-film absorption spectra of (a) **DPP-A** and (b) **DPP-S**. Temperature dependent absorption spectra of (c) **DPP-A** and (d) **DPP-S**. The lowest energy peaks at 680 nm, resulting from aggregates, disappear at elevated temperatures.

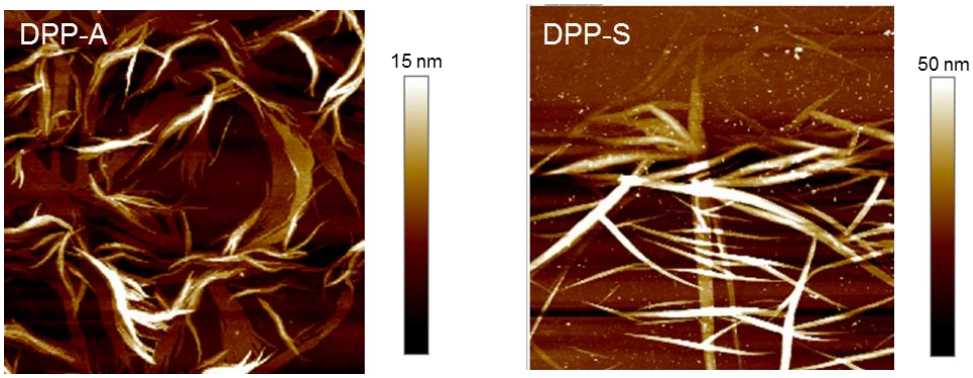

Figure 4-3. AFM height images of **DPP-A** and **DPP-S** films. Thin films were prepared by drop-casting 4 mg/mL toluene solutions onto glass slides. The substrates were allowed to dry slowly over 30 minutes in a petri dish with toluene vapors. Image size: 10 μm × 10 μm.

4.1.3.2. Cyclic Voltammetry and Differential Pulse Voltammetry

Electrochemical experiments were performed on the two molecules to investigate their electronic properties. The cyclic voltammograms (CV) and the differential pulse voltammograms (DPV) of both molecules (Figure 4-4 and summarized in Table 4-3) show two well-resolved reduction and oxidation features. The oxidation onsets of the differential pulse voltammetry (DPV) scans were used to provide estimations of the ionization potentials; and the reductive DPV onsets for the electron affinities. As predicted by theoretical calculations shown previously, both molecules have statistically identical energy levels, with EA and IP at -3.6 eV and -5.4 eV respectively, and energy gaps of 1.8 eV, which are slightly above optical absorption gaps (*vide infra*) and comparable to published results on materials with the same molecular backbone.[232,236]

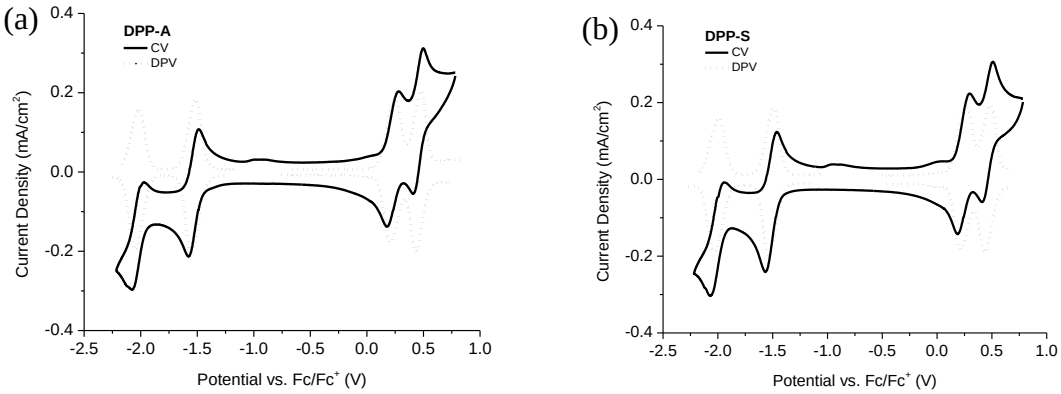

Figure 4-4. Solution cyclic voltammetry and differential pulse voltammetry (a) **DPP-A** and (b) **DPP-S** show two well-resolved and reversible oxidation and reduction features.

Table 4-3. Summary of electrochemical properties* of **DPP-A** and **DPP-S**.

	CV		DPV		
	$E_{1/2}^{ox}$ (V)	$E_{1/2}^{red}$ (V)	E_{on}^{ox}(V) / IP(eV)	E_{on}^{red}(V) / EA(eV)	E_{gap} (eV)
DPP-A	0.11	-1.50	0.24 / -5.36	-1.55 / -3.57	1.79
DPP-S	0.20	-1.48	0.25 / -5.37	-1.52 / -3.60	1.77

*Electrochemistry experiment of the molecules were recorded from DCM solutions. CV (scan rate 50 mV/s) and DPV differential pulse voltammetry (step size 2 mV, step time 50 ms, pulse amplitude 100 mV) of the molecules were measured using 0.01 cm^2 Pt disc electrodes in 0.5 M $TBAPF_6$/acetonitrile, using a Ag/Ag^+ reference electrode (0.01 M $AgNO^3$) and Pt flag counter electrode. IP and EA values were estimated by assuming SCE to be 4.74 eV vs. vacuum and Fc/Fc^+ to be +0.38 eV with respect to SCE.

4.1.3.3. Thermal Analysis

Differential scanning calorimetry was performed to investigate the phase behavior of the two DPP molecules. In Figure 4-5a, the DSC thermograms for both molecules show two endothermic transitions upon heating to ~100 ˚C and ~200 ˚C. Upon cooling, two corresponding exothermic transitions can be seen. We investigated these transitions with the molecular thin films under an optical microscope equipped with a heated stage. No visible physical changes were observed at the low temperature transitions, which may be detectable only in the bulk solids as prepared for the DSC experiments. The high temperature transitions, on the other hand, were observed and identified as melts and crystallizations of the molecules. The polarized optical micrographs of the **DPP-A** and **DPP-S** thin-films in Figure 4-5b and 4-5c further indicate the strong intermolecular orders in these materials. Strong birefringence was observed when the aligned thin films were positioned 45˚ with respect to the cross polarizer/analyzer (non-polarized and polarized optical microscopy images at various rotation angles can be found in Figure 4-6). Table 4-4 summarizes the thermal and optical properties of the two molecules.

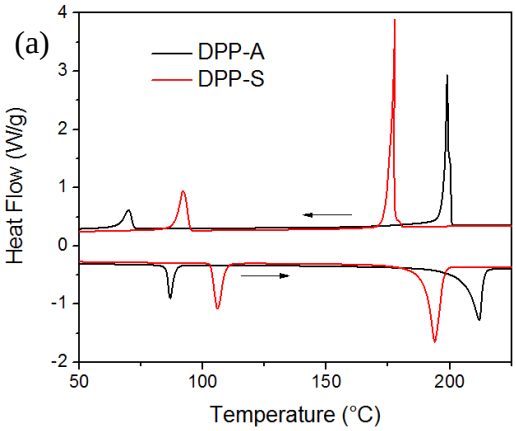

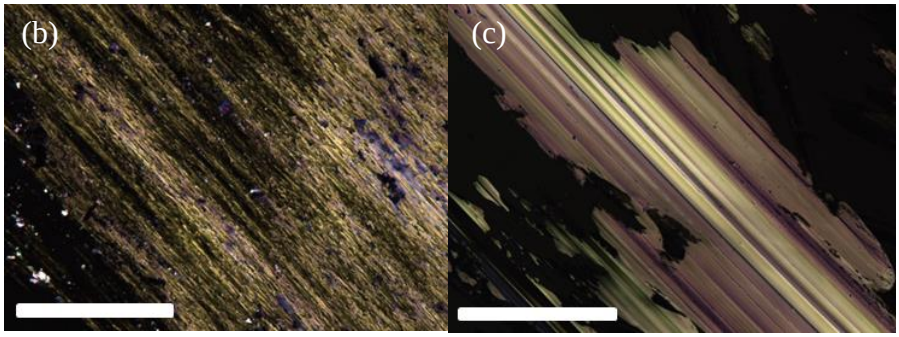

Figure 4-5. (a) Differential scanning calorimetry scans of **DPP-A** and **DPP-S** at a rate of 10 ˚C/min. The heating and cooling directions are indicated by the arrows. Transmission cross-polarized optical micrographs of (b) **DPP-A** and (c) **DPP-S** thin-films on glass slides. Strong birefringence can be seen when the substrates are oriented 45˚ with respect to the cross polarizer/analyzer. Scale bars are 100 μm.

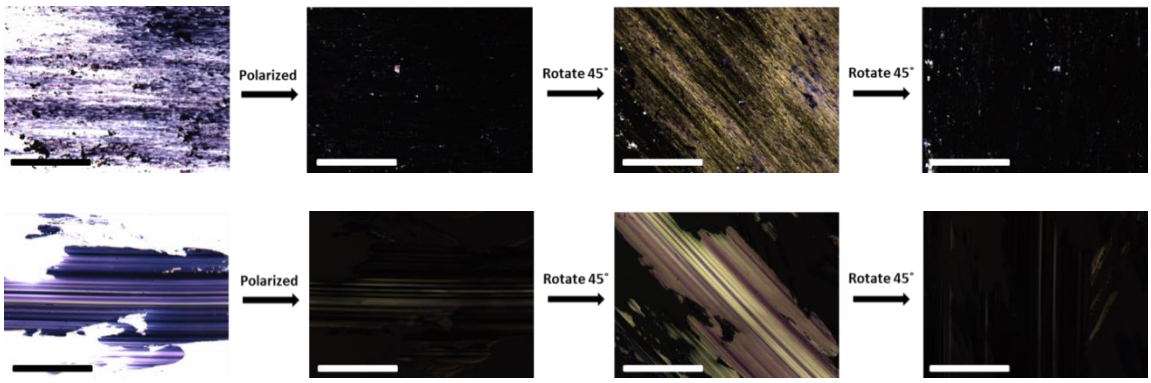

Figure 4-6. Cross-polarized optical micrographs of thin-films **DPP-A** (top) and **DPP-S** (bottom). All scale bars are 100 μm.

Table 4-4. Summary of thermal and absorption properties of **DPP-A** and **DPP-S**.

	Thermal properties		UV-Vis-NIR					
	T_d (˚C)	T_m/T_c (˚C)	$\lambda_{max}^{Solution\ a}$ (nm)	$\lambda_{max}^{Film\ b}$ (nm)	$\lambda_{max}^{Theory\ c}$ (nm)	$\lambda_{onset}^{Film\ d}$ (nm)	E_{gap}^{opt} (eV)	Molar Absorptivity (M^{-1} cm^{-1})
DPP-A	376	212 / 198	614, 645	578, 722	476, 627	834	1.49	60,000
DPP-S	409	194 / 177	614, 637	539, 669, 736	476, 628	808	1.53	63,000

[a] Measured in chloroform solution. [b] thin film spin-casted on glass slide. [c] The excited states energies (in Table 2) were obtained by means of time-dependent DFT calculation based on the TammDancoff approximation (TDA-TDDFT). All DFT calculations were performed with Q-chem 4 package.[238,239] [d] $Eg^{opt} = 1240 / \lambda^{onset,film}$

4.1.4. Layer-by-layer Langmuir-Blodgett Film Deposition

4.1.4.1. Monolayer Morphology

The amphiphilic and self-assembly properties of these molecules provided an opportunity to explore the usage of the Langmuir-Blodgett method to assemble mono- and multilayers.[240] Figure 4-7a displays the surface pressure versus mean molecular area (MMA) isotherm as the monolayer of **DPP-A** was compressed by two barriers after being spread on the water subphase from its chloroform solution in the Langmuir-Blodgett trough. The isotherm exhibits a gradual transition from an expanded to a compacted phase. A phase transition can be clearly seen at ~15 mN/m compression pressure. To investigate the quality of the monomer layer at different pressures, monolayers of **DPP-A** were compressed and transferred onto silicon substrates for morphological study. As shown in the atomic force microscopy (AFM) height image (in Figure 4-7b), the monolayer deposited at 10 mN/m contains multiple large areas of defect, which suggested a poorly formed monolayer on the LB water surface. The monolayers transferred at 20 mN/m had excellent coverages (Figure 4-7c), suggesting the phase transition at 15 mN/m on the isotherm is likely a result from compression of the well-

formed monolayer. As indicated by the isotherm, the MMA continues to decrease steadily as the surface pressure increases. The monolayer eventually collapses at ~60 mN/m. The AFM height images of the monolayers deposited at 30 and 40 mN/m (Figure 4-7d and 4-7e, respectively) indicated multiple layer formations.

The monolayer compression isotherm (Figure 4-8a) of **DPP-S** has a similar behavior to **DPP-A**, containing an obvious phase transition at ~15 mN/m and a collapse at ~55 mN/m. It also has similar monolayer coverage and stability, showing best coverage with the monolayer deposited at 20 mN/m (Figure 4-8b-e). Just like that of **DPP-A**, the isotherm of **DPP-S** signals a steady decrease in molecular area as compression pressure increases, which indicates that even the multilayer formations at compression pressures above 20 mN/m were reproducible and well-controlled, further confirming that these molecules could self-assemble into ordered structures.

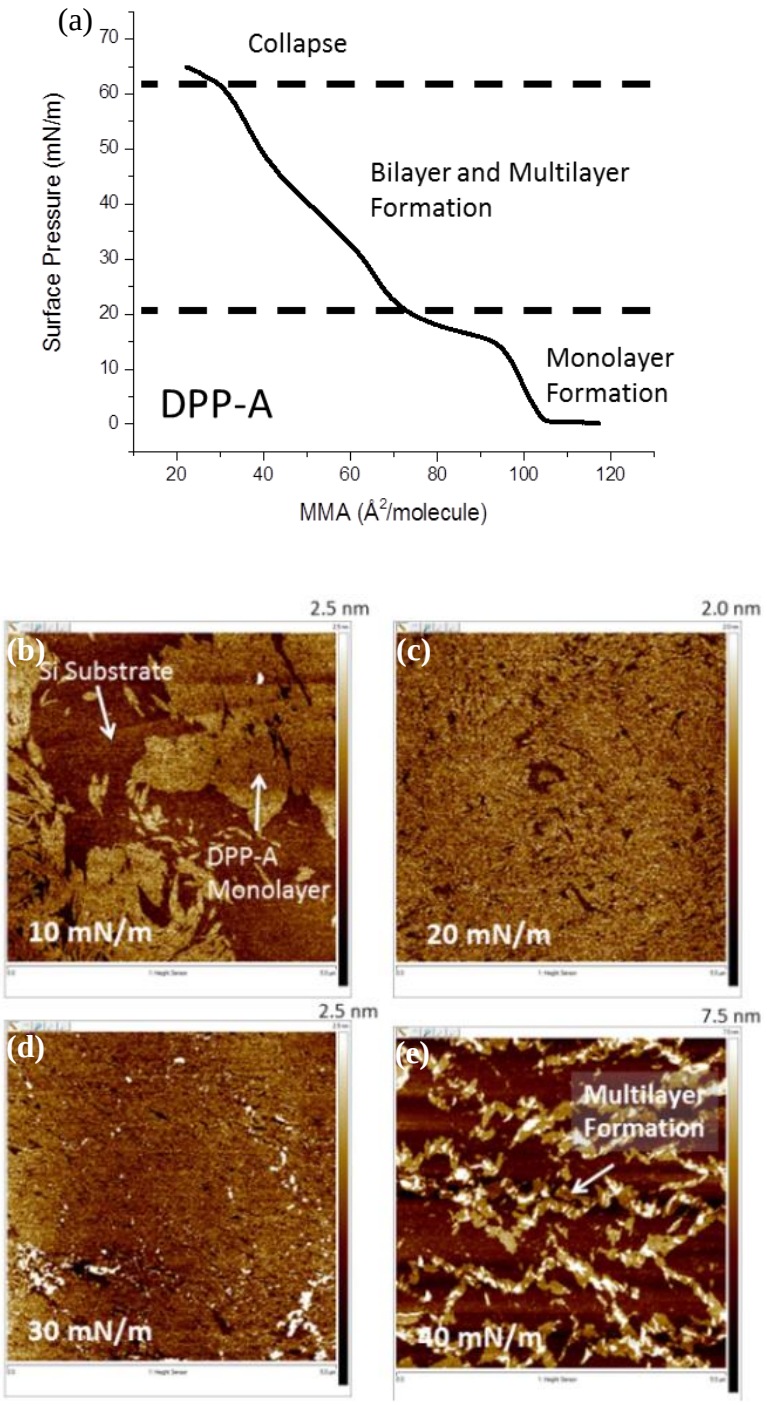

Figure 4-7. (a) Langmuir compression isotherm of **DPP-A**. (b-e) AFM height images of **DPP-A** LB monolayers deposited at different compression pressures. LB deposition at 20 mN/m produced an even and well-covered monolayer. AFM Image size: 5 μm × 5 μm

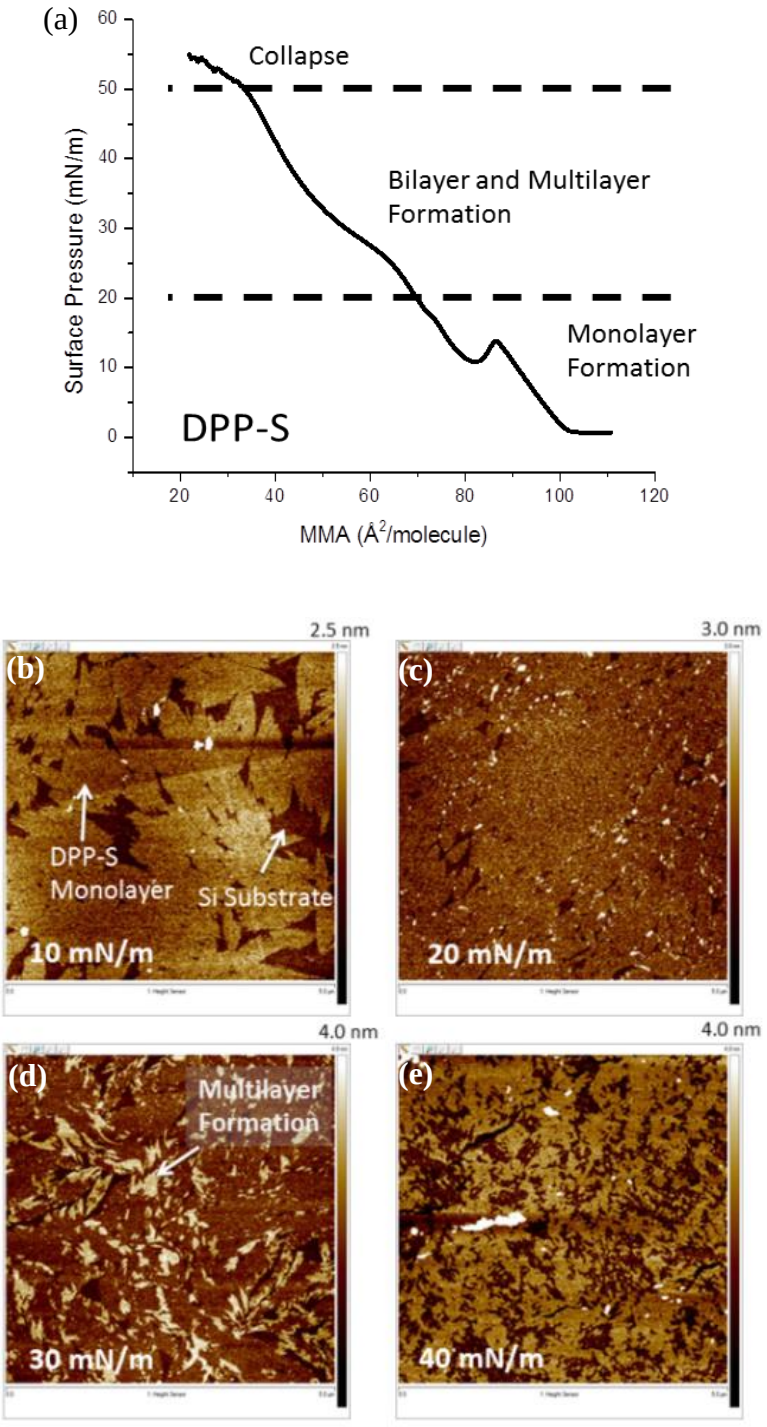

Figure 4-8. (a)Langmuir compression isotherm of **DPP-S**. (b-e) AFM height images of **DPP-S** LB monolayers deposited at different compression pressures. LB deposition at 20 mN/m produced an even and well-covered monolayer. AFM Image size: 5 μm × 5 μm

4.1.4.2. Controlled Deposition of Multilayer LB Films

The ability to control the formation and transfer of LB monolayers *via* compression pressure, the evidence of strong intermolecular interactions and orders in these molecules led us to explore LB multilayer transfers. Multiple layers of both molecules were deposited onto glass substrates treated with trichlorododecylsilane to ensure hydrophobicity of the substrates. It is an important step since the multilayer building process was unsuccessful past the first monolayer on hydrophilic substrates. The transfer ratio of each layer was 0.95 (±0.09) in both up- and down-strokes. The absorption spectra of LB films with various thicknesses, controlled by the number of deposited layers, were measured and the absorption at λ_{max} increased linearly with increasing number of layers (Figure 4-9). This result confirms the stable transfer of monolayers in creating the Y-type LB films (deposition during both upstroke and downstroke) containing up to 20 deposited layers. Comparing the LB multilayer absorption and the solution-processed thin film absorption (Figure 4-10), we observed the disappearance of the low energy peaks at ~750 nm, indicating differences in aggregation behavior in the LB films. Specifically for **DPP-S**, the λ_{max} is red-shifted for the LB film, potentially resulting from improved stacking of molecules in the solid-state due to the LB layer-by-layer deposition methods.[241]

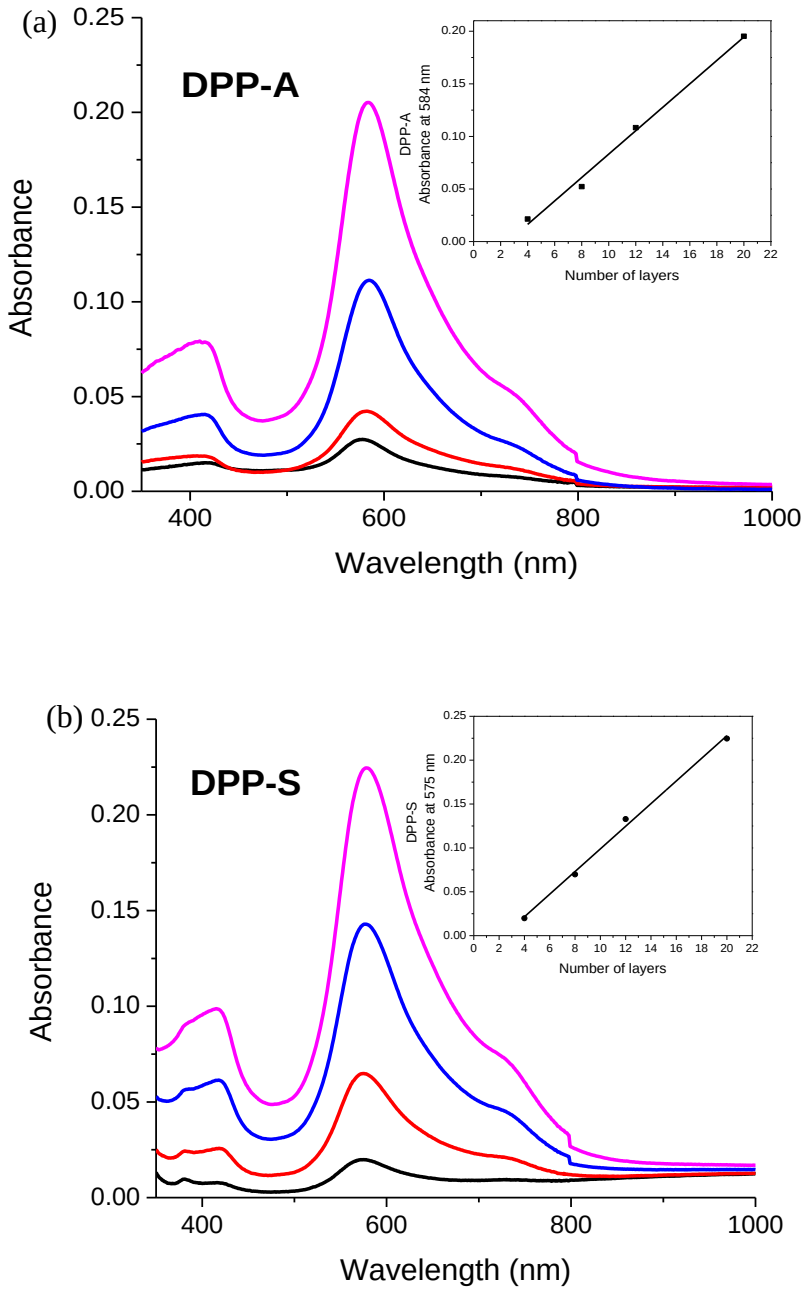

Figure 4-9. Thickness-dependent thin-film absorption spectra of (a) **DPP-A** and (b) **DPP-S**. The black, red, blue, and magenta spectra represent 4, 8, 12, and 20 monolayers deposited *via* Langmuir-Blodgett, respectively. Inset of each show the thickness-dependent absorption intensities at λ_{max}.

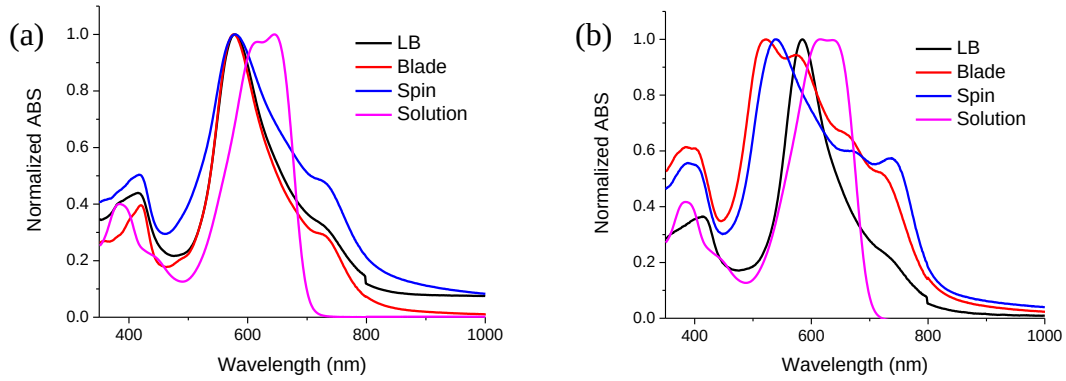

Figure 4-10. Solution vs thin-films absorption spectra of (a) **DPP-A** and (b) **DPP-S** deposited by LB, blade coating, and spin coating.

4.1.4.3. Intermolecular Interaction by GIWAXS

GIWAXS was used to confirm the differences in order with respect to the different deposition methods. The GIWAXS data of **DPP-A** and **DPP-S** for spin-coated, blade-coated and LB-coated films are displayed in Figure 4-11. It is immediately obvious that there is a big difference in spin-coated versus blade-coated films; the spin-coated films show a much more isotropic nature, indicating a random orientation of crystallites with respect to the substrate, whereas the blade-coated films have crystallites with a definite preferred edge-on orientation with respect to the substrate. Comparing the blade-coated and LB-coated **DPP-A** films, the diffraction is similar, the main difference is the "streaking" effect of the peak(s) at q_{xy}=0.62, this is due to the finite size effect for the very thin LB film. In contrast, there is an obvious difference for **DPP-S** from blade-coated versus LB-coated films: the peaks at q_{xy}=0.70 for the blade-coated film move to q_{xy}=0.61 when processed using the LB technique. In addition, the peaks around q_{xy}=1.3 are significantly different. Interestingly, upon annealing of the blade-coated **DPP-S** film (Figure 4-12), the diffraction pattern becomes similar to the diffraction of the LB film,

the diffraction at q_{xy}=0.70 moves to q_{xy}=0.61. This is consistent with a change in packing of the molecules, and with the peak in the DSC data (*vide supra*). This is further evidence of metastable crystal packing, which can change upon annealing as observed from DSC. Annealing of blade-coated **DPP-A** did not result in a change in GIWAXS data, indicating that the most stable packing state is immediately achieved upon deposition.

From the GIWAXS data it is clear that **DPP-A** and **DPP-S** pack in a similar fashion, whether deposited by blade coating or LB coating (after annealing in the case of blade-coated **DPP-S**). Given the similarity in molecular order and orientation, we predict similar performances of these two molecules in the organic field-effect transistor (OFET) and photovoltaic (OPV) devices.

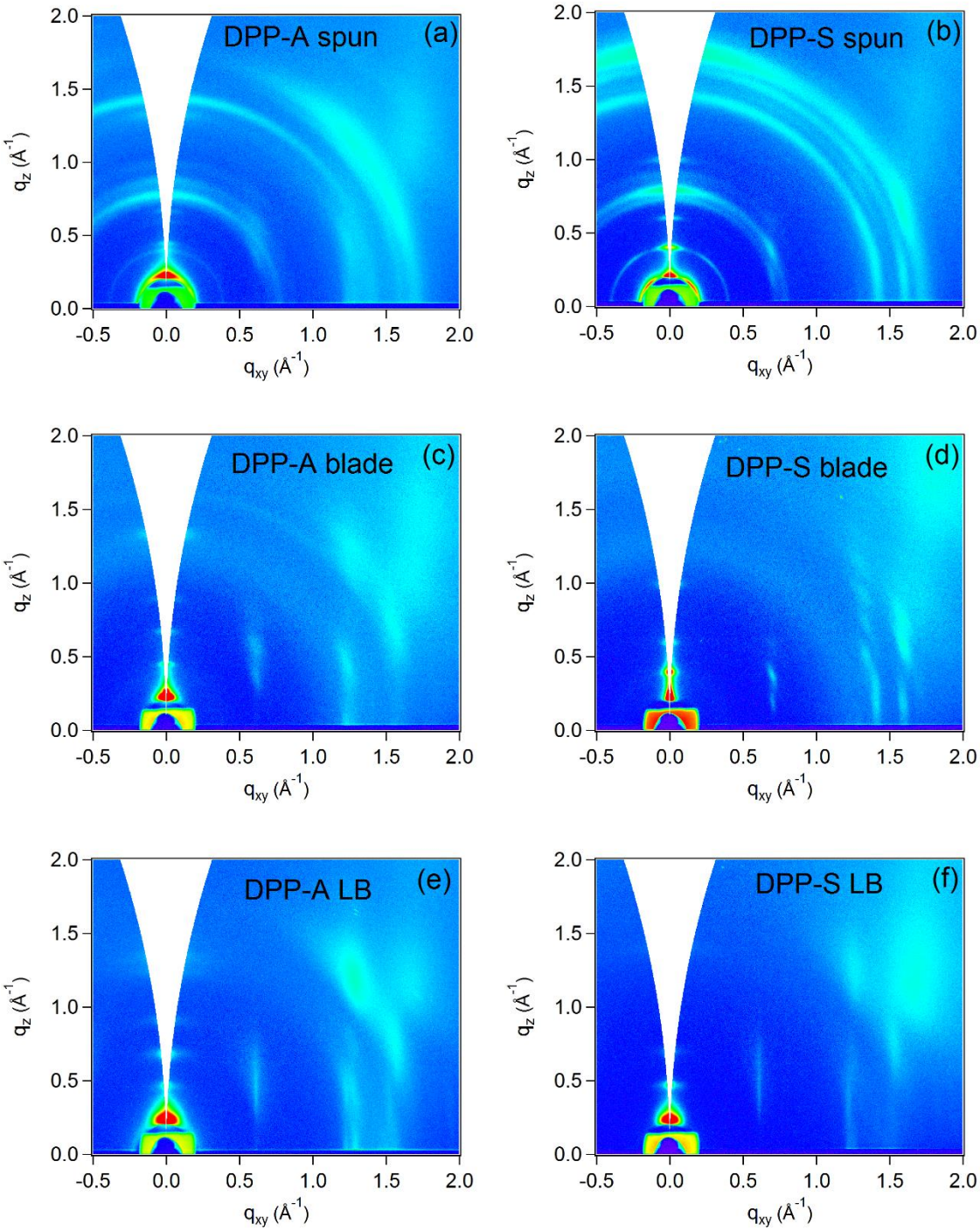

Figure 4-11. Two-dimensional (2D) grazing incidence wide-angle X-ray scattering (GIWAXS) images of thin-film **DPP-A** and **DPP-S** deposited by spin coating (a and b), blade coating(c and d), and LB (e and f).

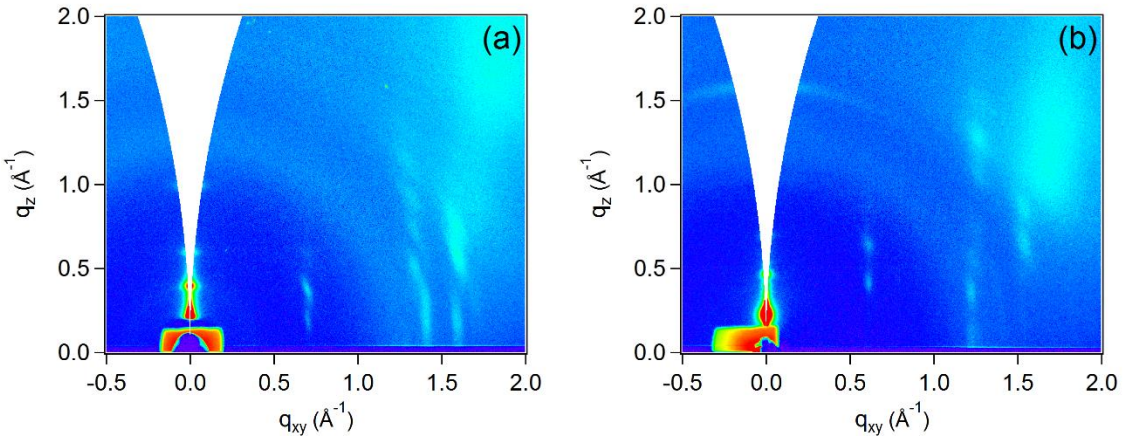

Figure 4-12. (a) As cast and (b) annealed GIWAXS of blade-coated **DPP-S**, measured at 120 °C.

4.1.5. Transport Properties in OFETs

To investigate the in-plane carrier transport of the materials, we fabricated OFET devices with LB deposited monolayers as the semiconductors. The amphiphilic molecules were deposited onto the gate dielectric at 20 mN/m compression pressure to ensure maximum coverage, and thus fully connected semiconducting pathways. As illustrated in Figure 4-13, the devices were fabricated in the bottom-gate top-contact architecture[175] in order to minimize disruption of the monolayers. The device results are shown in Figure 4-14 and summarized in Table S1. Overall, the mobility values obtained for these monolayer devices were on the order of 10^{-4} cm^2 V^{-1} s^{-1}, with an I_{on}/I_{off} ratio of 10^2. We had also fabricated LB deposited bilayer and multilayer devices and obtained performances comparable to the monolayer devices (Table 4-5). This further proved that the LB deposition condition shown above was successful in creating monolayers of high coverage and order, sufficient to provide 1-D horizontal carrier transport in OFET devices. Previously, a molecular perylene diimde-based LB monolayer OFET device achieved as high as 10^{-2} cm^2 V^{-1} s^{-1} carrier mobility.[242] It is important to note that unlike

the rigidly fused ring structure in the previous study, our **DPP-A** and **DPP-S** molecules are multi-ring systems with multiple carbon-carbon single bond connections. The higher degrees of freedom along the molecule backbones are likely the reason for the lower mobility. Nonetheless, we have successfully shown that OFET devices can be fabricated with monolayer D-A-D based semiconductors. The D-A-D molecular design allows for the fine-tuning of the ionization potential and electron affinity, which will facilitate the development of materials with ambipolar transport properties.

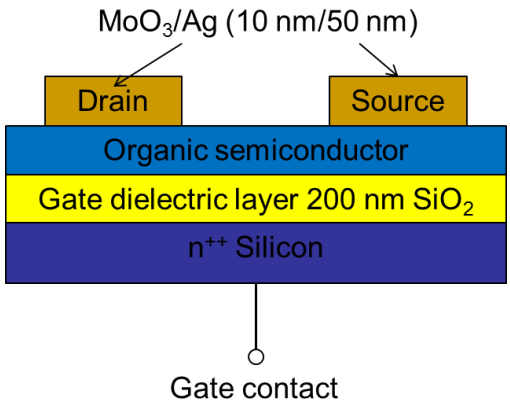

Figure 4-13. Bottom-gate top-contact architecture for monolayer LB-deposited OFET devices of **DPP-A** and **DPP-S**.

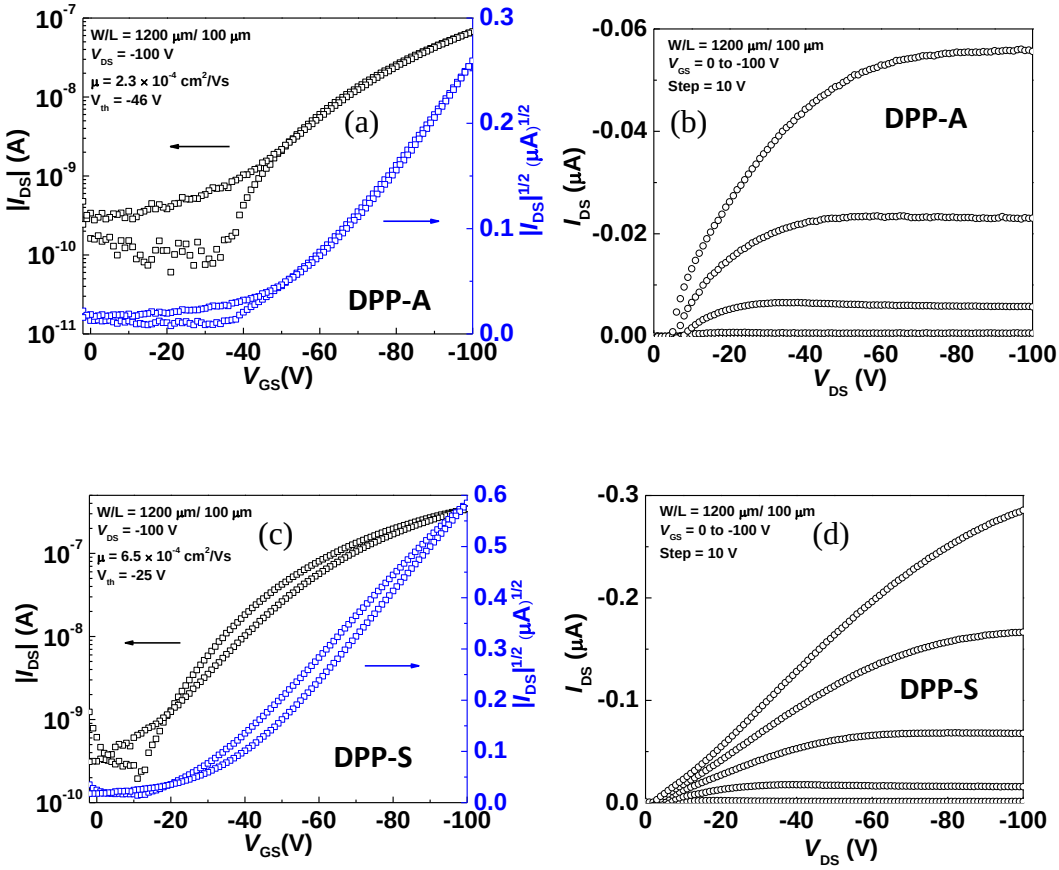

Figure 4-14. OFET device transfer curves of (a) **DPP-A** and (c) **DPP-S**. Output curves of (b) **DPP-A** and (d) **DPP-S**. Channel width and length were 1200 μm and 100 μm, respectively.

Table 4-5. Summary of LB and spin-coated OFET device performances of **DPP-A** and **DPP-S**. Channel width and length were 1200 mm and 100 mm, respectively. All device results were averaged over at least 4 devices.

	C_{in} (nF/cm^2)	S/D electrode	μ (cm^2 V^{-1} s^{-1})	V_{th} (V)	I_{ON}/I_{OFF}
DPP-A LB monolayer	16.5*	MoO_3/Ag	2.2 (±0.6) × 10^{-4} |R| > 0.99959	-42 (±5)	3.5 × 10^2
DPP-S LB monolayer	16.5*	MoO_3/Ag	4.5 (±2.0) × 10^{-4} |R| > 0.9998	-26 (±2)	5.4 × 10^2
DPP-A LB two layers	16.5*	MoO_3/Ag	1.1 (±0.1) × 10^{-4} |R| > 0.99984	-28 (±1)	1.1 × 10^2
DPP-S LB two layers	16.5*	MoO_3/Ag	6.5 (±1.1) × 10^{-6} |R| > 0.99883	-18 (±2)	1.2 × 10^1
DPP-A LB 12 layers	16.5*	MoO_3/Ag	6.6 (±1.2) × 10^{-4} |R| > 0.99993	-22 (±1)	1.3 × 10^3
DPP-S LB 4 layers	16.5*	MoO_3/Ag	2.1 (±0.1) × 10^{-4} |R| > 0.99965	-23 (±6)	2.0 × 10^2
DPP-A Spin-coated	16.5*	MoO_3/Ag	4.1 (±0.4) × 10^{-4} |R| > 0.99989	-2 (±1)	9.3 × 10^1

* Measured value on Si/SiO_2 wafer from the same batch

4.1.6. Molecule/PCBM OPV Device

BHJ OPV devices were fabricated using the two molecules as the donors and $PC_{61}BM$ as the acceptor. The blends of both glyme-containing molecules had high dielectric constants close to 5, which was not surprising since triglyme side chains had been shown to increase dielectric constant in DPP polymers and glyme-substituted PCBM.[87,243] Poor device performances in both molecules were a combination of low V_{oc}, J_{sc}, and FF as seen in Figure 4-15. Looking into the active layer morphologies illustrated by the AFM results in Figure 4-16, we discovered both blends of the molecules with $PC_{61}BM$ formed large domains. We have shown that these materials can self-assemble into ordered orientations from drop-casting depositions. These two molecules with polar

triglyme side chains also likely intermix poorly when blending with $PC_{61}BM$, leading to large-scale phase separations. Thus it is not surprising to observe these large domains hindering the diffusion of excitons to the donor-acceptor interface as well as efficient charge transfer and separation, resulting in low J_{sc} and FF, summarized in Table 4-6.

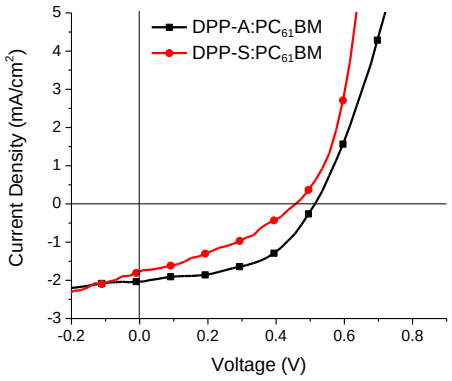

Figure 4-15. Current density-voltage characteristics of **DPP-A** and **DPP-S** OPV devices (ITO/PEDOT:PSS/active layer/Ca/Al device architecture).

Table 4-6. Summary of OPV device characteristics

	ε_r	J_{sc} (mA/cm^2)	V_{oc} (V)	FF (%)	η (%)
DPP-A:$PC_{61}BM$	4.94 ± 0.0	2.06 ± 0.14	0.53 ± 0.01	52.0 ± 4.5	0.57 ± 0.08
DPP-S:$PC_{61}BM$	4.98 ± 0.1	1.66 ± 0.12	0.44 ± 0.02	33.8 ± 0.9	0.25 ± 0.03

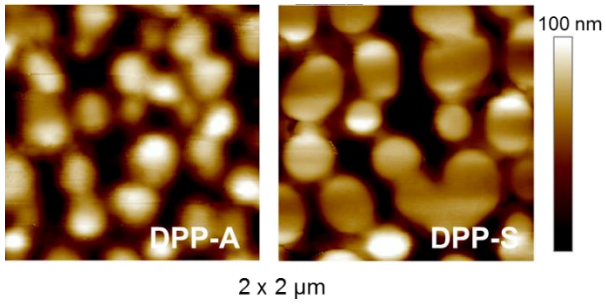

Figure 4-16. AFM height images of molecule:$PC_{61}BM$ blends. Large domains are visible in both active layers.

4.2. Summary

We have demonstrated the design, synthesis, and physical characterization of two amphiphilic DPP molecules. Their amphiphilic structures allowed for stable transfer of Langmuir-Blodgett mono- and multilayers, further improving their intermolecular order. LB monolayers of the molecules used as the semiconductors in organic field effect transistor devices showed mobility on the order of 10^{-4} cm^2 V^{-1} s^{-1}. Together with the bilayer photovoltaic devices, we highlight the application of ordered amphiphilic conjugated molecules in organic electronic applications, as well as show that Langmuir-Blodgett film formationcan be used as an effective deposition technique to study the fundamental impact of molecular order and packing in the field of organic electrons. Further exploration in LB deposited multilayers for the construction of the active layers in organic photovoltaics is currently underway to promote intermolecular order for the donor molecules and achieve sharp donor/acceptor interface in order to study the charge transfer mechanism in the devices.

4.3. Synthetic Details

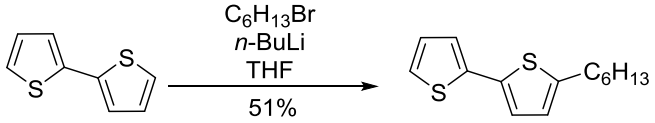

5-Hexyl-2,2′-bithiophene.[244] Bithiophene (5 g, 30 mmol) and anhydrous THF (25 mL) were added to a 100 mL round bottom flask. The mixture was cooled to -78 ˚C. *n*-BuLi (12.8 mL, 2.5 M in hexanes, 32 mmol) were added dropwise into the reaction mixture over 1 hour and stirred at -78 ˚C for an additional hour. A portion of 1-bromohexane (5.28 g, 32 mmol) was added dropwise. The reaction mixture was allowed to return to

room temperature and stirred for 16 hours. Water (10 mL) was added to quench the reaction. The crude mixture was extracted with Et_2O (25 mL), washed with water (2 × 25 mL), brine (25 mL) and dried over $MgSO_4$. Solvent was removed under reduced pressure. TLC indicated two close spots, potentially a mixture of mono- and dialkylated species. Purification *via* Kugelrohr distillation (0.5-1.0 mmHg) resulted in two main fractions at 100 ˚C and 150 ˚C. The latter fraction was collected as a clear oil (3.8 g, 15.2 mmol, 51%). ^{1}H NMR (300 MHz, $CDCl_3$) δ 7.20 (d, *J* = 1.2 Hz, 1H), 7.16 (d, *J* = 1.2 Hz, 1H), 6.98 (m, 2H), 6.66 (d, *J* = 3.9 Hz, 1H), 2.77 (t, *J* = 7.2 Hz, 2H), 1.67 (m, 2H) 1.28 (m, 10H), 0.87 (t, *J* = 6.6 Hz, 3H).

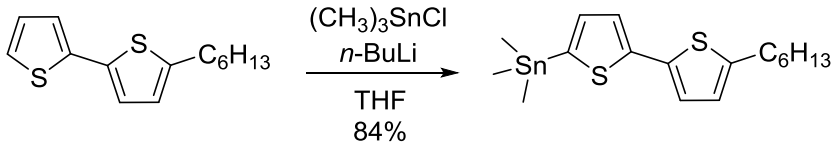

Trimethyl(5'-hexyl[2,2'-bithiophen]-5-yl)-stannane.[244] A portion of 2-hexyl-bithiophene (3.13 g, 12.5 mmol) and anhydrous THF (100 mL) were added to a 250 mL round bottom flask. The mixture was cooled to -78 ˚C. *n*-BuLi (6 mL, 2.5 M in hexanes, 15 mmol) were added dropwise into the reaction mixture over 15 minutes and stirred at -78 ˚C for an additional 2 hours. Trimethyltin chloride (16.3 mL, 1.0 M in THF, 16.3 mmol) was added dropwise over 15 minutes. The reaction mixture was allowed to return to room temperature and stirred for 12 hours. MeOH (30 mL) was added to quench the reaction. The crude mixture was extracted with Et_2O (100 mL), washed with water (2 × 50 mL), brine (50 mL) and dried over $MgSO_4$. Solvent was removed under reduced pressure to afford a clear oil (4.3 g, 10.5 mmol, 84%). This material was used without further purification in the following procedure to avoid destannylation.

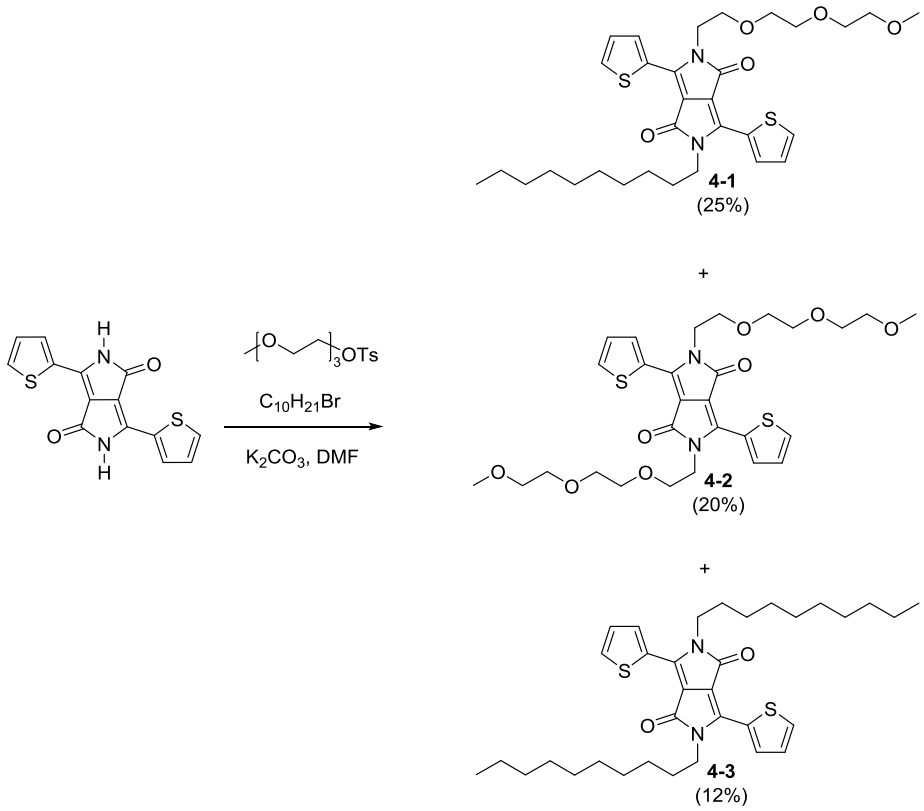

General Procedure for "one-pot" side chain attachment on DPP:[232]

To a 50 mL round bottom flask with potassium carbonate (0.41 g, 3 mmol) and DMF (10 mL), 3,6-bis-(thiophen-2-yl)-pyrrolo[3,4-c]pyrrole-1,4-dione (0.3 g, 1 mmol) was added in one portion. The mixture was heated to 120 ˚C. To the mixture, (2-(2-(2-Methoxyethoxy)ethoxy)ethoxy)p-toluenesulfonate (0.477 g, 1.5 mmol) was added dropwise over 15 minutes and first stirred for 12 hours. A portion of 1-bromodecane (0.374, 1.5 mmol) was then added to the reaction mixture and stirred for 8 hours. The reaction mixture was cooled to room temperature. Dichloromethane (30 mL) was added and the organic phase was washed with water (5 × 30 mL) and brine (1 × 30 mL) and dried over anhydrous $MgSO_4$. The mixture was filtered, concentrated, and purified by silica gel column chromatography with an eluent of 5% to 30% gradient of acetone in

dichloromethane. All products were obtained as maroon solid. Note: **3,6-bis(thiophen-2-yl)-N,N'-bis(decyl)-pyrrolo[3,4-c]pyrrole-1,4-dione (4-3)** was also isolated as a maroon solid (0.09 g, 12%).

2-Decyl-5-(2-(2-(2-methoxyethoxy)ethoxy)ethyl)-3,6-bis-(thiophen-2-yl)pyrrolo[3,4-c]pyrrole-1,4-dione (4-1). 0.17 g (25%). ^{1}H NMR (300 MHz, $CDCl_3$) δ 8.90 (dd, *J* = 3.9, 1.2 Hz, 1H), 8.76 (dd, *J* = 3.9, 1.2 Hz, 1H), 7.64 (dd, *J* = 5.1, 1.2 Hz, 1H), 7.61 (dd, *J* = 5.1, 1.2 Hz, 1H), 7.28 (dd, *J* = 5.1, 3.9 Hz, 1H), 7.24 (dd, *J* = 5.1, 3.9 Hz, 1H), 4.27 (t, *J* = 6.3 Hz, 2H), 4.05 (t, *J* = 6.9 Hz, 2H), 3.78 (t, *J* = 6.3 Hz, 2H), 3.68 – 3.42 (m, 10H), 3.33 (s, 3H), 1.81 – 1.67 (m, 2H), 1.50 – 1.12 (m, 14H), 0.86 (t, *J* = 6.7 Hz, 3H). ^{13}C NMR (75 MHz, $CDCl_3$) δ 161.45, 161.37, 140.32, 140.05, 135.33, 134.69, 130.84, 130.66, 129.72, 129.67, 128.62, 128.39, 108.16, 107.30, 71.88, 70.72, 70.54, 70.53, 68.95, 59.01, 42.19, 41.86, 31.87, 29.93, 29.51, 29.28, 29.23, 26.86, 22.67, 14.13. Note: some peaks in the ^{13}C NMR spectrum are overlapping and cannot be resolved. Anal. Calcd for $C_{31}H_{43}O_5N_2S_2$ (%): C, 63.45; H, 7.21; N, 4.77; S, 10.93. Found (%): C, 63.20; H, 7.13; N, 4.69; S, 10.80. HRMS (ESI, $[M+H]^+$) *m/z* calc'd for $C_{31}H_{43}O_5N_2S_2$ 587.2608; found, 587.2595.

2,5-Bis-(2-(2-(2-methoxyethoxy)ethoxy)ethyl)-3,6-bis-(thiophen-2-yl)-pyrrolo[3,4-c]pyrrole-1,4-dione (4-2).[232] 0.12 g (20%). ^{1}H NMR (300 MHz, $CDCl_3$) δ 8.75 (dd, *J* = 3.9, 1.1 Hz, 2H), 7.63 (dd, *J* = 5.0, 1.1 Hz, 2H), 7.25 (dd, *J* = 5.0, 3.9 Hz, 2H), 4.26 (t, *J* = 6.3 Hz, 4H), 3.78 (t, *J* = 6.3 Hz, 4H), 3.70 – 3.42 (m, 16H), 3.34 (s, 6H). ^{13}C NMR (75

MHz, $CDCl_3$) δ 161.51, 140.41, 134.75, 130.83, 129.64, 128.42, 107.84, 71.88, 70.70, 70.53, 70.52, 68.92, 59.02, 41.86.

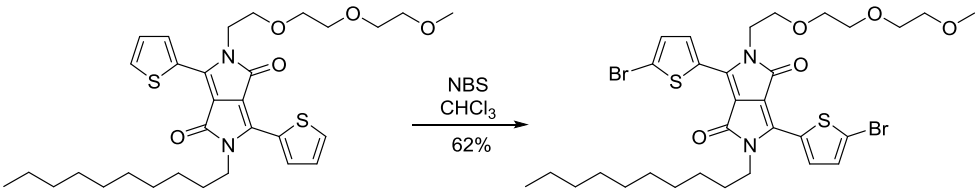

4-4

2-Decyl-5-(2-(2-(2-methoxyethoxy)ethoxy)ethyl)-3,6-bis-(5-bromo-thiophen-2-yl)pyrrolo[3,4-c]pyrrole-1,4-dione (4-4). To a 100 mL round bottom flask with Compound 4-1 (1.00 g, 1.7 mmol), chloroform (30 mL) was added in one portion. The mixture was cooled to 0 ˚C and kept in the dark. *N*-Bromosuccinimide (0.64 g, 3.6 mmol) was added in three portions over 10 minutes. The mixture was allowed to slowly return to room temperature and stirred for 16 hours in the dark. Water (100 mL) was added and the mixture was extracted with dichloromethane (3 × 20 mL). The combined organic extracts were dried over anhydrous MgSO4, filtered, and concentrated. The crude was purified by silica gel column chromatography with an eluent of 7:3 DCM:ethyl acetate. The product was obtained as a red waxy solid (0.80 g, 1.1 mmol, 62%). ^{1}H NMR (300 MHz, $CDCl_3$) δ 8.61 (d, *J* = 4.2 Hz, 1H), 8.49 (d, *J* = 4.2 Hz, 1H), 7.18 (d, *J* = 4.2 Hz, 2H), 7.15 (d, *J* = 4.1 Hz, 2H), 4.14 (t, *J* = 5.7 Hz, 2H), 3.92 (t, *J* = 6.6 Hz, 2H), 3.74 (t, *J* = 6.0 Hz, 2H), 3.67 – 3.41 (m, 8H), 3.31 (s, 3H), 1.67 (m, 2H), 1.52 – 1.10 (m, 14H), 0.85 (t, *J* = 6.6 Hz, 3H). ^{13}C NMR (75 MHz, $CDCl_3$) δ 161.01, 160.90, 139.10, 139.04, 135.39, 134.81, 131.59, 131.29, 131.15, 130.99, 119.28, 119.14, 108.12, 107.34, 71.88, 70.76, 70.55, 70.51, 68.92, 59.00, 42.22, 42.20, 31.86, 29.92, 29.49, 29.46, 29.27, 29.16, 26.80, 22.66, 14.12. Note: some peaks in the ^{13}C NMR spectrum are overlapping and

cannot be resolved. Anal. Calcd for $C_{31}H_{41}O_5N_2Br_2S_2$ (%): C, 50.01; H, 5.42; N, 3.76; S, 8.61. Found (%): C, 50.45; H, 5.67; N, 3.78; S, 8.63. HRMS (ESI, $[M+H]^+$) *m/z* calc'd for $C_{31}H_{41}O_5N_2Br_2S_2$ 743.0818; found, 743.0810.

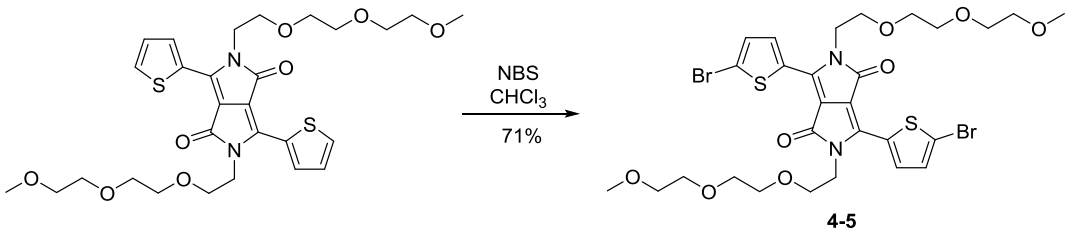

2,5-Bis-(2-(2-(2-methoxyethoxy)ethoxy)ethyl)-3,6-bis-(5-bromo-thiophen-2-yl)-pyrrolo[3,4-c]pyrrole-1,4-dione (4-5).[232] The synthesis of Compound 4-5 followed the same procedure as the synthesis of Compound 4-4 with the following starting materials: 2 (1.00 g, 1.7 mmol), *N*-Bromosuccinimide (0.66 g, 3.7 mmol), and chloroform (30 mL). The product was obtained as a red waxy solid (0.90 g, 71%). ^{1}H NMR (300 MHz, $CDCl_3$) δ 8.49 (d, *J* = 4.1 Hz, 2H), 7.20 (d, *J* = 4.2 Hz, 2H), 4.17 (t, *J* = 5.9 Hz, 4H), 3.77 (t, *J* = 5.9 Hz, 4H), 3.70 – 3.43 (m, 16H), 3.35 (s, 6H). ^{13}C NMR (75 MHz, $CDCl_3$) δ 160.81, 139.04, 134.39, 130.92, 130.63, 118.87, 107.49, 71.44, 70.31, 70.11, 70.08, 68.47, 58.58, 41.79.

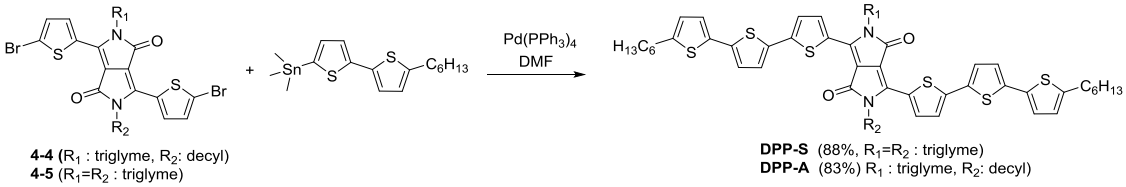

General Procedure for Stille Cross-coupling of Amphiphilic DPP Molecules:[232]

To a 35 mL microwave vial Compound 4-4 or Compound 4-5 (0.5 mmol), 5'-hexyl-bithiophen-2-yl stannane (0.52 g 1.25 mmol), tetrakis(triphenylphosphine)palladium(0) (46 mg, 0.04 mmol, 8 mol%), and DMF (6 mL) were added inside a glovebox under

argon. The reaction tube was sealed, removed from the glovebox. Microwave reaction was performed in a CEM Corporation Discover SP microwave synthesizer. The reaction mixture was heated to 80 ˚C and stirred for 1 hour. After returning to room temperature and atmospheric pressure, the crude was precipitated into methanol (50 mL). The crude solid was filtered onto a PTFE membrane. The solid was dissolved in chloroform (20 mL) and the mixture was heated to 60 ˚C and stirred for 12 hours with a spatula-tip amount of diethyldithiocarbamic acid diethylammonium salt (CAS# 2391-78-8) to scavenge the palladium catalyst. Workup and purification procedures and structural characterizations for each molecule are included below.

DPP-A. The mixture was precipitated into methanol (50 mL) and filtered onto a PTFE membrane. The precipitates were purified in a recycling silica column with ethyl acetate as the eluent. Once all impurities were eluted, a solution of 1:1 DCM:ethyl acetate was used to elute the product from the silica column. The product was obtained as a dark blue solid (444 mg, 0.41 mmol, 82%). ^{1}H NMR (300 MHz, $CDCl_3$, ppm): δ 8.89 (d, *J* = 4.2 Hz, 1H), 8.80 (d, *J* = 4.2 Hz, 1H), 8.80 (d, *J* = 4.2 Hz, 2H), 7.15 (dd, *J* = 6.6, 4.5 Hz, 2H), 7.12 (dd, *J* = 5.9, 3.6 Hz, 2H), 6.95 (d, *J* = 3.3 Hz, 4H), 6.65 (d, *J* = 3.6 Hz, 2H), 4.26 (t, *J* = 6.3 Hz, 2H), 4.02 (t, *J* = 6.0 Hz, 2H), 3.85-3.75 (m, 2H), 3.70 – 3.43 (m, 6H), 3.31 (s, 3H), 2.76 (t, *J* = 7.5 Hz, 4H), 1.90-1.55 (m, 6H), 1.55-1.17 (m, 28H), 1.00-0.80 (m, 9H). ^{13}C NMR (75 MHz, $CDCl_3$) 161.04, 160.98, 146.32, 146.25, 142.69, 142.50, 138.89, 138.77, 138.56, 134.03, 133.98, 133.96, 133.88, 127.89, 127.68, 125.76, 124.93, 124.39, 124.25, 123.89, 123.83, 123.66, 123.64, 108.39, 107.64, 71.89, 70.79, 70.57, 58.99, 31.93, 31.57, 31.49, 30.21, 29.61, 29.35, 29.28, 28.81, 26.96, 22.71, 22.59, 14.15,

14.10. Note: some peaks in the ^{13}C NMR spectrum are overlapping and cannot be resolved. Anal. Calcd for $C_{59}H_{74}N_2O_5S_6$ (%): C, 65.39; H, 6.88; N, 2.52; S, 17.75. Found (%): C, 65.65; H, 6.76; N, 2.66; S, 17.45. HRMS (MALDI-TOF, $[M+H]^+$) *m/z* calc'd for $C_{31}H_{41}O_5N_2Br_2S_2$ 1083.4000; found, 1083.3983.

DPP-S. The mixture was precipitated into methanol (50 mL) and filtered onto a PTFE membrane. The precipitates were purified in a recycling silica column with dichloromethane as the eluent. Once all impurities were eluted, a solution of 9:1 DCM:acetone was used to elute the product from the silica column. The product was obtained as a dark blue solid (480 mg, 0.44 mmol, 88%). ^1H NMR (300 MHz, $CDCl_3$, ppm): δ 8.79 (d, *J* = 4.2 Hz, 2H), 7.19 (d, *J* = 3.9 Hz, 2H), 7.17 (d, *J* = 3.9 Hz, 2H), 6.99 (d, *J* = 3.9 Hz, 2H), 6.98 (d, *J* = 3.9 Hz, 2H), 6.67 (d, *J* = 3.6 Hz, 2H), 4.28 (t, *J* = 6.2 Hz, 4H), 3.80 (t, *J* = 6.3 Hz, 4H), 3.56 (m, 16H), 3.32 (s, 6H), 2.78 (t, *J* = 7.6 Hz, 4H), 1.79 – 1.53 (m, 4H), 1.45 – 1.15 (m, 12H), 0.96 – 0.79 (t, *J* = 6.8 Hz, 6H). ^{13}C NMR (75 MHz, $CDCl_3$) δ 161.20, 146.35, 142.73, 138.99, 138.91, 136.30, 133.99, 133.93, 127.82, 125.97, 124.97, 124.34, 123.92, 123.73, 108.12, 71.89, 70.78, 70.57, 69.04, 58.99, 41.98, 31.56, 31.50, 30.21, 28.78, 22.58, 14.09. Anal. Calcd for $C_{56}H_{68}N_2O_8S_6$ (%): C, 61.73; H, 6.29; N, 2.57; S, 17.66. Found (%): C, 61.98; H, 6.30; N, 2.67; S, 17.62. HRMS (ESI, $[M]^+$) *m/z* calc'd for $C_{31}H_{41}O_5N_2Br_2S_2$ 1088.3290; found, 1088.3276.

CHAPTER 5

LOW ENERGY GAP POLYMERS BASED ON ACCEPTOR MOIETIES

This chapter presents a family of all-accepting polymers, which are designed to be used as the acceptor in the donor-acceptor active layer of organic photovoltaics. Through the utilization of accepting building blocks with different properties (i.e. planarity of backbones and electron-rich/poor moieties), the intention was to improve the organic solar cell power conversion efficiency by recognizing the intrinsic physical and chemical properties of the polymers, which in turn provides ideal intermixing between the donor and the acceptor polymers as well as proper alignment of the tunable energy levels of the acceptors with regard to those of the donors. Accepting polymers should possess deep electron affinities to allow enough energetic offsets and promote charge transfer from the donor. They should also have reduced bandgaps for enhanced absorptions of the low energy photons in the visible and infrared regions of the sun radiation. The polymers should also have a electron mobility of at least 10^{-4} cm^2 V^{-1} s^{-1} to ensure a balance of charge mobility between the donor and the acceptor, and to lower the recombination rate after charge separation. The morphological and transport properties of these materials will be correlated to device performances to highlight the importance of structure-property relationship in designing materials for specific applications in organic electronics.

5.1. Highly Accepting Polymer Synthesis Based on Electron-deficient Moieties

While $PC_{61}BM$ is an excellent universal electron acceptor with a strong tendency for aggregation and crystallization, its weak absorption in the visible and near-IR regions may limit its potential in further improving the power conversion efficiency in OPVs. Researchers have started using another fullerene derivative, $PC_{71}BM$, with a stronger absorption in the visible region than $PC_{61}BM$ and in most cases are able to improve OPV performance. However, using fullerene derivatives prohibits the tunability of the frontier energy levels, which in turn limits the ability to absorb light across the broad solar spectrum and adjust the energetic offset between the donor and the acceptor. Accepting polymers offer tunable energy levels with the utilization of different electron-deficient moieties and functional groups. Many of them also have absorption profiles extending well into the near-IR region, which will enhance the absorption of low energy photons.

Four low bandgap polymers with strong light absorption properties constructed using acceptor moieties isoindigo, thienoisoindigo, diketopyrrolopyrrole, and thienopyrrolodione are synthesized *via* direct arylation polymerizations. As discussed in Chapter 2, C-H activation has many advantages over the traditional cross-coupling reactions for conjugated polymer synthesis including the elimination of organometallic reagents such as toxic tin precursors and wastes, the reduction of synthetic steps, and the improvement of atom efficiency.

5.1.1. Direct Arylation Polymerization of P(iI-TPD), P(iI-DPP), P(TiI-TPD), and P(TiI-DPP)

Four accepting polymers were synthesized by C-H activation polymerization from four accepting monomer moieties: isoindigo, thienoisoindigo, thienopyrrolodione, and

diketopyrrolopyrrole. Their syntheses were mentioned in Chapter 3. Isoindigo is chosen as the brominated monomers since its precursor materials, 6-bromooxindole and 6-bromoisatin, are commercially available, and the alkylated isoindigo monomers are synthesized in two quick steps. Due to its structural similarity to isoindigo, thienoisoindigo was also selected to be the brominated monomer.

The dibromo-functionalized isoindigo and thienoisoindigo were reacted with the unfunctionalized thienopyrrolodione and diketopyrrolopyrrole to afford alternating copolymers **P(iI-TPD)**, **P(iI-T-DPP-T)**, **P(TiI-TPD)**, **and P(TiI-T-DPP-T)** as shown in Scheme 5-1. Tetrahydrofuran (THF) has a boiling point of 66 ˚C in ambient conditions. To increase reactivity, all C-H activation reactions in this chapter were done under high pressure within a pressure vessel or a Schleck flask, which allows THF to be heated to 120 ˚C. Hermann's catalyst (Scheme 5-2) was chosen as the palladium catalyst due to its excellent reactivity, air and thermal stability. The bulky tris(o-methoxyphenyl)phosphine ligand (Scheme 5-2) ensures the stability of the catalyst by providing extra coordination with the electron-rich methoxy groups.[152] This particular catalyst, ligand, and solvent combination has been optimized to create alternate copolymers based on electron-deficient moieties.[134,147,151,245] The reaction time lasted for 24 hours, much shorter than usual 72 to 120 hours required for Stille and Suzuki polymerizations. After the polymerization was over, the reaction mixture was cooled to 60 ˚C and stirred for 12 hours with a spatula-tip amount of diethyldithiocarbamic acid diethylammonium salt to scavenge the palladium catalyst. The mixture was precipitated into methanol and filtered. The crude polymer underwent soxhlet extraction and either the dichloromethane or

chloroform portion was collected and concentrated under reduced pressure, precipitated into methanol, and collected on a PTFE membrane.

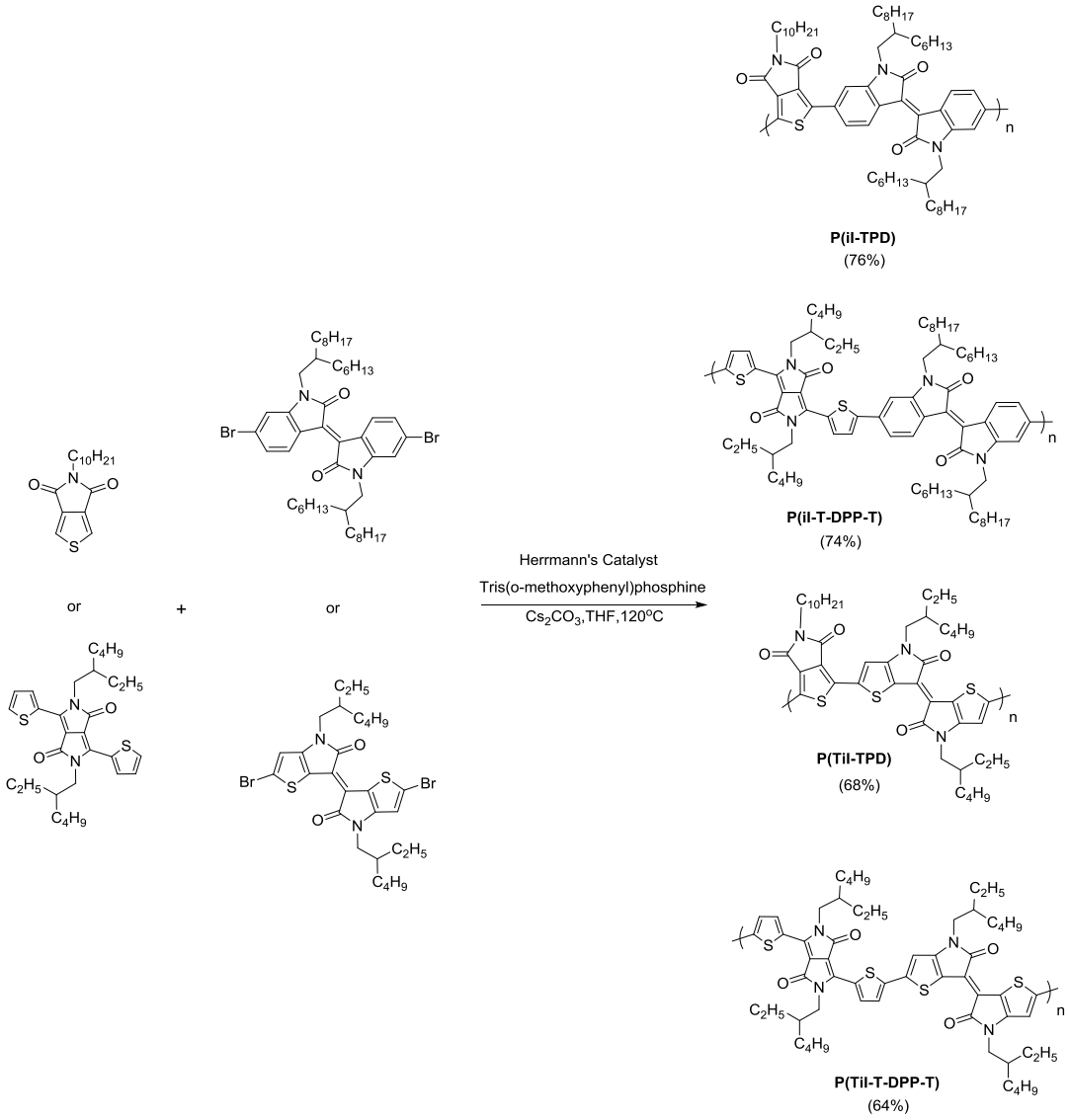

Scheme 5-1. C-H activation polymerizations of accepting polymers **P(iI-TPD)**, **P(iI-T-DPP-T)**, **P(TiI-TPD)**, **and P(TiI-T-DPP-T)**

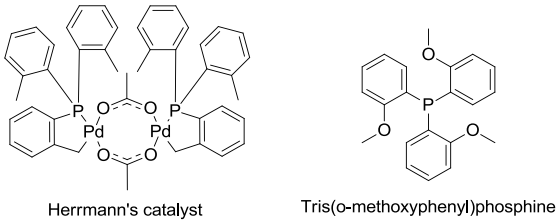

Scheme 5-2. Structures of Hermann's catalyst and tris(o-methoxyphenyl)phosphine

It is important to note that a side reaction may occur at the 3- and 4-positions on the thiophene rings attached to the non-functionalized DPP moiety, even when they are less reactive than the 2- and 5-positions. This π-reactivity for electrophilic substitution reaction can be explained by the resonance structures in Scheme 5-3. All resonance structures contain a zwitterionic positive charge on the sulfur atom and a negative charge on either the α- or the β-carbons. The regioselectivity of the thiophene electrophilic aromatic substitution towards the α-position over the β-position suggests that the resonance structures with the negative charges on the α-positions contribute more towards the overall hybrid representation. It is generally believed that the proximity between the positive sulfur atom and the π-anions at the α-carbon results in a more stable structural configuration.[137]

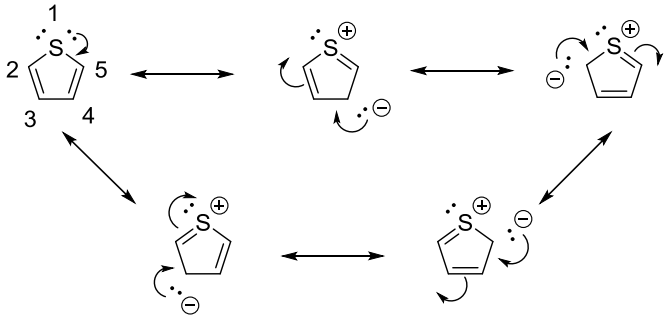

Scheme 5-3. Thiophene and its resonance structures

Molecular weights and dispersities were measured using a high-temperature 1,3,4-trichlorobenzene GPC calibrated versus polystyrene standards. **P(iI-TPD)**, **P(iI-T-DPP-T)**, **P(TiI-TPD)**, and **P(TiI-T-DPP-T)** exhibit M_n ($Đ_M$) of 10.3 kg/mol (1.55), 11.7 kg/mol (2.31), 14.0 kg/mol (1.64), and 11.5 kg/mol (1.44) respectively. The DPP polymers have $Đ_M$ and solubilities similar to those of TPD polymers, indicating that β-defects during polymerization should not be of concern in this C-H activation reaction.

5.1.2. Optoelectronic Properties of P(iI-TPD), P(iI-T-DPP-T), P(TiI-TPD), and P(TiI-T-DPP-T)

5.1.2.1. UV-Vis-NIR Absorption

The thin film absorption onsets of **P(TiI-TPD)**, and **P(TiI-T-DPP-T)** are 1145 nm and 1280 nm respectively. Compared to **P(iI-TPD)** (712 nm) and **P(iI-T-DPP-T)** (923 nm), the thienoisoindigo polymers have significant red-shifted onsets. The more electron-rich thiophene segment in the thienoisoindigo structure causes an increase in the ionization potentials. The absorbance of **P(iI-TPD)** and **P(iI-T-DPP-T)** extend through the visible region as shown in Figure 5-1a and 5-1b. In the case of **P(iI-T-DPP-T)**, its absorption extends into the near infrared and its thin film spin-cast from chloroform had an absorbance peak at 837 nm, bathochromically–shifted from its absorption in chloroform solution (peak at 816 nm). This bathochromic shift in absorbance is a characteristic of increased intermolecular interactions in the solid state due to an enhanced crystallinity and/or aggregation. Similar behaviors were observed for the absorption spectra of **P(TiI-TPD)** (from 770 to 785 nm) and **P(TiI-T-DPP-T)** (from 910 nm to 925 nm) in Figure 5-1c and 5-1d. These aggregate and/or crystalline regions of the films also contribute to light scattering, leading to "non-zero" baselines for **P(iI-T-DPP-T)**, **P(TiI-TPD)**, and **P(TiI-T-DPP-T)** at the low energy edge of the spectra.

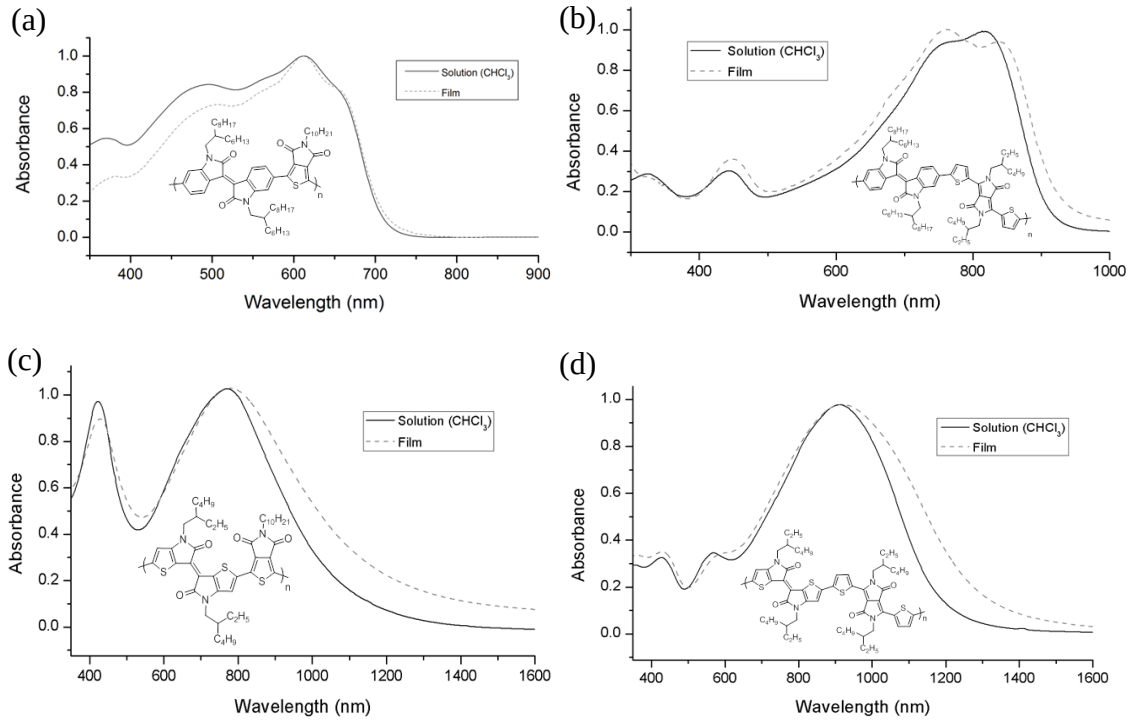

Figure 5-1. UV-Vis absorption spectra of (a) **P(iI-TPD)** (b) **P(iI-T-DPP-T)** (c) **P(TiI-TPD)** (d) **P(TiI-T-DPP-T)** in chloroform solutions and thin films on glass substrates.

5.1.2.2. Cyclic Voltammetry and Differential Pulse Voltammetry

The redox properties of each polymer in their thin-film were investigated using CV and DPV. All the oxidative CVs showed large drops in currents, indicative of non-reversible and unstable oxidative processes. In contrast, all polymers showed quasi-reversible reductive processes (Figure 5-2 to 5-7) with stable and reversible reductive scans, a reflection of their intended designs as strong acceptors. The reductive onsets for **P(iI-TPD)** and **P(iI-T-DPP-T)** shown in Figure 5-3 and 5-4 were estimated to be -0.94 V and -1.00 V, respectively. Converting these potentials calibrated against the Fc/Fc^{+} standard (-5.12 eV) in energy values against vacuum, the EAs were calculated to be -4.18 eV for **P(iI-TPD)** and -4.12 eV for **P(iI-T-DPP-T)**. Using the optical energy gap values obtained from the UV-Vis absorption onsets, the IPs for **P(iI-TPD)** and **P(iI-T-DPP-T)**

were calculated to be -5.92 eV and -5.46 eV respectively. The IP of **P(iI-TPD)** was 0.46 eV higher than that of **P(iI-T-DPP-T)**, which was not surprising due to the two electron-rich thiophene rings flanked to both sides of the DPP unit reducing the IP of **P(iI-T-DPP-T)**. Similarly, the IP of **P(TiI-TPD)** was 0.30 eV higher than that of **P(TiI-T-DPP-T)**.

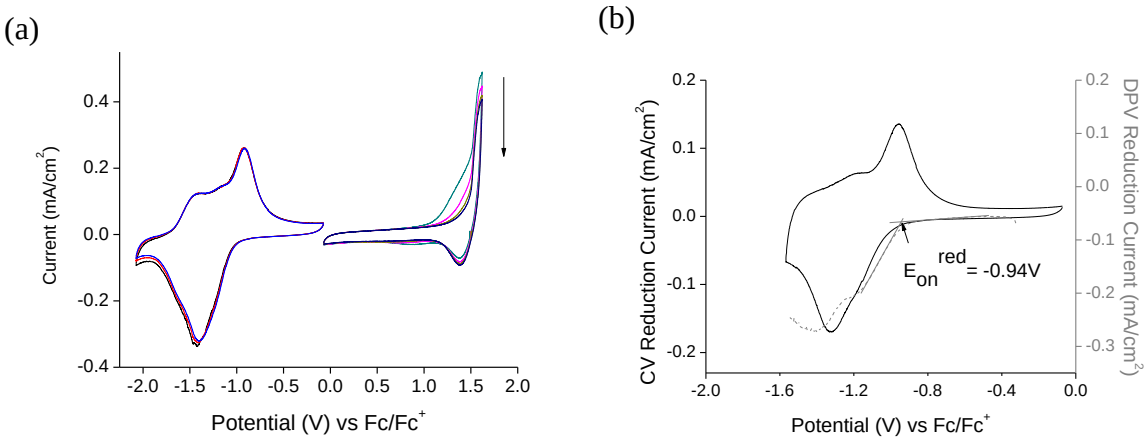

Figure 5-2. (a) Cyclic voltammetry and (b) differential pulse voltammetry of **P(iI-TPD)**. Measurements were performed in 0.5 M $TBAPF_6$/acetonitrile solution with a platinum counter electrode and a Ag/Ag^+ reference electrode.

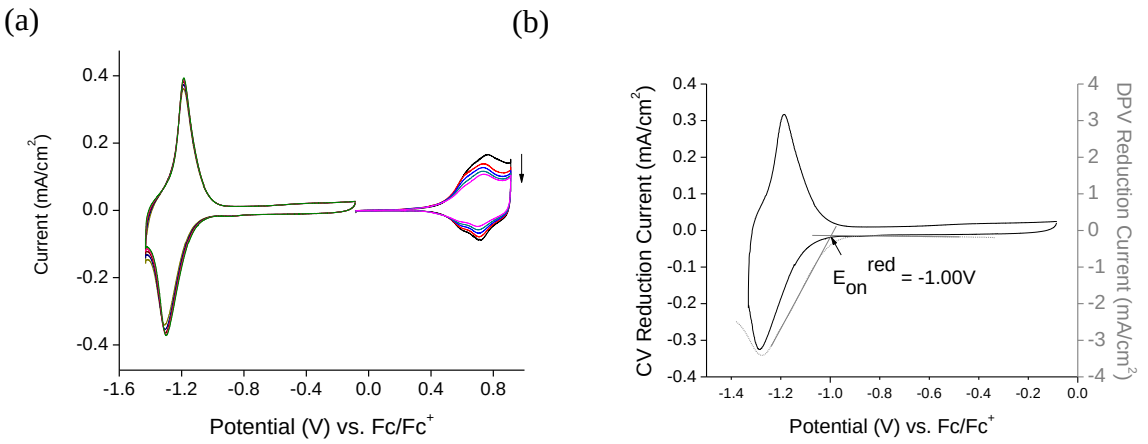

Figure 5-3. (a) Cyclic voltammetry and (b) differential pulse voltammetry of **P(iI-T-DPP-T)**. Measurements were performed in 0.5 M $TBAPF_6$/acetonitrile solution with a platinum counter electrode and a Ag/Ag^+ reference electrode.

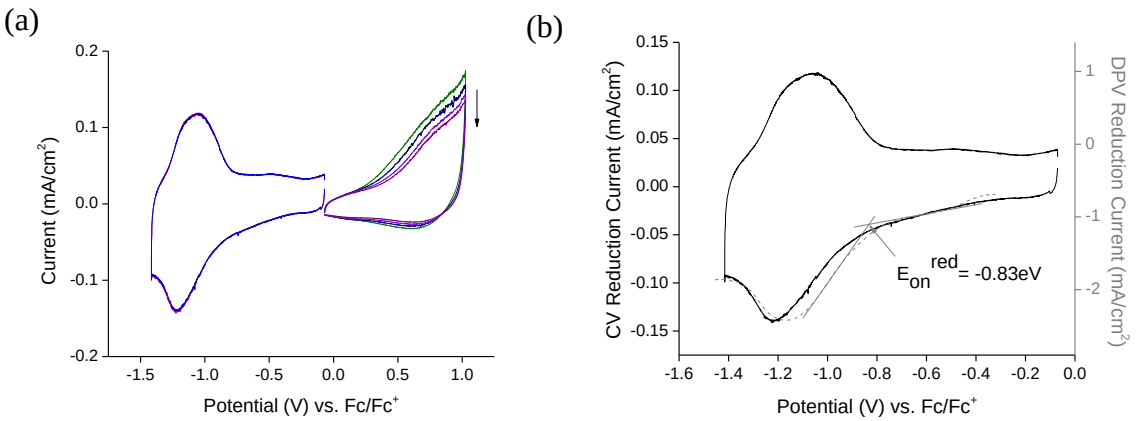

Figure 5-4. (a) Cyclic voltammetry and (b) differential pulse voltammetry of **P(TiI-TPD)**. Measurements were performed in 0.5 M $TBAPF_6$/acetonitrile solution with a platinum counter electrode and a Ag/Ag^+ reference electrode.

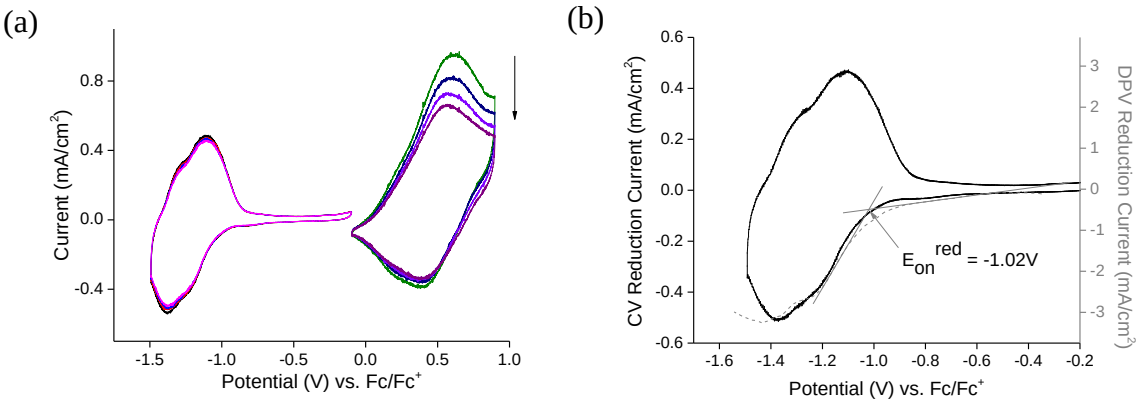

Figure 5-5. (a) Cyclic voltammetry and (b) differential pulse voltammetry of **P(TiI-T-DPP-T)**. Measurements were performed in 0.5 M $TBAPF_6$/acetonitrile solution with a platinum counter electrode and a Ag/Ag^+ reference electrode.

A similar comparison could also be made between iI and TiI, in which the phenyl units in iI were replaced by thienyl units in TiI. The more electron-rich TiI lowers the IPs of **P(TiI-TPD)** (by 0.55 eV) and **P(TiI-T-DPP-T)** (by 0.39 eV) compared to those of **P(iI-TPD)** and **P(iI-T-DPP-T)**, respectively. The optical and electrochemical characterizations of polymers are summarized in Table 5-1. A graphical representation of the frontier energy levels for each polymer is shown in Figure 5-6.

Table 5-1. Summary of optoelectronic properties of **P(iI-TPD)**, **P(iI-T-DPP-T)**, **P(TiI-TPD)**, and **P(TiI-T-DPP-T)**.

Polymer	IP* [eV]	EA* [eV]	E_g^{opt} [eV]	λ_{max}^{sol} (nm)	λ_{on}^{sol} (nm)	λ_{max}^{film} (nm)	λ_{on}^{film} (nm)
P(iI-TPD)	-5.92	-4.18	1.74	612	705	612	712
P(iI-T-DPP-T)	-5.46	-4.12	1.34	763, 816	925	760, 836	923
P(TiI-TPD)	-5.37	-4.29	1.08	422, 767	1069	430, 779	1145
P(TiI-T-DPP-T)	-5.07	-4.10	0.97	910	1192	918	1280

*EA values were obtained from electrochemical studies. IP values were obtained by subtracting $E_{gap}^{optical}$ from EA.

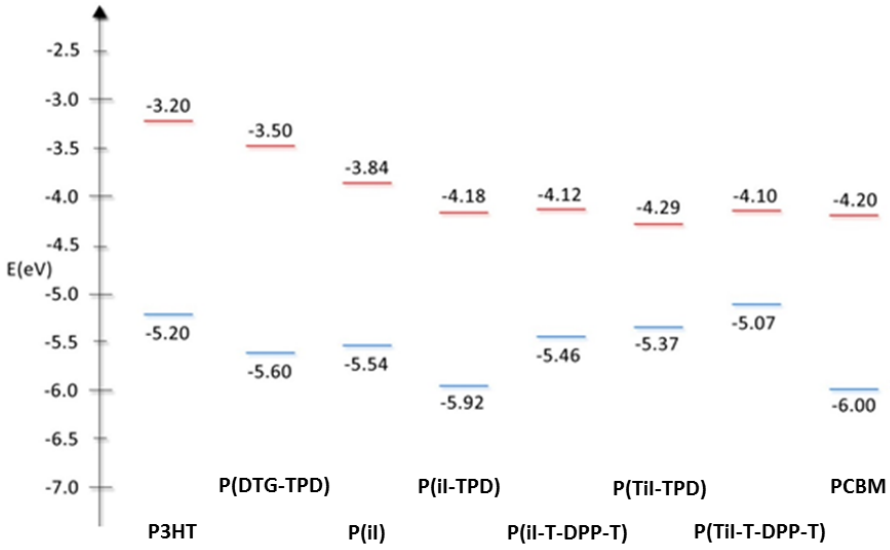

Figure 5-6. Frontier energy level diagram for **P(iI-TPD)**, **P(iI-T-DPP-T)**, **P(TiI-TPD)**, and **P(TiI-T-DPP-T)** and other related polymers with respect to P3HT and PCBM. *Note: P3HT[227] and PCBM[246] energy levels are reported from the literature. Energy levels are 5.12 eV relative to vacuum (assuming the energy of saturated calomel electrode (SCE) is 4.7 eV vs vacuum and the energy of Fc/Fc^+ is +0.42 V vs SCE.

5.1.3. OPV and OFET Device Performances

Encouraged by their favorable energetic offsets, as shown in Figure 5-6, and their complementary absorption characteristics to P3HT, the accepting polymers **P(iI-TPD)**, **P(iI-T-DPP-T)**, **P(TiI-TPD)**, and **P(TiI-T-DPP-T)** were used to fabricate conventional BHJ devices in all-polymer solar cells. Unfortunately, none of the devices resulted in diode responses. As presented in Grand's dissertation,[171] a large entropic barrier in

polymer:polymer mixing creates a high degree of phase separation and large domain size in the active layer blend. AFM image in Figure 5-7 shows that the active layer of P3HT:Polyisoindigo has domain size on the order of 100 nm, as opposed to 10 nm required for optimally interconnected charge transport pathway.[227] It is reasonable to expect that the poor polymer:polymer intermixing in this family of polymers contributes to their detrimental device performances.

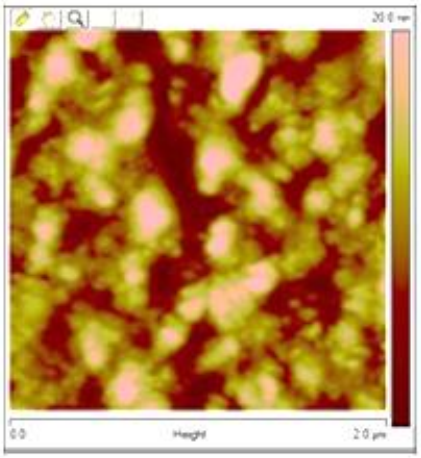

Figure 5-7. AFM height image of 1:1 blend of P3HT:Polyisoindigo. Large domains as a result of poor polymer:polymer mixing leads to poor OPV device performance. The image is 2 × 2 um., height scale is 20 nm. (Reproduced with permission from reference [227].)

To further understand this class of materials, charge mobility was measured using field effect transistor method. Devices were fabricated on n-doped silicon with 300 nm thermally grown silicon dioxide as the dielectric layer. Gold electrodes (60 nm) were evaporated onto the substrates with chromium as the adhesion layers. Polymers were spin-coated from 5 mg/mL chloroform solutions. Hole mobility and electron mobility were measured after devices were thermally annealed at 90 ˚C. Unexpectedly, electron mobility was not observed in these polymers and only hole mobility was measurable for **P(iI-T-DPP-T)** (4.35×10^{-6} cm^2 V^{-1} s^{-1}) and **P(TiI-T-DPP-T)** (6.96×10^{-5} cm^2 V^{-1} s^{-1}).

This observation further confirms our results on the all-polymer OPV devices and is consistent with Grand's observation[171] in these iI, TiI, TPD, and DPP-based accepting polymers.

In conclusion, we highlighted the synthesis of four new accepting polymers *via* C-H activation polymerization, which reduced the number of synthetic steps necessary to make these materials and eliminated the generation of toxic precursors and wastes common to the Stille reaction. While the polymers have broad absorptions in the visible region of the light spectrum and low absorption onset energies, their performances as acceptors in BHJ OPV devices were hindered by large phase separation in the all-polymer blends as well as low electron mobility. To further optimize the active layer morphology, processing conditions such as solvent choice and annealing condition can be altered. Structure-property design for new acceptor will be discussed in Chapter 6 to highlight the recent progress on the development of non-fullerene acceptors.

5.2. Synthetic Details

The synthetic details for this chapter's monomers, isoindigo, thienoisoindigo, thienopyrrolodione, and diketopyrrolopyrrole, are presented in Chapter 3 beginning on page 104.

General procedures of C-H activation polymerizations[147] for P(iI-TPD), P(iI-T-DPP-T), P(TiI-TPD), and P(TiI-T-DPP-T):

The dibrominated monomer (0.5 mmol), the dihydrogen monomer (0.5 mmol), Hermann's Catalyst (38 mg, 4 mol% of catalyst or 8 mol% of Pd), tris(o-methoxyphenyl)phosphine (28 mg, 8 mol%), and cesium carbonate (325.82 mg, 1 mmol) were added into a 50 mL Schlenk flask with a magnetic stirring bar. The vessel was sealed and purged with argon for 3 pump-fill cycles. THF (2 mL) was added and the reaction was heated to 120 °C and stirred for 24 hours. The reaction mixture was cooled to 60 ˚C and stirred for 12 hours with a spatula-tip amount of diethyldithiocarbamic acid diethylammonium salt (CAS# 2391-78-8) to scavenge the palladium catalyst. The mixture was precipitated into methanol (20 mL) and filtered onto a PTFE membrane. The crude polymer underwent soxhlet extractions with methanol, acetone, hexanes, dichloromethane, and chloroform. Either the dichloromethane or chloroform portion was concentrated under reduced pressure and precipitated into methanol, filtered onto a PTFE membrane, and collected.

Poly*(E)*-6,6′-bis(2-hexyldecyl)-[3,3′-biindolinylidene]-2,2′-dione-alt-1,3-(5-decyl-4H-thieno[3,4-c]pyrrole4,6(5H)-dione P(iI-TPD). Maroon solid (235 mg, 76% $CHCl_3$ fraction). Mn: 10.3 kg/mol , $Đ_M$: 1.55 (1, 2, 4-trichlorobenzene). Anal. Calcd for

$C_{64}H_{93}N_3O_4S$ C: 76.68%, H: 9.55%, N: 4.19%, S: 3.20%. Found C: 76.01%, H: 9.10%, N: 4.08%, S: 3.42%.

Poly(*E*)-6,6′-bis(2-hexyldecyl)-[3,3′-biindolinylidene]-2,2′-dione-alt-5,5’-bis (thiophen-2-yl)-N,N’-bis(2-ethylhexyl)-pyrrolo[3,4-c]pyrrole-1,4-dione P(iI-T-DPP-T). Maroon solid (218 mg, 74% CH_2Cl_2 fraction). Mn: 11.7 kg/mol, $Đ_M$: 2.31 (1, 2, 4-trichlorobenzene). Anal. Calcd for $C_{78}H_{110}N_4O_4S_2$ C: 75.93%, H: 9.15%, N: 4.54%, S: 5.20%. Found C: 75.59%, H: 8.87%, N: 4.49%, S: 5.17%.

Poly(*E*)-4,4’-bis(2-ethylhexyl)-[6,6’-bithieno[3,2-b]pyrrolylidene]-5,5’(4H,4’H)-dione-alt-1,3-(5-decyl-4H-thieno[3,4-c]pyrrole4,6(5H)-dione P(TiI-TPD). Maroon solid (104 mg, 68% CH_2Cl_2 fraction). Mn: 14.0 kg/mol, $Đ_M$: 1.64 (1, 2, 4-trichlorobenzene). Anal. Calcd for $C_{44}H_{57}N_3O_4S_3$ C: 66.88%, H: 7.53%, N: 5.32%, S: 12.17%. Found C: 66.49%, H: 7.34%, N: 5.02%, S: 12.53%.

Poly(*E*)-4,4’-bis(2-ethylhexyl)-[6,6’-bithieno[3,2-b]pyrrolylidene]-5,5’(4H,4’H)-dione-alt-5,5’-bis(-thiophen-2-yl)-N,N’-bis(2-ethylhexyl)-pyrrolo[3,4-c]pyrrole-1,4-dione P(TiI-T-DPP-T). Maroon solid (98 mg, 64% CH_2Cl_2 fraction). Mn: 11.5 kg/mol, $Đ_M$: 1.44 (1, 2, 4-trichlorobenzene). Anal. Calcd for $C_{58}H_{74}N_4O_4S_4$ C: 68.20%, H: 7.50%, N: 5.48%, S: 12.55%. Found C: 68.43%, H: 7.40%, N: 5.40, S: 12.52%.

CHAPTER 6

OUTLOOK AND PERSPECTIVES OF ORGANIC PHOTOVOLTAICS AND ORGANIC ELECTRONICS

Global energy consumption has grown steadily since the beginning of the Industrial Revolution. The rapid growth of developing economies such as China, India, and Brazil will be the main contributors to the 48% predicted increase in world energy demand between 2012 and 2040. Concerns over the volatility of oil prices, the limited reserves, and the environmental impact of fossil fuels have led to the acceleration of renewable energy development. Compared to other alternative energy technologies such as wind, hydropower, geothermal, and nuclear, solar energy presents a greater promise for the future due to the sun being the most abundant energy source and its utilization generating the least harmful impact on the environment.[247] One of the most important factors determining the success of the photovoltaic technology is the cost of large scale deployment.

6.1. Current Photovoltaic Market - Balancing Between Cost, Performance, and Functionality

Currently, 91% of the solar market (Figure 6-1) is dominated by multicrystalline-silicon (multi-Si) and monocrystalline-silicon (mono-Si) inorganic technology as a result of its reputable efficiency and low cost.[248] However, constraints in modularity and energy intensive manufacturing hinder their potential to replace fossil fuels. These solar cells are

also rigid, heavy, and thus non-portable with their deployment limited to rooftop utility applications. The rest of the current market is populated by thin-film technologies such as amorphous silicon (a-Si), cadmium telluride (CdTe), and copper indium gallium selenide (CIGS). Due to their thin-film nature, these technologies are certainly more versatile, but their manufacture still requires high-temperature deposition methods, preventing further cost reduction. One strategy to lower manufacturing cost in photovoltaic technology is the use of solution-processable organic semiconductors on large area devices. As mentioned previously in this dissertation, the organic photovoltaic technology allows for the production of light-weight, flexible, and low-cost devices with enhanced application flexibility.

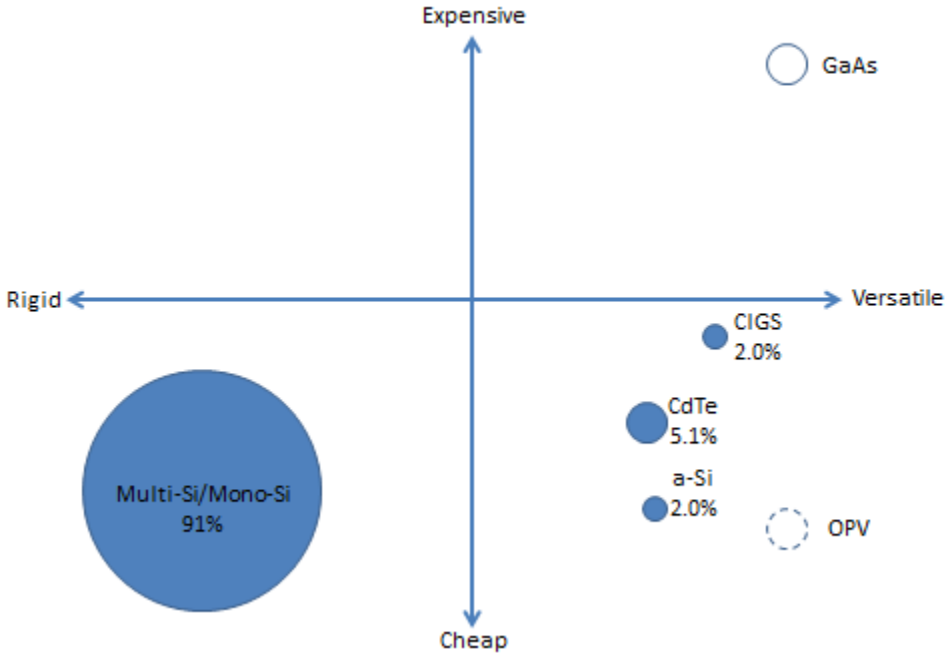

Figure 6-1. Competitive landscape of the photovoltaic market. Mono- and multi-silicon cells (mono-Si and multi-Si) dominate the market with 91% market share. Thin-film technologies such as amorphous silicon (a-Si), cadmium telluride (CdTe), and copper indium gallium selenide (CIGS) comprise the rest of the market. Gallium arsenide (GaAs) technology is primarily employed in aerospace applications. In order for OPV to enter the market, reductions in production and material cost are crucial.[249]

6.2. Material Designs for Organic Photovoltaics

6.2.1. Structure-property Investigation of Donor-Acceptor Polymers

6.2.1.1. Material Designs

It is crucial to understand the electronic properties of the electron-rich and poor moieties when designing D/A polymers in order to achieve favorable energy levels for charge transfer. As mentioned earlier in this dissertation, fullerenes remain the most frequently used acceptor due to their universal compatibility with most electron-rich materials. When designing donor polymers, organic chemists modulate the energy gaps of the materials to allow for maximum light absorption, and the energy levels to ensure favorable energy offsets with the fullerene acceptor. The tuning of the energy gaps and the energy offsets can be achieved by selecting adequate donor and acceptor units as well as by adding electron donating or electron withdrawing substituents.[8,34,250]

Molecular design should also take intermolecular packing into consideration. Unlike inorganic semiconductors, which have well-defined crystalline structures and domains, organic semiconductors are more amorphous and disordered. These molecules or polymers stack together by weak van der Waals forces and the charges are transported intermolecularly through hopping, leading to generally low charge mobility. Planarization of the polymeric or molecular backbones is crucial to increase effective conjugation and lower optical energy gap, promote intermolecular π-π stacking, and improve charge mobility. This can be effectively achieved by building ladder-type molecule design and covalently linking adjacent aromatic units.[32]

6.2.1.2. Thoroughness of Material and Device Characterizations

The quality of materials is crucial to ensure high performance in OPV devices. The OPV field, in general, should pay more attention to factors such as polymer molecular weight, dispersity, and material purity when comparing materials synthesized in different batches or by different groups. For polymers, end-capping should be done to reduce the number of reactive end functionalities such as bromide, tin, and boron groups, which can trap charges and reduce charge extraction, and power conversion efficiencies. Palladium scavenger can be used to remove residual palladium catalysts used during cross-coupling reactions. Elemental analysis and inductively coupled plasma mass spectrometry should be used to ensure high accuracy of elemental composition and low impurity (by measuring residual elemental contents such as Pd, Sn, P) within the polymer matrix, respectively. Gel permeation chromatographs should always be included when reporting polymer molecular weight and dispersity, and be discussed if multi-modal peaks are presented.

Many high performing OPV materials have different chemical structures, physical and optoelectronic properties. Thorough and systematic investigation on structure-property relationship will aid in further development in next generation OPV materials. Grazing-Incidence Wide-Angle X-ray Scattering technique provides information on intermolecular packing and material structural orientation, as well as crystallinity and aggregation behaviors. Photophysical methods such as pump-push-probe transient absorption spectroscopy[251] are used to observe non-emissive charge carriers resulting from photoexcitation. The charge carrier dynamics are correlated to the physical and chemical properties of materials such as bond length, side chain length and branching position, intermolecular stacking distances and backbone orientation as well as the OPV

device parameters such as photocurrent generation and fill factor. This improved understanding in structure-property relationship will aid the development of next generation high performing OPV materials.

6.2.2. Non-Fullerene Acceptors

As discussed throughout this dissertation, the balance between electron and hole carrier mobilites determines J_{sc} and FF in OPV devices. The material design strategy should first focus on creating novel materials with adequate mobility ($>10^{-3}$ cm^2 V^{-1} s^{-1}). It should then be followed by morphological control through the selection of solvents, additives, and other processing conditions such as solvent annealing and temperature annealing.

Research in replacing fullerenes with accepting polymers (as described in Chapter 5) and molecules has gone on for a decade. During this time, chemists and materials scientists have developed a respectable number of non-fullerene acceptors.[252,253,254,255,256] Two design trends have emerged: 1. Materials with extended ring and rigid systems; 2. Materials with twisted three-dimensional molecular structures.

6.2.2.1. Extended Fused Ring Systems

The advantages of the extended fused ring systems, for example, naphthalene diimide (NDI), perylene diimide (PDI), and indacenodithiophene (IDT) as shown in Figure 6-2, include high mobility resulting from the ease to achieve backbone planarity and intermolecular order, and thermal stability. The popular polymer P(NDI2OD-T2), also known as Polyera ActivInk™ N2200, was shown to be one of the first NDI based polymers with FET mobility reaching 1 cm^2 V^{-1} s^{-1}.[257] When used as an acceptor in an OPV device, 2% PCE was achieved which was a recorded efficiency for all-polymer

OPVs at the time.[258] The device performance was affected by the large segregated domains, resulting from the planar molecules' tendency to self-aggregate.[259] This also explains why the high mobility observed in FET devices do not directly translate into OPV performance, where active layer morphology, phase separation between donor and acceptor, and balance of electron mobility and hole mobility are as important as high carrier mobility.

6.2.2.2. Twisted Three-dimensional Systems

One strategy to mitigate the excessive self-aggregation problem is to connect the planar extended systems with bulky conjugated core units to induce highly twisted geometry. This method has proven effective in controlling morphology and processability in BHJ active layers.[260,261,262,263] Recently, the spiro/cruciform type cores were used to create true 3-dimensional designs. Molecular acceptor units based on the spiro-bifluorene core connected with four PDI units (SBF-PDI4, shown in Figure 6-3) have been shown to suppress self-aggregation, yet still facilitate excitation energy transfer between the PDI subunits. The 3D molecules interdigitate into a uniform interlocking geometry which prevents excessive rotation, promotes intermolecular order, and aids charge transport.[264,265]

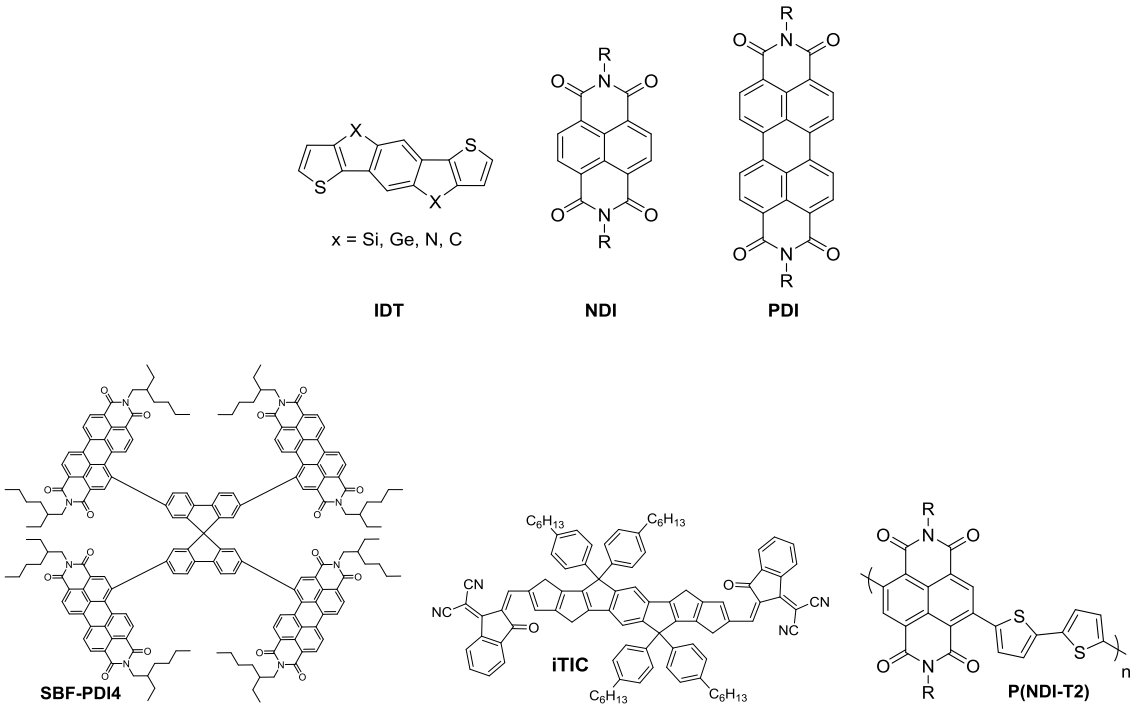

Figure 6-2. Planar extended fused ring moieties and examples of high performing acceptor molecules and polymers. (Adapted from reference[253,264,265,266,267].)

6.2.3. Choice of High Throughput Processing to Achieve Ordered Active Layer Morphologies and Structures

In Chapter 4, we showed for the first time that amphiphilic D-A-D DPP-based conjugated molecules were used to prepare stable and well-covered Langmuir-Blodgett films. The dipole-dipole interaction between amphiphilic and alkyl side chains and the π-π interaction of the conjugated backbone allowed the molecules to self-assemble into micron long fibrils *via* drop casting or ordered monolayer *via* LB, which was used to fabricate organic field effect transistors. The LB method is useful to fabricate layered structures in a layer-by-layer fashion. LB uses compression pressure to control and orient molecules into self-assembled monolayers. Multilayer LB films can be made by layer-by-layer deposition of the molecular monolayer. While LB can construct highly ordered thin films to investigate the fundamental effects of molecular orientation and the interfacial

molecular interaction on film quality, it cannot be transferred into commercial use due to its slow deposition process. For the development of organic electronic, high throughput roll-to-roll compatible printing methods are required. Large area and modular solution processing can advance the fabrication of electronic products as a result of efficient material use and low energy manufacturing. Blade coating[115,268,269] and slot-die coating[117,270] are especially attractive options since their usages have led to high performing devices that are comparable to those processed *via* the traditional spin-coating method. Other roll-to-roll compatible techniques such as screen printing,[271] spray coating,[272] and inkjet printing[119,120] have also been studied, but devices fabricated by these methods have significant drops in efficiency compared to spin-coated devices. Regardless of the printing methods, it will be important for the OPV fields to replace the use of toxic, halogenated solvents to reduce environmental impact during device fabrication.

OPV device performance is morphology dependent, therefore, regardless of the processing techniques, the ink formulation, film formation, aggregation behavior, and annealing conditions need to be optimized to obtain ideal active layer morphology. Careful characterization of the film formation process *via in-situ* and *ex-situ* morphological investigations such as UV-Vis absorption, x-ray diffraction, and atomic force microscopy have been used in an attempt to catalyze the transition of material processing from laboratory scale spin-coating to high throughput compatible systems.[273,274,275]

In term of material design, high-temperature stability and temperature-insensitive morphology within the range of device operating temperature are desirable to maintain

and prolong device lifetime. OPV materials are usually stable up to 350 ˚C before the onset of decomposition. Crosslinking (Figure 6-3) has proven to be a feasible strategy to freeze or lock-in the active layer morphology by covalently linking the fullerene acceptors and polymer donors, and thus suppressing fullerene aggregation at high temperature, leading to improved thermal stability of the device. Since these crosslinking moieties are typically insulators and poor light absorbers, to reduce their impact on the charge carrier mobility and optoelectronic properties of the active layer, they should be small in size and employed at low quantity.

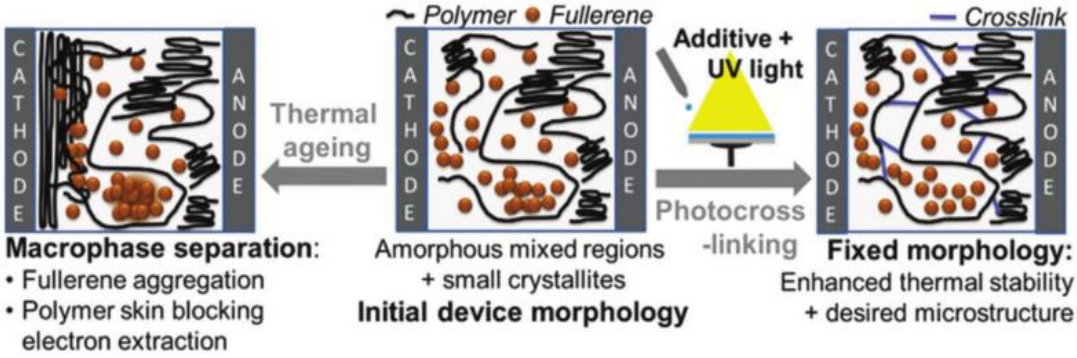

Figure 6-3. Improving thermal stability of OPV active layer by crosslinking polymer donors and fullerene acceptor. (Reproduced with permission from reference[276,277].)

6.3. Future of Organic Photovoltaics – Niche Applications

Much effort in OPV research focuses on materials development, which has led to high performing single-junction BHJ devices with over 10% PCE. With the increasing understanding of structure-property relationship, presented in Chapter 3 as an example, continuous discovery of novel high performing materials can be expected. However, materials design is only one of the many components in the commercialization of OPV technology. The performance of OPV devices also depends on the active layer morphology and structure; therefore, success in commercialization will require the

transfer of laboratory scale material processing to industrially compatible roll-to-roll processes to reach high-throughput manufacturing demand and high modular performance. The stability of the materials and the device lifetime will also need to be improved.

Commercially available, power grid-connected silicon solar panels are guaranteed to last over 30 years, making it difficult for OPVs to compete in the utility market. With a much shorter estimated device lifetime and poorer stability of the organic conjugated materials,[249] OPV will realize its market potential only if niche applications can be identified to utilize the lightweight, flexible, semi-transparent, and colorful aesthetic advantages of the technology. The shorter device lifespan will also require a thorough lifecycle assessment to consider end of life treatment of the device in order to reduce environmental impacts in recycling, incineration, and waste management.[278]

The Lighting Africa project has successfully implemented OPVs in remote and isolated areas of sub-Saharan Africa to generate and supply power for lamps, an example of fully utilizing OPV's advantages of low-cost, light-weight, and portability in commercially relevant niche applications.[279] However, Light Africa also provides solar panels based on other thin-film technology such as amorphous silicon. Given the high cost in producing organic light-absorbing materials and the short device lifetime, the value propositions of light weight and flexibility in the OPV technology are insufficient to extend wide-spread implementation.

One advantage of organic light-absorbing materials that is usually overlooked is their ability to absorb indoor ambient light due to the direct band gap nature of conjugated semiconductors.[112,280] A potential indoor application is to power pricing and

marketing displays at retail locations such as grocery stores. These displays can be powered by the OPV module and integrated with radio-frequency identification (RFID) and receivers to allow remote modification of pricing and marketing information.

The difference between an “invention” and an “innovation” is market creation. The transformation of OPV technology from a fundamental scientific invention to a profitable innovation adopted by the solar market will take a collective effort by chemists and materials scientists, chemical and process engineers, physicists and electrical engineers to address the technological challenges, as well as entrepreneurs and marketing experts to exploit the value propositions and develop commercialization strategies. I sincerely look forward to seeing one day soon the common market deployment of organic photovoltaics.

APPENDIX I

NMR RESULTS

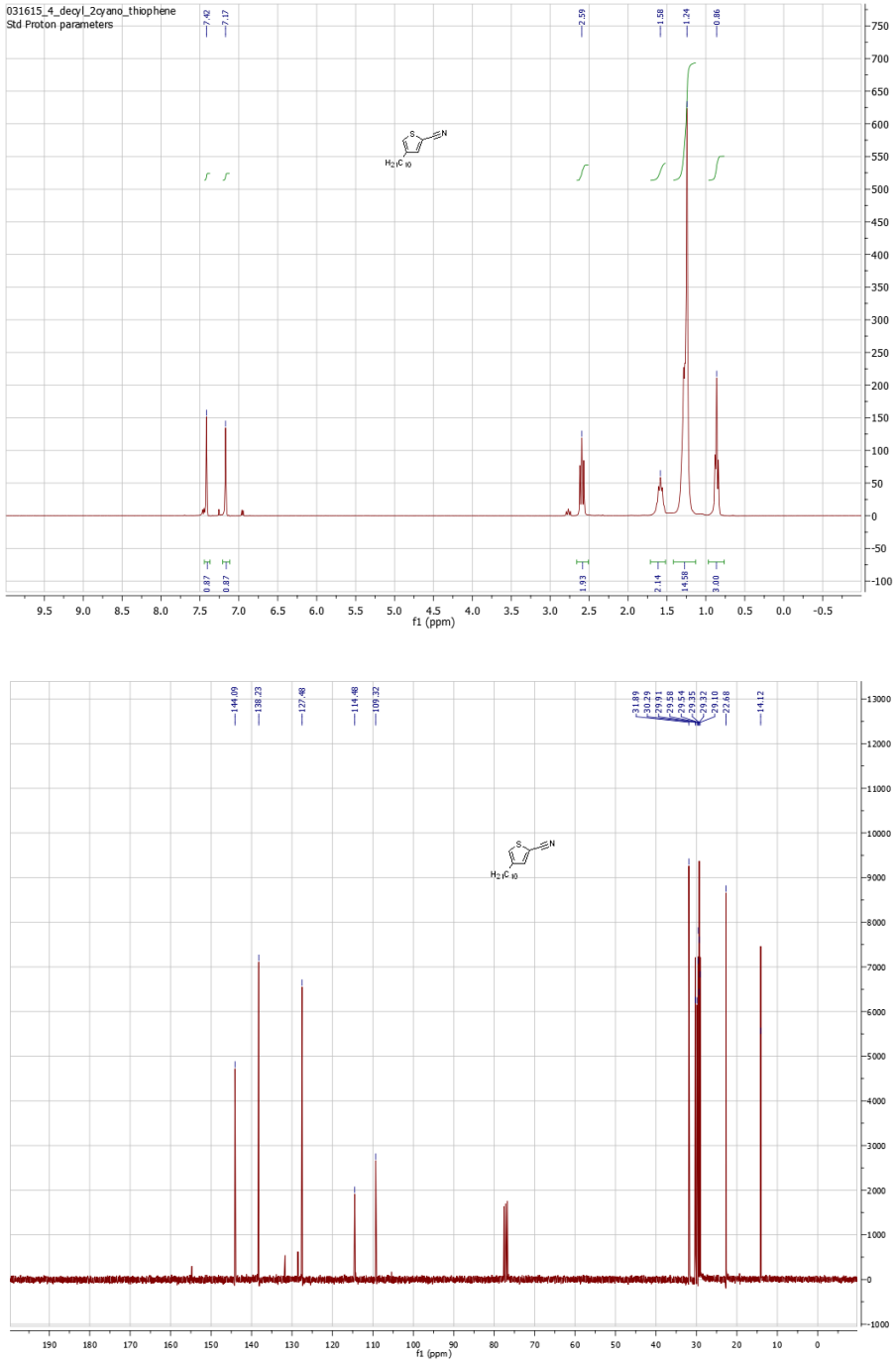

Figure A-I-1. ^{1}H (top) and ^{13}C (bottom) NMR spectra of **4-decylthiophene-2-carbonitrile.**

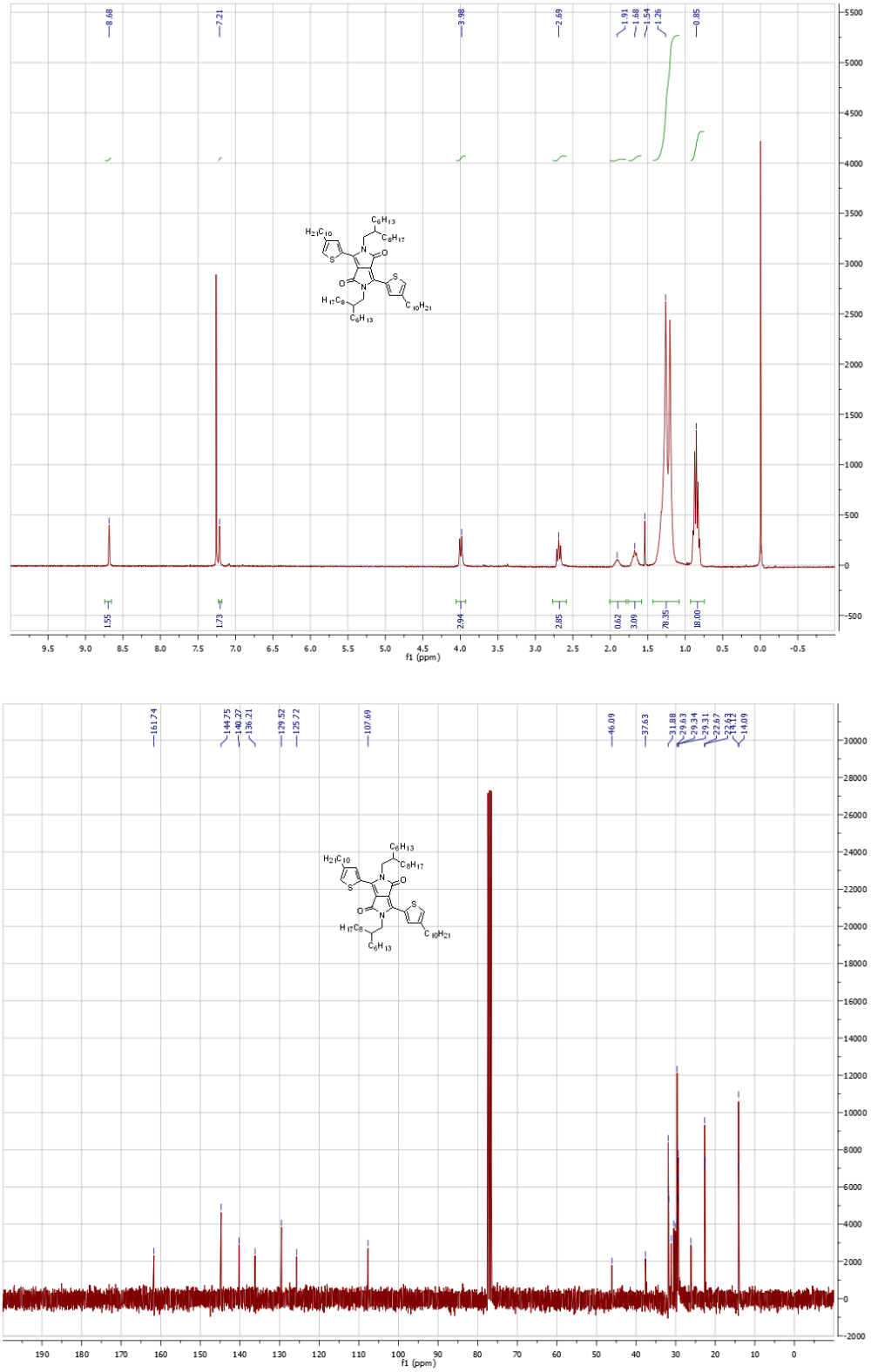

Figure A-I-2. ^{1}H (top) and ^{13}C (bottom) NMR spectra of **3,6-bis(4-decyl-thiophen-2-yl)-N,N'-bis(2-hexyldecyl)-pyrrolo[3,4-c]pyrrole-1,4-dione.**

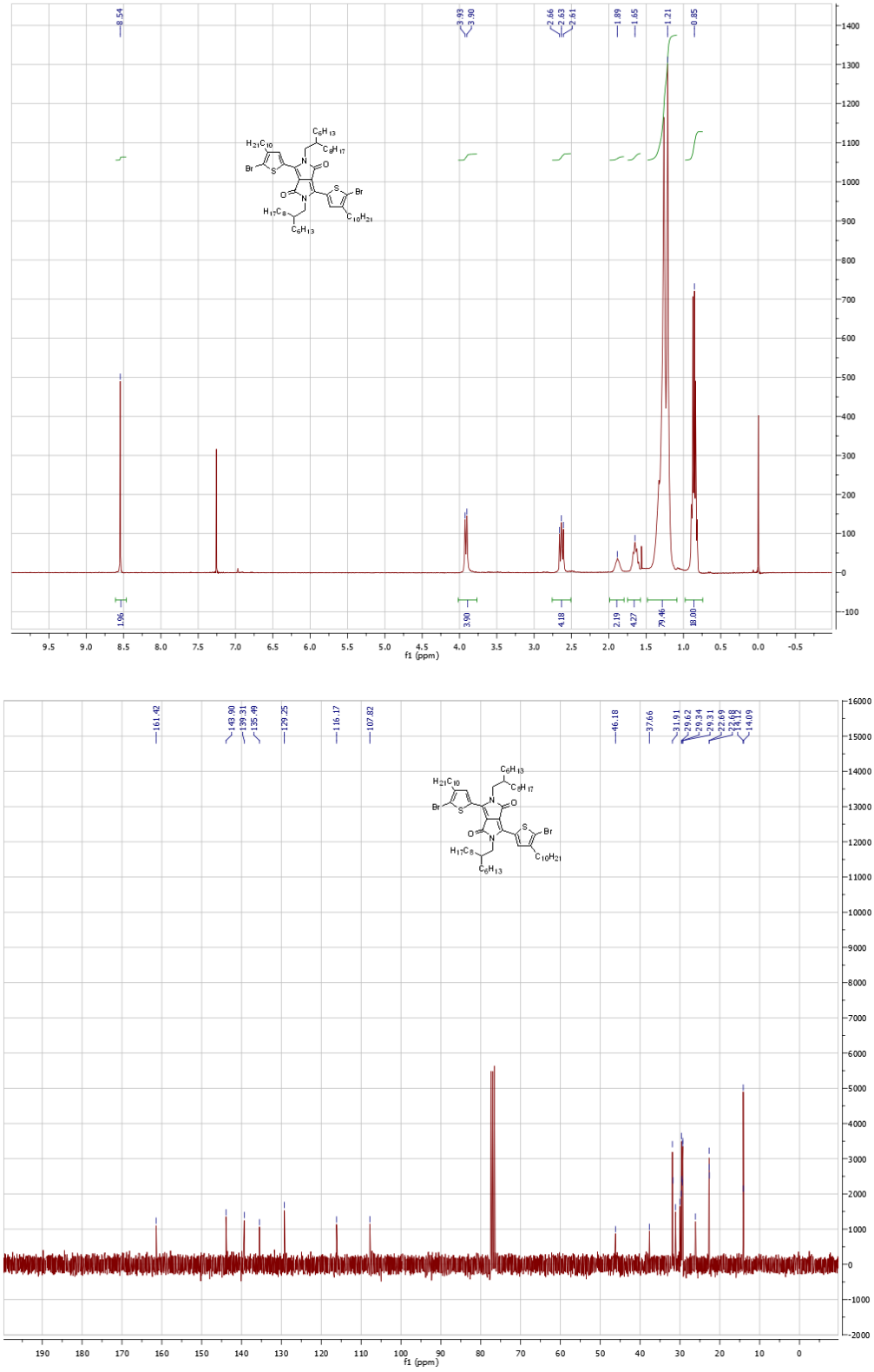

Figure A-I-3. ^{1}H (top) and ^{13}C (bottom) NMR spectra of **3,6-bis(5-bromo-4-decyl-thiophen-2-yl)-N,N'-bis(2-hexyldecyl)-pyrrolo[3,4-c]pyrrole-1,4-dione.**

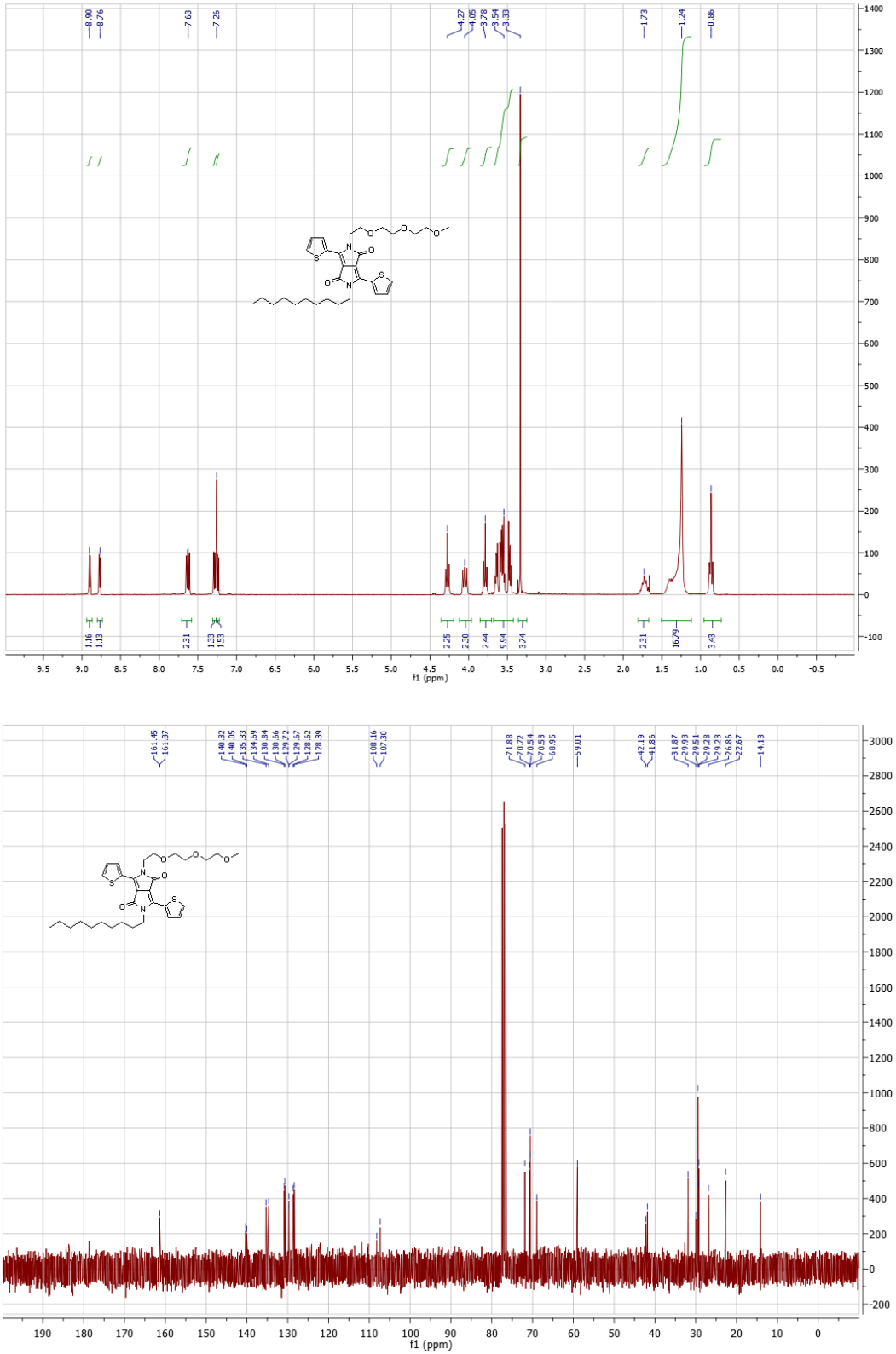

Figure A-I-4. ^{1}H (top) and ^{13}C (bottom) NMR spectra of **2-decyl-5-(2-(2-(2-methoxyethoxy)ethoxy)ethyl)-3,6-bis-(thiophen-2-yl)pyrrolo[3,4-c]pyrrole-1,4-dione.**

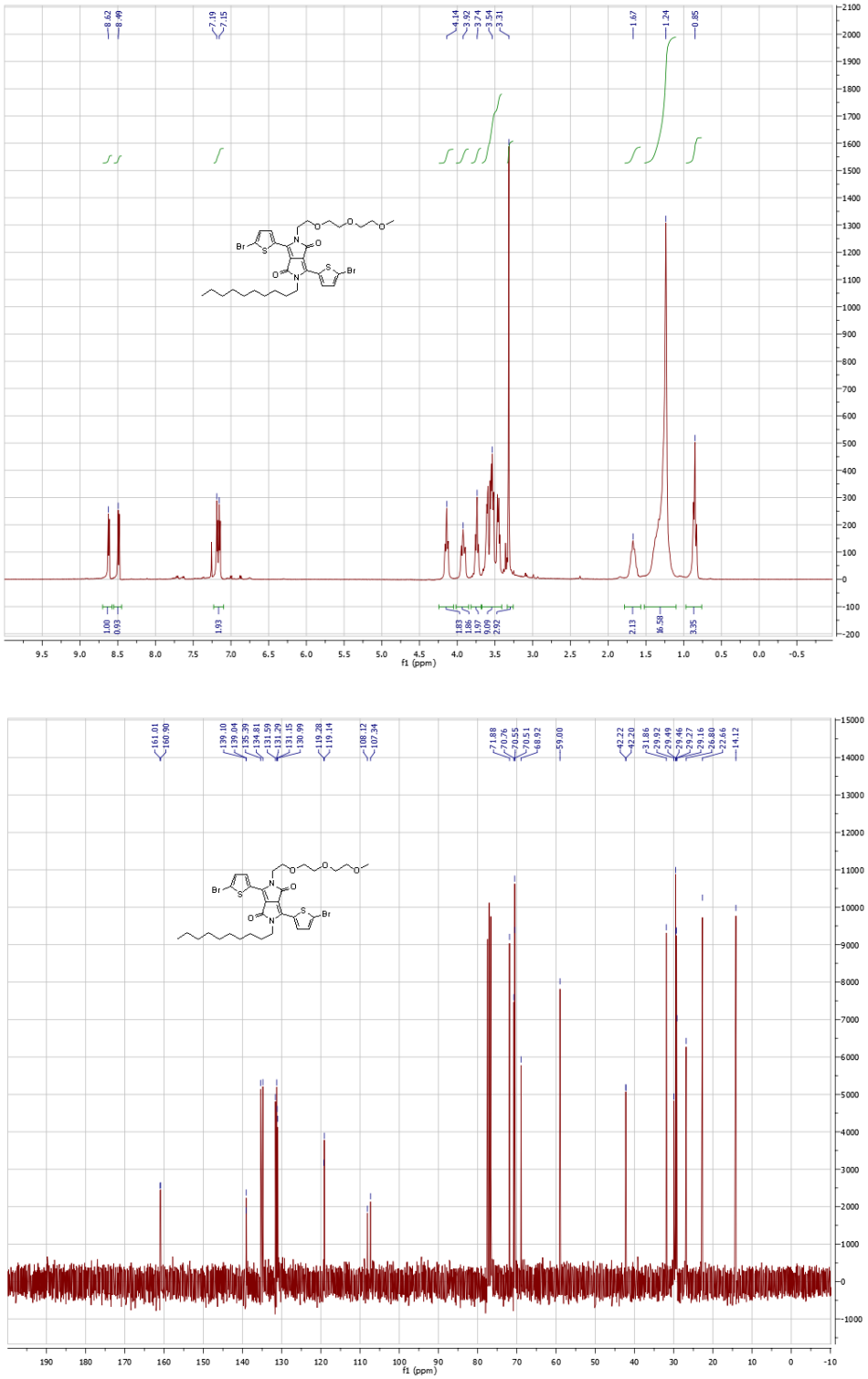

Figure A-I-5. ^{1}H (top) and ^{13}C (bottom) NMR spectra of **2-decyl-5-(2-(2-(2-methoxyethoxy)ethoxy)ethyl)-3,6-bis-(5-bromo-thiophen-2-yl)pyrrolo[3,4-c]pyrrole-1,4-dione.**

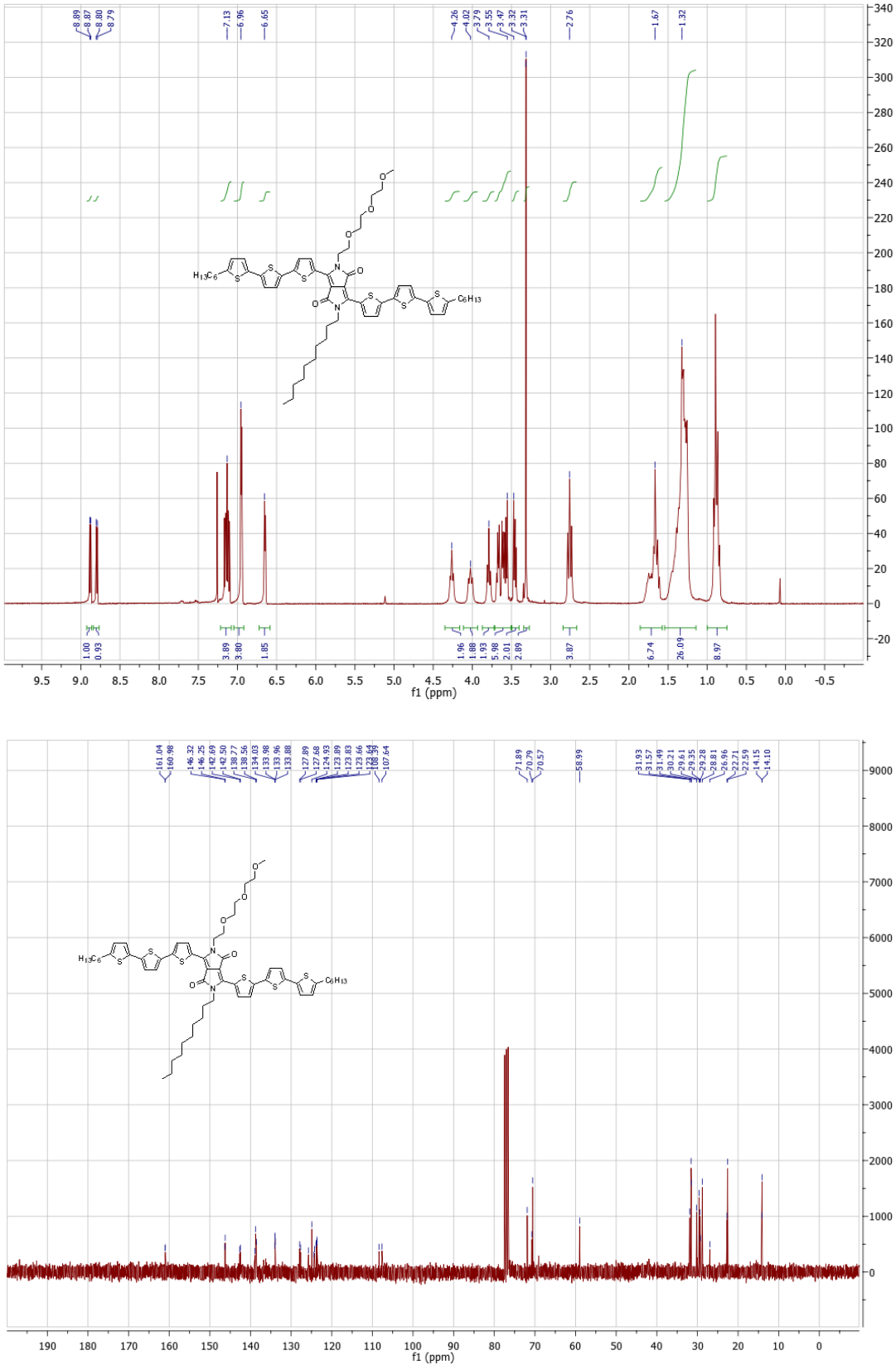

Figure A-I-6. ^{1}H (top) and ^{13}C (bottom) NMR spectra of **DPP-A**

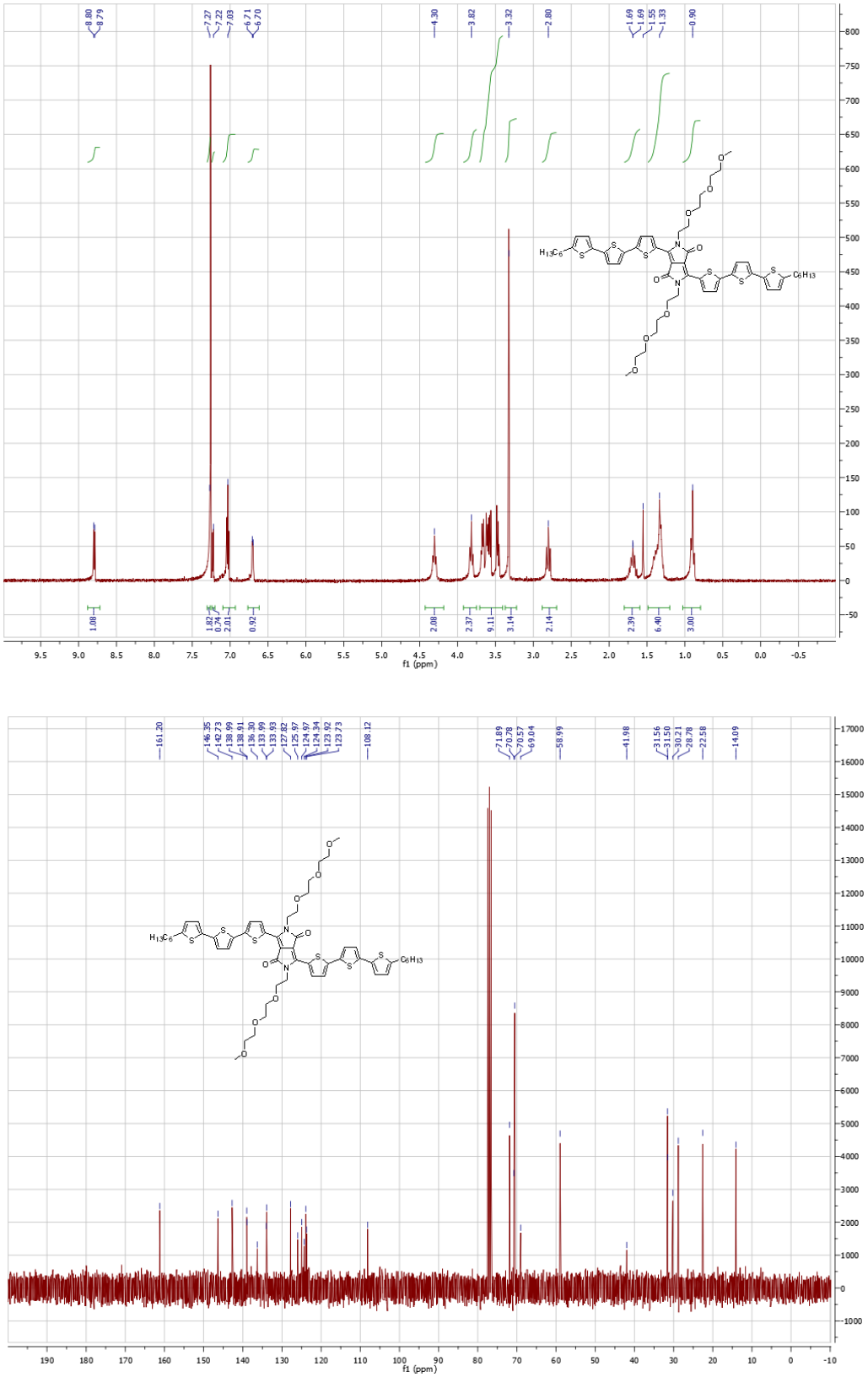

Figure A-I-7. ^{1}H (top) and ^{13}C (bottom) NMR spectra of **DPP-S**

APPENDIX II

HANDLING OF SOLVENTS FOR POLYMERIZATION

Solvents used in polymerization should be dried and degassed to ensure low water and oxygen contents.

1. Solvent drying

   Solvents coming from the SPS should be sufficiently dried, which can be confirmed by the Karl Fischer titrator. Alumina or molecular sieves (4Å pore size or smaller) can be used to dry the solvents otherwise, (see http://pubs.acs.org/doi/abs/10.1021/jo101589h for more on drying solvents).

2. Solvent degassing

   Solvents can be degassed through the "Freeze, Pump, Thaw" process. Fill a Schlenk flask with solvent to **at most** half. Make sure the opening is properly sealed. Connect a line from the inert gas/vacuum manifold onto the flask. Do not open the stopcock on the flask at this time but switch on the line so it is pulling vacuum. Double check to ensure it is pulling vacuum, but not pumping argon!

   Freeze - Submerge the Schlenk flask into liquid nitrogen until all the solvent is frozen.

   Pump - Open the stopcock. Pull vacuum for 5 minutes. Close the stopcock.

   Thaw - Lift the flask up and away from liquid nitrogen and allow the solvent to thaw. You should see gas bubbles emerging from the solvent and into the empty space above. Once the solvent is completely thawed, repeat the "Freeze, Pump, Thaw" steps at least 3 times, until little to no bubbles emerge during the thawing processing.

APPENDIX III

CHRONOLOGICAL ORDER IN POLYMER CHARACTERIZATION

1. Molecular weight

   Finding out the molecular weight of the polymer should always come first if at all possible. Do not go through all the characterizations and device fabrications then find out it is actually an oligomer.

2. Polymer structure and purity
   a. ^{1}H NMR
   b. Elemental analysis
   c. (optional) ICP-MS or ICP-OES
3. Optical and electrochemical properties
   a. Solution and thin-film UV-Vis absorption
   b. Solid-state echem (in the glovebox if needed, i.e. for OPV polymers)
4. Thermal analysis
   a. TGA
   b. DSC
5. Device fabrication

APPENDIX IV

DIGESTION METHODS FOR TRACE ELEMENT ANALYSIS

Impurities (from catalyst and ligand) can be introduced into the polymer matrix and alter device performance. Trace element analysis, i.e. ICP-MS and ICP-OES, can be used to analyze element content.

The polymer matrix first needs to be destroyed through acid digestion. Hot aqua regia, concentrated nitric acid, and concentrated sulfuric acid are all good candidates for digestion. The goal is to completely break down the polymer matrix and the digested solution should be transparent with little to no precipitates. If conventional digestion (i.e heating on a hot plate) is unsuccessful, microwave assisted digestion can be used.

Here's a microwave assisted digestion procedure that works well for digesting OPV polymers:

1. Heat the polymer to 200 ˚C in concentrated H_2SO_4 for 10 minutes. This should dehydrate and destroy the polymer matrix. The residual should be black and fully suspended in the solution.
2. An equal volume of concentrated HNO_3 is added and heated to 110 ˚C for 10 minutes. The solution now should be transparent and ready for dilution.

Note: Also prepare a "blank" solution without the polymer in it

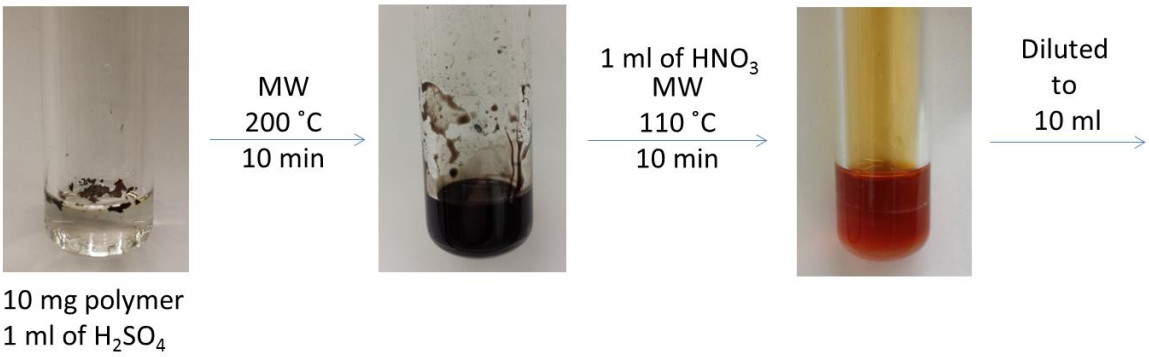

Figure A-IV-1. Solutions of Microwave assisted digestion for ICP analysis

The final concentration of the analyst solution should be 1-5% HNO_3 + 1-5% HCl.

The detection limits for metals commonly presence in our polymer synthesis:

Pd	0.02 ppm	Sn	0.06 ppm	P	0.81 ppm

For ICP-OED, contact Mike Buchanan (mike.buchanan@rbi.gatech.edu) and Tabassum Shah (tabassum.shah@rbi.gatech.edu) from the Renewable Bioproducts Institute for more details on sample preparation and analysis.

For ICP-MS, contact George Kamenov (kamenov@ufl.edu) at UF. The group has worked with him before and he is happy to help out.

REFERENCES

(1) Tsumura, A.; Koezuka, H.; Ando, T. *Appl. Phys. Lett.* **1986**, *49*, 1210–1212.

(2) Assadi, A.; Svensson, C.; Willander, M.; Inganäs, O. *Appl. Phys. Lett.* **1988**, *53*, 195–197.

(3) Wang, C.; Dong, H.; Hu, W.; Liu, Y.; Zhu, D. *Chem. Rev.* **2012**, *112*, 2208–2267.

(4) Nikolka, M.; Nasrallah, I.; Rose, B.; Ravva, M. K.; Broch, K.; Sadhanala, A.; Harkin, D.; Charmet, J.; Hurhangee, M.; Brown, A.; Illig, S.; Too, P.; Jongman, J.; McCulloch, I.; Bredas, J.-L.; Sirringhaus, H. *Nat. Mater.* **2016**, *16*, 356–362.

(5) Persson, N. E.; Chu, P.-H.; McBride, M.; Grover, M.; Reichmanis, E. *Acc. Chem. Res.* **2017**, acs.accounts.6b00639.

(6) Dyer, A. L.; Österholm, A. M.; Shen, D. E.; Johnson, K. E.; Reynolds, J. R. In *Electrochromic Materials and Devices*; Mortimer, R. J., Rosseinsky, D. R., Monk, P. M. S., Eds.; Wiley-VCH Verlag GmbH & Co. KGaA: Weinheim, 2015; pp 113–184.

(7) Kang, H.; Lee, W.; Oh, J.; Kim, T.; Lee, C.; Kim, B. J. *Acc. Chem. Res.* **2016**, *49*, 2424–2434.

(8) Liu, C.; Wang, K.; Gong, X.; Heeger, A. J. *Chem. Soc. Rev.* **2016**, *45*, 4825–4846.

(9) Jung, J. W.; Jo, J. W.; Jung, E. H.; Jo, W. H. *Org. Electron.* **2016**, *31*, 149–170.

(10) Lin, Y.; Zhao, F.; He, Q.; Huo, L.; Wu, Y.; Parker, T. C.; Ma, W.; Sun, Y.; Wang, C.; Zhu, D.; Heeger, A. J.; Marder, S. R.; Zhan, X. *J. Am. Chem. Soc.* **2016**, *138*, 4955–4961.

(11) Gong, X.; Tong, M.; Xia, Y.; Cai, W.; Moon, J. S.; Cao, Y.; Yu, G.; Shieh, C.-L.;

Nilsson, B.; Heeger, A. J. *Science* **2009**, *325*, 1665–1667.

(12) Armin, A.; Jansen-van Vuuren, R. D.; Kopidakis, N.; Burn, P. L.; Meredith, P. *Nat. Commun.* **2015**, *6*, 6343.

(13) Ma, L. P.; Liu, J.; Yang, Y. *Appl. Phys. Lett.* **2002**, *80*, 2997–2999.

(14) Chu, C. W.; Ouyang, J.; Tseng, J. H.; Yang, Y. *Adv. Mater.* **2005**, *17*, 1440–1443.

(15) Tan, C.; Liu, Z.; Huang, W.; Zhang, H. *Chem. Soc. Rev.* **2015**, *44*, 2615–2628.

(16) Tang, C. W.; Vanslyke, S. A. *Appl. Phys. Lett.* **1987**, *51*, 913–915.

(17) Kordt, P.; Van Der Holst, J. J. M.; Al Helwi, M.; Kowalsky, W.; May, F.; Badinski, A.; Lennartz, C.; Andrienko, D. *Adv. Funct. Mater.* **2015**, *25*, 1955–1971.

(18) Ito, T.; Shirakawa, H.; Ikeda, S. *J. Polym. Sci. Polym. Chem. Ed.* **1974**, *12*, 11–20.

(19) Chiang, C. K.; Fincher, C. R., J.; Park, Y. W.; Heeger, A. J.; Shirakawa, H.; Louis, E. J.; Gau, S. C.; MacDiarmid, A. G. *Phys. Rev. Lett.* **1977**, *39*, 1098–1101.

(20) Shirakawa, H.; Louis, E. J.; MacDiarmid, A. G.; Chiang, C. K.; Heeger, A. J. *J. Chem. Soc. Chem. Commun.* **1977**, 578–580.

(21) Su, W. P.; Schrieffer, J. R.; Heeger, A. J. *Phys. Rev. Lett.* **1979**, *42*, 1698–1701.

(22) Salzner, U.; Lagowski, J. B.; Pickup, P. G.; Poirier, R. A. *Synth. Met.* **1998**, *96*, 177–189.

(23) Hoppe, H.; Sariciftci, N. S. *J. Mater. Res.* **2011**, *19*, 1924–1945.

(24) Green, M. A.; Keevers, M. J. *Prog. Photovolt.* **1995**, *3*, 189–192.

(25) Powell, D. M.; Winkler, M. T.; Choi, H. J.; Simmons, C. B.; Needleman, D. B.; Buonassisi, T. *Energy Environ. Sci.* **2012**, *5*, 5874–5883.

(26) Singh, J. In *Semiconductor Devices: Basic Principles*; Wiley: New York, 2001; p 51.

(27) Mishra, U. K.; Singh, J. In *Semiconductor Device Physics and Design*; Springer: Dordrecht, The Netherlands., 2008; pp 46–50.

(28) Richard, S.; Aniel, F.; Fishman, G. *Phys. Rev. B* **2004**, *70*, 235204.

(29) Smith, D. L. *MRS Bull.* **2004**, *29*, 647–652.

(30) Siddiki, M. K.; Li, J.; Galipeau, D.; Qiao, Q. *Energy Environ. Sci.* **2010**, *3*, 867–883.

(31) Havinga, E. E.; ten Hoeve, W.; Wynberg, H. *Synth. Met.* **1993**, *57*, 299–306.

(32) Wu, J.-S.; Cheng, S.-W.; Cheng, Y.-J.; Hsu, C.-S. *Chem. Soc. Rev.* **2015**, *44*, 1113–1154.

(33) Lei, T.; Dou, J.-H.; Ma, Z.-J.; Yao, C.-H.; Liu, C.-J.; Wang, J.-Y.; Pei, J. *J. Am. Chem. Soc.* **2012**, *134*, 20025–20028.

(34) Dasari, R. R.; Dindar, A.; Lo, C. K.; Wang, C.-Y.; Quinton, C.; Singh, S.; Barlow, S.; Fuentes-Hernandez, C.; Reynolds, J. R.; Kippelen, B.; Marder, S. R. *Phys. Chem. Chem. Phys.* **2014**, *16*, 19345–19350.

(35) Winder, C.; Sariciftci, N. S. *J. Mater. Chem.* **2004**, *14*, 1077–1086.

(36) Huo, L.; Hou, J.; Chen, H.-Y.; Zhang, S.; Jiang, Y.; Chen, T. L.; Yang, Y. *Macromolecules* **2009**, *42*, 6564–6571.

(37) Zhang, G.; Fu, Y.; Xie, Z.; Zhang, Q. *Sol. Energ. Mat. Sol. Cells* **2011**, *95*, 1168–1173.

(38) Dou, L.; Liu, Y.; Hong, Z.; Li, G.; Yang, Y. *Chem. Rev.* **2015**, *115*, 12633–12665.

(39) Morin, P.-O.; Bura, T.; Leclerc, M. *Mater. Horiz.* **2013**, *3*, 11–20.

(40) Yu, G.; Gao, J.; Hummelen, J. C.; Wudl, F.; Heeger, A. J. *Science* **1995**, *270*, 1789–1791.

(41) Ganesamoorthy, R.; Sathiyan, G.; Sakthivel, P. *Sol. Energ. Mat. Sol. Cells* **2017**, *161*, 102–148.

(42) Guan, Z.-L.; Kim, J. B.; Wang, H.; Jaye, C.; Fischer, D. a.; Loo, Y.-L.; Kahn, A. *Org. Electron.* **2010**, *11*, 1779–1785.

(43) Nielsen, T. D.; Cruickshank, C.; Foged, S.; Thorsen, J.; Krebs, F. C. *Sol. Energ. Mat. Sol. Cells* **2010**, *94*, 1553–1571.

(44) Søndergaard, R. R.; Hösel, M.; Krebs, F. C. *J. Polym. Sci. Part B Polym. Phys.* **2013**, *51*, 16–34.

(45) Amb, C. M.; Craig, M. R.; Koldemir, U.; Subbiah, J.; Choudhury, K. R.; Gevorgyan, S. A.; Jørgensen, M.; Krebs, F. C.; So, F.; Reynolds, J. R. *ACS Appl. Mater. Interfaces* **2012**, *4*, 1847–1853.

(46) Zhan, Z.; An, J.; Wei, Y.; Tran, V.-T.; Du, H. *Nanoscale* **2017**, *9*, 965–993.

(47) Scholes, G. D.; Rumbles, G. *Nat. Mater.* **2006**, *5*, 683–696.

(48) Brédas, J.-L.; Kippelen, B. *Energy Environ. Sci.* **2009**, *2*, 251–261.

(49) Gélinas, S.; Paré-Labrosse, O.; Brosseau, C.-N.; Albert-Seifried, S.; McNeill, C.

R.; Kirov, K. R.; Howard, I. A.; Leonelli, R.; Friend, R. H.; Silva, C. *J. Phys. Chem. C* **2011**, *115*, 7114–7119.

(50) Tang, C. W. *Appl. Phys. Lett.* **1986**, *48*, 183–185.

(51) Brabec, C. J.; Durrant, J. R. *MRS Bull.* **2008**, *33*, 670–675.

(52) Mayer, A. C.; Scully, S. R.; Hardin, B. E.; Rowell, M. W.; McGehee, M. D. *Mater. Today* **2007**, *10*, 28–33.

(53) Sweetnam, S.; Graham, K. R.; Ndjawa, G. O. N.; Heumüller, T.; Bartelt, A.; Burke, T. M.; You, W.; Amassian, A.; Mcgehee, M. D. *J. Am. Chem. Soc.* **2014**, *136*, 14078–14088.

(54) Schumann, S.; Da Campo, R.; Illy, B.; Cruickshank, A. C.; McLachlan, M. A.; Ryan, M. P.; Riley, D. J.; McComb, D. W.; Jones, T. S. *J. Mater. Chem.* **2011**, *21*, 2381–2386.

(55) Hu, Z.; Zhang, J.; Liu, Y.; Hao, Z.; Zhang, X.; Zhao, Y. *Sol. Energ. Mat. Sol. Cells* **2011**, *95*, 2126–2130.

(56) Hau, S. K.; Yip, H. L.; Ma, H.; Jen, A. K. Y. *Appl. Phys. Lett.* **2008**, *93*, 233304.

(57) Zhou, N.; Guo, X.; Ortiz, R. P.; Li, S.; Zhang, S.; Chang, R. P. H.; Facchetti, A.; Marks, T. J. *Adv. Mater.* **2012**, *24*, 2242–2248.

(58) Burke, T. M.; Sweetnam, S.; Vandewal, K.; McGehee, M. D. *Adv. Energy Mater.* **2015**, *5*, 1500123.

(59) Taretto, K.; Soldera, M.; Troviano, M. *Prog. Photovolt. Res. Appl.* **2013**, *21*, 1489–1498.

(60) Qiab, B.; Wang, J. *Phys. Chem. Chem. Phys.* **2013**, *15*, 8972–8982.

(61) Mazzio, K. a.; Luscombe, C. K. *Chem. Soc. Rev.* **2015**, *44*, 78–90.

(62) Gray, J. L. In *Handbook of Photovoltaic Science and Engineering*; John Wiley & Sons Ltd: West Sussex, England, 2003; pp 61–112.

(63) Guerrero, A.; Loser, S.; Garcia-Belmonte, G.; Bruns, C. J.; Smith, J.; Miyauchi, H.; Stupp, S. I.; Bisquert, J.; Marks, T. J. *Phys. Chem. Chem. Phys.* **2013**, *15*, 16456–16462.

(64) Credgington, D.; Jamieson, F. C.; Walker, B.; Nguyen, T. Q.; Durrant, J. R. *Adv. Mater.* **2012**, *24*, 2135–2141.

(65) Deng, D.; Zhang, Y.; Yuan, L.; He, C.; Lu, K.; Wei, Z. *Adv. Energy Mater.* **2014**, *4*, 1400230.

(66) Proctor, C. M.; Kim, C.; Neher, D.; Nguyen, T. Q. *Adv. Funct. Mater.* **2013**, *23*, 3584–3594.

(67) Mihailetchi, V. D.; Wildeman, J.; Blom, P. W. M. *Phys. Rev. Lett.* **2005**, *94*, 126602.

(68) Wagenpfahl, A.; Deibel, C.; Dyakonov, V. *IEEE J. Sel. Top. Quantum Electron.* **2010**, *16*, 1759–1763.

(69) Baumann, A.; Lorrmann, J.; Rauh, D.; Deibel, C.; Dyakonov, V. *Adv. Mater.* **2012**, *24*, 4381–4386.

(70) Guo, X.; Kim, F. S.; Jenekhe, S. A.; Watson, M. D. *J. Am. Chem. Soc.* **2009**, *131*, 7206–7207.

(71) Wu, P. T.; Xin, H.; Kim, F. S.; Ren, G.; Jenekhe, S. A. *Macromolecules* **2009**, *42*, 8817–8826.

(72) Kang, I.; Yun, H.; Chung, D. S.; Kwon, S.; Kim, Y. *J. Am. Chem. Soc.* **2013**, *135*, 14896–14899.

(73) Fu, B.; Baltazar, J.; Sankar, A. R.; Chu, P. H.; Zhang, S.; Collard, D. M.; Reichmanis, E. *Adv. Funct. Mater.* **2014**, *24*, 3734–3744.

(74) Akkerman, H. B.; Mannsfeld, S. C. B.; Kaushik, A. P.; Verploegen, E.; Burnier, L.; Zoombelt, A. P.; Saathoff, J. D.; Hong, S.; Atahan-Evrenk, S.; Liu, X.; Aspuru-Guzik, A.; Toney, M. F.; Clancy, P.; Bao, Z. *J. Am. Chem. Soc.* **2013**, *135*, 11006–11014.

(75) McCulloch, I.; Heeney, M.; Bailey, C.; Genevicius, K.; Macdonald, I.; Shkunov, M.; Sparrowe, D.; Tierney, S.; Wagner, R.; Zhang, W.; Chabinyc, M. L.; Kline, R. J.; McGehee, M. D.; Toney, M. F. *Nat. Mater.* **2006**, *5*, 328–333.

(76) Cates, N. C.; Gysel, R.; Beiley, Z.; Miller, C. E.; Toney, M. F.; Heeney, M.; McCulloch, I.; McGehee, M. D. *Nano Lett.* **2009**, *9*, 4153–4157.

(77) Liu, T.; Pan, X.; Meng, X.; Liu, Y.; Wei, D.; Ma, W.; Huo, L.; Sun, X.; Lee, T. H.; Huang, M.; Choi, H.; Kim, J. Y.; Choy, W. C. H.; Sun, Y. *Adv. Mater.* **2016**, *29*, 1604251.

(78) Dong, C.; Hoppe, H.; Beenken, W. J. D. *J. Phys. Chem. A* **2016**, *120*, 3835–3841.

(79) Zerdan, R. B.; Shewmon, N. T.; Zhu, Y.; Mudrick, J. P.; Chesney, K. J.; Xue, J.; Castellano, R. K. *Adv. Funct. Mater.* **2014**, *24*, 5993–6004.

(80) Liu, J.; Zhang, Y.; Phan, H.; Sharenko, A.; Moonsin, P.; Walker, B.; Promarak, V.; Nguyen, T. Q. *Adv. Mater.* **2013**, *25*, 3645–3650.

(81) Graham, K. R.; Cabanetos, C.; Jahnke, J. P.; Idso, M. N.; Labban, E.; Ndjawa, G. O. N.; Heumueller, T.; Vandewal, K.; Chmelka, B. F.; Amassian, A.; Beaujuge, P.

M.; Mcgehee, M. D.; Cabanetos, C.; Salleo, A. *J. Am. Chem. Soc.* **2014**, *136*, 9608–9618.

(82) Wang, T.; Ravva, M. K.; Brédas, J. L. *Adv. Funct. Mater.* **2016**, *26*, 5913–5921.

(83) Ravva, M. K.; Wang, T.; Brédas, J. *Chem. Mater.* **2016**, *28*, 8181–8189.

(84) Meng, B.; Song, H.; Chen, X.; Xie, Z.; Liu, J.; Wang, L. *Macromolecules* **2015**, *48*, 4357–4363.

(85) Sengwa, R. J. *Polym. Int.* **1998**, *45*, 43–46.

(86) Sengwa, R. J.; Kaur, K.; Chaudhary, R. *Polym. Int.* **2000**, *49*, 599–608.

(87) Torabi, S.; Jahani, F.; Van Severen, I.; Kanimozhi, C.; Patil, S.; Havenith, R. W. a.; Chiechi, R. C.; Lutsen, L.; Vanderzande, D. J. M.; Cleij, T. J.; Hummelen, J. C.; Koster, L. J. A. *Adv. Funct. Mater.* **2015**, *25*, 150–157.

(88) Constantinou, I.; Yi, X.; Shewmon, N. T.; Klump, E. D.; Peng, C.; Garakyaraghi, S.; Lo, C. K.; Reynolds, J. R.; Castellano, F. N.; So, F. *Adv. Energy Mater.* **2017**, DOI: 10.1002/aenm.201601947.

(89) Breselge, M.; Van Severen, I.; Lutsen, L.; Adriaensens, P.; Manca, J.; Vanderzande, D.; Cleij, T. *Thin Solid Films* **2006**, *511–512*, 328–332.

(90) Shao, M.; He, Y.; Hong, K.; Rouleau, C. M.; Geohegan, D. B.; Xiao, K. *Polym. Chem.* **2013**, *4*, 5270–5274.

(91) Reitzel, N.; Greve, D. R.; Kjaer, K.; Howes, P. B.; Jayaraman, M.; Savoy, S.; McCullough, R. D.; McDevitt, J. T.; Bjørnholm, T. *J. Am. Chem. Soc.* **2000**, *122*, 5788–5800.

(92) Kanimozhi, C.; Yaacobi-gross, N.; Burnett, E. K.; Briseno, A. L.; Anthopoulos, T.

D.; Patil, S. *Phys. Chem. Chem. Phys.* **2014**, *16*, 17253–17265.

(93) Shi, C.; Yao, Y.; Yang, Y.; Pei, Q. *J. Am. Chem. Soc.* **2006**, *128*, 8980–8986.

(94) Qin, R.; Li, W.; Li, C.; Du, C.; Veit, C.; Schleiermacher, H.; Andersson, M.; Bo, Z.; Liu, Z.; Inganas, O.; Wuerfel, U.; Zhang, F. *J. Am. Chem. Soc.* **2009**, *131*, 14612–14613.

(95) Huang, H.; Chen, Z.; Ortiz, R. P.; Newman, C.; Usta, H.; Lou, S.; Youn, J.; Noh, Y. Y.; Baeg, K. J.; Chen, L. X.; Facchetti, A.; Marks, T. *J. Am. Chem. Soc.* **2012**, *134*, 10966–10973.

(96) Guo, X.; Quinn, J.; Chen, Z.; Usta, H.; Zheng, Y.; Xia, Y.; Hennek, J. W.; Ortiz, R. P.; Marks, T. J.; Facchetti, A. *J. Am. Chem. Soc.* **2013**, *135*, 1986–1996.

(97) Ruiz, J. P.; Nayak, K.; Marynick, D. S.; Reynolds, J. R. *Macromolecules* **1989**, *22*, 1231–1238.

(98) De Cremer, L.; Verbiest, T.; Koeckelberghs, G. *Macromolecules* **2008**, *41*, 568–578.

(99) Zhang, Q. T.; Tour, J. M. *J. Am. Chem. Soc.* **1998**, *120*, 5355–5362.

(100) Nielsen, C. B.; Sohn, E. H.; Cho, D. J.; Schroeder, B. C.; Smith, J.; Lee, M.; Anthopoulos, T. D.; Song, K.; McCulloch, I. *ACS Appl. Mater. Interfaces* **2013**, *5*, 1806–1810.

(101) Banno, M.; Yamaguchi, T.; Nagai, K.; Kaiser, C.; Hecht, S.; Yashima, E. *J. Am. Chem. Soc.* **2012**, *134*, 8718–8728.

(102) Chen, H.-Y.; Hou, J.; Zhang, S.; Liang, Y.; Yang, G.; Yang, Y.; Yu, L.; Wu, Y.; Li, G. *Nat. Photon.* **2009**, *3*, 649–653.

(103) Manceau, M.; Bundgaard, E.; Carlé, J. E.; Hagemann, O.; Helgesen, M.; Søndergaard, R.; Jørgensen, M.; Krebs, F. C. *J. Mater. Chem.* **2011**, *21*, 4132–4141.

(104) Huang, Y.; Huo, L.; Zhang, S.; Guo, X.; Han, C. C.; Li, Y.; Hou, J. *Chem. Commun.* **2011**, *47*, 8904–8906.

(105) Lu, L.; Yu, L. *Adv. Mater.* **2014**, *26*, 4413–4430.

(106) He, Z.; Xiao, B.; Liu, F.; Wu, H.; Yang, Y.; Xiao, S.; Wang, C.; Russell, T. P.; Cao, Y. *Nat. Photon.* **2015**, *9*, 174–179.

(107) Liu, C.; Yi, C.; Wang, K.; Yang, Y.; Bhatta, R. S.; Tsige, M.; Xiao, S.; Gong, X. *ACS Appl. Mater. Interfaces* **2015**, *7*, 4928–4935.

(108) Ariga, K.; Hill, J. P.; Ji, Q. *Phys. Chem. Chem. Phys.* **2007**, *9*, 2319–2340.

(109) Decher, G. In *Multilayer Thin Films: Sequential Assembly of Nanocomposite Materials*; Decher, G., Schlenoff, J. B., Eds.; Wiley-VCH Verlag GmbH & Co. KGaA, 2012; pp 1–21.

(110) Gong, X.; Wang, S.; Moses, D.; Bazan, G. C.; Heeger, A. J. *Adv. Mater.* **2005**, *17*, 2053–2058.

(111) Steirer, K. X.; Reese, M. O.; Rupert, B. L.; Kopidakis, N.; Olson, D. C.; Collins, R. T.; Ginley, D. S. *Sol. Energ. Mat. Sol. Cells* **2009**, *93*, 447–453.

(112) Hoth, C. N.; Schilinsky, P.; Choulis, S. A.; Balasubramanian, S.; Brabec, C. J. In *Applications of Organic and Printed Electronics, Integrated Circuits and Systems*; Cantatore, E., Ed.; Springer US: New York, 2013; pp 27–56.

(113) Cai, C.; Zhang, Y.; Song, R.; Peng, Z.; Xia, L.; Wu, M.; Xiong, K.; Wang, B.; Lin,

Y.; Xu, X.; Liang, Q.; Wu, H.; Wang, E.; Hou, L. *Sol. Energ. Mat. Sol. Cells* **2017**, *161*, 52–61.

(114) Fukuda, K.; Someya, T. *Adv. Mater.* **2016**, DOI: 10.1002/adma.201602736.

(115) Ye, L.; Xiong, Y.; Yao, H.; Gadisa, A.; Zhang, H.; Li, S.; Ghasemi, M.; Balar, N.; Hunt, A.; O'Connor, B. T.; Hou, J.; Ade, H. *Chem. Mater.* **2016**, *28*, 7451–7458.

(116) Chang, J.; Chi, C.; Zhang, J.; Wu, J. *Adv. Mater.* **2013**, *25*, 6442–6447.

(117) Hong, S.; Lee, J.; Kang, H.; Lee, K. *Sol. Energ. Mat. Sol. Cells* **2013**, *112*, 27–35.

(118) Eggenhuisen, T. M.; Galagan, Y.; Biezemans, a. F. K. V.; Slaats, T. M. W. L.; Voorthuijzen, W. P.; Kommeren, S.; Shanmugam, S.; Teunissen, J. P.; Hadipour, A.; Verhees, W. J. H.; Veenstra, S. C.; Coenen, M. J. J.; Gilot, J.; Andriessen, R.; Groen, W. A. *J. Mater. Chem. A* **2015**, *3*, 7255–7262.

(119) Eggenhuisen, T. M.; Galagan, Y.; Coenen, E. W. C.; Voorthuijzen, W. P.; Slaats, M. W. L.; Kommeren, S. A.; Shanmuganam, S.; Coenen, M. J. J.; Andriessen, R.; Groen, W. A. *Sol. Energ. Mat. Sol. Cells* **2015**, *134*, 364–372.

(120) Lamont, C. A.; Eggenhuisen, T. M.; Coenen, M. J. J.; Slaats, T. W. L.; Andriessen, R.; Groen, P. *Org. Electron.* **2015**, *17*, 107–114.

(121) Hussain, S. A.; Bhattacharjee, D. *Mod. Phys. Lett. B* **2009**, *23*, 3437–3451.

(122) Langmuir, I. *J. Am. Chem. Soc.* **1917**, *39*, 1848–1906.

(123) Blodgett, K. B. *J. Am. Chem. Soc.* **1935**, *57*, 1007–1022.

(124) Langmuir, I.; Schaefer, V. J. *J. Am. Chem. Soc.* **1938**, *60*, 1351–1360.

(125) Ariga, K.; Yamauchi, Y.; Mori, T.; Hill, J. P. *Adv. Mater.* **2013**, *25*, 6477–6512.

(126) Schwartz, D. K. *Surf. Sci. Rep.* **1997**, *27*, 245–334.

(127) Talham, D. R.; Yamamoto, T.; Meisel, M. W. *J. Phys. Condens. Matter* **2008**, *20*, 184006.

(128) Zhao, Y.; Zhao, X.; Roders, M.; Gumyusenge, A.; Ayzner, A. L.; Mei, J. *Adv. Mater.* **2017**, DOI: 10.1002/adma.201605056.

(129) Zhao, Y.; Zhao, X.; Roders, M.; Qu, G.; Diao, Y.; Ayzner, A. L.; Mei, J. *Chem. Mater.* **2015**, *27*, 7164–7170.

(130) Zhao, X.; Zhao, Y.; Ge, Q.; Butrouna, K.; Diao, Y.; Graham, K. R.; Mei, J. *Macromolecules* **2016**, *49*, 2601–2608.

(131) Carsten, B.; He, F.; Son, H. J.; Xu, T.; Yu, L. *Chem. Rev.* **2011**, *111*, 1493–1528.

(132) Seechurn, C. C. C. J.; Kitching, M. O.; Colacot, T. J.; Snieckus, V. *Angew. Chem. Int. Ed.* **2012**, *51*, 5062–5085.

(133) Segawa, Y.; Maekawa, T.; Itami, K. *Angew. Chem. Int. Ed.* **2015**, *54*, 66–81.

(134) Mercier, L. G.; Leclerc, M. *Acc. Chem. Res.* **2013**, *46*, 1597–1605.

(135) Lee, J.; Yun, M. H.; Kim, J.; Kim, J. Y.; Yang, C. *Macromol. Rapid Commun.* **2012**, *33*, 140–145.

(136) Bürckstümmer, H.; Weissenstein, A.; Bialas, D.; Würthner, F. *J. Org. Chem.* **2011**, *76*, 2426–2432.

(137) Parker, T. C.; Marder, S. R. In *Synthetic Methods in Organic Electronic and Photonic Materials: A Practical Guide*; The Royal Society of Chemistry: Cambridge, UK, 2015; pp 145–147.

(138) Espinet, P.; Echavarren, A. M. *Angew. Chem. Int. Ed.* **2004**, *43*, 4704–4734.

(139) Kosugi, M.; Fugami, K. *J. Organomet. Chem.* **2002**, *653*, 50–53.

(140) Zalesskiy, S. S.; Ananikov, V. P. *Organometallics* **2012**, *31*, 2302–2309.

(141) Helgesen, M.; Carlé, J. E.; dos Reis Benatto, G. a.; Søndergaard, R. R.; Jørgensen, M.; Bundgaard, E.; Krebs, F. C. *Adv. Energy Mater.* **2015**, *5*, 1401996.

(142) Goto, E.; Ando, S.; Ueda, M.; Higashihara, T. *ACS Macro Lett.* **2015**, *4*, 1004–1007.

(143) Schubert, M.; Dolfen, D.; Frisch, J.; Roland, S.; Steyrleuthner, R.; Stiller, B.; Chen, Z.; Scherf, U.; Koch, N.; Facchetti, A.; Neher, D. *Adv. Energy Mater.* **2012**, *2*, 369–380.

(144) Suraru, S.-L.; Lee, J. A.; Luscombe, C. K. *ACS Macro Lett.* **2016**, *5*, 724–729.

(145) Matsidik, R.; Komber, H.; Sommer, M. *ACS Macro Lett.* **2015**, *4*, 1346–1350.

(146) Estrada, L. A.; Deininger, J. J.; Kamenov, G. D.; Reynolds, J. R. *ACS Macro Lett.* **2013**, *2*, 869–873.

(147) Grenier, F.; Berrouard, P.; Pouliot, J.-R.; Tseng, H.-R.; Heeger, A. J.; Leclerc, M. *Polym. Chem.* **2013**, *4*, 1836–1841.

(148) Liu, S.-Y.; Shi, M.-M.; Huang, J.-C.; Jin, Z.-N.; Hu, X.-L.; Pan, J.-Y.; Li, H.-Y.; Jen, A. K.-Y.; Chen, H.-Z. *J. Mater. Chem. A* **2013**, *1*, 2795–2805.

(149) Wu, W.; Xin, H.; Ge, C.; Gao, X. *Tetrahedron Lett.* **2017**, *58*, 175–184.

(150) Lafrance, M.; Fagnou, K. *J. Am. Chem. Soc.* **2006**, *128*, 16496–16497.

(151) Marrocchi, A.; Facchetti, A.; Lanari, D.; Petrucci, C.; Vaccaro, L. *Energy Environ. Sci.* **2016**, *9*, 763–786.

(152) Wang, Q.; Takita, R.; Kikuzaki, Y.; Ozawa, F. *J. Am. Chem. Soc.* **2010**, *132*, 11420–11421.

(153) Okamoto, K.; Zhang, J.; Housekeeper, J. B.; Marder, S. R.; Luscombe, C. K. *Macromolecules* **2013**, *46*, 8059–8078.

(154) Broll, S.; Nübling, F.; Luzio, A.; Lentzas, D.; Komber, H.; Caironi, M.; Sommer, M. *Macromolecules* **2015**, *48*, 7481–7488.

(155) Bura, T.; Blaskovits, J. T.; Leclerc, M. *J. Am. Chem. Soc.* **2016**, *138*, 10056–10071.

(156) Koldemir, U.; Puniredd, S. R.; Wagner, M.; Tongay, S.; McCarley, T. D.; Kamenov, G. D.; Müllen, K.; Pisula, W.; Reynolds, J. R. *Macromolecules* **2015**, *48*, 6369–6377.

(157) Liebeke, M.; Dörries, K.; Meyer, H.; Lalk, M. In *Functional Genomics: Methods and Protocols*, *Methods in Molecular Biology*; Kaufmann, M., Klinger, C., Eds.; 2012; Vol. 815, pp 377–398.

(158) Thompson, B. C. Variable Band Gap Poly(3,4-alkylenedioxythiophene)-based Polymers for Photovoltaic and Electrochromic Applications, University of Florida, 2005.

(159) Cardona, C. M.; Li, W.; Kaifer, A. E.; Stockdale, D.; Bazan, G. C. *Adv. Mater.* **2011**, *23*, 2367–2371.

(160) Berera, R.; Van, R.; Ae, G.; Kennis, J. T. M. *Photosynth. Res.* **2009**, *101*, 105–118.

(161) Ohkita, H.; Ito, S. *Polymer* **2011**, *52*, 4397–4417.

(162) Ohkita, H.; Tamai, Y.; Benten, H.; Ito, S. *IEEE J. Sel. Top. Quantum Electron.* **2016**, *22*, 4100612.

(163) Mathot, V.; Pyda, M.; Pijpers, T.; Vanden Poel, G.; van de Kerkhof, E.; van Herwaarden, S.; van Herwaarden, F.; Leenaers, A. *Thermochim. Acta* **2011**, *522*, 36–45.

(164) Mueller, C. J.; Singh, C. R.; Thelakkat, M. *J. Polym. Sci. Part B Polym. Phys.* **2016**, *54*, 639–648.

(165) Zou, Q.; Leang, K.; Sadoun, E.; Reed, M.; Devasia, S. *Asian J. Control* **2004**, *6*, 164–178.

(166) Müller-Buschbaum, P. *Adv. Mater.* **2014**, *26*, 7692–7709.

(167) Zen, A.; Saphiannikova, M.; Neher, D.; Grenzer, J.; Grigorian, S.; Pietsch, U.; Asawapirom, U.; Janietz, S.; Scherf, U.; Lieberwirth, I.; Wegner, G. *Macromolecules* **2006**, *39*, 2162–2171.

(168) Sun, K.; Xiao, Z.; Lu, S.; Zajaczkowski, W.; Pisula, W.; Hanssen, E.; White, J. M.; Williamson, R. M.; Subbiah, J.; Ouyang, J.; Holmes, A. B.; Wong, W. W. H.; Jones, D. J. *Nat. Commun.* **2015**, *6*, 6013.

(169) Ilavsky, J. *J. Appl. Crystallogr.* **2012**, *45*, 324–328.

(170) Stribeck, N.; Nöchel, U. *J. Appl. Crystallogr.* **2009**, *42*, 295–301.

(171) Grand, C. Controlling Electronic Properties and Morphology of Isoindigo-Based Polymers for Photovoltaic Applications, Georgia Institute of Technology, 2015.

(172) Portale, G.; Hermida-Merino, D.; Bras, W. *Eur. Polym. J.* **2016**, *81*, 415–432.

(173) Graham, K. R.; Mei, J.; Stalder, R.; Shim, J. W.; Cheun, H.; Steffy, F.; So, F.; Kippelen, B.; Reynolds, J. R. *ACS Appl. Mater. Interfaces* **2011**, *3*, 1210–1215.

(174) Carr, J. A.; Nalwa, K. S.; Mahadevapuram, R.; Chen, Y.; Anderegg, J.; Chaudhary, S. *ACS Appl. Mater. Interfaces* **2012**, *4*, 2831–2835.

(175) Choi, S.; Fuentes-Hernandez, C.; Wang, C.-Y.; Khan, T. M.; Larraín, F. A.; Zhang, Y.; Barlow, S.; Marder, S. R.; Kippelen, B. *ACS Appl. Mater. Interfaces* **2016**, *8*, 24744–24752.

(176) Amb, C. M.; Chen, S.; Graham, K. R.; Subbiah, J.; Small, C. E.; So, F.; Reynolds, J. R. *J. Am. Chem. Soc.* **2011**, *133*, 10062–10065.

(177) Small, C. E.; Chen, S.; Subbiah, J.; Amb, C. M.; Tsang, S.-W.; Lai, T.-H.; Reynolds, J. R.; So, F. *Nat. Photon.* **2012**, *6*, 115–120.

(178) Zhang, Y.; Zou, J.; Yip, H.-L.; Sun, Y.; Davies, J. A.; Chen, K.-S.; Acton, O.; Jen, A. K.-Y. *J. Mater. Chem.* **2011**, *21*, 3895.

(179) Hong, Y. R.; Ng, J. Y.; Wong, H. K.; Moh, L. C. H.; Yip, Y. J.; Chen, Z. K.; Norsten, T. B. *Sol. Energ. Mat. Sol. Cells* **2012**, *102*, 58–65.

(180) Zhao, X.; Tang, H.; Yang, D.; Li, H.; Xu, W.; Yin, L.; Yang, X. *Chin. J. Chem.* **2012**, *30*, 2052–2058.

(181) Cai, W.; Liu, P.; Jin, Y.; Xue, Q.; Liu, F.; Russell, T. P.; Huang, F.; Yip, H.-L.; Cao, Y. *Adv. Sci.* **2015**, *2*, 1500095.

(182) Aïch, B. R.; Beaupré, S.; Leclerc, M.; Tao, Y. *Org. Electron.* **2014**, *15*, 543–548.

(183) Guo, X.; Zhou, N.; Lou, S. J.; Hennek, J. W.; Ponce Ortiz, R.; Butler, M. R.; Boudreault, P. L. T.; Strzalka, J.; Morin, P. O.; Leclerc, M.; López Navarrete, J.

T.; Ratner, M. A.; Chen, L. X.; Chang, R. P. H.; Facchetti, A.; Marks, T. J. *J. Am. Chem. Soc.* **2012**, *134*, 18427–18439.

(184) Gendron, D.; Morin, P.-O.; Berrouard, P.; Allard, N.; Aïch, B. R.; Garon, C. N.; Tao, Y.; Leclerc, M. *Macromolecules* **2011**, *44*, 7188–7193.

(185) Constantinou, I.; Lai, T.-H.; Zhao, D.; Klump, E. D.; Deininger, J. J.; Lo, C. K.; Reynolds, J. R.; So, F. *ACS Appl. Mater. Interfaces* **2015**, *7*, 4826–4832.

(186) Kim, J. S.; Fei, Z.; Wood, S.; James, D. T.; Sim, M.; Cho, K.; Heeney, M. J.; Kim, J.-S. *Adv. Energy Mater.* **2014**, *4*, 1400527.

(187) Nielsen, C. B.; Bjørnholm, T. *Org. Lett.* **2004**, *6*, 3381–3384.

(188) Drozdov, F. V.; Myshkovskaya, E. N.; Susarova, D. K.; Troshin, P. A.; Fominykh, O. D.; Balakina, M. Y.; Bakirov, A. V.; Shcherbina, M. A.; Choi, J.; Tondelier, D.; Buzin, M. I.; Chvalun, S. N.; Yassar, A.; Ponomarenko, S. A. *Macromol. Chem. Phys.* **2013**, *214*, 2144–2156.

(189) Hou, J.; Chen, H.-Y.; Zhang, S.; Li, G.; Yang, Y. *J. Am. Chem. Soc.* **2008**, *130*, 16144–16145.

(190) Kuwabara, J.; Yasuda, T.; Choi, S. J.; Lu, W.; Yamazaki, K.; Kagaya, S.; Han, L.; Kanbara, T. *Adv. Funct. Mater.* **2014**, *24*, 3226–3233.

(191) Leong, W. L.; Welch, G. C.; Kaake, L. G.; Takacs, C. J.; Sun, Y.; Bazan, G. C.; Heeger, A. J. *Chem. Sci.* **2012**, *3*, 2103–2109.

(192) Katsouras, A.; Gasparini, N.; Koulogiannis, C.; Spanos, M.; Ameri, T.; Brabec, C. J.; Chochos, C. L.; Avgeropoulos, A. *Macromol. Rapid Commun.* **2015**, *36*, 1778–1797.

(193) Yamaguchi, S.; Itami, Y.; Tamao, K. *Organometallics* **1998**, *17*, 4910–4916.

(194) Kohn, P.; Huettner, S.; Komber, H.; Senkovskyy, V.; Tkachov, R.; Kiriy, A.; Friend, R. H.; Steiner, U.; Huck, W. T. S.; Sommer, J. U.; Sommer, M. *J. Am. Chem. Soc.* **2012**, *134*, 4790–4805.

(195) Wong, W. W. H.; Banal, J. L.; Geraghty, P. B.; Hong, Q.; Zhang, B.; Holmes, A. B.; Jones, D. J. *Chem. Rec.* **2015**, *15*, 1006–1020.

(196) Sirringhaus, H.; Brown, P. J.; Friend, R. H.; Nielsen, M. M.; Bechgaard, K.; Langeveld-Voss, B. M. W.; Spiering, A. J. H.; Janssen, R. A. J.; Meijer, E. W.; Herwig, P.; de Leeuw, D. M. *Nature* **1999**, *401*, 685–688.

(197) Dimitrov, S.; Schroeder, B.; Nielsen, C.; Bronstein, H.; Fei, Z.; McCulloch, I.; Heeney, M.; Durrant, J. *Polymers* **2016**, *8*, 14.

(198) Kawashima, K.; Tamai, Y.; Ohkita, H.; Osaka, I.; Takimiya, K. *Nat. Commun.* **2015**, *6*, 10085.

(199) Szarko, J. M.; Rolczynski, B. S.; Lou, S. J.; Xu, T.; Strzalka, J.; Marks, T. J.; Yu, L.; Chen, L. X. *Adv. Funct. Mater.* **2014**, *24*, 10–26.

(200) Shivanna, R.; Shoaee, S.; Dimitrov, S.; Kandappa, S. K.; Rajaram, S.; Durrant, J. R.; Narayan, K. S. *Energy Environ. Sci.* **2014**, *7*, 435.

(201) Chow, P. C. Y.; Gélinas, S.; Rao, A.; Friend, R. H. *J. Am. Chem. Soc.* **2014**, *136*, 3424–3429.

(202) Gehrig, D. W.; Howard, I. A.; Laquai, F. *J. Phys. Chem. C* **2015**, *119*, 13509–13515.

(203) Rao, A.; Chow, P. C. Y.; Gélinas, S.; Schlenker, C. W.; Li, C.-Z.; Yip, H.-L.; Jen,

A. K.-Y.; Ginger, D. S.; Friend, R. H. *Nature* **2013**, *500*, 435–439.

(204) Vandewal, K.; Tvingstedt, K.; Gadisa, A.; Inganäs, O.; Manca, J. V. *Phys. Rev. B* **2010**, *81*, 125204.

(205) Flores, J.-C.; Berens, U.; Bienewald, F.; Kirner, H. J.; Turbiez, M. G. R. Ketopyrroles as Organic Semiconductors. WO2009053291 A1, 2010.

(206) Mei, J.; Graham, K. R.; Stalder, R.; Reynolds, J. R. *Org. Lett.* **2010**, *12*, 660–663.

(207) Mullekom, H. A. M. van; Vekemans, J. A. J. M.; Havinga, E. E.; Meijer, E. W. *Mater. Sci. Eng. R* **2001**, *32*, 1–40.

(208) Wang, E.; Ma, Z.; Zhang, Z.; Vandewal, K.; Henriksson, P.; Inganäs, O.; Zhang, F.; Andersson, M. R. *J. Am. Chem. Soc.* **2011**, *133*, 14244–14247.

(209) Ashraf, R. S.; Kronemeijer, A. J.; James, D. I.; Sirringhaus, H.; McCulloch, I. *Chem. Commun.* **2012**, *48*, 3939–3941.

(210) Van Pruissen, G. W. P.; Gholamrezaie, F.; Wienk, M. M.; Janssen, R. A. J. *J. Mater. Chem.* **2012**, *22*, 20387–20393.

(211) Conboy, G.; Spencer, H. J.; Angioni, E.; Kanibolotsky, A. L.; Findlay, N. J.; Coles, S. J.; Wilson, C.; Pitak, M. B.; Risko, C.; Coropceanu, V.; Brédas, J.; Skabara, P. J. *Mater. Horiz.* **2016**, *3*, 333–339.

(212) Li, W.; Lee, T.; Oh, S. J.; Kagan, C. R. *ACS Appl. Mater. Interfaces* **2011**, *3*, 3874–3883.

(213) Dou, L.; You, J.; Yang, J.; Chen, C.-C.; He, Y.; Murase, S.; Moriarty, T.; Emery, K.; Li, G.; Yang, Y. *Nat. Photon.* **2012**, *6*, 180–185.

(214) Ma, Z.; Sun, W.; Himmelberger, S.; Vandewal, K.; Tang, Z.; Bergqvist, J.; Salleo,

A.; Andreasen, J. W.; Inganäs, O.; Andersson, M. R.; Müller, C.; Zhang, F.; Wang, E. *Energy Environ. Sci.* **2014**, *7*, 361–369.

(215) Lee, J. K.; Ma, W. L.; Brabec, C. J.; Yuen, J.; Moon, J. S.; Kim, J. Y.; Lee, K.; Bazan, G. C.; Heeger, A. J. *J. Am. Chem. Soc.* **2008**, *130*, 3619–3623.

(216) Liu, F.; Wang, C.; Baral, J. K.; Zhang, L.; Watkins, J. J.; Briseno, A. L.; Russell, T. P. *J. Am. Chem. Soc.* **2013**, *135*, 19248–19259.

(217) Li, W.; Hendriks, K. H.; Furlan, A.; Roelofs, W. S. C.; Wienk, M. M.; Janssen, R. A. J. *J. Am. Chem. Soc.* **2013**, *135*, 18942–18948.

(218) Zhou, H.; Yang, L.; Xiao, S.; Liu, S.; You, W. *Macromolecules* **2010**, *43*, 811–820.

(219) Lo, C. K.; Reynolds, J. R. *Polymer* **2016**, *99*, 741–747.

(220) Homyak, P.; Liu, Y.; Liu, F.; Russel, T. P.; Coughlin, E. B. *Macromolecules* **2015**, *48*, 6978–6986.

(221) Berrouard, P.; Pron, A.; Veilleux, J.; Leclerc, M. *J. Org. Chem.* **2012**, *77*, 8167–8173.

(222) Zhu, Z.; Waller, D.; Gaudiana, R.; Morana, M.; Mühlbacher, D.; Scharber, M.; Brabec, C. *Macromolecules* **2007**, *40*, 1981–1986.

(223) Zhou, J.; Xie, S.; Amond, E. F.; Becker, M. L. *Macromolecules* **2013**, *46*, 3391–3394.

(224) Kim, K.-H.; Yu, H.; Kang, H.; Kang, D. J.; Cho, C.-H.; Cho, H.-H.; Oh, J. H.; Kim, B. J. *J. Mater. Chem. A* **2013**, *1*, 14538–14547.

(225) Deng, P.; Lei, Y.; Wu, B.; Zheng, X.; Lu, Y.; Zhu, F.; Ong, B. S. *Dye. Pigm.* **2016**,

134, 251–257.

(226) Yue, W.; Zhao, Y.; Song, D.; Tian, H.; Xie, Z.; Yan, D.; Geng, Y.; Wang, F. *Macromolecules* **2009**, *42*, 6510–6518.

(227) Stalder, R.; Mei, J.; Subbiah, J.; Grand, C.; Estrada, L. A.; So, F.; Reynolds, J. R. *Macromolecules* **2011**, *44*, 6303–6310.

(228) Estrada, L. A.; Stalder, R.; Abboud, K. A.; Risko, C.; Brédas, J.-L.; Reynolds, J. R. *Macromolecules* **2013**, *46*, 8832–8844.

(229) Shao, J.; Zhang, X.; Tian, H.; Geng, Y.; Wang, F. *J. Mater. Chem. C* **2015**, *3*, 7567–7574.

(230) Tamayo, A. B.; Walker, B.; Nguyen, T. *J. Phys. Chem. C* **2008**, *112*, 11545–11551.

(231) Walker, B.; Tamayo, A. B.; Dang, X.-D.; Zalar, P.; Seo, J. H.; Garcia, A.; Tantiwiwat, M.; Nguyen, T.-Q. *Adv. Funct. Mater.* **2009**, *19*, 3063–3069.

(232) Mei, J.; Graham, K. R.; Stalder, R.; Tiwari, S. P.; Cheun, H.; Shim, J.; Yoshio, M.; Nuckolls, C.; Kippelen, B.; Castellano, R. K.; Reynolds, J. R. *Chem. Mater.* **2011**, *23*, 2285–2288.

(233) Hendriks, K. H.; Li, W.; Heintges, G. H. L.; Pruissen, G. W. P. Van; Wienk, M. M.; Janssen, R. A. J. *J. Am. Chem. Soc.* **2014**, *136*, 11128–11133.

(234) Morita, D. K.; Stille, J. K.; Norton, J. R. *J. Am. Chem. Soc.* **1995**, *117*, 8576–8581.

(235) Ye, E.; Tan, H.; Li, S.; Fan, W. Y. *Angew. Chem.* **2006**, *118*, 1138–1141.

(236) Tamayo, A. B.; Tantiwiwat, M.; Walker, B.; Nguyen, T. Q. *J. Phys. Chem. C* **2008**, *112*, 15543–15552.

(237) Jackson, N. E.; Savoie, B. M.; Kohlstedt, K. L.; Olvera de la Cruz, M.; Schatz, G. C.; Chen, L. X.; Ratner, M. A. *J. Am. Chem. Soc.* **2013**, *135*, 10475–10483.

(238) Shao, Y.; Molnar, L. F.; Jung, Y.; Kussmann, J.; Ochsenfeld, C.; Brown, S. T.; Gilbert, A. T. B.; Slipchenko, L. V.; Levchenko, S. V.; O'Neill, D. P.; DiStasio Jr, R. A.; Lochan, R. C.; Wang, T.; Beran, G. J. O.; Besley, N. A.; Herbert, J. M.; Yeh Lin, C.; Van Voorhis, T.; Hung Chien, S.; Sodt, A.; Steele, R. P.; Rassolov, V. A.; Maslen, P. E.; Korambath, P. P.; Adamson, R. D.; Austin, B.; Baker, J.; Byrd, E. F. C.; Dachsel, H.; Doerksen, R. J.; Dreuw, A.; Dunietz, B. D.; Dutoi, A. D.; Furlani, T. R.; Gwaltney, S. R.; Heyden, A.; Hirata, S.; Hsu, C.-P.; Kedziora, G.; Khalliulin, R. Z.; Klunzinger, P.; Lee, A. M.; Lee, M. S.; Liang, W.; Lotan, I.; Nair, N.; Peters, B.; Proynov, E. I.; Pieniazek, P. A.; Min Rhee, Y.; Ritchie, J.; Rosta, E.; David Sherrill, C.; Simmonett, A. C.; Subotnik, J. E.; Lee Woodcock III, H.; Zhang, W.; Bell, A. T.; Chakraborty, A. K.; Chipman, D. M.; Keil, F. J.; Warshel, A.; Hehre, W. J.; Schaefer III, H. F.; Kong, J.; Krylov, A. I.; Gill, P. M. W.; Head-Gordon, M. *Phys. Chem. Chem. Phys.* **2006**, *8*, 3172–3191.

(239) Krylov, A. I.; Gill, P. M. W. *Wiley Interdiscip. Rev. Comput. Mol. Sci.* **2013**, *3*, 317–326.

(240) Borshchev, O.; Sizov, A.; Agina, E.; Bessonov, A.; Ponomarenko, S. *Chem. Commun.* **2017**, *53*, 885–888.

(241) Kim, J.; Levitsky, I. a; McQuade, D. T.; Swager, T. M. *J. Am. Chem. Soc.* **2002**, *124*, 7710–7718.

(242) Musumeci, C.; Salzmann, I.; Bonacchi, S.; Röthel, C.; Duhm, S.; Koch, N.; Samorì, P. *Adv. Funct. Mater.* **2015**, *25*, 2501–2510.

(243) Chen, X.; Zhang, Z.; Ding, Z.; Liu, J.; Wang, L. *Angew. Chem. Int. Ed.* **2016**, *55*, 10376 –10380.

(244) Chen, C. Y.; Wu, S. J.; Wu, C. G.; Chen, J. G.; Ho, K. C. *Angew. Chem. Int. Ed.* **2006**, *45*, 5822–5825.

(245) Marzano, G.; Ciasca, C. V.; Babudri, F.; Bianchi, G.; Pellegrino, A.; Po, R.; Farinola, G. M. *Eur. J. Org. Chem.* **2014**, *30*, 6583–6614.

(246) Thompson, B. C.; Kim, Y.; Reynolds, J. R. *Macromolecules* **2005**, *38*, 5359–5362.

(247) Kannan, N.; Vakeesan, D. *Renew. Sustain. Energy Rev.* **2016**, *62*, 1092–1105.

(248) Green, M. A.; Emery, K.; Hishikawa, Y.; Warta, W.; Dunlop, E. D. *Prog. Photovolt. Res. Appl.* **2016**, *24*, 905–913.

(249) Polman, A.; Knight, M.; Garnett, E. C.; Ehrler, B.; Sinke, W. C. *Science* **2016**, *352*, 4424.

(250) Mei, J.; Bao, Z. *Chem. Mater.* **2014**, *26*, 604−615.

(251) Jakowetz, A. C.; Böhm, M. L.; Sadhanala, A.; Huettner, S.; Rao, A.; Friend, R. H. *Nat. Mater.* **2017**, DOI: 10.1038/NMAT4865.

(252) Hwang, Y.-J.; Li, H.; Courtright, B. A. E.; Subramaniyan, S.; Jenekhe, S. A. *Adv. Mater.* **2016**, *28*, 124–131.

(253) Yao, H.; Yu, R.; Shin, T. J.; Zhang, H.; Zhang, S.; Jang, B.; Uddin, M. A.; Woo, H. Y.; Hou, J. *Adv. Energy Mater.* **2016**, *6*, 1600742.

(254) Li, Y.; Qian, D.; Zhong, L.; Lin, J.-D.; Jiang, Z.-Q.; Zhang, Z.-G.; Zhang, Z.; Li, Y.; Liao, L.-S.; Zhang, F. *Nano Energy* **2016**, *27*, 430–438.

(255) Hadmojo, W. T.; Nam, S. Y.; Shin, T. J.; Yoon, S. C.; Jang, S.-Y.; Jung, I. H. *J. Mater. Chem. A* **2016**, *4*, 12308–12318.

(256) Nielsen, C. B.; Holliday, S.; Chen, H.-Y.; Cryer, S. J.; McCulloch, I. *Acc. Chem. Res.* **2015**, *48*, 2803–2812.

(257) Yan, H.; Chen, Z.; Zheng, Y.; Newman, C.; Quinn, J. R.; Dötz, F.; Kastler, M.; Facchetti, A. *Nature* **2009**, *457*, 679–686.

(258) Li, Z.; Lin, J. D. a.; Phan, H.; Sharenko, A.; Proctor, C. M.; Zalar, P.; Chen, Z.; Facchetti, A.; Nguyen, T.-Q. *Adv. Funct. Mater.* **2014**, *24*, 6989–6998.

(259) Li, M.; Wang, L.; Liu, J.; Zhou, K.; Yu, X.; Xing, R.; Geng, Y.; Han, Y. *Phys. Chem. Chem. Phys.* **2014**, *16*, 4528–4537.

(260) Liu, Y.; Mu, C.; Jiang, K.; Zhao, J.; Li, Y.; Zhang, L.; Li, Z.; Lai, J. Y. L.; Hu, H.; Ma, T.; Hu, R.; Yu, D.; Huang, X.; Tang, B. Z.; Yan, H. *Adv. Mater.* **2015**, *27*, 1015–1020.

(261) Zhao, J.; Li, Y.; Lin, H.; Liu, Y.; Jiang, K.; Mu, C.; Ma, T.; Lai, J. Y. L.; Hu, H.; Yu, D.; Yan, H. *Energy Environ. Sci.* **2015**, *8*, 520–525.

(262) Zhong, H.; Wu, C. H.; Li, C. Z.; Carpenter, J.; Chueh, C. C.; Chen, J. Y.; Ade, H.; Jen, A. K. Y. *Adv. Mater.* **2016**, *28*, 951–958.

(263) Duan, Y.; Xu, X.; Yan, H.; Wu, W.; Li, Z.; Peng, Q. *Adv. Mater.* **2017**, *29*, 1605115.

(264) Lee, J.; Singh, R.; Sin, D. H.; Kim, H. G.; Song, K. C.; Cho, K. *Adv. Mater.* **2016**, *28*, 69–76.

(265) Yi, J.; Wang, Y.; Luo, Q.; Lin, Y.; Tan, H.; Wang, H.; Ma, C.-Q. *Chem. Commun.* **2016**, *52*, 1649–1652.

(266) Lin, Y.; Zhan, X. *Mater. Horizons* **2014**, *1*, 470–488.

(267) Zhao, W.; Qian, D.; Zhang, S.; Li, S.; Inganäs, O.; Gao, F.; Hou, J. *Adv. Mater.* **2016**, *28*, 4734–4739.

(268) Tait, J. G.; Merckx, T.; Li, W.; Wong, C.; Gehlhaar, R.; Cheyns, D.; Turbiez, M.; Heremans, P. *Adv. Funct. Mater.* **2015**, *25*, 3393–3398.

(269) Xiong, K.; Hou, L.; Wu, M.; Huo, Y.; Mo, W.; Yuan, Y.; Sun, S.; Xu, W.; Wang, E. *Sol. Energ. Mat. Sol. Cells* **2015**, *132*, 252–259.

(270) Krebs, F. C. *Sol. Energ. Mat. Sol. Cells* **2009**, *93*, 465–475.

(271) Krebs, F. C.; Jørgensen, M.; Norrman, K.; Hagemann, O.; Alstrup, J.; Nielsen, T. D.; Fyenbo, J.; Larsen, K.; Kristensen, J. *Sol. Energ. Mat. Sol. Cells* **2009**, *93*, 422–441.

(272) Vak, D.; Van Embden, J.; Wong, W. W. H.; Watkins, S. *Appl. Phys. Lett.* **2015**, *106*, 33302.

(273) Ro, H. W.; Downing, J. M.; Engmann, S.; Herzing, A. A.; DeLongchamp, D. M.; Richter, L. J.; Mukherjee, S.; Ade, H.; Abdelsamie, M.; Jagadamma, L. K.; Amassian, A.; Liu, Y.; Yan, H. *Energy Environ. Sci.* **2016**, *9*, 2835–2846.

(274) Abdelsamie, M.; Zhao, K.; Niazi, M. R.; Chou, K. W.; Amassian, A. *J. Mater. Chem. C* **2014**, *2*, 3373–3381.

(275) Shin, N.; Richter, L. J.; Herzing, A. a.; Kline, R. J.; DeLongchamp, D. M. *Adv. Energy Mater.* **2013**, *3*, 938–948.

(276) Rumer, J. W.; Ashraf, R. S.; Eisenmenger, N. D.; Huang, Z.; Meager, I.; Nielsen, C. B.; Schroeder, B. C.; Chabinyc, M. L.; McCulloch, I. *Adv. Energy Mater.* **2015**, *5*, 1401426.

(277) Kwon, S.; Kang, H.; Lee, J.; Lee, J.; Hong, S.; Kim, H.; Lee, K. *Adv. Energy Mater.* **2016**, *6*, 1601496.

(278) Chatzisideris, M. D.; Espinosa, N.; Laurent, A.; Krebs, F. C. *Sol. Energ. Mat. Sol. Cells* **2016**, *156*, 2–10.

(279) Krebs, F. C.; Nielsen, T. D.; Fyenbo, J.; Wadstrom, M.; Pedersen, M. S. *Energy Environ. Sci.* **2010**, *3*, 512–525.

(280) Cutting, C. L.; Bag, M.; Venkataraman, D. *J. Mater. Chem. C* **2016**, *4*, 10367–10370.

VITA

盧智健

Chi Kin Lo

Chi Kin Lo was born and lived in Hong Kong for the first nineteen years of his life, during which “the Pearl of the Orient” was British-governed for thirteen years and Chinese-governed for six years. His family name Lo, 盧 was given by his father and his first name, consisting of both Chi, 智 and Kin, 健, was given by his mother. 智 is one of the five constant virtues of Confucianism, means wisdom; 健 means health. He began his undergraduate study at the University of Arizona and obtained his bachelor’s degree in chemistry from Duquesne University in 2007. He entered the Olin Business School at Washington University immediately after and finished his Master of Business Administration degree in 2009. He enrolled in the Georgia Institute of Technology and joined the group of John R. Reynolds in 2012 to embark on a journey of becoming a true scientist. His interest in organic electronics and alternative energy led him to the field of organic photovoltaics, in which he focused on the design of polymers and molecules to unveil the structure-property relationship of conducting organic materials. He graduated in the Spring of 2017 with a doctorate degree in chemistry.